ISSN
2712-8172

Magazine of Civil Engineering

122(6), 2023

Magazine of Civil Engineering

ISSN 2712-8172

Online peer-reviewed open-access scientific journal in the field of Civil and Construction Engineering

Founder and Publisher: Peter the Great St. Petersburg Polytechnic University

This journal is registered by the Federal Service for Supervision of Communications, Information Technology, and Mass Media (ROSKOMNADZOR) in 2020. Certificate El No. FS77-77906 issued February 19, 2020.

Periodicity: 8 issues per year

Publication in the journal is open and free for all authors and readers.

Indexing: Scopus, Web of Sceince (ESCI, RSCI), DOAJ, Compendex, Google Academia, Index Copernicus, ProQuest, Ulrich's Serials Analysis System, CNKI

Corresponding address: 29 Polytechnicheskaya st., Saint Petersburg, 195251, Russia

Chief science editor: associate member of RAS, D.S. in Engineering, Vitaly V. Sergeev

Deputy chief science editors:
D.S. in Engineering, Galina L. Kozinetc

D.S. in Engineering, Sergey V. Korniyenko

Executive editor: Ekaterina A. Linnik

Translator, editor: Darya Yu. Alekseeva

DT publishing specialist:
Anastasiya A. Kononova

Contacts:
E-mail: mce@spbstu.ru
Web: http://www.engstroy.spbstu.ru

Date of issue: 02.10.2023

Contents

Magazine of Civil Engineering

ISSN 2712-8172

journal homepage: http://engstroy.spbstu.ru/

Research article

UDC 624.014.2

DOI: 10.34910/MCE.122.1

Stress-strain conditions of steel rod structures nodes

***Al.V. Golikov*[1], *I.M. Garanzha*[2] ✉, *K.S. Cherkasova*[1]**

[1] *Volgograd State Technical University, Volgograd, Russian Federation*

[2] *Moscow State University of Civil Engineering (National Research University), Moscow, Russian Federation*

✉ *garigo@mail.ru*

Keywords: stress-strain state, gusset, rod fastening, recommended thicknesses, safety factor, equivalent stress

Abstract. To obtain qualitative and quantitative indicators of changes in the stress-strain state of the nodes of steel bar structures, we identified four characteristic types of nodes. On the basis of modeling in the "Lira-CAD" software package, we analyzed the stress-strain state of four types of nodes for steel trusses with a symmetric and asymmetric design solution. For the research, a calculation of volumetric models of nodes according to the fourth strength theory was performed. At the current moment, the choice of the required thickness of the truss gusset is performed according to the value of the maximum force in the rods. During the nodes modeling it was found that the safety factors depending on the node type for the symmetrical design solution are more than 40 %. The obtained data allow us to reduce the thickness of the gusset taking into account design constraints. It was found that the safety factors depending on the node type for the asymmetric design solution are 7–90 %. The simulation results substantiated the possibility of reducing the gusset thickness for node type 3, and for node types 1, 2 and 4, they showed the necessity of increasing the thickness taking into account design constraints. We derived the refined dependences between the gusset thickness and the maximum force in the attached rods for each structural type of nodes. Based on results of the analysis, we developed recommendations for calculating the most typical types of nodes and presented them in the form of tables and dependencies. For a constructive solution of fastening of gusset braces at an acute angle, we analyzed the influence of the eccentricity value on the stress in gussets. We determined that the main parameter influencing to the stress-strain state of the gusset is the displacement of attached element relative to the axis of the elements fastening. We derived dependences and made graphs of the displacement influence on stresses for different values of gusset thickness.

Citation: Golikov, Al.V., Garanzha, I.M., Cherkasova, K.S. Stress-strain conditions of steel rod structures nodes. Magazine of Civil Engineering. 2023. 122(6). Article no. 12201. DOI: 10.34910/MCE.122.1

1. Introduction

1.1. Definition of the research object

More than 60 % of all building structures can be safely attributed to rod systems. More than 30 % of them are hinge-rod systems: roof trusses structures, braces elements.

In modern normative, guidance and reference literature fully describes the work of rods under load and formalizes it in the form of calculation methods. Most rod fastenings in hinge-rod systems are made using fastening plates (gussets). Currently, there are tables for choosing the gussets thickness, but the methodology for plates design is not formalized.

It is noteworthy that the regulatory documents allow the calculation of rods of lattice structures with rod length to cross-sectional ratio of more than 10:1, however, the gusset is undergoing the complex stress-strain state (SSS).

Complex SSS is caused not only by the fact that the force from the rods acts on the plate in different directions, causing both tension zones and zones of constrained compression (shear), but also due to the arising local moments. Local moments arise in the area of fastening of the plate's rods in case of fastening with two or more bolts or fastening by welding.

The research subject is the phenomenon of changing the stress-strain state of the plates under study when changing the variable parameters.

1.2. Analytical literature review, which examines the current situation in the modern scientific community on this problem

The field of the plates operation was researched by V. Biderman [1], H. Osama [2], S. Timoshenko [3], N. Streletskiy [4], V. Ignat'ev [5].

I. Bubnov proposed the method for integrating differential equations for solving boundary value problems [1].

B. Galerkin proposed the similar method for integrating differential equations, which is widely used for calculating rectangular plates for various models of loading and plate fastening [2].

S. Timoshenko aspired to solve the problems of stability of homogeneous and isotropic thin rectangular plates under the assumption that the deflections of the plates are small in comparison with their thickness, which ensures the non-deformability of the middle surface. Such problems are described by the linear homogeneous equation in partial differentials [3].

Chapter 12 of Timoshenko's book [3] considered the principles of calculating a plate under the combined action of transverse loads and forces in its midplane, uniform tension. N. Streletskiy investigated the experimental installation of gussets in the nodes of heavy trusses [4]. The works of V. Ignat'ev showed that the most effective method for solving problems of rod systems calculating is the method of discrete finite elements (MDFE). The method makes it possible to consider the features of structural geometry, fastening conditions and the load form with the most possible accuracy [5].

In the regulatory and guideline literature there are no researches that form the basis for the table of recommended thicknesses [6] and [7], as well as the method for calculating plates for the action of longitudinal multidirectional forces.

A review of the shaping of steel rod systems is performed in a number of modern researches [12, 13].

Operation under load of plates in rod structures is considered in researches [14, 15].

The plane stress-strain state of steel is described in the relevant chapters of the normative documents [11].

Currently, active numerical and experimental researches of operation under load are being carried out for steel plates working as stiffening diaphragms in the frames of multistory buildings. The results are described in the works of M. Ramezani [17, 18], I. Verma [19], Y. Ly [20], Z. Zhou [21], O. Haddad [22] and also in the works [23–25].

The truss' gussets plates act like diaphragm plates of multistory buildings in a complex stress-strain state, however, the truss gusset plate is fixed on only one side, and the stiffening diaphragm plates are fixed on four sides.

Modeling of truss rods with a section from corners is performed in a work by Z. Deng [26].

Summarizing the results of the detailed analysis of the existing experience in the plates design and studies carried out with models of steel plates at the time of writing this work, we state the absence of clear results of modeling the operation of truss gusset plates for working conditions in the complex stress-strain state.

1.3. Statement of the research relevance

The relevance of the research topic is due to the fact that the existing regulatory, reference literature and scientific researches on the plates design quite fully developed methods for bending analysis under the action of moments, transverse loads and the combination of transverse loads and forces acting along the median plane, but the plates design for action of the longitudinal alternating load received little attention. There are tables for choosing the recommended thicknesses of gussets, but there are no design methods or documented researches substantiating these tables.

The presented work was done to fill the indicated gap.

1.4. Research goals and objectives

The main research goal is to establish the nature of the SSS distribution in the plates and to develop recommendations for the plates design.

To achieve this goal, the authors solved the following tasks:

- to classify by design the types of rods' junctions using connecting plates;
- to identify the types of nodes most common in practice for research;
- to perform the critical analysis of the existing experience in plates design for forces directed along the median plane of the plate;
- to develop design models of the investigated nodes for numerical research; perform design load cases and obtain stress fields;
- based on the results of factorial and regression analysis to derive dependencies that describe the nature of the change in the stress-strain state in the plate for the studied types of nodes;
- to develop recommendations for the design of the most characteristic types of nodes.

2. Methods

The gusset is in a complex stress-strain state (Fig. 1), significant local stresses arise in the zones of the elements' fastening due to the influence of the weld form and possible defects that are often found in the near-weld zone.

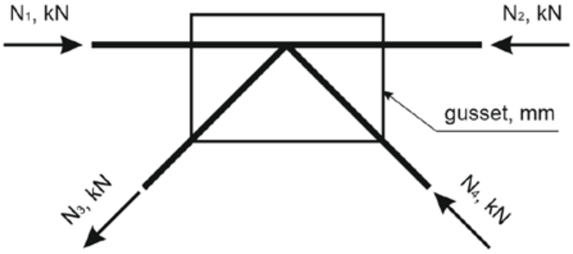

Figure 1. Gusset loading diagram by forces N from adjacent rods (N1 – N4 – rod forces).

The gusset operation is influenced by such features of the geometry of the heat-affected zone as defects in welded joints, concentration of stresses in the zones of holes and welds, initial curvatures, as well as the action of multidirectional forces.

In practice, four types of nodes are most common:

- symmetrical fastening of rods to gusset (Fig. 2, a);
- truss support node (Fig. 2, b);
- node of fastening the rack to truss belt (Fig. 2, c);
- node of fastening the braces elements to gusset with eccentricity (Fig. 2, d).

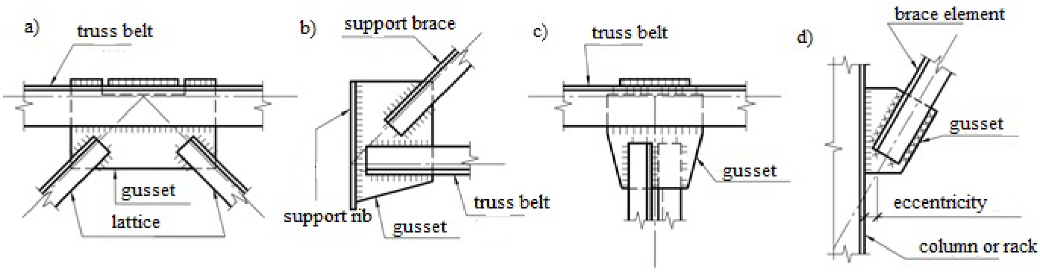

Figure 2. Types of nodes: symmetrical fastening of rods to the gusset (*a*); reference node (*b*); fastening of a rack to the truss belt (*c*); fastening of brace elements to columns and racks with eccentricity (*d*).

The research object is steel plates (gussets) connecting rods in hinged rod systems for the types of nodes shown in Fig. 2.

In this research using the finite element method implemented in Lira-SAPR software package, the nature of distribution of stress-strain state of truss gussets from paired corners is established depending on design solution of unit and value of acting loads. In the process the pattern of stress distribution in body of the gusset was assessed for four types of nodes of a symmetrical design solution: symmetrical fastening of rods, support node, post fastening node and eccentricity fastening node respectively. Was also analyzed the degree of influence of eccentricity's value on stress in gusset. Also sas determined the dependence of gussets' thickness on the maximum force in the attached rods and the subsequent conclusion about the level of safety margin. Subsequently, the thickness of the gussets was assigned not only based on the results of calculations, but also based on design considerations - the minimum design restrictions were taken into account in accordance with the requirements of regulatory documents (codes of rules).

The study was carried out on solid models of steel truss nodes. The main variable parameters are the configuration of the junction of the rods and the loads acting on the junction from the adjoining rods.

3. Results and Discussion

3.1. Research results of the work of trusses gussets with double-sided fastening of lattice elements

Material – mild steel with design yield strength of R_y = 240 MPa, modulus of elasticity E = 2.06×10^5 MPa, Poisson's ratio μ = 0.3.

The calculation of the steel trusses' nodes was performed in the software package Lira-SAPR. Rods and gussets were modeled by volumetric finite elements of the FE-36 type. Triangular volumetric finite elements were applied with an angle not less than 15°. The range of angles of lattice elements fastening was 30 – 60^0.

The load was evenly distributed over the cross-sectional area (Fig. 4). The load on the knots was taken according to the average values of forces from the intervals of values, according to which it was decided to take the thickness of the facings from the reference literature (intervals of forces are given in the header of Table 2 and Table 4). The cross-sections of the elements were taken on the basis of the bearing capacity to absorb the forces acting in them. The transition from the forces in the rods to the pressure on the loaded faces of the cross-sections of the rod models was carried out by the equation:

$$q_i = \frac{N_i}{A_i}, \tag{1}$$

where q_i is load in the form of pressure on the loaded cross-section faces of rod models; N_i is rod force; A_i is cross-sectional area of the rods.

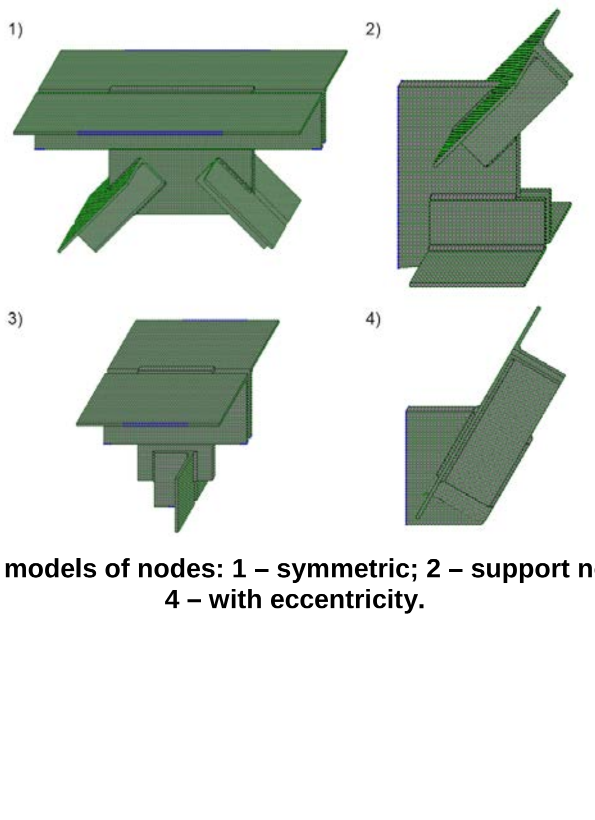

Figure 3. Finite element models of nodes: 1 – symmetric; 2 – support node; 3 – rack fastening; 4 – with eccentricity.

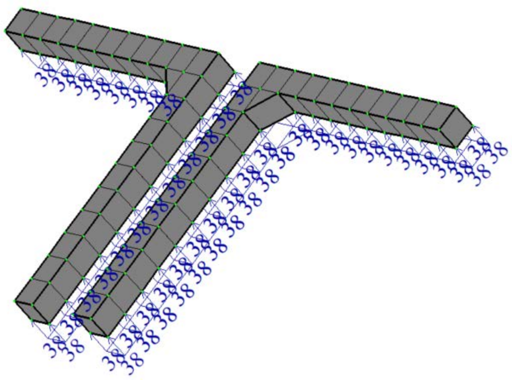

Figure 4. Model of load application (load, *q*, is given in MPa).

Considered the equivalent stresses variation in structural elements depending on the structural nodes solution. Fig. 5–8 show the isofields of equivalent stresses in the gusset for four types of nodes of symmetric design solution: symmetric fastening of rods, support node, fastening node of the rack and eccentric fastening of the brace, respectively.

According to the calculation results to determine the nature of the of stress fields distribution, gussets of trusses are separately identified. Diagrams with stress distribution in gussets of trusses for the studied design solutions of nodes are shown in Fig. 5–8. The analysis of the values of the reduced stresses in the trusses of the recommended thickness makes it possible to determine the value of the reserves under the action of the recommended values of the design forces.

To determine the actual load-carrying capacity of the truss beams, we corrected the values of design forces on the rods so that the stresses in the beams satisfy the condition $\sigma_{red} < R_y$ with a margin of 1–5 %. Based on the calculations results, built the diagrams for the dependence of the gusset thicknesses on the maximum force in the attached rods of models 1 – 4 and, accordingly, the obtained approximating dependences (2) – (5):

$$t_{f.1} = 17.36\left(1 - e^{-0.00251N}\right); \quad (2)$$

$$t_{f.2} = 17.04\left(1 - e^{-0.00261N}\right); \quad (3)$$

$$t_{f.3} = 14.44\left(1 - e^{-0.00373N}\right); \quad (4)$$

$$t_{f.4} = 16.46\left(1 - e^{-0.00292N}\right). \quad (5)$$

Note to formulas (2) – (5): force in kN, thickness of beams in mm.

Nomograms were obtained from the results of processing the data sets of a series of experiments on numerical models. Standard error: 0.15–0.18. Correlation coefficient: 0.98 – 0.99. The results obtained from the formulas are applicable for the force range from 150 to 2000 kN.

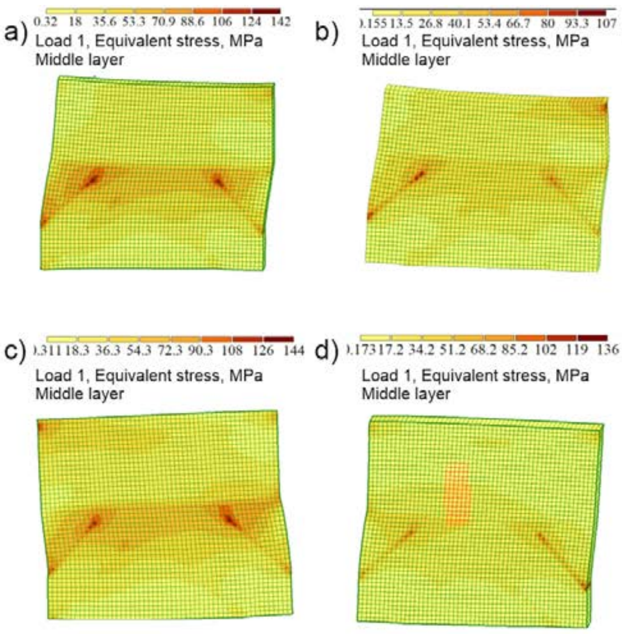

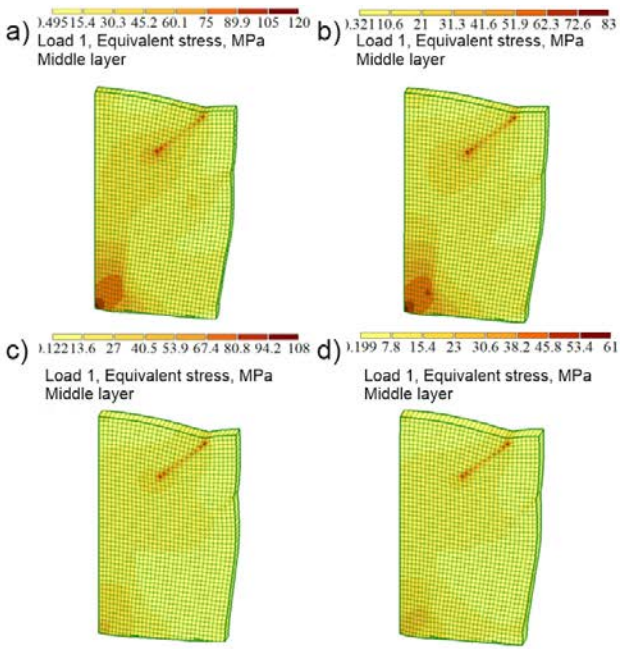

Figure 5. Isofields of equivalent stresses of finite element model for node type 1: a) t_f = 8 mm; b) t_f = 10 mm; c) t_f = 12 mm; d) t_f = 14 mm.

Figure 6. Isofields of equivalent stresses of the finite element model for node type 2: a) t_f = 10 mm; b) t_f = 12 mm; c) t_f = 14 mm; d) t_f = 16 mm.

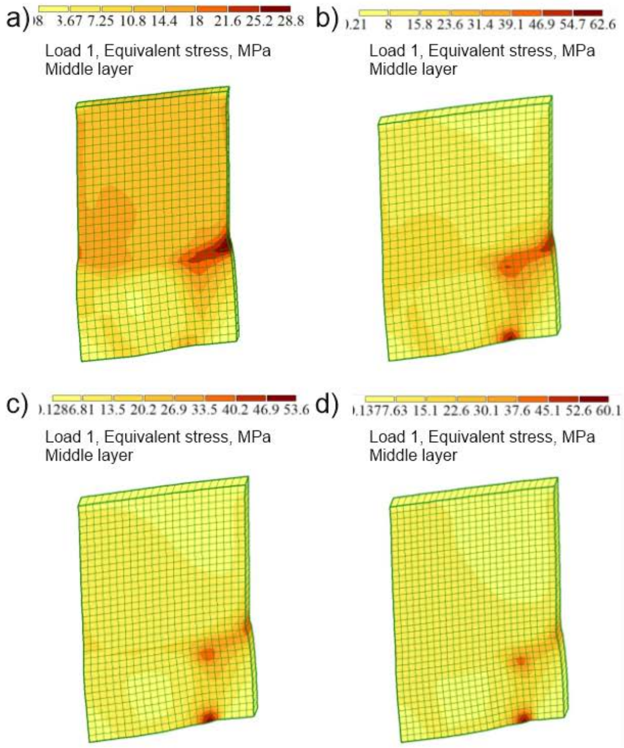

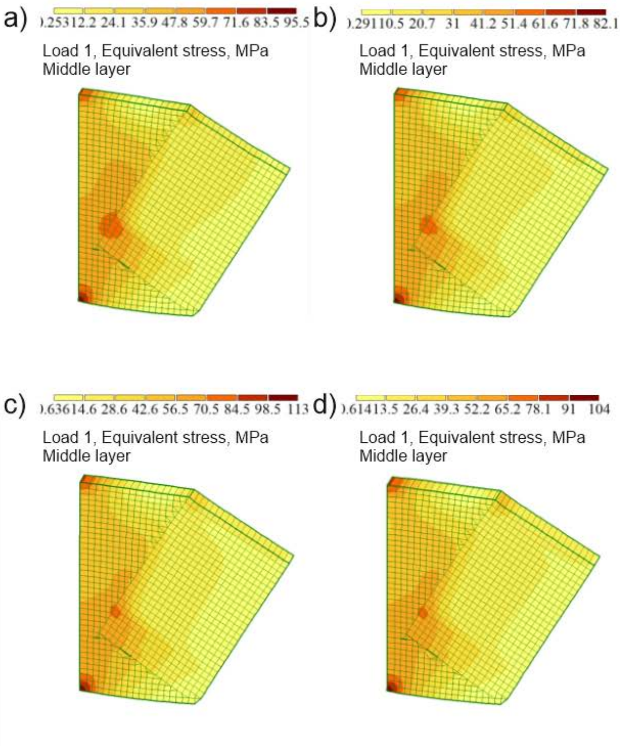

Figure 7. Isofields of equivalent stresses of the finite element model for node type 3: a) t_f = 6 mm; b) t_f = 10 mm; c) t_f = 12 mm; d) t_f = 14 mm.

Figure 8. Isofields of equivalent stresses of the finite element model for node type 4: a) t_f = 8 mm; b) t_f = 10 mm; c) t_f = 12 mm; d) t_f = 14 mm

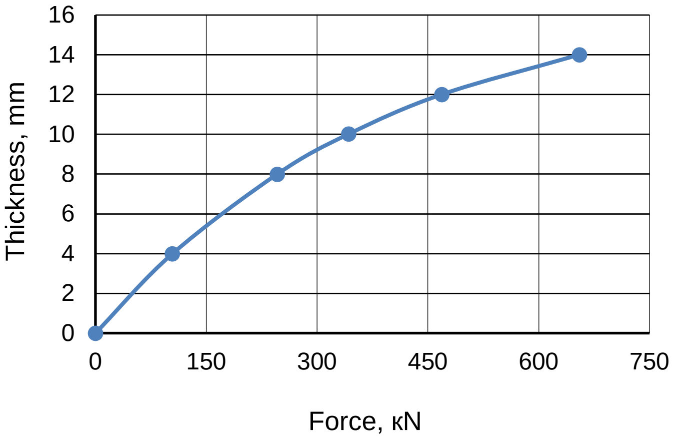

Figure 9. Dependence of the gusset thickness on the maximum force in the attached rods of the finite element model for node type 1.

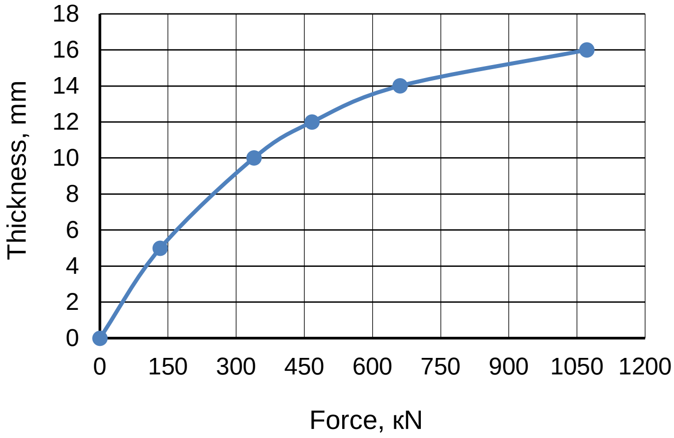

Figure 10. Dependence of the gusset thickness on the maximum force in the attached rods of the finite element model for node type 2.

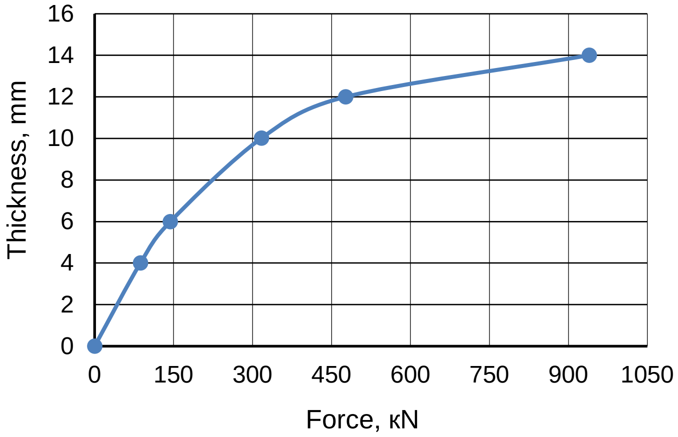

Figure 11. Dependence of the gusset thickness on the maximum force in the attached rods of the finite element model for node type 3.

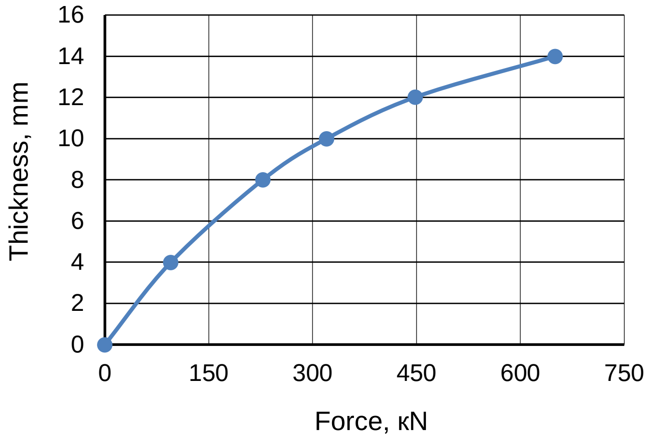

Figure 12. Dependence of the gusset thickness on the maximum force in the attached rods of the finite element model for node type 4.

The gusset thickness values were assigned not only based on calculations results, but also on the basis of design considerations: the minimum design restrictions were considered in accordance with the requirements of SP 16.13330.

Table 1. Stresses and safety factors for various nodes' types for a symmetrical design solution.

No.		Actual equivalent stress, MPa	Safety factor, %
1	1a	142.0	40.8
	1b	104.0	56.6
	1b	144.0	40.0
	1d	136.0	43.3
2	2a	120.0	50.0
	2b	83.0	65.4
	2c	108.0	55.0
	2d	61.0	74.5
3	3a	28.8	88.0
	3b	62.6	73.9
	3c	53.6	77.6
	3d	60.1	74.9
4	4a	95.5	60.2
	4b	82.1	65.8
	4c	113.0	52.9
	4d	104.0	56.6

Note to Table 1: design resistance R_y = 240 MPa.

The analysis of the results obtained allows us to conclude that the safety factors for each node model for the symmetric design solution are in the range of 40–88 %. Based on economic considerations, the thickness of the gusset can be reduced considering design constraints:

- for model 1 by 20 %;
- for model 2 by 30 %;
- for model 3 by 50 %;
- for model 4 by 30 %.

Table 2. Recommended gusset thickness values for symmetrical design solution.

Maximum force in rods of the lattice, кN	Up to 150	160 - 250	260 - 400	410 - 600	610 - 1000	1010 - 1400	1410 - 1800	More than 1800
Reference literature data, mm	**6**	**8**	**10**	**12**	**14**	**16**	**18**	**20**
Thickness for node type 1, mm	5	7	8	10	12	13	15	16
Thickness for node type 2, mm	5	6	7	9	10	12	13	14
Thickness for node type 3, mm	4	4	5	6	7	8	9	10
Thickness for node type 4, mm	5	6	7	9	10	12	13	14

3.2. Research results of the work of trusses gussets with double-sided fastening of lattice elements

Trusses with one-sided fastening of lattice elements are trusses made of rods with a section of single corners.

Figs. 14–21 show isofields of equivalent stresses in the gusset plate for four types of nodes with one-sided fastening of lattice elements: for symmetric fastening of rods, support node, rack fastening node and eccentric link fastening node, respectively.

Figs. 14–17 show that when fastened with an offset to the corner, the gusset experiences overstress. In order to reduce the stress, in some cases the gusset is fastened end-to-end and the braces are placed on the corner (Fig. 13).

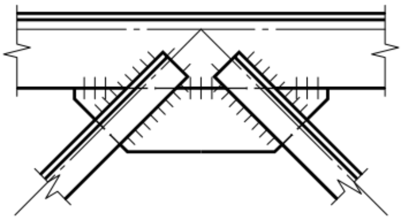

Figure 13. Fastening of the gusset end-to-end to the belt.

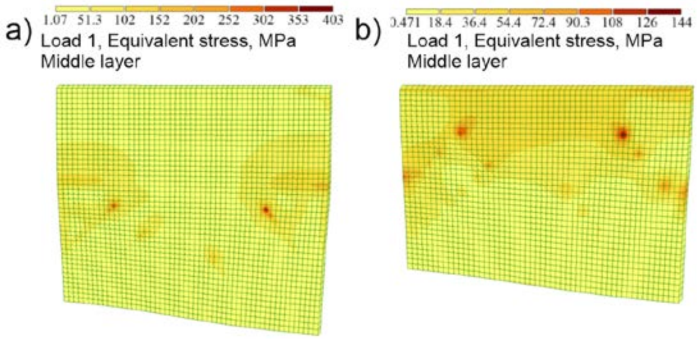

Figure 14. Isofields of equivalent stresses of the finite element model for node type 1a: a) t_f = 6 mm; b) butt gusset t_f = 6 mm.

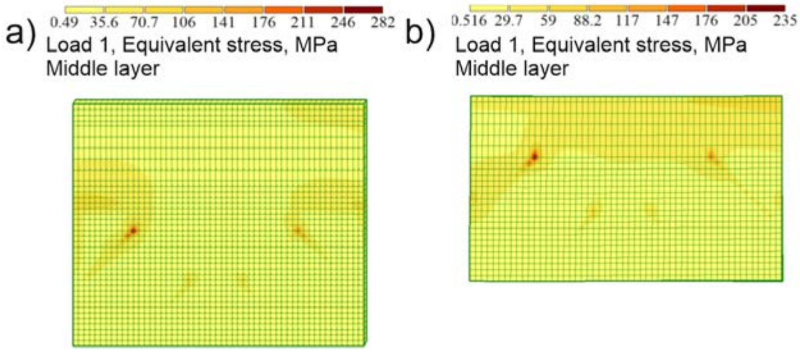

Figure 15. Isofields of equivalent stresses of the finite element model for node type 1b: a) t_f = 8 mm; b) butt gusset t_f = 8 mm.

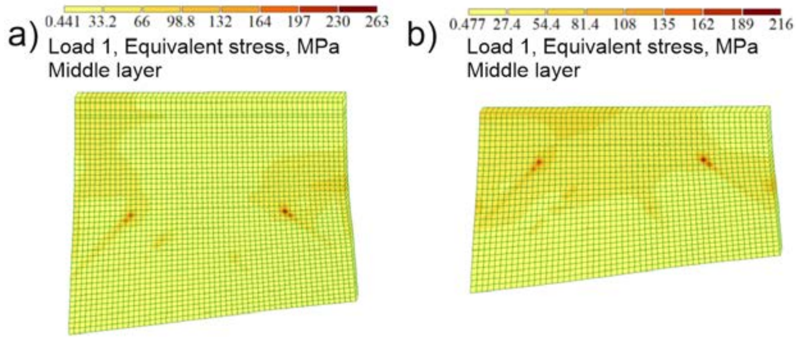

Figure 16. Isofields of equivalent stresses of the finite element model for node type 1c: a) t_f = 10 mm; b) butt gusset t_f = 10 mm.

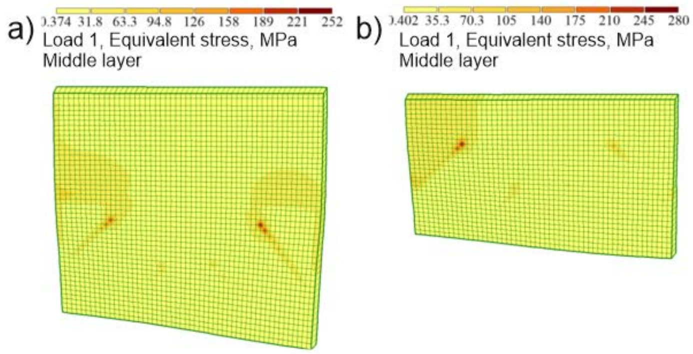

Figure 17. Isofields of equivalent stresses of the finite element model for node type 1d: a) t_f = 12 mm; b) butt gusset t_f = 12 mm.

For models 1a-1c (Fig. 14–16), butt-fastening completely solves the problem of overstressing. For model 1d (Fig. 17) butt-fastening does not solve the problem of overstressing, which is due to the small thickness of the corners of the chords. Local reinforcement of the chords is required to reduce stresses in the chords.

Fig. 18a shows the isofields of equivalent stresses for gusset of node type 2 with the recommended thickness t_f of 8 mm by Table 2.1. As you can see, the choice of this thickness leads to overstress, which is 16 %. By calculation the required thickness t_f is 14 mm (Fig. 18, b).

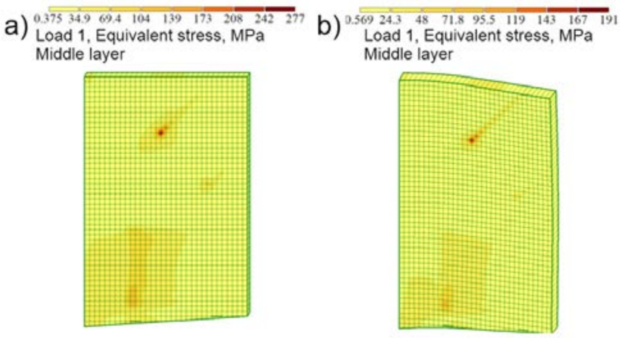

Figure 18. Isofields of equivalent stresses of the finite element model for node type 2, a: a) t_f = 8 mm; b) t_f = 14 mm.

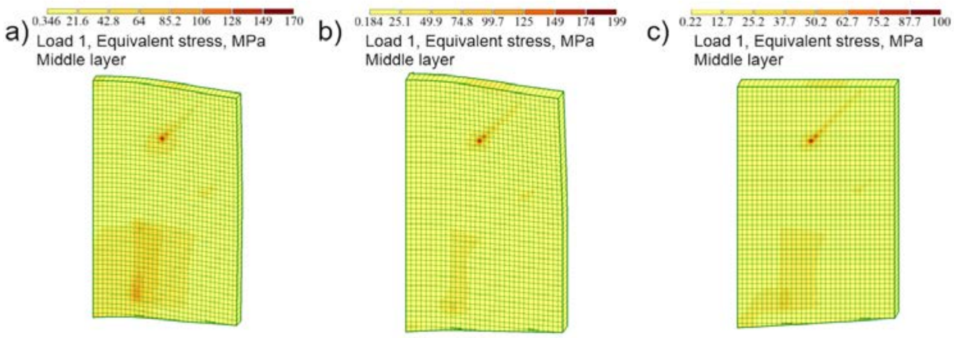

Figure 19. Isofields of equivalent stresses of the finite element model for node type 2, b-d: b) t_f = 10 mm; c) t_f = 12 mm; d) t_f = 14 mm.

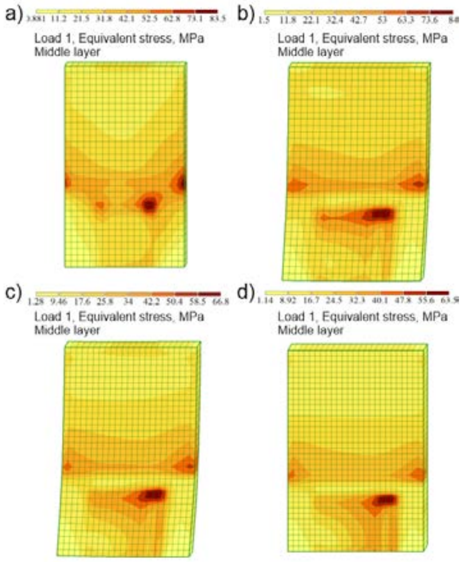

Figure 20. Isofields of equivalent stresses of the finite element model for node type 3: a) t_f = 6 mm; b) t_f = 8 mm; c) t_f = 10 mm; d) t_f = 12 mm.

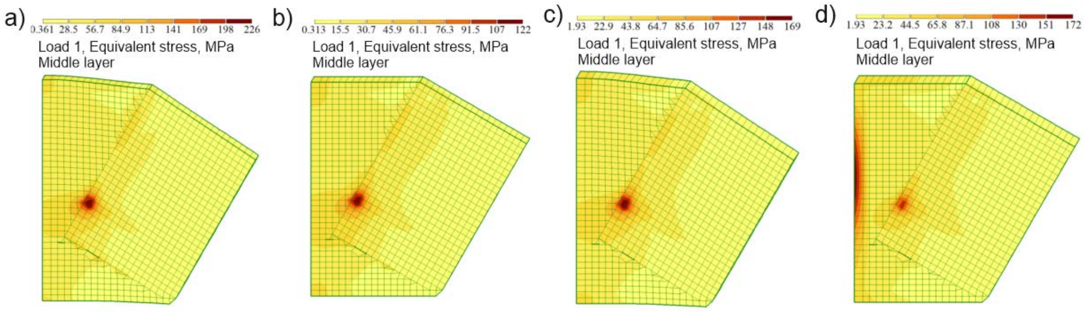

Figure 21. Isofields of equivalent stresses of the finite element model for node type 4: a) t_f = 6 mm; b) t_f = 8 mm; c) t_f = 10 mm; d) t_f = 12 mm.

Based on the calculations results, we built the diagrams for the dependence of the gusset thickness values on the maximum force in the attached rods of models 1-4 and, accordingly, the obtained approximating dependences (6) – (9):

$$t_{f.1} = 17.45\left(1 - e^{-0.00367N}\right); \tag{6}$$

$$t_{f.2} = 15.48\left(1 - e^{-0.00348N}\right); \tag{7}$$

$$t_{f.3} = 12.47\left(1 - e^{-0.00695N}\right); \tag{8}$$

$$t_{f.4} = 13.33\left(1 - e^{-0.00618N}\right). \tag{9}$$

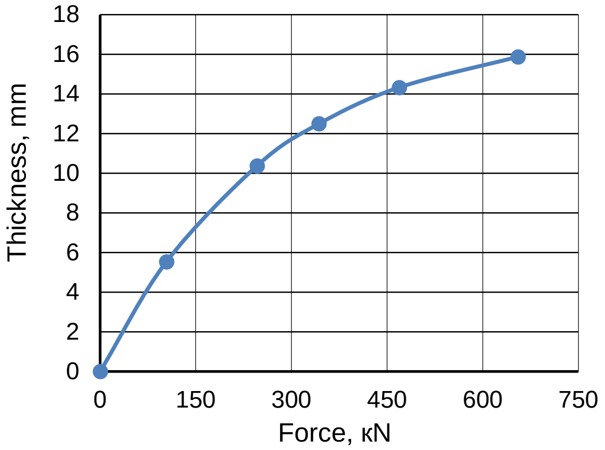

Figure 22. Dependence of the gusset thickness on the maximum force in the attached rods of the finite element model for node type 1.

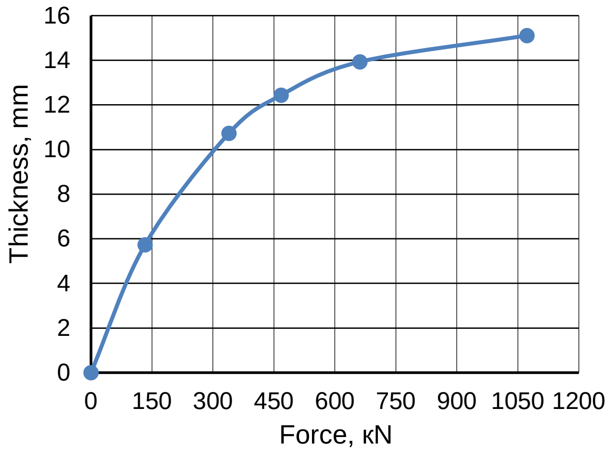

Figure 23. Dependence of the gusset thickness on the maximum force in the attached rods of the finite element model for node type 2.

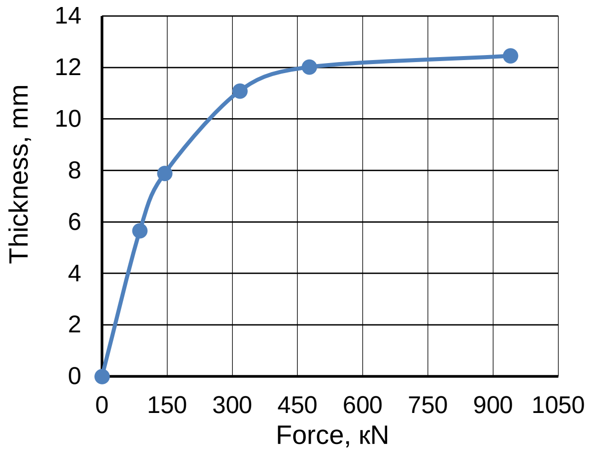

Figure 24. Dependence of the gusset thickness on the maximum force in the attached rods of the finite element model for node type 3.

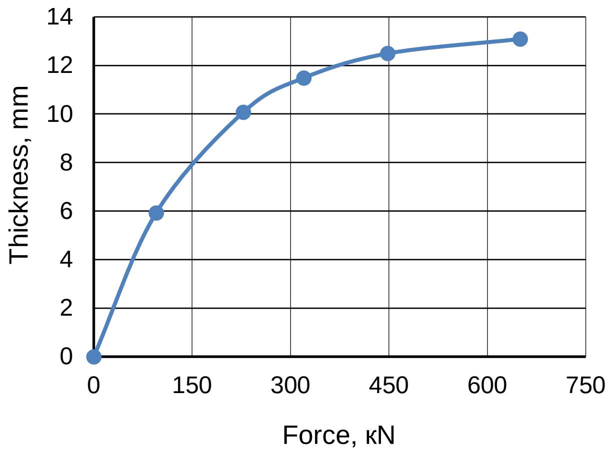

Figure 25. Dependence of the gusset thickness on the maximum force in the attached rods of the finite element model for node type 4.

Table 3. Stresses and safety factors for various types of nodes for asymmetrical design solution.

No.		Actual equivalent stress, MPa	Safety factor, %
1	1a	144	40.0
	1b	235	2.1
	1c	216	10.0
	1d	280	–16.7
2	2a	191	20.4
	2b	170	29.2
	2c	199	17.1
	2d	100	58.3
3	3a	83.5	65.2
	3b	84	65.0
	3c	66.8	72.2
	3d	63.5	73.5
4	4a	226	5.8
	4b	122	49.2
	4c	169	29.6
	4d	172	28.3

Note to table 3: design resistance R_y = 240 MPa.

The analysis of the results obtained allows us to conclude that the safety margins for the types of nodes 1 and 2 of the design solution with one-sided fastening of the lattice to the belt are insufficient. Thus, the gusset thickness, taking into account design constraints can be reduced:

– for model 3 by 40 %;
– need to increase:
– for model 1 by 40–60 %;
– for model 2 by 20 %.

Table 4. Recommended gusset thickness values for asymmetrical design solution.

Maximum force in rods of the lattice, кN	Up to 150	160 - 250	260 - 400	410 - 600	610 - 1000	1010 - 1400	1410 - 1800	More than 1800
Reference literature data, mm	**6**	**8**	**10**	**12**	**14**	**16**	**18**	**20**
Thickness for node type 1, mm	10	12	14	16	18	20	22	24
Thickness for node type 2, mm	7	9	11	13	15	17	19	21
Thickness for node type 3, mm	4	5	6	8	9	10	11	12
Thickness for node type 4, mm	5	6	7	9	10	12	13	14

The improved method for selecting the gusset thickness:

1. To calculate the truss, determine the forces in rods.
2. According to the greatest force, depending on the node type and the design solution, select the required gusset thickness from Tables 2 or 4.

2.1. Research results of the gussets' work of brace elements fastening with eccentricity

A study was performed on the influence of the eccentricity value on the stress in the gusset. The main variable parameter is the displacement of the attached element relative to the axis of the abutment of elements.

Based on the calculations results, we made graphs of the dependence of the change in stresses of the gusset relative to the value of the abutment eccentricity and obtained the approximating dependences.

Dependence of stress change for 10 mm thickness of the gusset:

$$\sigma_{f.10} = 1.432 + 1.707 e_x - 4.789 \cdot 10^{-3} e_x^2. \tag{10}$$

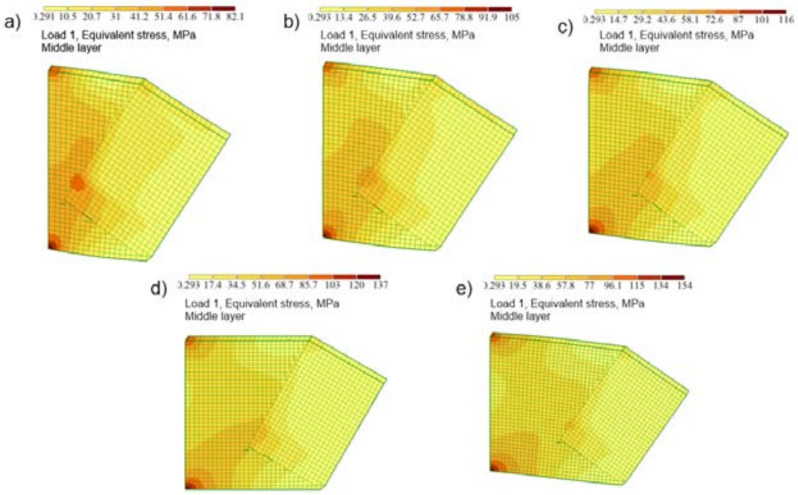

Figure 26. Isofield of equivalent stresses for node type 4 with the gusset thickness t_f = 10 mm and the value of the eccentricity: a) 50 mm; b) 75 mm; c) 100 mm; d) 125 mm; e) 150 mm.

When constructing the graphs, the reduced stresses were taken at a distance of one thickness from the edge of the attachment, which takes into account the catheters of the weld.

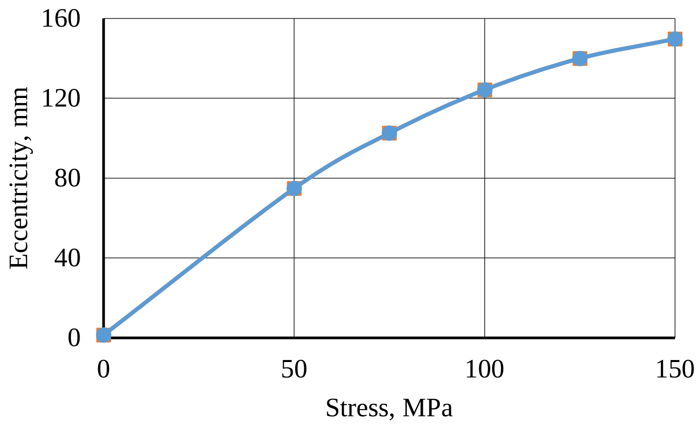

Figure 27. Dependence of the displacement influence on stress for the gusset thickness t_f = 10 mm.

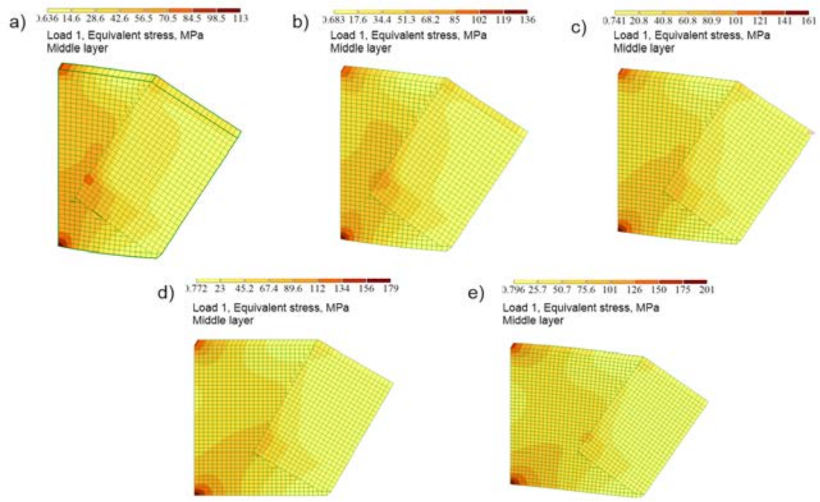

Figure 28. Isofield of equivalent stresses for node type 4 with the gusset thickness t_f = 12 mm and the value of the eccentricity: a) 50 mm; b) 75 mm; c) 100 mm; d) 125 mm; e) 150 mm.

Dependence of stress change for 12 mm thickness of the gusset:

$$\sigma_{f.12} = 1.883 + 2.347 e_x - 7.055 \cdot 10^{-3} e_x^2. \quad (11)$$

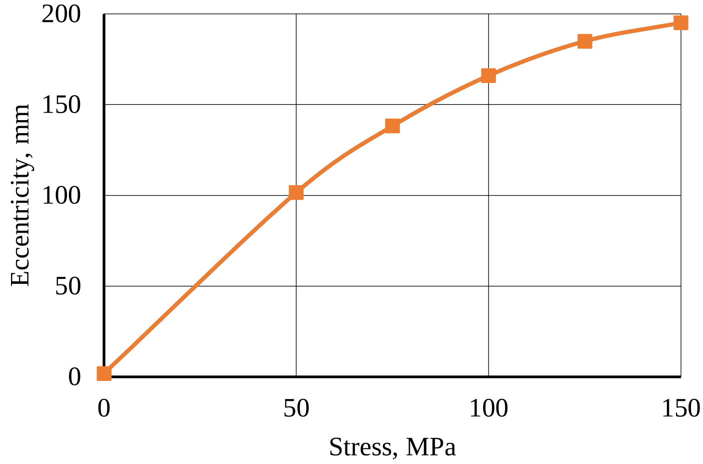

Figure 29. Dependence of the displacement influence on stress for the gusset thickness t_f = 12 mm.

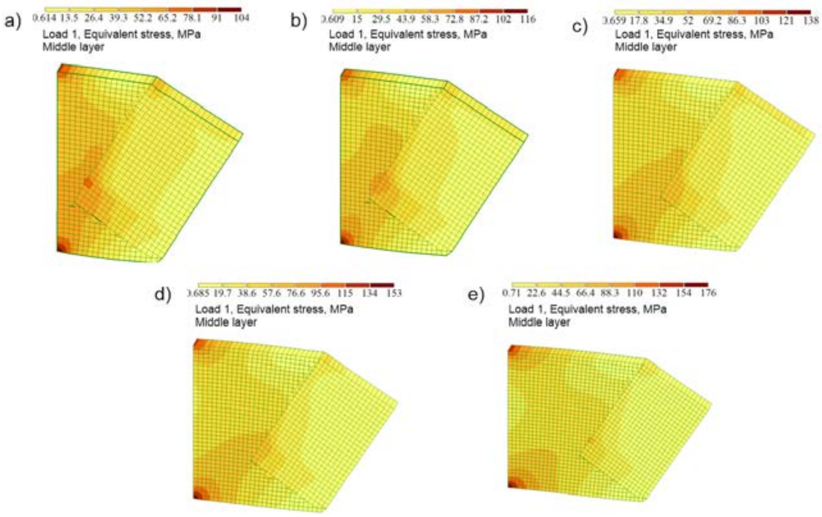

Figure 30. Isofield of equivalent stresses for node type 4 with the gusset thickness t_f = 14 mm and the value of the eccentricity: a) 50 mm; b) 75 mm; c) 100 mm; d) 125 mm; e) 150 mm.

Dependence of stress change for 14 mm thickness of the gusset:

$$\sigma_{f.14} = 3.611 + 1.841 e_x - 6.264 \cdot 10^{-3} e_x^2. \quad (12)$$

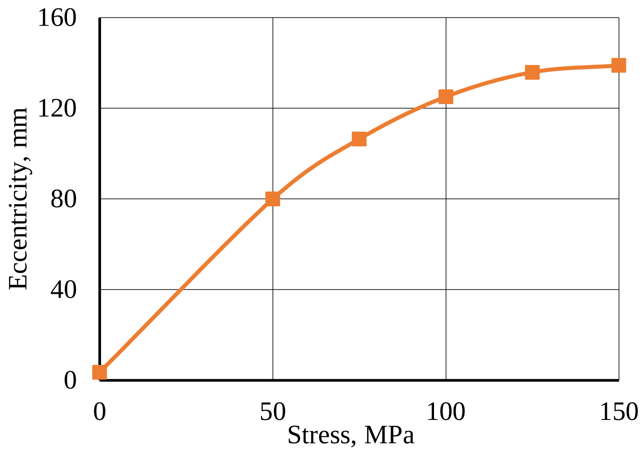

Figure 31. The dependence of the effect of displacement on stress at the thickness of the gusset plate t_f = 14 mm.

The diagrams show that the nature of the change in the stress-strain state in gussets with constant thickness during increasing eccentricity values is described by a quadratic function.

When carrying out practical calculations and design of steel structures, the engineer can assign the gusset thickness, having the initial knowledge about the value of the force acting from the side of the rods, the node type and the possible displacement when fixing the element.

For intermediate values of the initial parameters the gusset thickness can be determined by linear interpolation.

A comparison of the results of this study with the results presented in the reference literature is given for symmetrical sections and for asymmetric sections in Table 2 and Table 4, respectively.

Table 2 data analysis shows that the thickness values of gussets recommended for use by the reference literature are overestimated on average for various types of nodes from 21 % to 94 %, which leads to a significant overspending of the material when applying recommendations for the construction of building roofing. Knowing that the weight of gussets is 25–30 % of the total weight of steel trusses, the use of optimal values of gusset thickness substantiated by the research will reduce the metal consumption of trusses by 35–40 %.

Table 4 data analysis shows that the thickness values of gussets recommended for use by the reference literature are underestimated on average for the first two types of nodes by 20–60 %, which can lead to failure of the structure as a result of the exhaustion of the bearing capacity.

To increase the load capacity of nodes using a single corner, it is recommended to use butt plates.

In order to achieve the tasks of using efficient and rational structures in the field of steel construction it is necessary to amend the regulatory documents in terms of including the methodology for calculating the plates of truss gussets and introduce the specified thickness values recommended for use as truss gussets with rods of symmetrical and asymmetric sections into the new editions of the designer's reference books.

4. Conclusions

1. The authors analyzed trusses' gussets under load for constructive solution with two-sided and Tone-sided fastening of lattice elements for four characteristic types of nodes. Their stress-strain state was investigated depending on the value of the acting loads to the node and on the rod interface configuration.

2. It was established that the safety factors, depending on the type of unit of the structural solution with two-sided fastening of the lattice elements, are more than 40 %. This allows reducing the gussets' thickness taking into account design constraints.

3. It was established that the safety factors for node type 3 of structural solution with one-sided fastening of the lattice elements are 7–90 %. This makes it possible to reduce the gusset thickness for node type 3. The calculation results showed that for node types 1, 2, and 4, gussets are characterized by overstress, which requires an increase in thickness, taking into account design constraints.

4. We analyzed the influence of the eccentricity value on the stress in the gusset. It was determined that the main parameter influencing the stress-strain state of the gusset is the displacement of the attached element relative to the axis of the elements abutment. We derived dependences and made diagrams of the displacement influence on stress for different values of gusset thickness.

5. The obtained data can be used in the design of new structures and in assessing the bearing capacity of structures in operation.

References

1. Biderman, V.L. Mekhanica tonkostennykh konstruktsiyi [Mechanics of thin-walled structures]. Moscow : ASV Publishing, 2012. 214 p.
2. Osama, H. Theory of plates and shells. London : LAB Lambert Academic Publishing, 2022. 243 p.
3. Timoshenko, S.P., Voinovsky-Krieger, S.M. Plastinki i obolochki [Plates and shells]. Moscow: Nauka, 1986. 439 p.
4. Tusnin, A.R. Metallicheskie konstruktsii (part 1) [Metal structures (part 1)]. Moscow: ARSS, 2020. 468 p.
5. Ignat'ev, A.V., Ignat'ev, V.A., Gamzatova, E.A. Calculation of thin plates by the finite element method in the form of a classical mixed method with the exclusion of finite element displacements as a rigid whole. News of higher educational institutions. Construction. 2018. 3 (711). Pp. 5–13.
6. Belyi, G.I. Deformation calculation and stability of rod elements of steel structures with an asymmetric cross-section. Bulletin of Civil Engineers. 2021. 4(87). Pp. 45–53. DOI: 10.23968/1999-5571-2021-18-4-44-53
7. Serpik, I., Komshin, B. Optimum synthesis of steel plane trusses with subdivided panels. MATEC Web of Conferences. 2017. 106. 04020. DOI: 10.1051/matecconf/20171060
8. Partskhaladze, G., Mshvenieradze, I., Medzmariashvilli, E., Chavleshvilli, G. Buckling Analysis and Stability of Compressed Low-Carbon Steel Rods in the Elastoplastic Region of Materials. Advanced in Civil Engineering. 2019. 7601260. Pp. 1–9. DOI: 10.1155/2019/7601260
9. Weinberg, D.V. Plastiny, disky, balki-stenky (Prochnost', ustoichovost' I kolebaniya) [Plates, discs, wall-beams (Strength, stability and vibrations)]. Kiev: Gosstroyizdat of the Ukrainian SSR, 1959. 692 p.
10. Kudishin, Yu.I., Belenya, E.I., Ignatieva, V.S. Metallicheskiye konstruktsii [Metal constructions]. Moscow: Publishing Center "Academy", 2013. – 624 p.
11. AISC Committee. Specification for structural steel buildings (ANSI/AISC 360-16). Chicago: American Institute of Steel Construction, 2016. 177 p.
12. Doroftei, I.A., Bujoreanu, C.C., Doroftei, I.N. An overview on the applications of mechanisms in architecture. Part I: bar structures. Materials Science and Engineering. 2018. 444. 052018. DOI: 10.1088/1757-899X/444/5/052018
13. Gasii, G.M. Structural and Design Specifics of Space Grid Systems. Science and Technique. 2017. 16 (6). Pp. 475–484. DOI: 10.21122/2227-1031-2017-16-6-475-484
14. Abedin, M., Kiani, N., Shahrokhinasab, E., Mokhtari, S. Net Section Fracture Assessment of Welded Rectangular Hollow Structural Sections. Civil Engineering Journal. 2020. 7 (6). Pp. 154–163. http://dx.doi.org/10.28991/cej-2020-03091544
15. Lavalette, N.P., Bergsma, O.K., Zarouchas, D., Benedictus, R. Comparative study of adhesive joint designs for composite trusses based on numerical models. Applied Adhes Science. 2017. 8 (2). Pp. 28–38. https://doi.org/10.1186/s40563-017-0100-1
16. Ramezani, M., Vilches, J., Neitzert, T. Pull-out behavior of galvanized steel strip in foam concrete. International Journal of Advanced Structural Engineering. 2013. 11. Pp. 99–111.
17. Raisszadeha, A., Rahaia, A., Deylami, A. Behaviour of Steel Plate Shear Wall in Multi Span Moment Frame with Various Infill Plate Connection to Column. Civil Engineering Journal. 2018. 1 (4). Pp. 26–40.
18. Raisszadeha, A., Deylami, A., Rahaia, A. Experimental and Numerical Research on Steel Plate Shear Wall with Infill Plate Connected to Beam Only. Civil Engineering Journal. 2018. 3 (4). Pp. 128–139. http://dx.doi.org/10.28991/cej-0309113
19. Verma, I., Setia, S. Seismic Behaviour of Stiffened Steel Plate Shear Walls. International Journal of Innovative Technology and Exploring Engineering. 2019. 8 (8). Pp. 77–90.

20. Lu, Y., Li, L., Wu, D., Zhong, B., Chen, Y., Chouw, N. Experimental Investigation of Steel Plate Shear Walls under Shear-Compression Interaction. Shock and Vibration. 2019. 12. Article 8202780. https://doi.org/10.1155/2019/8202780
21. Zhou, Z., Qian, J., Huang, W. Numerical Study on Deformation Capacity of Steel Plate Reinforced Concrete Shear Walls. Advances in Civil Engineering. 2019. 14. Article 9701324. https://doi.org/10.1155/2019/9701324
22. Haddad, O., Ramli Sulong, N.H., Ibrahim, Z. Cyclic performance of stiffened steel plate shear walls with various configurations of stiffeners. Journal of Vibroengineering. 2018. 20 (1). Pp. 459–476. https://doi.org/10.21595/jve.2017.18472
23. Zhang, Y., Zhan, X. Study on Seismic Behavior of Steel Frame-Steel Shear Wall with Assembled Two-Side Connections. Mathematical Problems in Engineering. 2019. 17. Article 3024912. https://doi.org/10.1155/2019/3024912
24. Fadhil, H., Ibrahim, A., Mahmood, M. Effect of Corrugation Angle and Direction on the Performance of Corrugated Steel Plate Shear Walls. Civil Engineering Journal. 2018. 11 (4). Pp. 107–119.
25. Ebadi, P., Farajloomanesh, S. Seismic design philosophy of special steel plate shear walls. Magazine of Civil Engineering. 2020. 95 (3). Pp. 3–18. DOI: 10.18720/MCE.95.1
26. Deng, Z., Xu, Ch., Hu, Q., Zeng, J. Xiang P. Investigation on the Structural Behavior of Shear Walls with Steel Truss Coupling Beams under Seismic Loading. Advances in Materials Science and Engineering. 2018. 2. Pp. 112–128. https://doi.org/10.1155/2018/5602348

Information about authors:

Alexander Golikov, *PhD in Technical Sciences*
ORCID: https://orcid.org/0000-0001-6588-6031
E-mail: alexandr_golikov@mail.ru

Igor Garanzha, *PhD in Technical Sciences*
ORCID: https://orcid.org/0000-0002-6687-7249
E-mail: garigo@mail.ru

Ksenya Cherkasova,
E-mail: cherkasova.ksenya@yandex.ru

Received 16.03.2021. Approved after reviewing 27.02.2023. Accepted 09.03.2023.

Magazine of Civil Engineering

ISSN
2712-8172

journal homepage: http://engstroy.spbstu.ru/

Research article

UDC 691.328.43

DOI: 10.34910/MCE.122.2

Structural behavior of concrete arches reinforced with glass textiles

O.N. Stolyarov , ***A.E. Dontsova*** ✉, ***G.L. Kozinetc***

Peter the Great St. Petersburg Polytechnic University, St. Petersburg, Russian Federation

✉ *anne.dontsoova@gmail.com*

Keywords: textile-reinforced concrete, arch structures, thin-walled structures, flexural test, strength

Abstract. Thin-walled concrete structures with textile reinforcement have a number of advantages over conventional reinforced concrete. This article discusses the manufacturing method and investigates the structural behavior of the arch made of textile-reinforced concrete (TRC). The possibility of manufacturing an experimental arched structure with textile reinforcement is demonstrated. This study includes the arch design, mold preparation and loading test. With the use of a 3D printer, the mold of the arched structure was printed, which made it possible to implement a distributed loading scheme. Three concrete arches including a reference non-reinforced arch and two concrete arches reinforced with glass textiles were designed and tested. The test results showed a slight increase in the strength of the reinforced arch compared to the control non-reinforced arch. The effectiveness of the reinforcement of the arch structure amounts to about 10 % increase in contrast to arches with external reinforcement, where the increase in strength reaches 40–85 %. However, the main advantage of such reinforcement is the significant residual strength of the arch structure, which prevents catastrophic collapse of it. The textile reinforcement continued to hold the failed concrete matrix in contrast to the external reinforcement, where the loss of cohesion leading to delamination could cause the fracture of parts of the concrete.

Citation: Stolyarov, O.N., Dontsova, A.E., Kozinetc, G.L. Structural behavior of concrete arches reinforced with glass textiles. Magazine of Civil Engineering. 2023. 122(6). Article no. 12202. DOI: 10.34910/MCE.122.2

1. Introduction

An increasing interest in fibrous concrete reinforcement is dictated by the need to design lightweight concrete structures. To date, a large number of lightweight arch structures are manufactured using polycarbonate. Along with several advantages, such as light weight, low cost, etc., there is also a number of disadvantages associated primarily with the service life of such plastic structures. Weather conditions periodically cause a situation in which the snow load on the extrados can increase significantly, for example due to melting of snow and subsequent formation of ice when the temperature drops. In practice, this leads to the destruction of brittle structures made of polycarbonate. At the same time, these structures are practically non-repairable and are subject to disposal. Thus, for example, in St. Petersburg every spring there is a large amount of polycarbonate structures waste. In turn, this causes an environmental problem associated with both the growing production of plastics and the difficulties of their recycling. An alternative to polycarbonate arch structures are thin-walled concrete structures. These designs can be produced with a thickness of 15–20 mm. Of course, the cost of such structures is somewhat higher than the cost of plastic structures, but the main advantage is their significant durability compared to polycarbonate structures. Durability of such structures is primarily due to two main factors. Firstly, the concrete structure is less susceptible to mechanical stress and local damages, for example, due to the formation of ice. Secondly, concrete is less exposed to sun and weather. Thus, due to exposure to ultraviolet radiation, plastics undergo significant degradation, leading both to a deterioration in mechanical properties and to loss of their original appearance due to tarnishing. At the same time, the fine-grained concrete used for the production of TRC has an excellent smooth surface and can be used without additional finishing materials. The higher cost of such arches can easily be offset by their service life. According to the observations of the authors of this work, single pilot projects on lightweight TRC arch are used as shelters for parking bicycles, small pavilions for at least 10 years without visible surface damages, and in structures with polycarbonate arches, there is a periodical replacement of some damaged sections after the winter period.

Arch structures are the object of this research. Arch structures find increasing use in various structures including bridges, tunnels, domes, etc. Arch structures are widely used due to load bearing capacity and ability to bridge between large spans without any need for columns [1]. Arches are both made of masonry and concrete. Research fields in arched structures using composite materials can be divided into two major groups. The first involves strengthening existing arch structures, both brick [2–7] and concrete [8–11]. The second group involves the development of lightweight floor structures [12, 13]. In each of these fields, the main role is played by high-strength fiber composites. Their main advantages are high load-bearing capacity, corrosion resistance and ease of installation.

Currently, there is a trend towards the manufacture of economically efficient and durable building structures. One of the promising materials used for reinforcing concrete is textile reinforcement. Advanced composite materials based on it include TRC that has already proved itself in various fields of application in construction [14, 15]. Examples of the implementation of TRC include wall panels, light ceilings, bridges, etc. A certain amount of material has been accumulated on the properties of textile reinforcement and textile-based composites. To a lesser extent, the elements of finished building structures made of TRC have been studied. There are only limited examples of research on, for instance, arched structures made of TRC. The researchers mainly concern the application of external reinforcement for masonry vaults [16] and reinforced concrete structures [17]. And here the main task is to analyze the interaction at the interface between the concrete matrix and the reinforcing fiber since significant stress concentration can lead to delamination of fiber reinforcement [17]. A full-scale pavilion entirely in TRC was designed and erected by P. Valeri, P. Guaita et al. [13]. D.L.N.D.F. Amorim et al. [18] developed a simplified model of cracking and damage in reinforced concrete arches for their structural assessment. A. Khaloo, H. Moradi et al. [19] have studied the behavior of arches reinforced with steel rebars and unidirectional glass fabric composites. It was shown that extrados strengthening is more effective (up to 200%) than intrados strengthening. However, the use of excessive glass fabric layers may lead to brittle collapse in shear failure mode. T. Martin, S. Taylor et al. [20] have used basalt and carbon fiber reinforced polymers while strengthening of concrete floor slabs to enhance slab capacity. In [21] carbon fiber reinforced polymers (CFRP) were applied to repair the damaged buried arch structure subjected to underground explosions. Z. Tang, Y. Zhou et al. [22] used basalt fiber reinforced polymer (BFRP) bars to build concrete arches. It was shown that the BFRP bars reinforced arch has comparable or even better blast resistance than the steel bars reinforced arch. In [23], glass fiber reinforced polymer (GFRP) was applied to strengthen the laminated bamboo arches. It is found that the GFRPS effectively restrains the delamination and greatly enhances the load carrying capacity. Z. Qiu, M. Yan et al. [24] used CFRP for strengthening of laminated bamboo arches. In [25], Ultra-high Performance Concrete was used for strengthening pre-damaged reinforced concrete arches. It was found that the bearing capacity of arch intrados strengthened with UHPC increased by 85 %. In [26], the possibility of using fiber reinforced concrete FRC precast tunnel segments was demonstrated. Full-scale tests on both traditional reinforced concrete and FRC elements have been performed. The tests results showed the fiber reinforced concrete can substitute the traditional reinforcement. H.J. Dagher, D.J. Bannon et al. [8] investigated the concrete-filled fiber-reinforced polymer (FRP) tubes for buried arch bridge structures. The tubes were fabricated from braided E-glass and carbon fiber infused with resin. In [27], failure mechanisms of carbon fiber reinforced polymer (CFRP) wrapped arches under static and blast loadings were investigated. Load carrying ability of CFRP arches achieves the level of steel bar reinforced concrete (RC) arch in the static loading experiment. Subjected to explosive loading, CFRP plays an important blast protective role in arch. In [11] different techniques including bonding and bonding/wrapping with carbon fiber reinforced polymers were applied to improve the strength of reinforced concrete arches. It is shown that bonding/wrapping technique is much more effective than bonding method. Also, in general, loading occurs through one point in the center. RC arches are usually tested under centrally concentrated point load. At the same time, the distributed load more realistically reveals the structural properties of arched structures. In this paper, an attempt was made to develop an arched canopy made of textile-reinforced concrete. A distinctive feature of this work is the proposed approach to the design of mold for the implementation of a distributed loading scheme, the manufacture of an arched structure and mechanical testing.

Relevance of this study includes manufacturing method, analysis of the structure and flexural properties of textile-reinforcing concrete arches.

The aim of this work is to develop arch structures made of TRC and investigate their structural characteristics and flexural behavior.

The objectives of this work are:

- experimental studies of manufacturing process to produce TRC arch with tailored properties;
- optimization of 3D printing for manufacturing of mold for casting of the arch structures;
- study the flexural behavior of TRC arch structures and to develop a technical approach that facilitates the measurement of the deformations.

2. Materials and Methods

2.1. Test samples

Three arch samples with a cross section of 20×260 mm were designed and manufactured. Two of them (Type I) were reference (non-reinforced) and reinforced with glass fiber warp-knitted fabric. These arches have span length of 367 mm and span-to-rise ratio of 6.1. The third arch (Type II) has span length of 1068 mm and span-to-rise ratio of 6.7. The reinforcing fabric was placed in the tension area at a distance of 5 mm from the intrados. Geometric properties of specimens are presented in Fig. 1. Two molds of polylactic acid (PLA) plastic were fabricated using 3D printer Raise 3D (Model Pro2 Plus). All samples were cast using concrete mix listed in Table 1. Mechanical properties of the reinforcing fabric and concrete are listed in Table 2.

Table 1. The constituents of fine-grained concrete (kg/m^3).

Portland cement	750
Sand (0–0.63 mm)	1365
Plasticizer	8
Water	275

Table 2. Mechanical characteristics of the reinforcing textiles.

	Units	Fabric	Concrete
Tensile strength		900	-
Compression strength	MPa	-	40
Flexural strength		-	4.8
Young Modulus	GPa	47.2	32.0

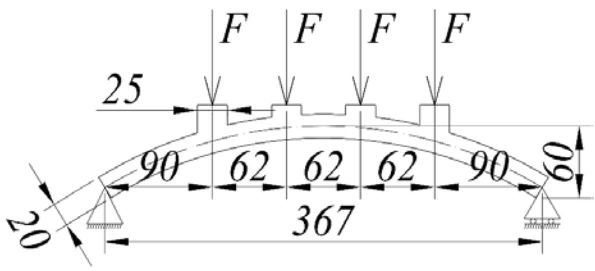

(a)

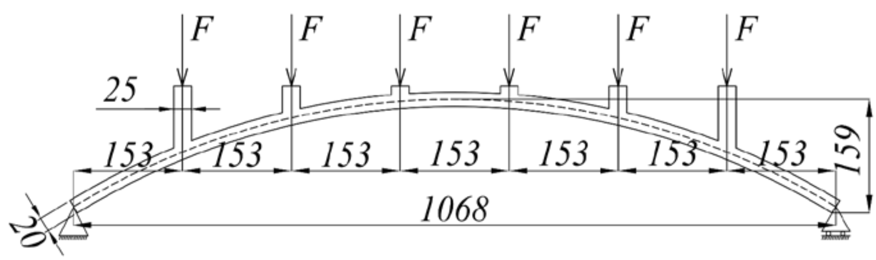

(b)

Figure 1. Geometry and supporting conditions of the TRC arch under a uniformly distributed load (units: mm).

2.2. Manufacturing of 3D printed mold for concrete casting

One of the most difficult tasks in the manufacture of test specimens is the manufacture of a mold. In contrast to a realistic structure, in the manufacture of mold, it becomes necessary to provide a uniformly distributed load in order to realistically reflect the service conditions of the structure. When analyzing the literature, it was revealed that basically there is a single point loading. Only in [12] the mold was made in the form of an arch with additional columns at the top through which a distributed load was transmitted.

Molds for arched structures are mainly made of wood. This is due to the simplicity and low cost of the raw material. However, the use of wooden mold limits the possibilities of applying the distributed loading scheme, and, as a result, the presence of only mold with concentrated loading indicates the difficulties encountered by the research. The difficulty lies in designing several points (usually 5 or 6) of load application due to the formation of a profile with columns having different heights, increasing with distance from the center of the arch. Joining of numerous parts of a wooden panel leads to the need to seal the joints to prevent leakage of the fine-grained concrete mix. Alternatively, plastic extrusion on a 3D printer can be used. The devices have proven themselves in the printing of various parts and products. There are also many individual examples of using 3D printing for the manufacture of mold for small concrete products. The main advantage of 3D printing is the seamlessness of the technology, i.e., the mold is made entirely and is completely suitable for concrete casting.

In this work, 3D printing of polyactide (PLA) plastic, which is a biodegradable thermoplastic aliphatic polyester, was used to manufacture the mold for the arch sample. This material is one of the most popular in 3D printing. Since it was planned to produce two standard sizes of arches, then, accordingly, two types of molds were designed. Fig. 2 shows the main steps in the manufacture of mold for an arch type I with four columns. Fig. 2a shows the beginning of the PLA printer printing with plastic. The speed of 3D printing is relatively low. Time for mold printing with a height of 260 mm takes approximately 45–50 hours. Fig. 2b shows the final stage of mold printing. The resulting mold, in principle, can be reusable. However, it is difficult to extract an arch sample without damaging the columns from above, so the decision was made to print a single use mold with the smallest possible thickness to ensure strength and stability. Finished molds are shown in Fig. 2c. Mold for arch Type II was made in a similar way but consisted of three parts due to limitations in the size of the 3D printer table. In this case, the number of columns was increased to 6. It was designed with appropriate tolerances for a smooth assembly.

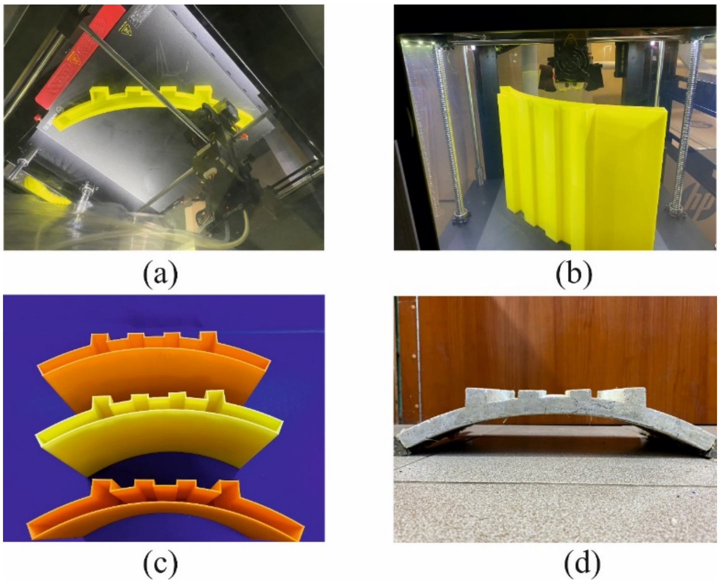

Figure 2. 3D printed mold for concrete casting:
(a) and (b) printing the mold; (c) printed molds; (d) cast arch Type I.

2.3. Concrete casting

Concrete mix was prepared according to the constituents listed in Table 1. The mold was filled with concrete mix. After casting, it was left to dry and then the mold was carefully disassembled. Abrasive paper was used to repair imperfections. Prior to testing, the test samples were stored for 60 days at 22 °C and 95 % RH. The reinforced arch type II is shown in Fig. 2d. Fig. 3 shows cast arch Type II.

Figure 3. Cast arch Type II.

2.4. Test setup

The mechanical behavior of the cast arches was investigated by using an Instron universal testing machine (model 5965). The test setup is shown in Fig. 4. The supported arch specimens were loaded by a uniformly distributed load. Load was applied with a rate of 1 mm/min. Monitoring devices include load cell at the crosshead of the testing machine and dial gauges at the arch columns. The load was applied simultaneously at four and six columns for the arch Type I and Type II, respectively.

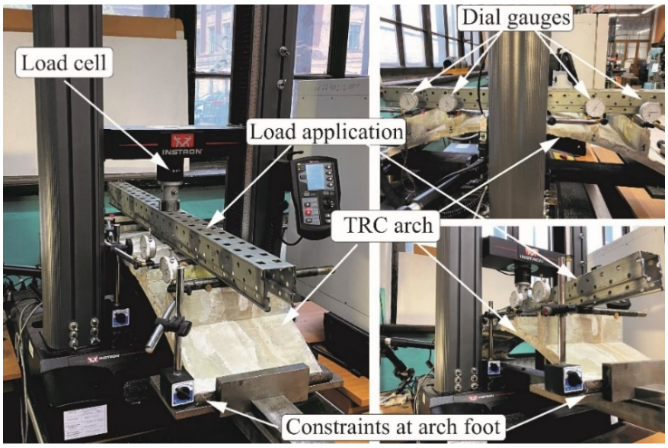

Figure 4. TRC arch (Type II) under testing.

3. Results and Discussion

3.1. Strength efficiency

The smaller type 1 arch was designed to test the performance of the reinforcement and the performance of the reinforced arch under load. The flexural test results for the reinforced and non-reinforced (control) arches are shown in Fig. 5 as load – vertical displacement curves. According to the obtained curves, a significant difference in the mechanical behavior of the two samples is observed. It can be seen that the load of the control sample increases dramatically and failure occurs at a value of about 3000 N. A crack is formed and the sample instantly breaks into two parts. Destruction occurs approximately in the middle at the location with the maximum bending moment. The reinforced arch sample (shown with red dashed line) exhibits a fundamentally different behavior. So, after reaching the strength at the first crack, a slight decrease in the load occurs and then a reinforcing fabric is switched to the work, which does not allow the sample to break into pieces. As a result, we have a sufficiently high residual strength on the sample of the reinforced arch. This behavior continues for quite a long time, turning into a horizontal displacement of the movable support. This is an indisputable advantage of such reinforcement, because there will be no sudden destruction of the entire structure. If we analyze both curves in terms of reinforcement efficiency, then insignificant differences between them are found. First, the strength of the reinforced arch is about 10 % higher than that of the control arch. This difference is insignificant, and even when using a carbon reinforcing fabric, one should not expect a significant increase, because textiles in a concrete matrix work mainly in tension. Secondly, there is an increase in vertical displacement without fatal destruction and debonding of textiles from the arch [12]. When analyzing the curves, one should also note the selection of slacks in the initial stage of loading, which is due to the tooling used.

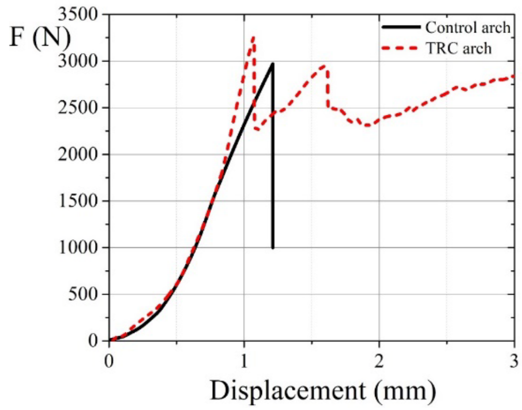

Figure 5. Load versus vertical displacement of the reinforced arch compared to control arch (Type I).

3.2. Load versus vertical displacement

Fig. 6 shows the test results for a reinforced arch type II. The mechanical behavior is similar to what we observed in the arch type I. Initially, the load increases sharply, and then there is a decrease after the formation of a crack, and further the reinforcement is put into operation. In this case, the initial section of the curve is fairly flat. There is no slack, like it was observed in the arch type I. This is due to the massiveness of the manufactured sample of the arched structure.

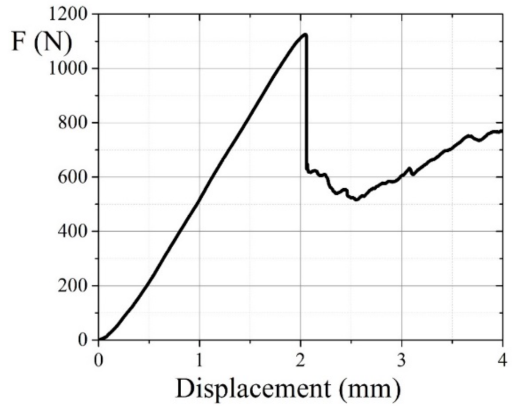

Figure 6. Load versus vertical displacement of the arch Type II.

When analyzing the mechanical behavior of a reinforced arch structure, it is of interest to determine the vertical displacements. For this, dial indicators were used, located on top of the columns as shown in Fig. 4. The measurement results are presented in Fig. 7. These diagrams are constructed in such a way as to show vertical displacement along the entire length of the arch. The ratio of the current coordinate to the entire length of the arch is plotted on the horizontal scale. According to the results obtained, it can be seen that with an increase in the load, approximately the same increment of displacement occurs on symmetrically installed indicators: s/L = 0.143 and s/L = 0.858; s/L = 0.286 and s/L = 0.715. At greater loads, there is a significant increase in vertical displacement on the indicator in the position s/L = 0.286. This may be due to the fact that a crack developed in this place. With the approach of loads to destructive vertical displacements increase significantly.

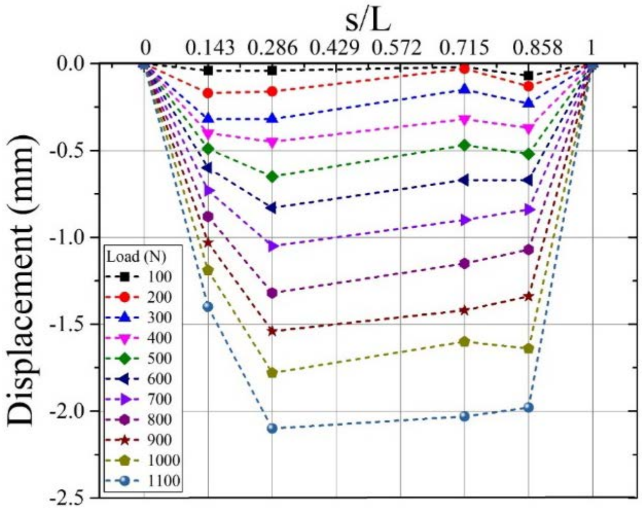

Figure 7. Experimental displacement in the arch Type II at different locations: s is a coordinate along the arch and L is the length of the arch).

Additionally, load-displacement diagrams were built for each dial indicator. These curves are shown in Fig. 8. The resulting curves more clearly characterize the mechanical behavior of such arch structures and can be used for further calculations.

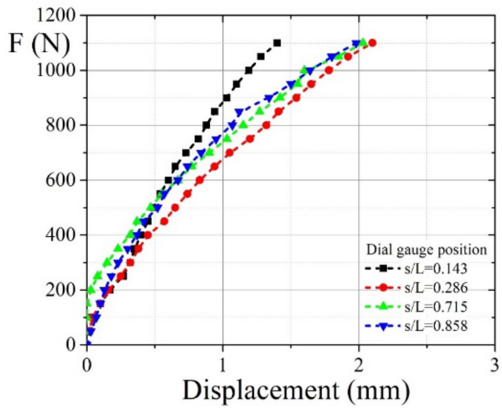

Figure 8. Load versus vertical displacement of the arch Type II at different locations.

One of the main tasks of this work is to focus on the reinforcement efficiency. The results showed a slight increase in strength characteristics. The main advantage, in fact, is a significant residual strength, which allows maintaining the integrity of the arched structure. Unfortunately, it is not possible to compare it with the works of other authors, because they studied the external reinforcement of arched structures, and the results they achieve are due to the work of fiberglass or carbon fiber on intrados or extrados of the arch. Therefore, sometimes strength was achieved with an increase in the intrados surface by 40 % [12] and even by 85 % [25]. All this is due to the work of directional reinforced plastics with high mechanical characteristics. In fact, this is an additional layer of composite material that forms a hybrid system held by good bonding. That is, we have an arch in the arch. The strength and rigidity of such a layer provide a desired effect on strength efficiency. Thus, an increase in this composite layer increases the strength of the entire structure. At the same time, A. Khaloo, H. Moradi et al. [19] note that the excessive increase in the layers of the glass sheet can lead to brittle fracture of the structure.

4. Conclusions

In this work, an experimental study was carried out on the possibility of reinforcing an arched structure made of textile-reinforced concrete using a textile fabric made of glass rovings. The study included the development of mold, its 3D printing, the production of samples of concrete arches and the study of their mechanical behavior. The results showed that

- the concrete casting method should include application of a distributed load using a printed plastic mold;
- samples of arch concrete structures reinforced with glass textiles are developed, the correlation between the reinforcement and flexural properties of concrete composite was established;

- effectiveness of the reinforcement of the arch structure is insignificant and amounts to about 10 % increase in contrast to arches with external reinforcement, where the increase in strength reaches 40–85 %;
- the main advantage of arches with internal reinforcement is their significant residual strength, which prevents catastrophic collapse of the structure. The textile reinforcement continues to hold the failed concrete matrix in contrast to the external reinforcement, where the loss of cohesion leading to delamination can cause parts of the concrete to fall out.

References

1. Ma, Y., Xu, F., Wang, L., Zhang, J., Zhang, X. Influence of corrosion-induced cracking on structural behavior of reinforced concrete arch ribs. Engineering Structures. 2016. 117. Pp. 184–194. DOI: 10.1016/J.ENGSTRUCT.2016.03.008
2. Baratta, A., Corbi, O. Stress analysis of masonry vaults and static efficacy of FRP repairs. International Journal of Solids and Structures. 2007. 44 (24). Pp. 8028–8056. DOI: 10.1016/J.IJSOLSTR.2007.05.024
3. Briccoli Bati, S., Rovero, L. Towards a methodology for estimating strength and collapse mechanism in masonry arches strengthened with fibre reinforced polymer applied on external surfaces. Materials and Structures. 2008. 41. Pp. 1291–1306. DOI: 10.1617/S11527-007-9328-8
4. Cancelliere, I., Imbimbo, M., Sacco, E. Experimental tests and numerical modeling of reinforced masonry arches. Engineering Structures. 2010. 32 (3). Pp. 776–792. DOI: 10.1016/J.ENGSTRUCT.2009.12.005
5. Foraboschi, P. Strengthening of masonry arches with fiber-reinforced polymer strips. Journal of Composites for Construction. 2004. 8 (3). Pp. 191–202. DOI: 10.1061/(ASCE)1090-0268(2004)8:3(191)
6. Oliveira, D.V., Basilio, I., Lourenço, P.B. Experimental Behavior of FRP Strengthened Masonry Arches. Journal of Composites for Construction. 2010. 14 (3). Pp. 312–322. DOI: 10.1061/(ASCE)CC.1943-5614.0000086
7. Tao, Y., Stratford, T.J., Chen, J.F. Behaviour of a masonry arch bridge repaired using fibre-reinforced polymer composites. Engineering Structures. 2011. 33 (5). Pp. 1594–1606. DOI: 10.1016/J.ENGSTRUCT.2011.01.029
8. Dagher, H.J., Bannon, D.J., Davids, W.G., Lopez-Anido, R.A., Nagy, E., Goslin, K. Bending behavior of concrete-filled tubular FRP arches for bridge structures. Construction and Building Materials. 2012. 37. Pp. 432–439. DOI: 10.1016/J.CONBUILDMAT.2012.07.067
9. Elmalich, D., Rabinovitch, O. Stress Analysis of Monolithic Circular Arches Strengthened with Composite Materials. Journal of Composites for Construction. 2009. 13 (5). Pp. 431–441. DOI: 10.1061/(ASCE)1090-0268(2009)13:5(431)
10. Gai, X., He, D., Wang, H. Shear strengthening of RC beam using RFRP composites. Magazine of Civil Engineering. 2022. 114 (6). Article No. 11401. DOI: 10.34910/MCE.114.1
11. Zhang, X., Wang, P., Jiang, M., Fan, H., Zhou, J., Li, W., Dong, L., Chen, H., Jin, F. CFRP strengthening reinforced concrete arches: Strengthening methods and experimental studies. Composite Structures. 2015. 131. Pp. 852–867. DOI: 10.1016/J.COMPSTRUCT.2015.06.034
12. Hamed, E., Chang, Z., Rabinovitch, O. Strengthening of Reinforced Concrete Arches with Externally Bonded Composite Materials: Testing and Analysis. Journal of Composites for Construction. 2015. 19 (1). Article No. 04014031. DOI: 10.1061/(ASCE)CC.1943-5614.0000495
13. Valeri, P., Guaita, P., Baur, R., Ruiz, M.F., Fernández-Ordóñez, D., Muttoni, A. Textile reinforced concrete for sustainable structures: Future perspectives and application to a prototype pavilion. Structural Concrete. 2020. 21 (6). Pp. 2251–2267. DOI: 10.1002/SUCO.201900511
14. Kirsanov, A. I., Stolyarov, O. N. Mechanical properties of synthetic fibers applied to concrete reinforcement. Magazine of Civil Engineering. 2018. 4 (80). Pp. 15–23. DOI: 10.18720/MCE.80.2
15. Volkova, A.A., Paykov, A.V., Stolyarov, O.N., Semenov, S.G., Melnikov, B.E. Structure and properties of textile reinforced concrete. Magazine of Civil Engineering. 2015. 59 (7). Pp. 50–56. (rus). DOI: 10.5862/MCE.59.5
16. D'Ambrisi, A., Feo, L., Focacci, F. Masonry arches strengthened with composite unbonded tendons. Composite Structures. 2013. 98. Pp. 323–329. DOI: 10.1016/J.COMPSTRUCT.2012.10.040
17. Wang, J., Zhang, C. A three-parameter elastic foundation model for interface stresses in curved beams externally strengthened by a thin FRP plate. International Journal of Solids and Structures. 2010. 47 (7–8). Pp. 998–1006. DOI: 10.1016/J.IJSOLSTR.2009.12.017
18. Amorim, D.L.N.D.F., Proença, S.P.B., Flórez-López, J. A model of fracture in reinforced concrete arches based on lumped damage mechanics. International Journal of Solids and Structures. 2013. 50 (24). Pp. 4070–4079. DOI: 10.1016/J.IJSOLSTR.2013.08.012
19. Khaloo, A., Moradi, H., Kazemian, A., Shekarchi, M. Experimental investigation on the behavior of RC arches strengthened by GFRP composites. Construction and Building Materials. 2020. 235. Article No. 117519. DOI: 10.1016/J.CONBUILDMAT.2019.117519
20. Martin, T., Taylor, S., Robinson, D., Cleland, D. Arching in concrete slabs strengthened with near surface mounted fibre reinforced polymers. Engineering Structures. 2019. 184. Pp. 257–277. DOI: 10.1016/J.ENGSTRUCT.2019.01.076
21. Chen, H., Xie, W., Jiang, M., Wang, P., Zhou, J., Fan, H., Zheng, Q., Jin, F. Blast-loaded behaviors of severely damaged buried arch repaired by anchored CFRP strips. Composite Structures. 2015. 122. Pp. 92–103. DOI: 10.1016/J.COMPSTRUCT.2014.11.049
22. Tang, Z., Zhou, Y., Feng, J., Wang, P., Liu, Y., Zhou, J., He, H., Li, S., Wang, H., Chen, X., Qiu, Z., Jin, F., Fan, H. Blast responses and damage evaluation of concrete protective arches reinforced with BFRP bars. Composite Structures. 2020. 254. Article No. 112864. DOI: 10.1016/J.COMPSTRUCT.2020.112864
23. Yang, Y., Qiu, Z., Hu, W., Tao, Y., Jiang, R., Lin, J., Liu, F., Fan, H. Braided GFRP sleeving reinforced curved laminated bamboo beams: An efficient way to attenuate delamination. Composite Structures. 2022. 300. Article No. 116141. DOI: 10.1016/J.COMPSTRUCT.2022.116141
24. Qiu, Z., Yan, M., Yang, Y., Li, J., Zhu, W., Fan, H. Flexural behaviors of CFRP strengthened laminated bamboo arches. Construction and Building Materials. 2021. 305. Article No. 124759. DOI: 10.1016/J.CONBUILDMAT.2021.124759

25. Yang, J., Xia, J., Zhang, Z., Zou, Y., Wang, Z., Zhou, J. Experimental and numerical investigations on the mechanical behavior of reinforced concrete arches strengthened with UHPC subjected to asymmetric load. Structures. 2022. 39. Pp. 1158–1175. DOI: 10.1016/J.ISTRUC.2022.03.087
26. Caratelli, A., Meda, A., Rinaldi, Z., Romualdi, P. Structural behaviour of precast tunnel segments in fiber reinforced concrete. Tunnelling and Underground Space Technology. 2011. 26 (2). Pp. 284–291. DOI: 10.1016/J.TUST.2010.10.003
27. Wang, P., Chen, H., Zhou, J., Zhou, Y., Wang, B., Jiang, M., Jin, F., Fan, H. Failure mechanisms of CFRP-wrapped protective concrete arches under static and blast loadings: Experimental research. Composite Structures. 2018. 198. Pp. 1–10. DOI: 10.1016/J.COMPSTRUCT.2018.05.063

Information about authors:

Oleg Stolyarov, *PhD in Technical Sciences*
ORCID: https://orcid.org/0000-0002-2930-5022
E-mail: stolyarov_on@spbstu.ru

Anna Dontsova,
E-mail: anne.dontsoova@gmail.com

Galina Kozinetc, *Doctor of Technical Sciences*
E-mail: kozinets_gl@spbstu.ru

Received 16.03.2023. Approved after reviewing 14.06.2023. Accepted 14.06.2023.

Magazine of Civil Engineering

ISSN 2712-8172

journal homepage: http://engstroy.spbstu.ru/

Research article

UDC 621.315.616.9

DOI: 10.34910/MCE.122.3

Heat-conducting and dielectric characteristics of polyorganosiloxane composites

V.Yu. Chukhlanov ✉, ***N.N. Smirnova***, ***I.A. Krasilnikova***, ***N.V. Chukhlanova***

Vladimir State University, Vladimir, Russian Federation

✉ *kripton0@mail.ru*

Keywords: polymers, oligodimethylsiloxane, boron nitride, strength, adhesion, permittivity, thermal conductivity

Abstract. The article considers the actual problem of improving the physico-mechanical, thermophysical and electrical properties of polyorganosiloxane coatings. In this article, we propose a method for obtaining a multifunctional heat-resistant composition based on oligodimethylsiloxane with terminal hydroxyl groups filled with boron nitride. The curing process of oligodimethylsiloxane and the possible interaction of boron nitride with reactive resin groups are described. The structure of the manufactured composition is investigated, it is established that the filler in the form of dispersed particles touching throughout the volume is evenly distributed in the polymer matrix. The results of experimental studies of the dependence of the tensile strength on the percentage of boron nitride, indicating the hardening of the composite, are graphically presented. Studies of the strength at separation of the cured composition from the substrate (adhesion) of various materials have shown that this value increases with the introduction of boron nitride. The dependence of the thermal conductivity coefficient on the ratio of components is established. The percolation point is determined by the Monte Carlo method. The dependences of the electrical resistivity and temperature dependence on the content of boron nitride are determined. The Poisson equation is solved in MathCad and graphical results of solving the heat transfer problem for traditional and developed composites are presented. Based on the results obtained, the areas of application of the developed composites in construction are proposed.

Funding: Ministry of Science and Higher Education of the Russian Federation (theme FZUN-2020-0015, state assignment of the VlSU).

Citation: Chukhlanov, V.Yu., Smirnova, N.N., Krasilnikova, I.A., Chukhlanova, N.V. Heat-conducting and dielectric characteristics of polyorganosiloxane composites. Magazine of Civil Engineering. 2023. 122(6). Article no. 12203. DOI: 10.34910/MCE.122.3

1. Introduction

Currently, the compositions based on thermoplastic polymers and thermosetting polymer resins are widely used in construction for the supply and distribution cables at traditional and nuclear thermal power facilities and other construction areas. These are numerous polymer concretes, protective materials and coatings, adhesives and sealants [1–4]. Although in general, polymer compositions reveal common disadvantages such as insufficient heat resistance and a tendency to destruction under the impact of various external factors [5–6]. This facilitates the recent interest in new organoelement polymers, including organosilicon (polyorganosiloxane).

Polyorganosiloxane materials are well-known to be characterized by proper resistance towards adverse factors: UV radiation, high temperature, chemicals and microbiological impact [7–8]. However, unfilled polysiloxane resins are characterized by very mediocre physical and mechanical properties due to the insufficient intensity of the implemented intermolecular interactions. Moreover, thermal protection causes problems with the coating stability at local overheating due to poor thermal conductivity of organosilicon resin [9–10]. To improve the heat-conducting and physico-mechanical properties, transition metal oxides (iron, zinc, titanium, etc.) are often introduced into polyorganosiloxane coatings as fillers. Nowadays the mechanisms of modifying polyorganosiloxane polymers by transition metal oxides are properly studied. A number of detailed studies resulted in the creation of Vixint protective sealing compositions [11].

The developed polymer composites are observed to find wide application not only in construction, but in other branches of science and technology, including high technologies sphere as well [12]. However, the heat-conducting properties do not correspond to the values required for the effective removal of the released heat during the heat-generating conductors operation in extreme operating mode. Therefore, polyorganosiloxanes are relatively often filled with metal powders [13]. The most common filler is aluminum powder. In this case, the composite acquires improved thermal stability not only due to the elimination of local overheating, but also because of chemical interaction of aluminum with reactive hydroxyl groups of polyorganosiloxane resin causes the formation of more stable polyaluminoorganosiloxanes [14]. However, irreversible deterioration of dielectric characteristics makes such compositions unsuitable for the manufacturing of electrical structural elements for buildings and structures, for example, thermal power plants located near electric generators and high-voltage transformers, as well as other similar equipment. Similar restrictions concern the protective panels of high-voltage equipment. It is noteworthy that transition metal oxides additionally reduce the dielectric characteristics, in particular the composition electrical resistance [15].

The creation of new types of composites with increased heat-conducting and dielectric characteristics is an urgent task, the solution of which will increase the cooling efficiency of heat-generating conductors in extreme operating conditions. It is possible to increase the electrical resistance of compositions by using heat-conducting materials possessing high dielectric characteristics as fillers. Boron nitride represents an example of such interesting materials. This substance belongs to semiconductors exceeding the traditional aluminum nitride and silicon carbide in the energy-gap width and the breakdown electric field magnitude [16].

The purpose of this research is to demonstrate the results of a study of the physico-mechanical, thermophysical and electrical properties of a polymer composite based on oligodimethylsiloxane with reactive hydroxyl groups filled with boron nitride, which will allow us to establish the possibilities of its use in the construction industry when operating under conditions of elevated temperatures and electric fields.

2. Methods

2.1. Research objects

The following materials were used in the research: oligodimethylsiloxane (ODMS) with terminal hydroxyl groups, manufactured under the trade name of dimethylsiloxane rubber SKTN-1 GOST 13835-73 as a binder, catalyst K-18 (mixture of tin diethyldicaprilate and tetraethoxysilane) produced by Silan LLC, Moscow, and boron (III) nitride of “ultrapure” brand by Shandong Pengcheng Advanced Ceramics Co., Ltd China.

2.2. Production of samples

The experimentally specified amount of ODMS and boron nitride was added into the porcelain mortar and the mixture was thoroughly ground during four hours. Catalyst K-18 was added into the resulting mixture at the rate of catalyst 4 wt. p. per 100 wt. p. of oligomer and after five minutes of intensive mixing, the composition was poured into the molds for curing the samples during 72 hours at 25 °C.

2.3. Experimental methods

The tensile strength study was carried out in compliance with the standard tensile testing method according to Russian State Standard GOST 15873-70.

The composite adhesion to the surface was assessed using digital adhesive meter PSO-MG4 by tearing off a 20 mm diameter steel cylinder glued to the composite deposited on a metal substrate with high-strength glue. The adhesive meter PSO-MG4 is equipped with a spring device applying tensile force to the cylinder. When detached from the surface, the indicator shows the numerical value of adhesion on the scale, expressed in the force required to detach the cylinder.

The composite samples hardness by Shore A was determined using a digital hardness tester in compliance with Russian State Standard GOST 263-75 “Rubber. Method for the determination of Shore A hardness” (ASTM D2240).

The thermal conductivity coefficient was measured using the MGT-4 device. The research objects were samples 100×100×10 mm in size. A detailed description of the device operation is given in the operating manual [17].

To measure the composition electrical conductivity, we used the device consisting of a measuring cell comprising two stainless steel electrodes (one movable and one stationary) and a clamping device. Prior to measuring the sample, the ends in contact with the electrodes were treated with electrically conductive paste. The sample size selection, subsequent measurements and results processing were carried out in compliance with Russian State Standard GOST6433.2-71 (ASTM D257) "Solid electrical insulating materials. Methods for evaluation of electrical resistance at d. c. voltages". The high-precision teraohmmeter UNI-T UT513 running Windows 11 OS was used as a data logger for measuring the dielectrics electrical conductivity.

Mathematical modeling and mathematical processing of the experimental results were carried out using Mathcad and OriginLab mathematical packages.

3. Results and Discussion

3.1. ODMS curing and possible filler interaction with reactive resin groups

The ODMS curing process is caused by the interaction of terminal functional hydroxyl groups with tetraethoxysilane being a part of catalyst K-18. Thus, the hydroxyl group interaction with the neighboring macromolecules occurs causing the formation of the cross-linked three-dimensional structure, accompanied by the ethanol molecule release:

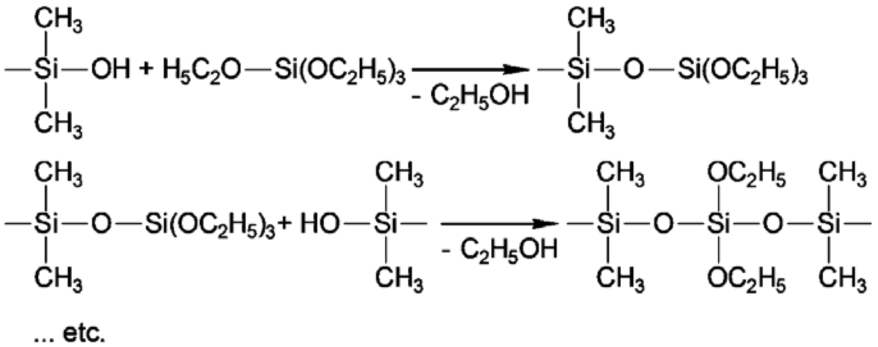

(1)

The reaction is proceeding at room temperature during 72 hours [18].

The previously published papers [19] proved that boron introduction causes a drastic change of the composition rheological properties and its strong structuring, thus making it unacceptable to be used as a filler in potting technologies. Under the similar conditions boron nitride does not affect the composition rheology. Although in general, high probability of boron nitride interaction with the ODMS hydroxyl groups causing the formation of chemical bonds between the binder and the filler but only at high temperatures is quite obvious.

3.2. Study of physical and mechanical properties

Most polymer compositions possess the following structure: filler as dispersed particles evenly distributed in the polymer matrix touching throughout the volume.

The experiments with boron nitride used in the research were conducted using microanalyzer Horiba LB-550. They showed that the basic part of its particles is concentrated in a narrow area from 3 to 5 microns (Fig. 1). The introduction of the filler into ODMS and its distribution in the binder proceeds relatively easily without agglomeration.

Fig. 2 displays the composition structure. The geometry of boron nitride particles significantly differs from the spherical shape and largely resembles the structure of graphite. The specific distribution of particles is observed, externally resembling the conducting clusters. The percolation point can be assumed to be slightly lower than the theoretical one [20].

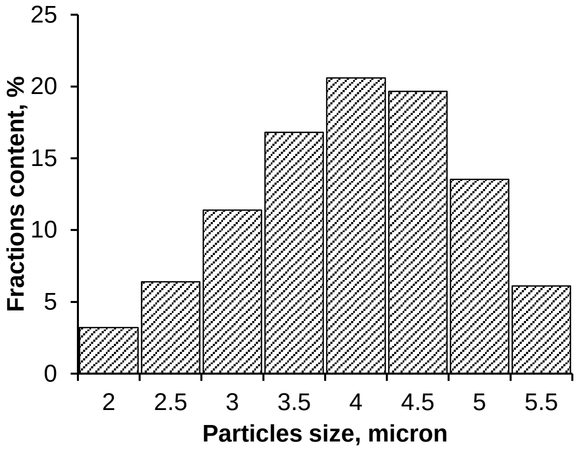

Figure 1. Fractional composition of boron nitride.

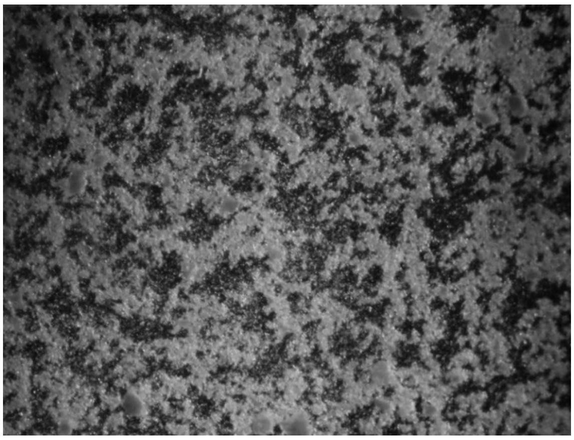

Figure 2. Boron nitride particles distribution in the composite (magnification ×100).

Strength characteristics are extremely important for most composites. Based on theoretical concepts and numerous experiments dealing with the strength characteristics of organosilicon resins filled with polar fillers, we can talk about the regularity of increasing strength in the samples received in this work (see Table 1). When the filler is introduced into elastomer, the strength increase of the material is often observed. The studied systems demonstrated similar behavior (Fig. 3). The hardening can be explained using the model of elastomer molecules sliding along the filler surface (Dannenberg model [21]): if there is no filler, the short chains break first, and the filler increases the number of loaded chains, thus causing the load redistribution. If over 5% (vol.) of boron nitride is added, the composite strength increase is observed. When the filler content in the composite exceeds 20 %, the increase in strength characteristics is slowing down.

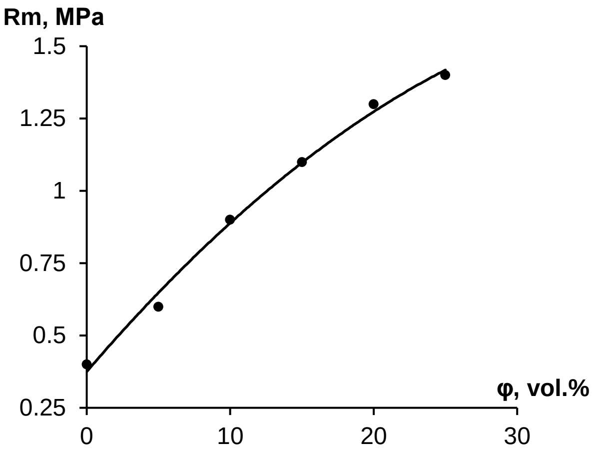

Figure 3 Tensile strength dependence (Rm) on boron nitride amount (φ).

The amplification effect might depend on the strong physical bonds formed between the binder and the filler, for instance, non-reacted hydroxyl groups and polar groups on boron nitride surface. Based on theoretical concepts, the composite strength can be expected to decrease when the filler amount exceeds 25 % (vol.), associated with the lack of binder and incomplete encapsulation of boron nitride particles.

Adhesive properties are quite essential when the composite is supposed to be used as a sealing material. In general, non-modified polyorganosiloxanes are characterized by relatively low adhesion. Studies of tensile strength of the cured composition and the base from various materials demonstrate that boron nitride introduction increases this value (see Table 1). It can be explained by the absorption theory of adhesion, relating to the appearance of submicron boron nitride phase in the composition alongside the increase of intermolecular interaction between the substrate and the base. In practice, the strength increase at tearing polysiloxanes from bases made of various materials is observed at the introduction of a number of oxides, such as iron, zinc and titanium into them [22].

Undoubtedly, the adhesive characteristics of the composition largely depend on the substrate material. Thus, the strength when the discs are detached from the Steel 3 substrate is slightly higher than from the aluminum substrate. The introduction of boron nitride also contributes to the relative hardness increase of the sealing material (see Table 1), which is associated with the polymer structuring. It should be noted that the introduction of up to 25 % (vol.) boron nitride due to the structuring causes almost a double increase in Shore A hardness compared to the pure polymer.

Table 1. Composition properties

Filler content, %	Density, kg/m^3	Tensile strength (aluminum substrate), MPa	Tensile strength (steel substrate), MPa	Shore A hardness
-	980	0.08	0.11	24
10	1020	0.12	0.15	35
20	1160	0.21	0.24	44
25	1208	0.44	0.53	51

3.3. Thermophysical characteristics of the composite

As previously mentioned, studies have revealed that distribution of the filler particles in the composite is statistical. Judging by the percolation theory, the transition depends on the filler volume fraction [23]:

$$\sigma_{DC} \propto \left(v_f - v_{fc}\right)^t, \tag{2}$$

where v_f is volume fraction of conductive component; v_{fc} is percolation threshold.

Monte-Carlo simulation for the composition containing spherical particles equals the value v_{fc} = 0.16 [24].

In addition to the particles shape, the thermo-physical characteristics of the composition largely depend on both the nature of binder and filler, and the components ratio. The thermal conductivity of composite materials consisting of several components can be determined by the following relation [29]:

$$\lambda = \lambda_{\mathrm{PDMS}}(1-\varphi) + \lambda_{\mathrm{SP}}\varphi \tag{3}$$

where λ is thermal conductivity of the multicomponent material; λ_{PDMS}, λ_{SP} are the thermal conductivity of the first and second components; φ is the volume fraction of the filler.

However, the discrepancies are frequently observed between the design and experimental data, associated with certain unevenness in the filler particles arrangement in the composition, moisture absorption, insignificant amount of remaining gas phase after composition preparing due to abnormally high binder viscosity etc. Therefore, in practice, thermal conductivity coefficient, obtained by experimental methods is used.

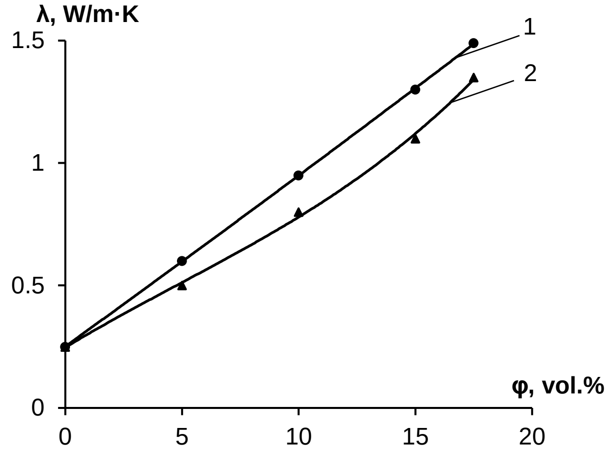

Figure 4. The dependence of thermal conductivity coefficient (λ) on filler content: 1− design; 2 – experiment.

Fig. 4 demonstrates the design and experiment values of the of thermal conductivity coefficient of SP with PDMS binder at 25 °C. In the studied max 20 % filling interval, thermal conductivity is described as follows:ascending linear dependence for design (see Fig. 4, curve 1), close to linear ascending dependence for experiment (see Fig. 4, curve 2). Thermal conductivity coefficient rises linearly as boron nitride content increases. However, the filler concentration increase up to the percolation point can be assumed to cause an abrupt increase of heat-conducting properties.

It should be noted that higher thermal conductivity coefficient of the unfilled organosilicon oligomer, compared to similar organic materials, is explained by high flexibility of polyorganosiloxane macromolecules associated with low intermolecular interaction of silicone chains.

To evaluate the effectiveness of the developed composites in MathCad environment, model calculations were performed showing the temperature distribution on the plane applying the Poisson equation. The two-dimensional Poisson equation is an example of elliptic partial differential equation including the second derivatives of the function $T(x, y)$ by two spatial variables [25]:

$$\frac{\partial^2 T(x, y)}{\partial x^2} + \frac{\partial^2 T(x, y)}{\partial y^2} = -f(x, y). \quad (4)$$

The Poisson equation frequently describes stationary distribution of temperature $T(x, y)$ on the plane with the heat sources (or absorbers) with $f(x, y)$ intensity. Poisson equation will be further considered in this very physical interpretation. Therefore, the sought-for function was denoted by T symbol. The correct formulation of the boundary value problem for Poisson equation requires four boundary conditions setting. To simplify the solution, all boundary conditions were equated to zero.

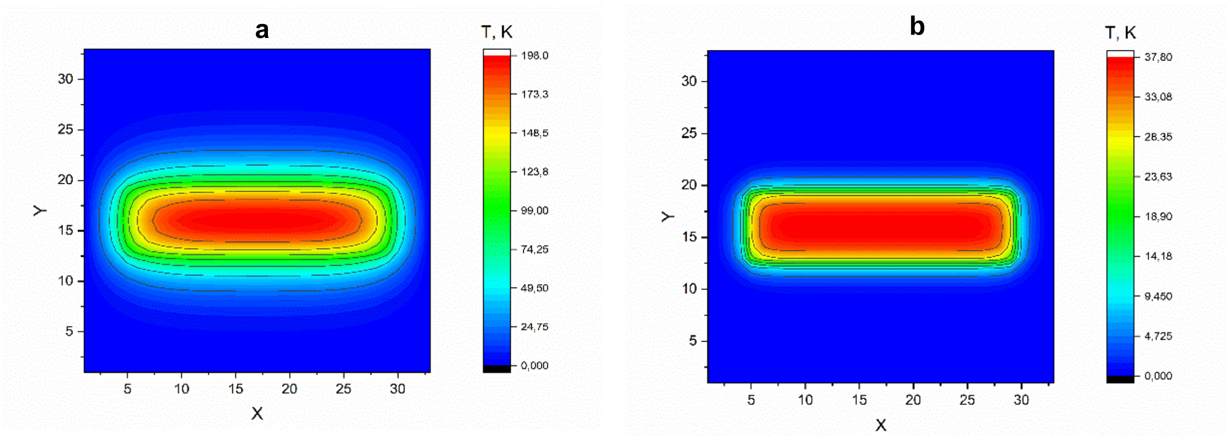

Figure 5. Lines of equal heating levels of the conductor sheath: Sheath – PVC λ = 0.2 Wt/m×K (a); Sheath – composite λ = 1.3 Wt/m×K (b).

The solution was carried out in MathCad environment applying numerical method using the built-in Relax function. The calculation results are presented in Fig. 5 as equal temperature levels on the plane.

Fig. 5 reveals that similar energy load on the conductor made from traditional polyvinyl chloride can cause the temperature rise at the metal-polymer interface exceeding 200 °C. At these temperatures, the destructive processes occur in the PVC composition, accompanied by irreversible deterioration of physical, mechanical and electrical properties [26]. But similar energy load on the heat-conducting composite does not cause the temperature rise in the system over 40 K, relative to the original.

3.4. Electrical properties of the composition

The application of hexagonal boron nitride poses the question of why boron nitride possessing high thermal conductivity, does not conduct electricity. Polar B-N bonds interfere with electron transfer, thus boron nitride in this form is not an electrical conductor, unlike graphite conducting electricity through the Pi Bonds network in the plane of its hexagonal crystals.

The available theoretical concepts do not contradict the nature of the dependence of the polymer composition electrical resistance on the boron nitride content and the fact that the percolation point is manifested at the filler content in the composition of at least 0.16 volume fractions (see Eq. 2).

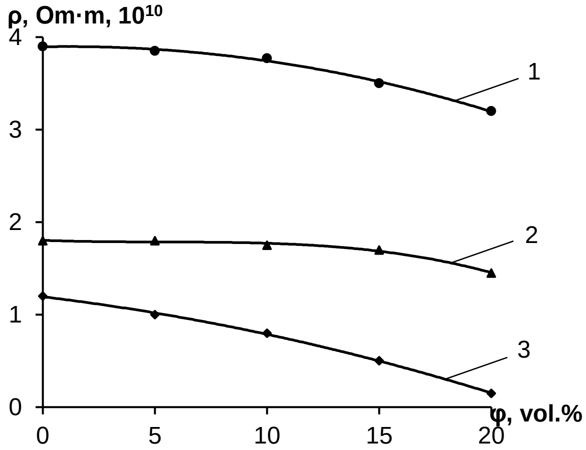

Figure 6. The electrical resistivity dependence (ρ) on boron nitride content:
1 − at 25 °C; 2 − at 50 °C; 3 − at 75 °C.

Fig. 6 shows the experimental dependences of the sealing material resistivity on the temperature and filler content in the form of specific electrical conductivity dependence on the boron nitride content at different temperatures. The measurements were carried out at 1000 V voltage at the electrodes.

In general, temperature increase causes a decrease in electrical resistance of sealing materials. At 25 °C, the dependence is downward (see Fig. 6, curve 1). When temperature reaches 50 °C, the resistivity decreases by half, but the dependence nature does not change significantly (see Fig. 6, curve 2). Further increase in temperature makes the electrical resistance decrease (see Fig. 6, curve 3). The electrical resistance decrease within the studied temperature range largely depends on ionic conductivity increase.

4. Conclusions

According to the research results, the following conclusions can be drawn:

- Within the limits of preserving rheological properties (up to 20–25 % by volume), the boron nitride introduction causes the increase in mechanical properties; similar effect is observed in the adhesive characteristics studied by the method of determining the tensile strength. The greatest tensile strength is fixed on the steel substrate, the lowest − on aluminum, depending on hydroxyl groups on the steel surface.
- The introduction of 20 % of boron nitride increases the thermal conductivity coefficient up to 1.5 W/m·K.
- The thermal conductivity problem described by the elliptic Poisson equation, was solved by numerical method in MathCad environment applying the built-in Relax function. The temperature distribution during the conductor operation in a sheath from polyvinyl chloride and an oligodimethylsiloxane based composite filled with boron nitride was shown, demonstrating more efficient operation under equal conditions.

- The dependence of electrical resistivity on temperature and filler amount was established: the temperature increase causes the electrical resistivity decrease, associated with polyorganosiloxane ionic conductivity.
- The research results can find wide application in construction industry.

References

1. Dando, K.R., Cross, W.M., Robinson, M.J., Salem, D.R. Production and characterization of epoxy syntactic foams highly loaded with thermoplastic microballoons. Journal of Cellular Plastics. 2017. 54. Pp. 499–514. DOI: 10.1177/0021955X17700093
2. Vishnu Chandar, J., Mutharasu, D., Mohamed, K., Marsilla, K. I. K., Shanmugan, S., Azlan, A.A. High thermal conductivity, UV-stabilized poly(3-hydroxybutyrate-co-3-hydroxyvalerate) hybrid composites for electronic applications: effect of different hybrid fillers on structural, thermal, optical, and mechanical properties. Polymer-Plastics Technology and Materials. 2021. 60(12). Pp. 1273–1291. DOI: 10.1080/25740881.2021.1888990
3. Hemn, Q.A., Dilshad, K.J, Sinan, A.Y. Flexural strength and failure of geopolymer concrete beams reinforced with carbon fibre-reinforced polymer bars. Construction and Building Materials. 2020. 231. 117185. DOI: 10.1016/j.conbuildmat.2019.117185
4. Proença, M., Garrido, M., Correia, J.R., Gomes, M.G. Fire resistance behaviour of GFRP-polyurethane composite sandwich panels for building floors. Composites Part B: Engineering. 2021. Vol. 224. 109171. DOI: 10.1016/j.compositesb.2021.109171
5. Cuce, E., Cuce, P.M., Wood, C.J., Riffat, S.B. Toward aerogel based thermal superinsulation in buildings: A comprehensive review. Renewable and Sustainable Energy Reviews. 2014. Vol. 34. Pp. 273–299. DOI: 10.1016/j.rser.2014.03.017
6. Fedosov, S.V., Rumyantseva, V.E., Krasilnikov, I.V., Konovalova, V.S., Evsyakov, A.S. Mathematical modeling of the colmatation of concrete pores during corrosion. Magazine of Civil Engineering. 2018. 7(83). Pp. 198–207. DOI: 10.18720/MCE.83.18
7. Lomakin, S.M., Koverzanova, E.V., Shilkina, N.G., Usachev, S.V., Zaikov, G.E. Thermal Degradation of Polystyrene-Polydimethylsiloxane Blends. Russian Journal of Applied Chemistry. 2003. 76(3). Pp. 472–482. DOI: 10.1023/A:1025677423514
8. Mastalygina, E.E., Ovchinnikov, V.A., Chukhlanov, V.Yu. Light heat-resistant polymer concretes based on oligooxyhydridesilmethylensiloxysilane and hollow spherical fillers. Magazine of Civil Engineering. 2019. 90(6). Pp. 37–46. DOI: 10.18720/MCE.90.4
9. Robeynsa, C., Picardb, L., François, G. Synthesis, characterization and modification of silicone resins: An “Augmented Review”. Progress in Organic Coatings. 2018. 125. Pp. 287−315. DOI: 10.1016/J.PORGCOAT.2018.03.025
10. Anthony, J., O’Lenick, A.J. Silicone polymers: new possibilities in nanotechnology. American Chemical Society. Symposium series. 2007. 961. Pp. 165–175. DOI: 10.1021/bk-2007-0961.ch009
11. Zelyakova, T.I., Krutov, L.N. Issledovaniya vlagozashchitnykh svoystv kompaunda marki "Viksint k-68" (rezinopodobnyy) [Studies of moisture-proof properties of the compound of the brand "Vixint K-68" (rubber-like)]. Trudy mezhdunarodnogo simpoziuma "Nadezhnost i kachestvo". 2016. 2. Pp. 332–335.
12. Nambiar, S., Yeow, J.T.W. Polymer-composite materials for radiation protection. ACS Appl. Mater. Interfaces. 2012. 4. Pp. 5717–5726. DOI: 10.1021/am300783d
13. Matsuda, R., Isano, Y., Ueno, K., Ota H. Highly stretchable and sensitive silicone composites with positive piezoconductivity using nickel powder and ionic liquid. APL Bioengineering. 2023. 7. 016108. DOI: 10.1063/5.0124959
14. Khelevina, OG. Fireproof Materials with a Vulcanised Coating based on Heteroorganic Siloxane Oligomers. International Polymer Science and Technology. 2014. 41(7). Pp. 17–20. DOI: 10.1177/0307174X1404100703
15. Dixit, C.K., Pandey, K. Study of Electrical Properties of Iron (III) Oxide (Fe2O3) Nanopowder by Impedance Spectroscopy. International Journal of Electrical Engineering and Technology (IJEET). 2020. 11(8). Pp. 127–133. DOI: 10.34218/IJEET.11.8.2020.012
16. Khrustalyov, A., Zhukov, I., Nikitin, P., Kolarik, V., Klein, F., Akhmadieva, A., Vorozhtsov, A. Study of Influence of Aluminum Nitride Nanoparticles on the Structure, Phase Composition and Mechanical Properties of AZ91 Alloy. Metals. 2022. 12. 277. DOI: 10.3390/met12020277
17. Izmeritel teploprovodnosti ITP-MG4. Rukovodstvo po ekspluatatsii E 12.102.010RE [Thermal conductivity meter ITP-MG4 Operating Manual E 12.102.010RE]. SKB Stroypribor Chelyabinsk. 2020. 45 p.
18. Yarmolenko, M.A., Rogachev, A.A., Rogachev, A.V., Gorbochev, D.L. Kinetic characteristics of dispersion of organosilicon compounds in vacuum and molecular structure of the coatings, deposited from volatile products of dispersion. Problems of Physics, Mathematics and Technics. 2011. 8(3). Pp. 32–38.
19. Chukhlanov, V.Y., Selivanov, O.G., Chukhlanova, N.V. Sealing Formulations on the Basis of Low-Molecular Dimethyl–Siloxane Rubber Modified by Amorphous Boron. Polymer Science, Series D. 2019. 12. Pp. 1–4. DOI: 10.1134/S1995421219010040
20. Kerber, M.L., Vinogradov, V.M., Golovkin, G.S., Gorbatkina, Yu.A., Krzhizhanovskiy, V.K., Kuperman, A.M., Simonov-Yemelyanov, I.D., Khaliulin, V.I., Bunakov V.A. Polimernyye kompozitsionnyye materialy: struktura, svoystva, tekhnologiya [Polymer composite materials: structure, properties, technology.]. SPb.: Professiya. 2008. 560 p.
21. Bazhenov, S.L., Berlin, A.A., Kulkov, A.A., Oshmyan, V.G. Polimernyye kompozitsionnyye materialy [Polymer composite materials]. Intellekt. 2010. 352 p.
22. Shui, Y., Huang, L., Wei, Ch., Sun, G., Chen, J., Lu, A., Sun, L., Liu, D. How the silica determines properties of filled silicone rubber by the formation of filler networking and bound rubber. Composites Science and Technology. 2021. 215. 109024. DOI: 10.1016/j.compscitech.2021.109024
23. Landauer, R. Zeitschrift für Physik. Condensed Matter. 1987.68. No. 2. Rp. 217–223.
24. Blythe, T., Bloor, D. Electrical properties of polymers. 2nd edn. Cambridge: Cambridge University Press, 2008. 480 p.
25. Geuzaine, C., Remacle, J.-F. Gmsh: a three-dimensional finite element mesh generator with built-in pre- and post-processing facilities. International Journal for Numerical Methods in Engineering. 2009. 79(11). Pp. 1309–1331. DOI: 10.1002/nme.2579
26. Lewandowski, K.; Skórczewska, K. A Brief Review of Poly(Vinyl Chloride) (PVC) Recycling. Polymers. 2022. 14. 3035. DOI: 10.3390/polym14153035

Information about authors

Vladimir Chukhlanov, *Doctor of Technical Sciences*
ORCID: https://orcid.org/0000-0002-2995-388X
E-mail: kripton0@mail.ru

Natalia Smirnova, *Doctor of Chemical Sciences*
ORCID: https://orcid.org/0000-0001-7588-3555
E-mail: smirnovann@list.ru

Irina Krasilnikova, *PhD in Technical Sciences*
ORCID: https://orcid.org/0000-0002-4342-4255
E-mail: krasilnikovaia@list.ru

Natalia Chukhlanova,
E-mail: natalyferre@yandex.ru

Received 11.04.2023. Approved after reviewing 20.06.2023. Accepted 23.06.2023.

Magazine of Civil Engineering

ISSN 2712-8172

journal homepage: http://engstroy.spbstu.ru/

Research article

UDC 691.3

DOI: 10.34910/MCE.122.4

Mechanical and microstructural properties of self-healing concrete based on Hay Bacillus

V. Prasad [1], M.M.S. Sabri [2], S. Devi [1], H.M. Najm [3], S. Majeed [4], S.M.A. Qaidi [5]

[1] *Vignana Bharathi Institute of Technology, Hyderabad, India*
[2] *Peter the Great St. Petersburg Polytechnic University, St. Petersburg, Russian Federation*
[3] *Department of Civil Engineering, Zakir Husain Engineering College, Aligarh, India*
[4] *Nawroz University, Duhok, Iraq*
[5] *Department of Civil Engineering, College of Engineering, University of Duhok, Duhok, Iraq*

mohanad.m.sabri@gmail.com

Keywords: self-healing concrete, hydrostructures, Hay Bacillus, crushed stone sand, river sand, calcite, microstructural

Abstract. The experimental investigation delves into assessing the influence of varying ratios of calcite (Cc) and sand on the mechanical and microstructural characteristics of self-healing concrete (SHC). This study employs Hay Bacillus as a catalyst for initiating calcite precipitation within the concrete matrix. The proportions of calcite under scrutiny encompass 5%, 10%, and 15% of the cement's weight. Additionally, two distinct types of sand, crushed stone sand (CSS) and river sand (RS) are juxtaposed for comparative analysis. The primary focus of this research is on evaluating the compressive and flexural strengths of the SHC, with particular emphasis on the utilization of a 10% bacterial solution. This proportion emerged as the optimal dosage for enhancing concrete strength. To gain a comprehensive understanding of the underlying mechanisms, the microstructure of the concrete is probed through scanning electron microscopy (SEM) and X-ray diffraction (XRD) techniques. These tests allow elucidating the impact of varying calcite and sand ratios on the formation of calcium lactate, as well as the production of calcium silicate hydrate (CSH) gel and non-expanding ettringite within the concrete matrix. This investigation contributes valuable insights into the development of self-healing concrete with improved mechanical properties, underpinned by a deeper comprehension of its microstructural transformations.

Funding: This research was supported by a grant from the Russian Science Foundation No. 22-79-10021, https://rscf.ru/project/22-79-10021/

Citation: Prasad, V., Sabri, M.M.S., Devi, S., Najm, H.M., Majeed, S., Qaidi, S.M.A. Mechanical and microstructural properties of self-healing concrete based on Hay Bacillus. Magazine of Civil Engineering. 2023. Article no. 12204. DOI: 10.34910/MCE.122.4

1. Introduction

Concrete, apart from liquids, is one of the most widely used materials on the planet. However, it is susceptible to developing small cracks and holes, which can serve as pathways for water and harmful substances, resulting in reinforcement rust and concrete deterioration. It can lead to a loss of concrete strength and durability, resulting in significant expenses for repairing and maintaining concrete structures globally. Although several methods exist for repairing cracks, most conventional restoration techniques involve chemicals, require significant labor, are costly, and pose environmental and health risks. Recently, a new, efficient method for repairing microcracks and pores in concrete using microbiologically induced calcium carbonate precipitation has been proposed [1–3]. This bacterial remediation method is superior to other methods because it is bio-based, environmentally friendly, cost-effective, and sustainable [4–8]. Moreover, it was found that locally isolated Bacillus Sonorensis bacteria from Iraqi soil samples, with their high urease-producing abilities, can be used to increase cementation between soil particles and improve the undrained shear strength of soft clay soil by utilizing the MICP technique. This sustainable technique can be used for biocementation in the construction industry [9].

Recent discoveries have revealed that bacteria that can produce the enzyme urease can significantly impact $CaCO_3$ precipitation. The enzyme facilitates the hydrolysis of urea to produce CO_2 and ammonia, which increases pH and promotes the precipitation of $CaCO_3$ in bacterial settings. This innovative and eco-friendly technique has been successfully used to repair concrete cracks and prevent channel leaching. Bacillus pasteurii and Bacillus sphaericus are highly effective in inducing $CaCO_3$ precipitation, remediating concrete cracks, and improving compressive strength. These findings hold significant potential for developing new approaches for repairing and strengthening concrete structures in an environmentally sustainable manner [10–12]. Compared to untreated regular concrete specimens, the durability of concrete specimens treated with Bacillus pasteurii and subjected to alkaline, sulfate, and freeze-thaw environments improved [13].

Strength is one of the most important characteristics of concrete. It can be defined as the ability of concrete to withstand loads [14]. Concrete can be accepted or rejected for structure use based on its strength properties. High strength in concrete is desirable for many applications, such as bridges, tall buildings, and other massive structures. High-strength concrete can be made by adding admixtures [15]. The addition of any material to concrete should not hamper its strength. Another crucial factor in concrete construction is durability. The ability of a concrete structure to last for an extended period without significant deterioration is referred to as its durability. Because of its longevity, a durable construction helps conserve resources, as there is no need to produce new building materials [16].

Additionally, it lessens the production of building trash, thus decreasing environmental pollutants. From an economic point of view, it lowers repair and maintenance costs. High strength alone does not guarantee the durability of concrete [4]. Concrete contains microcracks and pores, which increase the material's permeability. The increased permeability allows the passage of water and other substances. Water entry leads to reinforcement corrosion, which is the primary cause of deterioration and loss of durability in concrete [17].

The bacteria, capable of healing apertures and micro-blows in concrete by precipitating Cc, may be used for the bioremediation of concrete. These bacteria can attract Ca^{2+} from the surrounding environment and produce a urease enzyme. This urease enzyme catalyzes urea and produces carbon dioxide and ammonia. This process causes a rise in pH and Ca^{2+}, which combine with carbon dioxide to form Cc. The bacteria for use in concrete should be capable of creating endospores. Endospores can withstand the harsh concrete environment and remain dormant for up to [12, 18]. The formation of cracks, water, and air seeps inside the concrete, creating a favorable environment for the endospores to germinate. After germination, the bacteria will start precipitating C_c to seal the pores and cracks in the concrete. Adding cementitious materials made from byproducts to concrete provides manifold advantages as it supports ecological and energy maintenance and advances the strength and toughness of concrete [14].

The cost of SHC, when compared to predictable concrete, would be high. The substrate for growing bacteria is the primary factor contributing to the bacterial treatment's cost. The inclusion of cheaper substrates will thus reduce the cost of SHC. The SHC will also lead to the economy over the long run because of reduced costs for the repair of cracks and maintenance [19]. Microbial mineral precipitation arising from the metabolic operations of beneficial concrete microorganisms has recently enhanced the general concrete behavior. The procedure may be carried out within or outside the microbial cell or within the concrete uniform some distance away. Bacterial operations often merely cause a shift in the chemistry of solutions that mains to over-saturation and precipitation of minerals. The use of these ideas of bio-mineralogy in concrete mains to the possible creation of a fresh solid named SHC.

2. Materials and Methods

2.1. Materials

2.1.1. Cement

53-grade Portland cement cast-offs in this research. This Portland cement was verified as per IS 4031-1996 [20], and the physical belongings are presented in Table 1.

Table 1. Properties of Portland cement.

Property	Specific gravity	Blaine's fineness	Soundness	7-d CS	28-d CS
Value	3.02	283 m^2/kg	2.2 mm	42 MPa	55 MPa

2.1.2. Fine aggregates

Resident-offered crushed stone sand (CSS) and river sand (RS) are utilized as fine aggregates. For the fine aggregate, the distribution of the gradation curve is presented in Figure 1. The specific gravities of CSS and RS are 2.76 and 2.67, respectively.

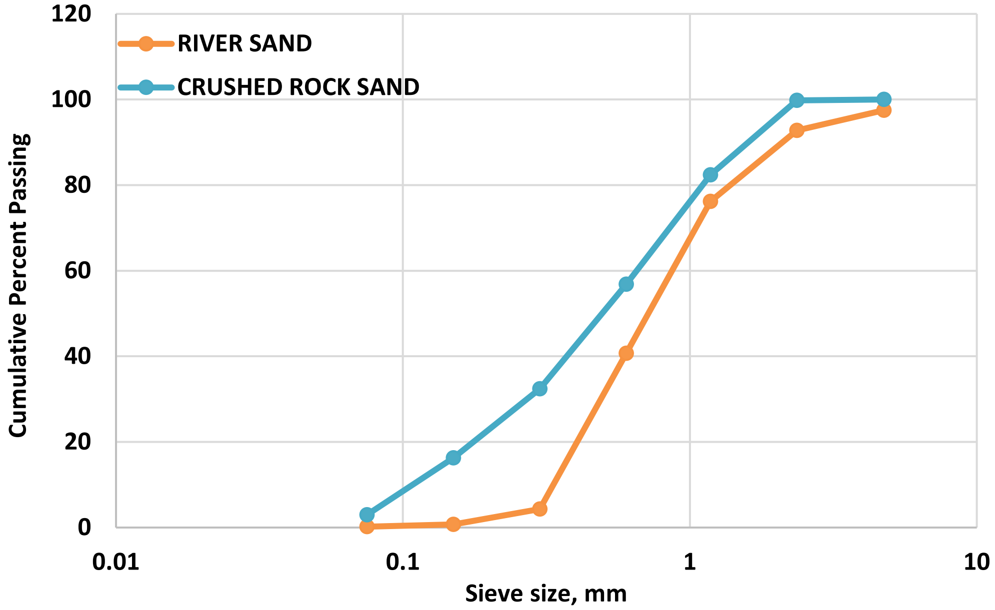

Figure 1. Grading curve of fine aggregate.

2.1.3. Coarse aggregates

Wrinkled granite cracked stones of nominal size 20 mm are cast off as coarse aggregate. Table 2 presents the properties of coarse aggregate. The grading curve of coarse aggregate is illustrated in Figure 2.

Table 2. Test Properties of coarse aggregate.

Property	Water absorption	Specific gravity	ACV	AIV
Value	0.52%	2.72	20.5%	21.7%

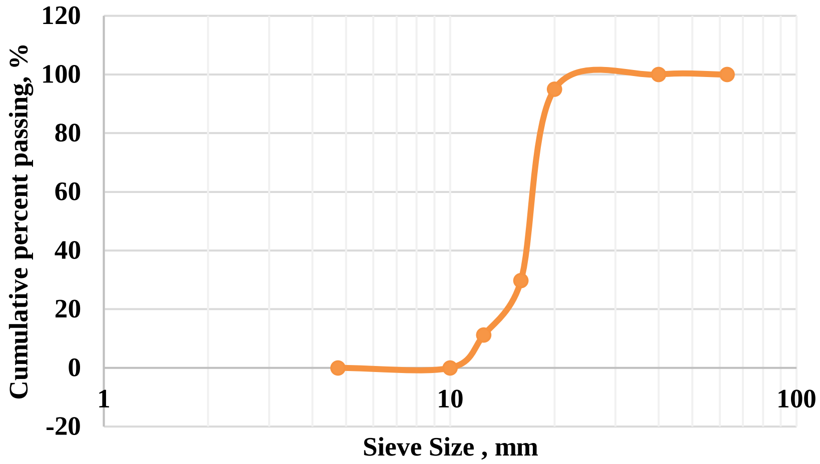

Figure 2. Grading curve of coarse aggregate.

2.1.4. Culturing of Hay Bacillus

Refined Hay Bacillus microscopic organisms were used to achieve the aim of the research. $Ca(LaC)_2$ was utilized with the bacteria Hay Bacillus and nutritious broth. It is available in powder form with white coloring. 500ml of distilled water, 2.5 gm of peptone, 2.5 gm of sodium chloride, and 1.5 gm of beef extract concentrate were combined to create the nutritious broth. A silver thimble and a cotton plug for security protected this flask. Afterward, the arrangement was preserved in an autoclave for 20 minutes at 121 °C and 150 lbs. The arrangement was orange in color, and the clarity of pollution after this treatment. The cup opened in the laminar wind current chamber, and the Hay Bacillus were introduced to this configuration. Afterward, the arrangement hatched in an orbital shaker at 125 rpm and 37 °C. This arrangement turned into white-yellow turbidity after one day, as presented in Figure 3, illustrating the development of Hay Bacillus.

Figure 3. Culturing of Hay Bacillus.

2.1.5. Calcium lactate $Ca(LaC)_2$

Calcium lactate, also known as $Ca(LaC)_2$, was used along with Hay Bacillus as nutrient broth, as shown in Figure 4, to ensure successful bacterial growth and to obtain accurate and reliable experimental results.

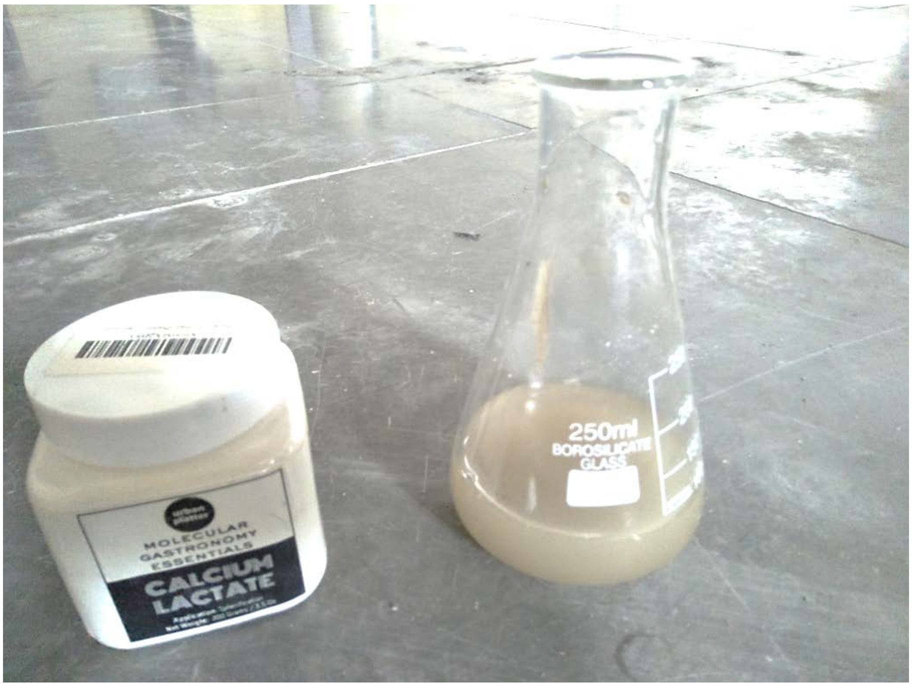

Figure 4. Calcium lactate and Hay Bacillus.

2.2. Methods

2.2.1. Mix Design

The mix proportions for M40-grade concrete are designed using IS 10262-2009 [21]. Resources essential per one m^3 of concrete are presented in Table 3.

Table 3. The volume of materials to one cum of concrete.

Type of Fine aggregate	Mixture Designation	Cement (kg/m^3)	RS (kg/m^3)	CSS (kg/m^3)	Coarse Aggregate (kg/m^3)	w/c ratio	Bacterial Cells (CFU/ml)	Percent of bacterial-sol
River sand (RS)	RSHC00			-				00
	RSHC05		642	-				05
	RSHC10			-				10
	RSHC15			-				15
Crushed sandstone (CSS)	CSHC00	390	-		1261	0.45	105	00
	CSHC05		-					05
	CSHC10		-	642				10
	CSHC15		-					15

2.2.2. Samples preparation and test methods

2.2.2.1. Samples preparation

Before placing concrete, the cast iron molds of the cylinder, cube, and prism are entirely cleaned and oiled on the inside surfaces. The molds are filled with evenly mixed SHC.

2.2.2.2. Compressive strength (CS) test

According to IS 516-1959 [22] requirements, CSs on SHC specimens with 150×150×150 mm dimensions were performed. According to IS 456-2000 [23] criteria, these specimens were produced and cured at 7, 14, 28, and 90-d.

2.2.2.3. Flexural strength (FS) test

According to IS 516-1959 [22], concrete prism specimens with bacteria were subjected to an FS.

2.2.2.4. Microstructural analysis test

For better visualization, SEM analyses are done on the SHC aimed at which the concrete is made into powder by crushing it into small pieces. The powdered specimen is placed on nerve ends with the help of carbon tape, and before they are analyzed at 20 kV, they are coated with gold. As is customary, the specimens are tested after curing for 28-d.

3. Results and Discussion

3.1. Compressive strength (CS)

The results of the M40 grade concrete experiment of RS and CSS mixtures show the influence of bacteria on the compressive strength of the modified concrete, as shown in Figure 5. The obtained data indicate that the sand mixtures' compressive strength is higher than that of all ages of RS mixtures, irrespective of the amount of bacterial sol. This can be attributed to the fact that CSS, which is cubic and has sharp edges, helps to achieve higher compressive strength than RS mixtures.

The CS of the control mixture concrete was compared with the CS of SHC-5%, SHC-10%, and SHC-15% at 28-d and 90-d. The results showed that the percentage increase in CS for SHC-5%, SHC-10%, and SHC-15% at 28-d was 8.98%, 17.02%, and 4.65%, respectively. Similarly, CS at 90-d was found to increase by 8.49%, 12.27%, and 2.59%, respectively.

In the CSS mixtures, the CS at 28-d for SHC-5%, SHC-10%, and SHC-15% increased by 6.94%, 14%, and 2.28%, respectively. While at 90-d, the percentage increase in CS of the CSS mixture was 9.0%, 14.9%, and 3.09%, respectively. Furthermore, it was observed that the increase in CS at 90-d was higher than the increase at 28-d. It is justified by the role of hay-Bacillus bacteria and $Ca(LaC)_2$ in enhancing CS at ages beyond 28-d for both RS and CSS mixtures [24].

The CS was found to increase as the percentage of bacterial sol in concrete increased from 0% to 10%, but at 15%, it decreased. This is because the hydration products were saturated at 10% bacterial sol, and further increase in bacterial sol did not enhance the strength, resulting in a reduction in CS.

The bacteria used in this technology are typically spore-forming, which means that they remain dormant until activated by moisture. When the concrete cracks and water enters, the bacteria are activated and start to produce calcium carbonate, which fills in the cracks and restores the strength of the concrete. However, when the bacterial solution is added to the concrete in concentrations higher than 10%, it can have adverse effects on the compressive strength of the concrete. This is because the bacteria consume some of the nutrients in the concrete mixture, which can weaken the concrete matrix and reduce its strength. Additionally, higher concentrations of bacterial solution can also increase the water content of the concrete, which can negatively affect its strength, which are other factors justifies the decreases of the CS at concentrations higher than 10%

Moreover, Figure 6 (a and b) shows the relationship between the volume of the hay-Bacillus bacteria solution and compressive strength with River sand (RS) and Crushed sandstone (CSS), respectively. Strong R2 values were found for SHC samples with CSS more than RS.

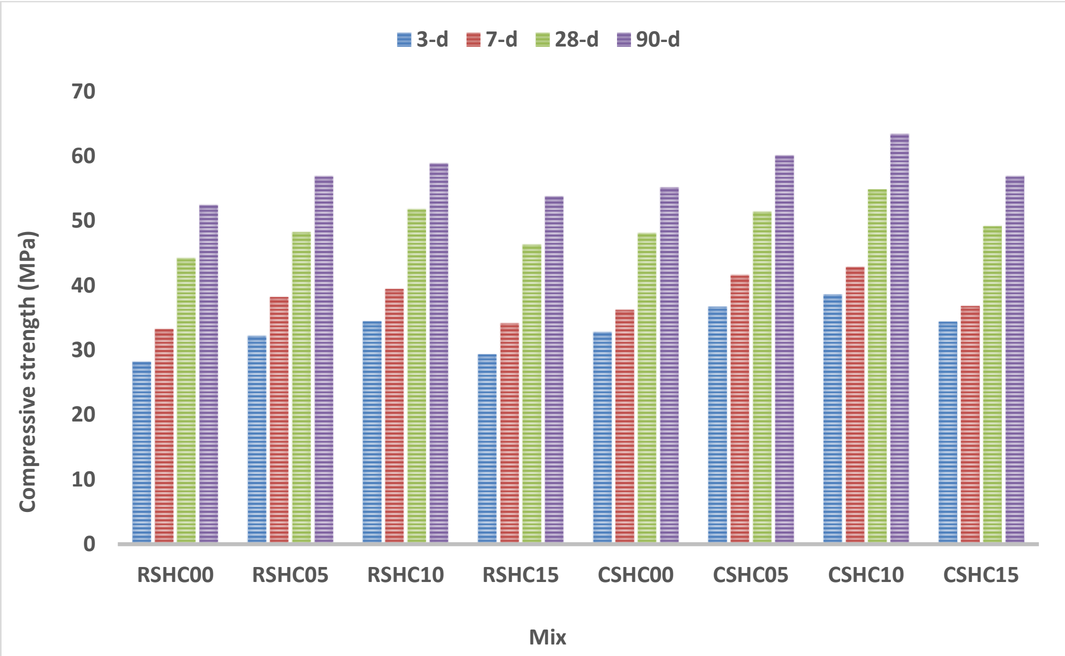

Figure 5. Result of compressive strength of SHC.

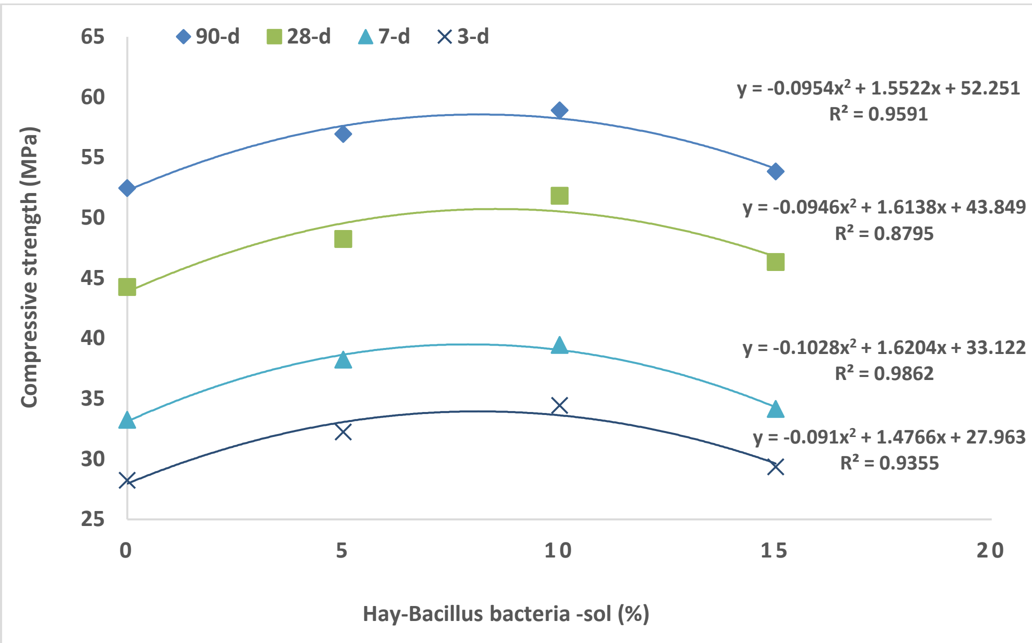

(a)

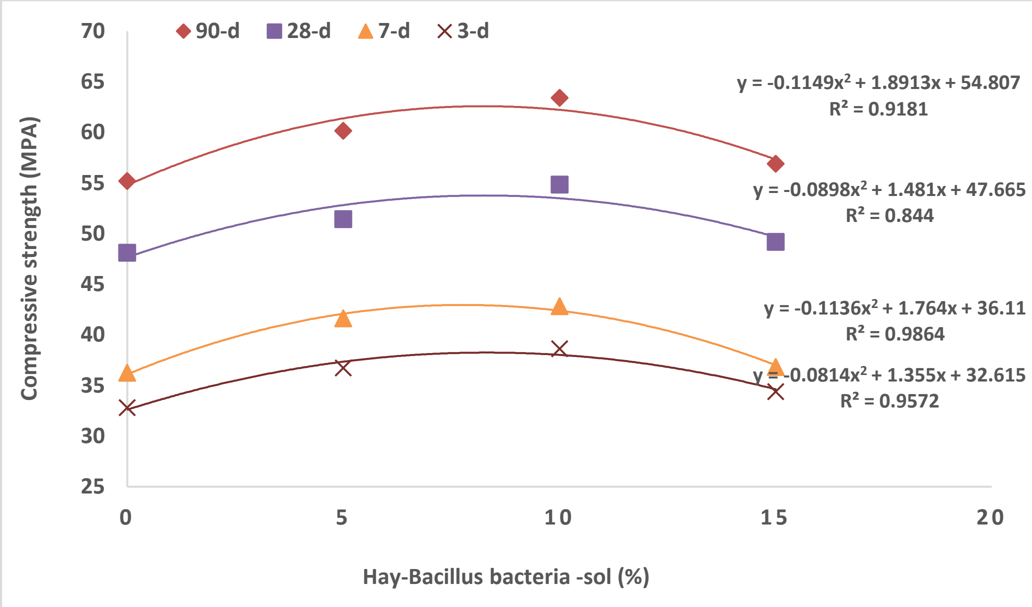

(b)

Figure 6. Relationship between the volume of hay-Bacillus bacteria-solution and compressive strength with (a) River sand (RS) and (b) Crushed sandstone (CSS).

2.3. Flexural strength (FS)

Figure 7 shows how the FS of SHC varies with curing time for mixtures made from RS and CSS. As the curing age of SHC grows, so does its FS. According to these findings, CSS mixtures have stronger FS than RS mixtures at all ages, regardless of the amount of bacterial sol. At 28-d, the percentage increases for RS mixtures with SHC-5%, SHC-10%, and SHC-15% are 4.97%, 9.04%, and 2.26%, respectively. Like this, at 90-d, the percentage increase in FS is 5.5%, 12.71%, and 2.54%, respectively. The percentage increases in FS for CSS mixtures at 28-d for SHC-5%, SHC-10%, and SHC-15% are 3.8%, 6.84%, and 1.14%, respectively. Like this, at 90-d, the FS percentage increase was 4.65%, 10.03%, and 1.43%, respectively. Additionally, as the percentage of SHC increased from 0% to 10%, the FS also increased. However, at 15%, the FS decreased due to the saturation of the hydration products with 10% bacterial-sol, which prevents further increases in bacterial-sol from increasing FS [25].

Moreover, Figure 8 (a and b) shows the relationship between the volume of hay-Bacillus bacteria solution and flexural strength with River sand (RS) and Crushed sandstone (CSS), respectively. Strong R2 values were found for SHC samples with CSS more than RS. Besides, Figure 9 shows a relationship between compressive strength and flexural strength. R2 indicates a strong relationship between them in both RS and CCS.

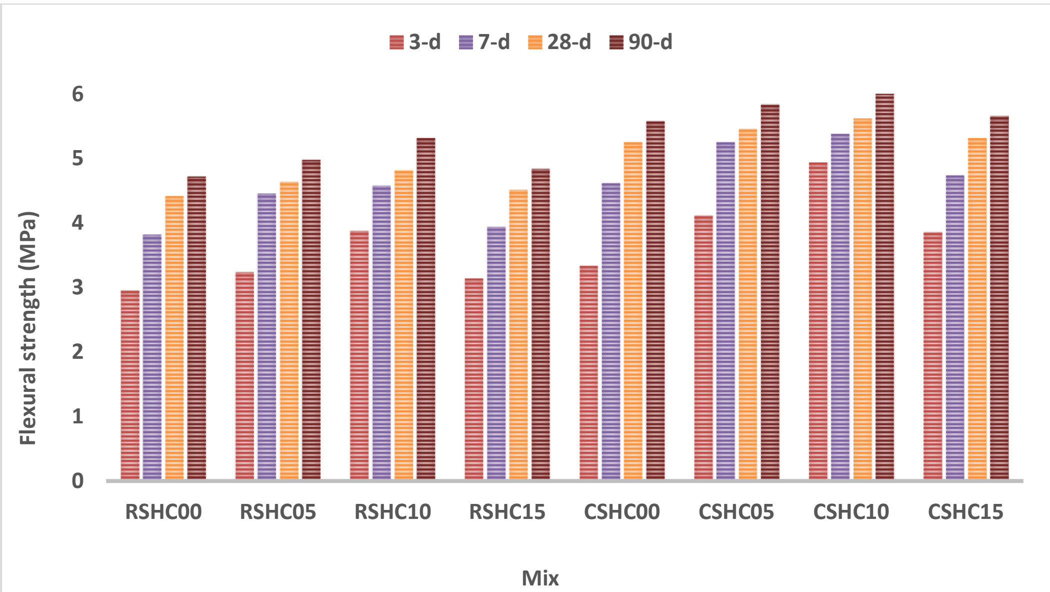

Figure 7. Result of flexural strength of SHC.

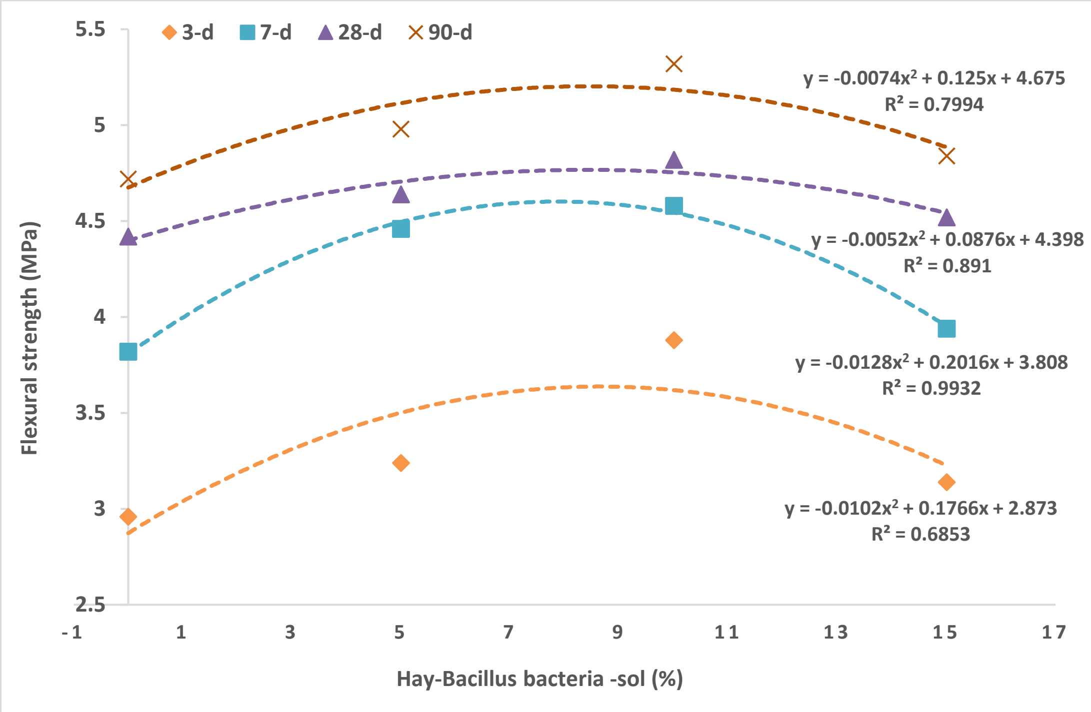

(a)

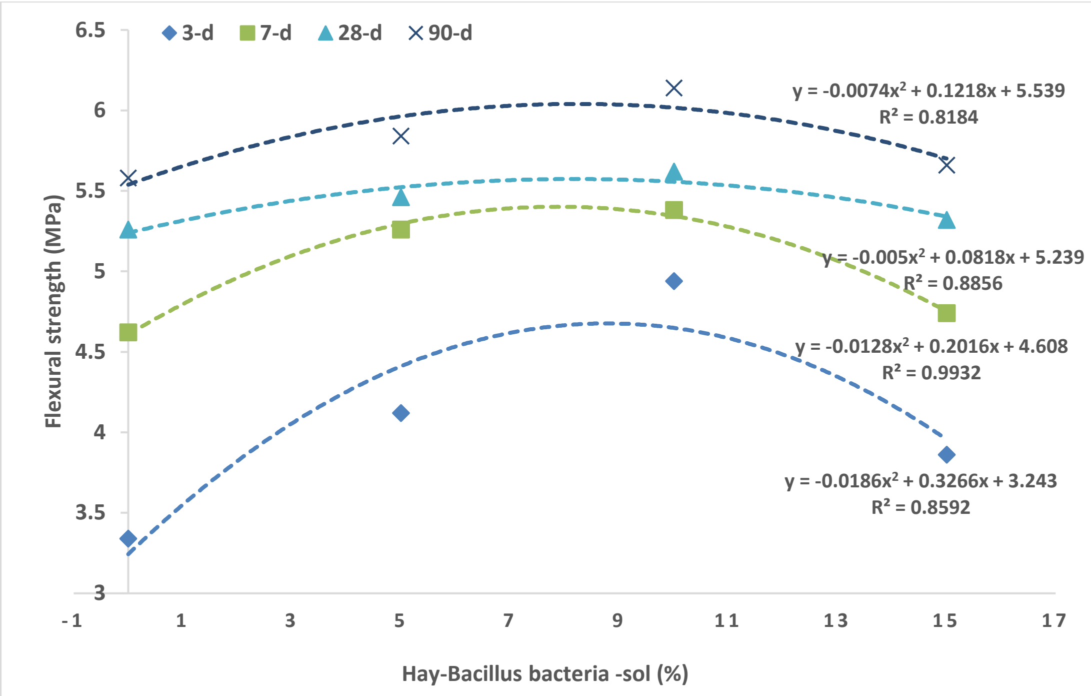

(b)

Figure 8. Relationship between the volume of hay-Bacillus bacteria-solution and flexural strength with: (a) River sand (RS) and (b) Crushed sandstone (CSS)

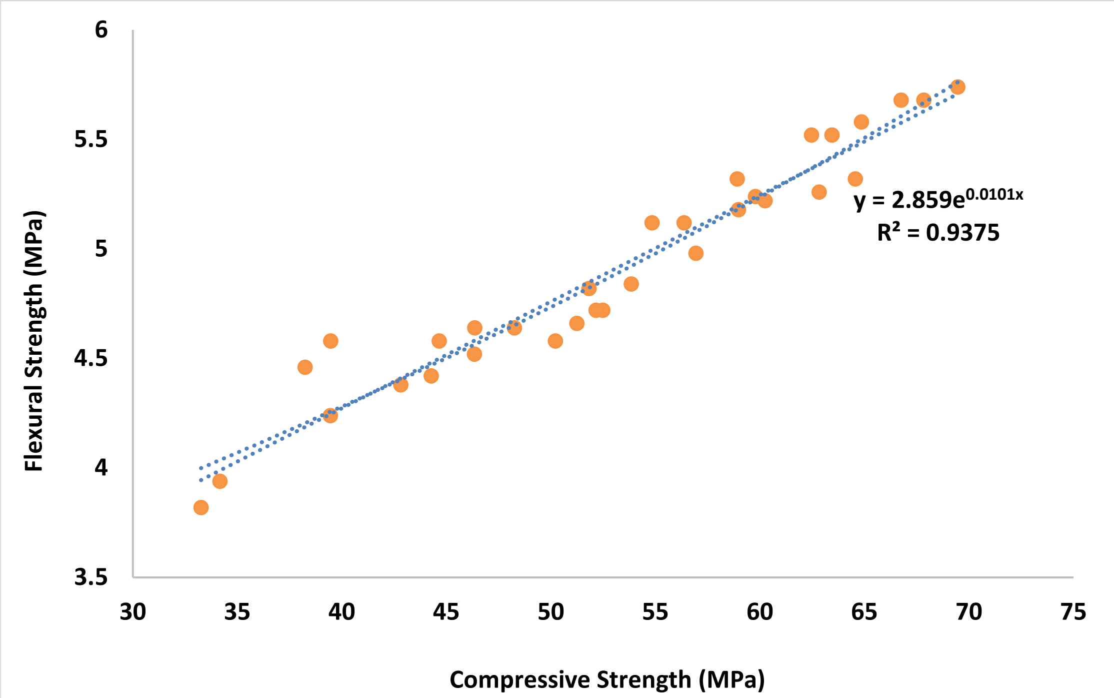

(a)

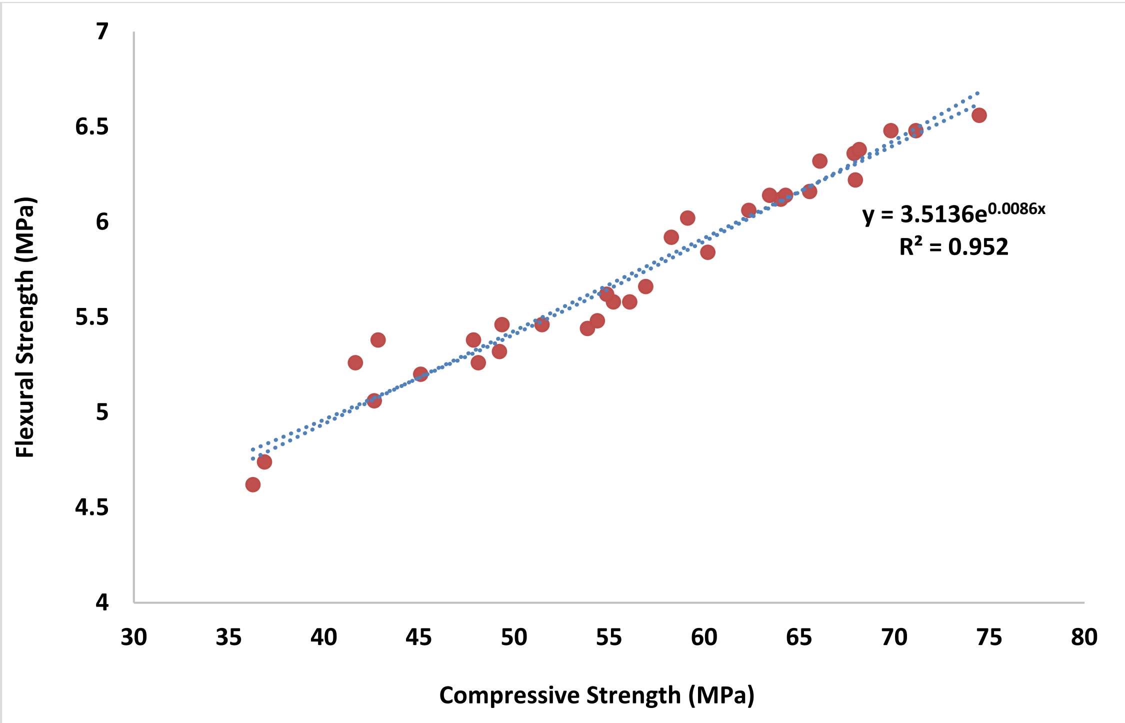

(b)

Figure 9. Relationship between compressive strength and flexural strength with: (a) River sand (RS) and (b) Crushed sandstone (CSS).

3.2. Microstructural analysis

3.3.1. Scanning electron microscope (SEM)

SEM analyses are used to imagine the occurrence of Cc crystals precipitated by bacteria inside concrete specimens.

The findings of the SEM analyses for regular concrete are considered at different amplifications. Sub-acceleration voltage and pixel sizes have been presented in Figures 10 and 11, which show the microstructure of normal concrete. SHC analyses are carried out in a similar setting. SEM analyses demonstrated the emergence of Cc prepetition in the SHC. It shows that the reduction in permeability and rise in the strength and curing of crashes in concrete are due to the formation of Cc [7,8]. In contrast, pores, calcium silicate hydrate (CSH), and CH, have occurred in almost all the specimens.

This method was utilized to investigate bacteria-treated and untreated concrete specimens. The SEM images are displayed in Figures 10 and 11. The concrete specimens had identifiable Cc crystals, according to the SEM analyses. The presence of Cc in the form of $CaCO_3$ was verified by the high calcium concentrations in all the bacterial specimens. Bacteria acted as nucleation sites during mineralization since crystalline Cc is associated with bacteria.

Calcite crystal growth was examined in both the treated and untreated bacteria specimens. While the matrix of the concrete specimens treated with the microbe seems crystalline, and individual crystals could be distinguished, the untreated specimens (those without bacteria) appear amorphous and show no trace of crystal formation. The degree of crystallization in the treated specimens' matrix is relatively diverse. Concentrations of somewhat large crystals can be found at the boundaries between the sand particles and the matrix. This textural setting implies that preferential crystallization at the concrete-matrix interfaces is likely enhancing the coherence between cement particles and the matrix at the microscale.

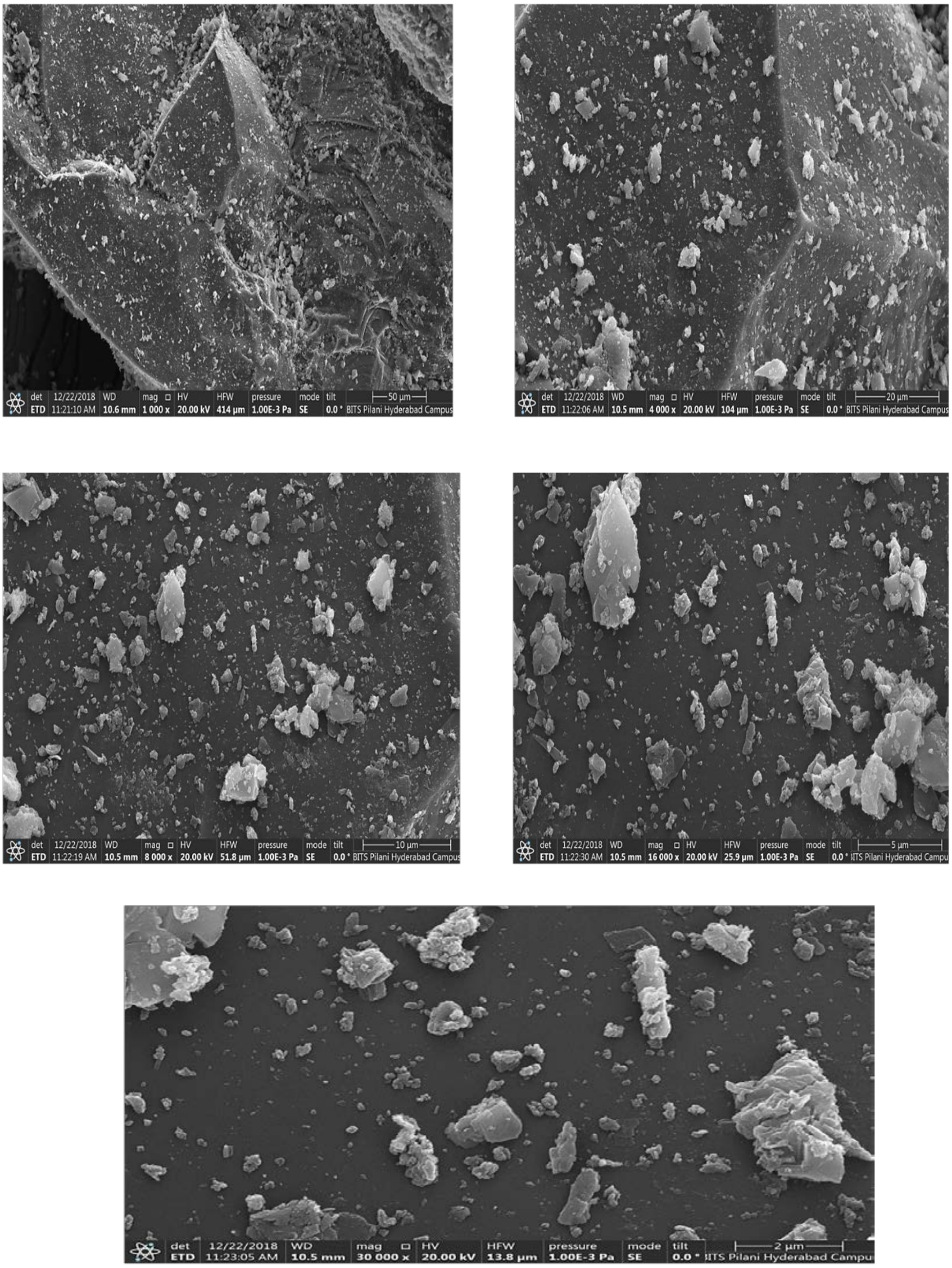

Figure 10. SEM Micrograph for SHC with river sand (RS).

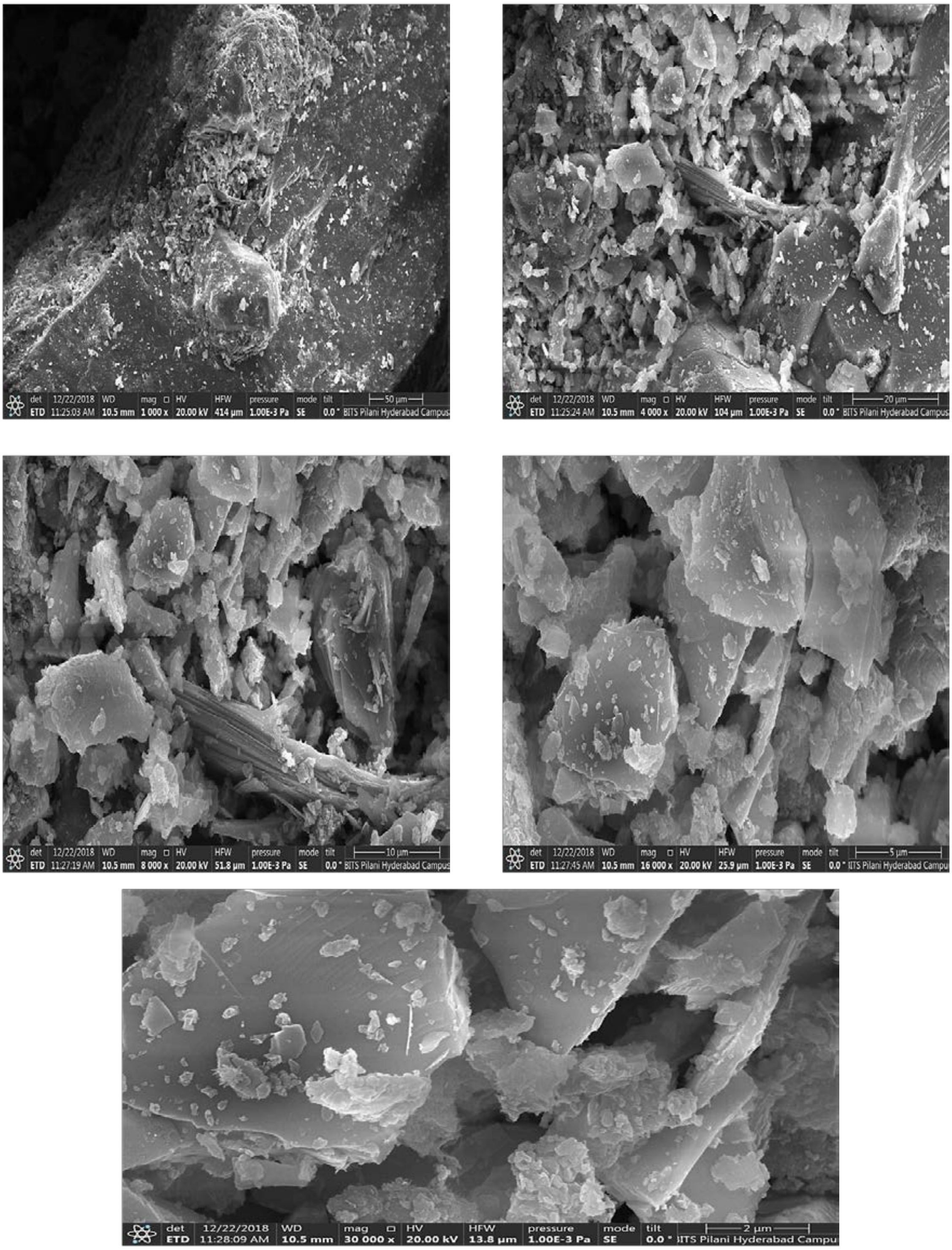

Figure 11. SEM Micrograph for SHC with crushed sandstone (CSS).

3.3.2. X-ray diffraction (XRD)

As shown in Figure 12, the crests are seen at various stages when the recordings are obtained at a wavelength of 1.54 Å. From the observed highest peak at the respective theta, the value obtained is 27.914, representing pure Cc. These peaks can be seen for some other specimens, which represent a few other materials like calcium silicate hydrate (CSH), quartz (Q), calcite (Cc), ettringite (E), and Larnite (L). All these results are shown in Figure 12. Compared to the non-bacterial samples, the composition of Cc is visually peaked for bacteria after the quantitative analysis. The existence of amorphous content with the addition of the crystalline phase of Cc, portlandite, and larnite has been shown in the form of a hump in Figure 12.

The presence of CSH and Cc in concrete samples with Bacillus subtilis was identified using XRD analysis. The presence of CSH peaks demonstrates the cause for the strength development of concrete specimens [8]. The presence of Cc peaks will confirm the Cc precipitation by bacteria which is the reason for the increased strength and durability of concrete specimens.

Each crystalline solid has a distinct XRD powder pattern that can be used as a "fingerprint" for identification. XRD is also used to characterize fingerprints and determine the structure of crystalline minerals such as CSH and Cc. Broken cube specimens collected from compressive strength tests and precipitates in cracks of concrete beam specimens were used to evaluate crack healing [26]. XRD analysis was performed on the fraction that passed through a sieve size of 5μm.

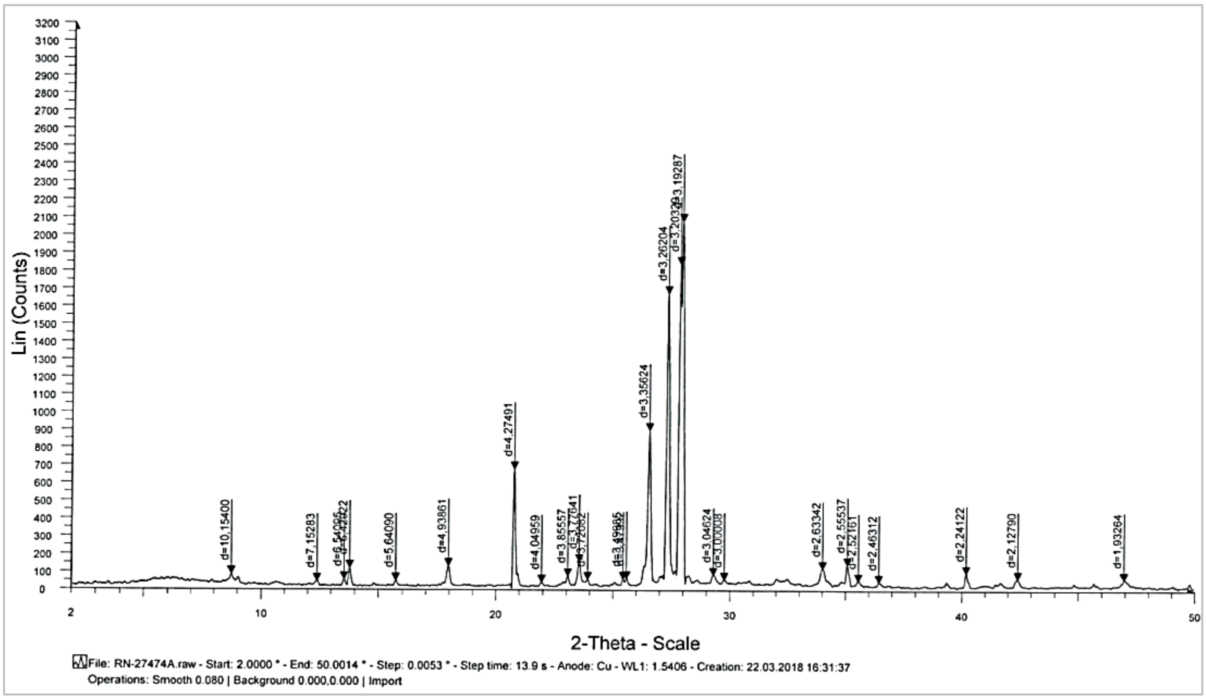

Figure 12. XRD diffraction of SHC.

4. Conclusions

The conclusions drawn from this study are as follows:

1. The CS of SHC of Grade M40 is improved with a 10% increase in bacterial sol for both RS and CSS mixtures due to the formation of $Ca(LaC)_2$ in concrete. However, the strength is condensed beyond 10% bacterial sol due to the saturation of hydrated compounds. As a result, it is estimated that 10% of the bacterial sol is used in concrete applications.

2. The FS results also show similar patterns of increase in strength up to 10% bacterial sol at all curing ages.

3. Due to the cubical particles and increased hardness of CSS mixtures, they outperformed RS mixtures in CS and FS. To create SHC for structural usage, CSS can be utilized.

4. After 28-d, all SHC mixtures showed evidence of the creation of Cc, which is CaCO3, according to microstructure analyses.

5. SEM and XRD studies revealed that the enhanced CSH gel and non-expanding ettringite production confirms the improved CS at 10% bacterial sol.

References

1. Pacheco-Torgal, F., Jalali, S., Labrincha, J., John, V.M. Eco-efficient concrete. 2013. A volume in Woodhead Publishing Series in Civil and Structural Engineering. DOI: 10.1533/9780857098993.
2. Achal, V., Mukerjee, A., Sudhakara Reddy, M. Biogenic treatment improves the durability and remediates the cracks of concrete structures. Construction and Building Materials. 2013. 48. 1–5. DOI: 10.1016/j.conbuildmat.2013.06.061
3. De Muynck, W., De Belie, N., Verstraete, W. Microbial carbonate precipitation in construction materials: A review. Ecological Engineering. 2010. 36. 118–136. DOI: 10.1016/j.ecoleng.2009.02.006
4. Botusharova, S., Gardner, D., Harbottle, M. Augmenting Microbially Induced Carbonate Precipitation of Soil with the Capability to Self-Heal. J Geotech Geoenviron. 2020. 146. DOI: 10.1061/(asce)gt.1943-5606.0002214
5. Wu, Y., Han, T., Huang, X., Lin, X., Hu, Y., Chen, Z.Z., Liu, J., Yan, D., Liu, X., Chen, Z.Z., et al. Effect of Bacteria on Durability of Concrete: A Review. Studies in Indian Place Names. 2022. 922. 116789–116789. DOI: 10.1016/j.carbon.2022.08.081
6. Thakor, R.R., Vaghela, K.B., Pitroda, J.R. Effect of Bacteria on Durability of Concrete: A Review. Studies in Indian Place Names 2020. 40. 276–291.
7. Morsali, S., Yucel Isildar, G., Hamed Zar gari, Z., Tahni, A. The application of bacteria as a main factor in self-healing concrete technology. Journal of Building Pathology and Rehabilitation. 2019. 4. 1–6. DOI: 10.1007/s41024-019-0045-9

8. Althoey, F., Amin, M.N., Khan, K., Usman, M.M., Khan, M.A., Javed, M.F., Sabri, M.M.S., Alrowais, R., Maglad, A.M. Machine learning based computational approach for crack width detection of self-healing concrete. Case Studies in Construction Materials. 2022. 17. DOI: 10.1016/j.cscm.2022.e01610
9. Ali, N.A., Karkush, M.O. Improvement of Unconfined Compressive Strength of Soft Clay using Microbial Calcite Precipitates. Journal of Engineering. 2021. 27. 67–75. DOI: 10.31026/j.eng.2021.03.05
10. Xu, J., Du, Y., Jiang, Z., She, A. Effects of calcium source on biochemical properties of microbial $CaCo_3$ precipitation. Frontiers in Microbiology. 2015. 6. DOI: 10.3389/fmicb.2015.01366
11. Vijay, K., Murmu, M. Effect of calcium lactate and Bacillus subtilis bacteria on properties of concrete and self-healing of cracks. International Journal of Structural Engineering. 2020. 10. 217. DOI: 10.1504/ijstructe.2020.10029530
12. Khan, M.A., Khan, H., Javed, M.H., Ullah, Z., Khan, A.M., Bakhsh, K. Investigating Cracks Prevention in Concrete Utilizing the Self-Healing Concept of Bacillus Subtilis Bacteria. Journal of ICT, Design, Engineering and Technological Science. 2021. 5. DOI: 10.33150/jitdets-5.2.4
13. Vijay, K., Murmu, M., Deo, S.V. Bacteria based self healing concrete – A review. Construction and Building Materials. 2017. 152. 1008–1014. DOI: 10.1016/j.conbuildmat.2017.07.040
14. Abishek, K.A.A, Eveena, S., Merin, G., Ansaf, M., Naveen, C. Evaluation of Strength and Durability Properties for Various Amount of Bacillus Subtilis Bacteria in Concrete. International Journal Of Engineering Research & Technology (IJERT). 2020. 9(6). DOI: 10.17577/IJERTV9IS060315
15. Saiful Islam, M., Saiful Islam, Md. Development of compressive strength and ultrasonic pulse velocity relationship of microbial concrete using bacillus subtilis bacteria. International Journal of Advanced Research. 2021. 9. 412–421. DOI: 10.21474/ijar01/13758
16. Tziviloglou, E., Wiktor, V., Jonkers, H., Schlangen, E. Performance requirements to ensure the crack sealing performance of bacteria-based self-healing concrete. Proceedings of the 9th International Conference on Fracture Mechanics of Concrete and Concrete Structures. 2015. DOI: 10.21012/FC9.148
17. Wang, J., Van Tittelboom, K., De Belie, N., Verstraete, W. Use of silica gel or polyurethane immobilized bacteria for self-healing concrete. Construction and Building Materials. 2012. 26. 532–540. DOI: 10.1016/j.conbuildmat.2011.06.054
18. Venkata Siva Rama Prasad, C., Vara Lakshmi, T.V.S. Experimental investigation on bacterial concrete strength with Bacillus subtilis and crushed stone dust aggregate based on ultrasonic pulse velocity. Materials Today: Proceedings. 2020. 27. 1111–1117. DOI: 10.1016/j.matpr.2020.01.478
19. Li, V.C., Herbert, E. Robust Self-Healing Concrete for Sustainable Infrastructure. Journal of Advanced Concrete Technology. 2012. 10. 207–218. DOI: 10.3151/jact.10.207
20. IS 4031-1: Methods of physical tests for hydraulic cement. 1996.
21. IS 10262:2009: Concrete mix proportioning-guidelines. IS Code 2009, 10262.
22. IS 516: Method of tests for strength of concrete. Bureau of Indian Standards 1959, 1991-1907.
23. IS **456:** Plain and reinforced concrete-code of practice. New Delhi: Bureau of Indian Standards 2000.
24. Qaidi, S.M.A., Dinkha, Y.Z., Haido, J.H., Ali, M.H., Tayeh, B.A. Engineering properties of sustainable green concrete incorporating eco-friendly aggregate of crumb rubber: A review. Journal of Cleaner Production. 2021. 324. 129251. DOI: 10.1016/j.jclepro.2021.129251
25. Vijay, K., Murmu, M. Effect of calcium lactate and Bacillus subtilis bacteria on properties of concrete and self-healing of cracks. International Journal of Structural Engineering. 2020. 10. 217–231. DOI: 10.1504/IJSTRUCTE.2020.10029530
26. Neeladharan, C., Sharpudin, J., Loganath, V., Jagan, B., Chinnarasu, C., Vijaykaran, K. Application of Bacillus subtilis bacteria for improving properties and healing of cracks in concrete. International Journal of Advanced Research Trends in Engineering and Technology. 2018. 5. 118–123.

Information about authors:

Venkata Prasad,
E-mail: cvsrprasad90@gmail.com

***Mohanad Sabri,** PhD*
ORCID: https://orcid.org/0000-0003-3154-8207
E-mail: mohanad.m.sabri@gmail.com

***Sree Devi**,*
E-mail: sreelakshmidevi159@gmail.com

Hadee Najm,
E-mail: gk4071@myamu.ac.in

Samadar Majeed,
E-mail: heerlen1990@gmail.com

Shaker Qaidi,
E-mail: shaker.abdal@uod.ac

Received 01.02.2023. Approved after reviewing 10.04.2023. Accepted 02.08.2023.

Magazine of Civil Engineering. 2023. 122(6). Article No. 12205

Magazine of Civil Engineering

ISSN 2712-8172

journal homepage: http://engstroy.spbstu.ru/

Research article

UDC 624.131

DOI: 10.34910/MCE.122.5

Validation metrics for non-linear soil models using laboratory and in-situ tests

R.F. Sharafutdinov

Gersevanov Research Institute of Bases and Underground Structures (NIIOSP), JSC Research Center "Stroitelstvo", Moscow, Russia

linegeo@mail.ru

Keywords: numerical modeling, verification, validation, laboratory tests, in-situ testing, statistical analysis, back analysis

Abstract. The article discusses the application of statistical metrics for the validation of comprehensive non-linear soil models. The assessment was carried out on the basis of triaxial, oedometer, consolidation and plate load tests of sandy and clay soils. Validation of non-linear soil models was divided depending on the problem type: strength-type problem and strain-type problem. For a strength-type problem the indicators of failure points should be compared. In the course of strain-type problem the stress-strain curves should be compared. Average ratio of experimental data to calculated and coefficient of variation showed the highest efficiency for standard triaxial and oedometer tests, as they allow taking into account the specificity of the deviation and its variability. Other statistical metrics are less effective in geotechnical engineering. Validation according to consolidation tests is recommended to be performed based on the analysis of the time of 100% primary consolidation and the slope of the consolidation curve during the creep phase. In the course of stress paths analysis (for example, in the course of unloading and further reloading), the advantage should be given to visual assessment. Acceptable values of validation metrics for geotechnical engineering are proposed. The specific values of deviations should be determined by the analyst depending on the required accuracy of calculations, the responsibility of the construction object and the assessment of the risk of an accident.

Acknowledgements: The author extended appreciation to the staff of the Gersevanov Research Institute of Bases and Underground Structures (NIIOSP) for aid and the materials provided.

Citation: Sharafutdinov, R.F. Validation metrics for non-linear soil models using laboratory and in-situ tests. Magazine of Civil Engineering. 2023. 122(6). Article no. 12205. DOI: 10.34910/MCE.122.5

1. Introduction

Comprehensive geomechanical models of soils (hereinafter "non-linear models") that take into account physical and geometric non-linearity, plastic behavior, hardening, filtration and rheological behavior are widely used for geotechnical analysis. Such models are: Duncan-Chang, Hardening soil, Cam-Clay, Soft soil, etc. [1–6]. This became possible due to the widespread introduction of Finite Element Method (FEM) software, such as PLAXIS, MIDAS GTS, Z-Soil, etc.

Correct description confirmation of the soil's real behavior model is carried out on the basis of validation [7, 8], by comparing the model with experimental or reference data.

The model should be selected depending on the type of the problem, the soil type and the factors that should be taken into account in the calculation [9]. When using non-linear models, it is recommended to evaluate the adequacy of the simulated environment's behavior for the required loading trajectory. For the first approximation, it is advisable to compare the results of back analysis with real soil tests. It shows the possibilities and boundaries of models for specific tasks [10]. However, the actual behavior may differ from the laboratory one due to the influence of the stress state and the history of its formation, the real density of the soil in the array, anisotropy and so on.

However, the use of non-linear models may not be sufficient for exact analysis. The fact is that different FEM software has various model implementations [9], which is confirmed by research [11, 12]. It is customary to compare the reliability and applicability of models with known solutions [13–15]. However, the listed works perform a comparison in analysis of different groups of specialists, different approaches, prerequisites, and models. Brinkgreve&Engin admit a discrepancy in the results of various models of no more than 10 %. They also indicate that non-linear soil models should be reliable and repeatable which counts as the partial responsibility of software developers [9].

Russian geotechnical regulatory documents enact the verification and validation of soil models. Thus, in accordance with Russian Rules of Constructions SP 22.13330.2016, to obtain reliable and accurate results using non-linear models, it is necessary to perform their validation (i.e. prove the adequacy of their application) by comparing the calculation results with monitoring data, laboratory and in-situ soil tests. However, geotechnical codes and publications do not contain clear validation metrics. The regulations of SP 22.13330.2016 are only limited to the requirements for validation of bearing capacity based on its upper and lower estimates. So the model can be considered acceptable if the obtained calculation results are in the range between the upper and lower estimates of the bearing capacity. In this case, the difference between the values of the upper and lower estimates should be no more than 10% of the calculated value. This approach is considered valid, but Russian Rules of Constructions SP 22.13330.2016 does not explain whether this refers to average or partial values, or how to take into account variability, etc.

V.N. Shirokov and M.P. Golub [16] suggested using the maximum deviation from experimental values by no more than 15 % as a metric for the possibility of using the model. The approach is similar to Interstate Standard GOST 20522-2012, however, the authors here perform a deviation that is relative to particular values at different stages of plate load test.

Model validation has found wide application in modeling practice. Analysis of most publications [9, 10, 13–15] shows that the assessment of the adequacy of models in geotechnical engineering is carried out mainly qualitatively, not quantitatively.

Requirements for quantifying the adequacy of models using various validation metrics can be seen in related disciplines: hydrodynamics, thermodynamics [17] and solid mechanics [18–19]. In Russia, matters of validation are described in Interstate Standards GOST R 57188-2016 and GOST R 57700.2-2017 and are used for software certification. The validation metric depends on the modeled process and the corresponding experiment. Preference should be given to metrics that contain an assessment of variability based on confidence level.

The validation metrics should determine the maximum acceptable difference between the analysis and the experiment and it also should take into account: the accuracy of the model, the limitations associated with obtaining experimental data (accuracy of sensors, equipment, cost of testing, etc.), the stage of engineering evaluation (conceptual solutions, final project) and the consequences of model non-compliance with the requirements of reliability and safety. At the same time, the validation requirements should include recommendations for action in case if results are not acceptable. In such cases, it may be: model improvements, refinement of experimental data, mitigation of validation metrics, etc.

In the manual ASME V&V 10.1-2012 two validation approaches are considered: (a) when the system response quantities (SRQ) are limited and the information about the error is nonexistent or received from experts in the subject area[1] (Fig. 1a); (b) when there is a series of system response quantities and error data available (Fig. 1b). The errors in the simulation results are detected using probabilistic analysis with undefined model inputs that are obtained from various types of repeated tests.

Validation is based on a comparison of cumulative distribution functions (CDF). The validation metrics is the area enclosed between the experimental and model CDF, normalized by the absolute mean of the experimental outcomes (Fig. 2) [20]. The relative area is calculated by the formula:

$$M^{SRQ} = \frac{1}{\left|\bar{y}_o\right|} \int_{-\infty}^{\infty} \left| F_{y_c}(y) - F_{y_o}(y) \right| dy, \tag{1}$$

[1] For example, in the Russian GOST 20522-2012 engineering-geological elements are separated, taking into account the limitation of the coefficient of variation $\nu \le 0.30$ in mechanical characteristics. The actual ν can be taken as the error of the experimental data.

where M^{SRQ} is relative difference in area of cumulative distribution functions (CDF), y_o are experimental values; y_c are calculated values; $F_{y_c}(y)$ is the CDF of calculated values; $F_{y_o}(y)$ is the CDF of observed (experimental) values.

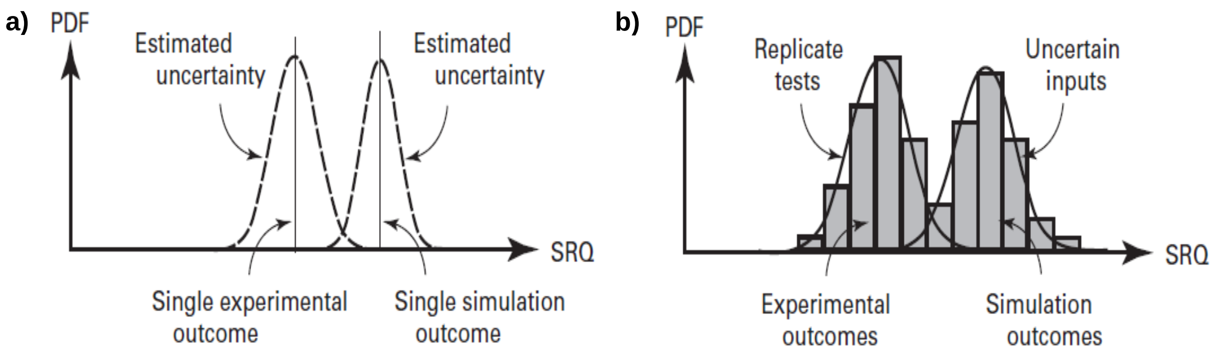

(a) when the SRQ are limited and the information about the error is nonexistent or received from experts in the subject area

(b) when there is a series of system response quantities and error data available

Figure 1. Illustration of two approaches to validation.

This metric, in fact, is a relative absolute error. The M^{SRQ} parameter has positive value and approaches zero, in the case when both CDF functions coincide. When two CDF functions do not intersect, the integral of equation (1) represents the absolute difference between the mean values. In the case of deterministic values, the CDF are stepwise, and the area between them is simply the absolute value of the difference. In solid mechanics, it is customary to limit $M^{SRQ} \le 0.1$. The application of this metric and the limit value in geotechnics requires verification and clarification, because soils have heterogeneity that is not comparable with other materials (metal, reinforced concrete, etc.).

This approach allows taking into account the error of experimental data as well as the model error. The approach is suitable for comparing the final experimental and calculated data. However, to compare calculation results of non-linear models, the approach is not the most convenient and requires special mathematical processing to calculate the CDF. Also, in order to apply the approach, it is necessary to know the distribution of the results of the model curve, which requires numerous series of calculations and is tied to certain geotechnical model [21–25].

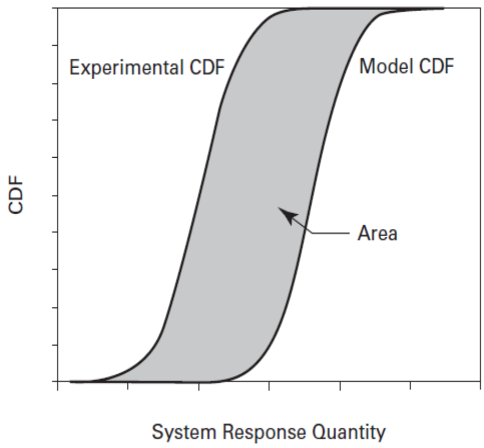

Figure 2. Validation metric for the area of the space enclosed between the experimental and model CDF curves.

For quantitative comparison of calculated and observed designations, S.S. Vyalov [26] proposed using the Pearson's correlation coefficient ρ, the ratio of experimental data to theoretical is $y_i = y_{oi}/y_{ci}$ and their coefficient of variation. Thus, the relationship is considered strong at $\rho > 0.8$; with a valid description of the experimental model values, the average ratio of experimental data to calculated $y_a = 1$, and the coefficient of variation ν should have the smallest value. However, the approaches used by S.S.

Vyalov were developed mainly for linear and linearized functions. The results of calculations based on comprehensive models are usually non-linear and these approaches cannot be used directly. Notwithstanding this fact, they were taken as the basis for these studies.

Generally, the lack of clear validation metrics in geotechnical engineering causes a subjective analysis using non-linear models. Practice shows that nowadays such analysis is performed mainly qualitatively, based on visual assessment. Approaches used in solid mechanics and hydro-thermodynamics are not widely used in geotechnical engineering. The lack of strictly selected approaches and metrics affects the reliability and repeatability of analysis results.

It is worth noting that the validation of non-linear soil models is part of the overall validation process of the computational model, which is advisable to regulate by special documents containing information about the accuracy of analysis. Performing validation of a non-linear model is a necessary, but not the only one condition for positive verification of the model [9]. When performing validation of the soil model, the type of analysis for which it is performed should be taken into account.

This paper considers the application of validation metrics of comprehensive non-linear soil models. The results of evaluating the applicability of the metrics for triaxial, oedometer test, consolidation and in-situ soil tests are presented. The most effective validation metrics depending on the type of analysis are revealed. Acceptable validation metrics are proposed.

2. Methods and Materials

2.1. The validation metrics of non-linear soil models

The following metrics were considered for the validation of non-linear soil models in the present research.

Visual assessment allows us to qualitatively assess the description of experimental data performed by the model.

The relative difference in area CDF M^{SRQ}, is described in the introduction and is determined by the formula (1).

The mean average error MAE characterizes the average between the absolute experimental and calculated values and is determined by the formula:

$$MAE = \frac{1}{n} \sum_{i=1}^{n} \left| y_{ci} - y_{oi} \right|. \tag{2}$$

The mean absolute percentage error $MAPE$ is the mean average error, divided by the actual values, determined by the formula:

$$MAPE = \frac{1}{n} \sum_{i=1}^{n} \left| \frac{y_{ci} - y_{oi}}{y_{oi}} \right| 100\%. \tag{3}$$

The lower the value of the parameters M^{SRQ}, MAE and $MAPE$, the better the model describes experimental values.

The coefficient of determination R^2 is an explanatory variable and characterizes how much the model explains the experimental data. The parameter is widely used in regression analysis and is determined by the relationship:

$$R^2 = 1 - \frac{D\left[y \middle| x \right]}{D\left[y \right]}, \tag{4}$$

where $D\left[y \middle| x \right]$ is the dispersity of the model error (the difference between the experimental data and the model); $D\left[y \right]$ is the dispersity of the experimental data.

$$D\left[y|x\right]=\frac{\sum_{i=1}^{n}\left[\left(y_{ci}-y_{oi}\right)-MAE\right]^2}{n-1}; \tag{4a}$$

$$D\left[y\right]=\frac{\sum\left[y_{oi}-\overline{y_o}\right]^2}{n-1}. \tag{4b}$$

The parameter ranges from 0 to 1; the closer to 1, the higher the strength of the relationship.

The theoretical correlation ratio η along with the coefficient of determination is an explanatory variable.

$$\eta=\sqrt{1-\frac{D\left[y|x\right]}{D\left[y\right]}}. \tag{5}$$

The parameter is in the range from 0 to 1; proximity to 1 indicates a strong relationship. For the linear function $|\rho|=\eta$. The parameter η is convent for the Cheddock scale [27] (Table 1).

The Cheddock scale characterizes the link strength of factors in a fairly wide range and is used in various disciplines as well. For the validation of non-linear models, it is advisable to limit the parameter η to "strong" and "very strong" strength on the Cheddock scale.

Table 1. Strength of relationship between factors and responses on the Cheddock scale [27].

Value η	0 ≤ η < 0.3	0.3 ≤ η < 0.5	0.5 ≤ η < 0.7	0.7 ≤ η < 0.9	0.9 ≤ η < 1	1
Value R^2	0 ≤ R^2 < 0.09	0.09 ≤ R^2 < 0.25	0.25 ≤ R^2 < 0.49	0.49 ≤ R^2 < 0.81	0.81 ≤ R^2 < 1	1
Interpretation	Weak (absent)	Moderate	Notable	Strong	Very strong	Functional

The average value of the experimental data to the calculated y_a *ratio* characterizes the relative deviation of the model from the experimental data and were calculated by the formula:

$$y_a=\frac{1}{n}\sum_{i=1}^{n}y_i=\frac{1}{n}\sum_{i=1}^{n}\frac{y_{oi}}{y_{ci}}, \tag{6}$$

where y_i is the value of the ratio of the partial experimental value y_{oi} to the partial calculated value y_{ci}.

A model with a value close to 1 will be considered adequate.

The coefficient of variation ν characterizes the scatter of y_i and was calculated by the formula:

$$\nu=\frac{\sigma_y}{y_a}, \tag{7}$$

σ_y is the standard deviation *of* y_i.

The lower the ν value, the lower the dispersion.

2.2. Characteristics of the investigated soils

The research was performed for four sandy soils and three clay soils of the Moscow region.

Medium and fine sands, of alluvial and fluvioglacial genesis of Quaternary-age were considered. (Fig. 3). The depth of sampling varied from 8–20 m. Disturbed soil samples were collected in the Moscow construction site at Kosino and Lermontovsky Prospekt metro stations. Sands S(1)...S(3) were characterized as: homogeneous (C_u = 2.0...2.8); sands S(4) heterogeneous (C_u = 6.3).

The S(1)-S(4) sands were subjected to laboratory tests by consolidated isotropic drained triaxial (d = 50 mm, h = 100 mm) and oedometer tests (d = 87 mm, h = 25 mm). Reconstituted sand specimens were prepared from the disturbed soil samples by compacting sand in the air followed by saturation. Additionally, the sands S(1), S(2) and S(4) were subjected to a plate load test with a foot area of 0.6 m^2 (d = 276 mm) followed by unloading and loading according to GOST 20276.1-2020.

Jurassic-age clay soils were represented as very stiff and stiff clay and firm-stiff loam. Undisturbed samples of clay soils were collected from a depth of 20-45 m at construction sites in Moscow at Kosino and Lermontovsky Prospekt S(5) and at Minskaya S(6), S(7) metro stations.

Specimens S(5) were subjected to oedometer and consolidation tests (d = 87 mm, h = 25 mm). The S(6) and S(7) were subjected to consolidation tests.

The studies were performed for the non-linear Hardening soil model (Table 2) and Soft Soil Creep model (Table 3). For the Hardening soil model, the power factor m was obtained from triaxial m_s and oedometer m_{od} tests. The parameters were determined from the performed tests.

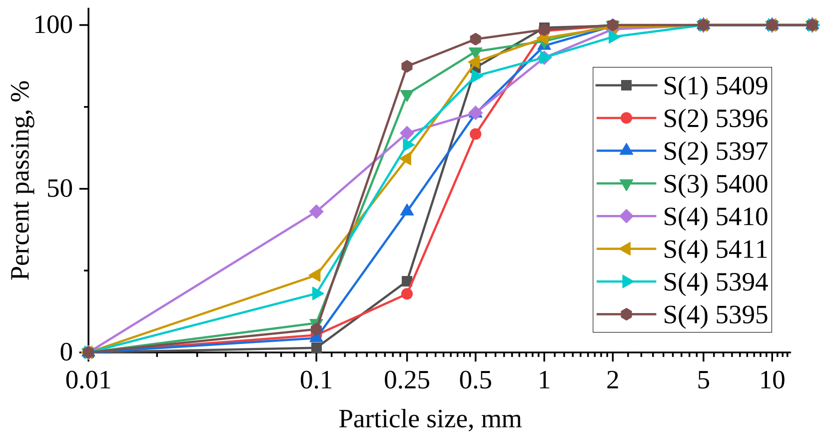

Figure 3. Cumulative curve of the particle size distribution, plotted for the studied sands.

Table 2. Parameters of the Hardening Soil model.

Soil type	γ, kN/m^3	e	p^{ref}, kPa	E_{oed}^{ref}, MPa	E_{50}^{ref}, MPa	E_{ur}^{ref}, MPa	ν_{ur}	m_s	m_{od}	c, kPa	φ,°	ψ,°
S(1) Medium sand	19.0	0.62	75	14.04	14.5	91.0	0.39	0.751	1.12	11.5	35.8	6.6
S(2) Medium sand	20.9	0.60	75	12.64	13.21	85.3	0.42	0.741	1.21	11.1	35.7	6.44
S(3) Fine sand	20.8	0.51	75	4.97	8.99	76.8	0.41	0.634	1.56	8.8	36.8	6.8
S(4) Fine sand	20.0	0.60	75	7.4	10.3	83.6	0.39	0.544	1.18	21.8	33.5	5.3

Note: γ is unit weight; e is void ratio; p^{ref} is reference pressure; E_{oed}^{ref} is reference primary oedometer stiffness; E_{50}^{ref} is reference primary stiffness from CID triaxial tests at the 50 % stress level; E_{ur}^{ref} is reference unloading/reloading stiffness from CID triaxial tests; ν_{ur} is unloading/reloading Poisson's ratio; m_s is power for stress dependent stiffness from triaxial tests; m_{od} is power for stress dependent stiffness from oedometer tests; c is cohesion; φ is friction angle; ψ is dilatancy angle.

Table 3. Parameters of the Soft Soil Creep model.

Soil type	γ kN/m^3	e	φ,°	c, kPa	OCR	POP, MPa	λ^*	κ^*	μ^*	K_f, m/day	B
S(5) Clay I_L<0.25	17.8	1.15	12.8	179	3.85	1.275	0.0995	0.0128	0.00087	2.14E-06	0.39
S(6) Clay I_L<0	19.7	0.69	23	73	2.6	0.810	0.052	0.0069	0.00131	8.14E-06	0.43
S(7) Loam 0.25≤ I_L <0.5	19.5	0.66	27	49	3.7	1.100	0.04	0.0046	0.00097	8.93E-06	0.47

Note: OCR is overconsolidation ratio; POP is pre-overburden pressure; λ^* is modified compression index; κ^* is modified swelling index; μ^* is modified creep index; K_f is coefficient of filtration; B is Skemton's coefficient.

2.3. Characteristic of the back-analysis

The applicability of the validation metrics was evaluated for the Hardening soil (HS) for sandy soils and Soft Soil Creep (SSC) for clay soils. Both models are implemented in the PLAXIS software.

The HS model was evaluated using the results of: consolidated isotropic drained triaxial, oedometer and in-situ plate load tests. The results of the triaxial tests were evaluated for strength-type and strain-type problems; for the other tests, the results were evaluated by the strain-type problem.

The SSC model was evaluated using the results of oedometer and consolidation tests.

Calculation diagrams for triaxial and odometer tests were constructed in the SoilTest module.

Calculation curves for plate load tests were obtained on the basis of back-analysis. For this purpose, the axisymmetric problem was solved in accordance with the computational scheme shown in Fig. 4a. The depth of the plate load test and the loading steps were taken in accordance with the tests performed beforehand. The plate load tests were performed under the stress-controlled loading mode.

The model consolidation curves were obtained on the basis of numerical modeling of oedometer test. For this purpose, a specimen with a height of 25 mm and a diameter of 87 mm was simulated in the axisymmetric formulation, with two-way filtration, which corresponds to the tests performed (Fig. 4b).

The strength-type problem was validated by comparing the calculated and experimental maximum deviator stress $q_{\max}$ at different confining pressures. This allows a comparison of stresses during soil. For strength-type problems, the $MAE,\ MAPE,\ y_a$ and ν metrics were used. The R^2 and η metrics were not used because their analysis required functions (a group of points) rather than partial SRQ values.

Validation by strain-type problem and by consolidation tests was performed visually and using the $M^{SRQ},\ MAE,\ MAPE,\ R^2,\ \eta,\ y_a$ and ν metrics described in Section 2.1. For the consolidation tests, additionally the comparison of the 100th primary consolidation time t_{100} was performed. For the parameters specified $y_{a(t_{100})},\ \nu_{(t_{100})},\ MAE_{(t_{100})}$ and $MAPE_{(t_{100})}$ were calculated.

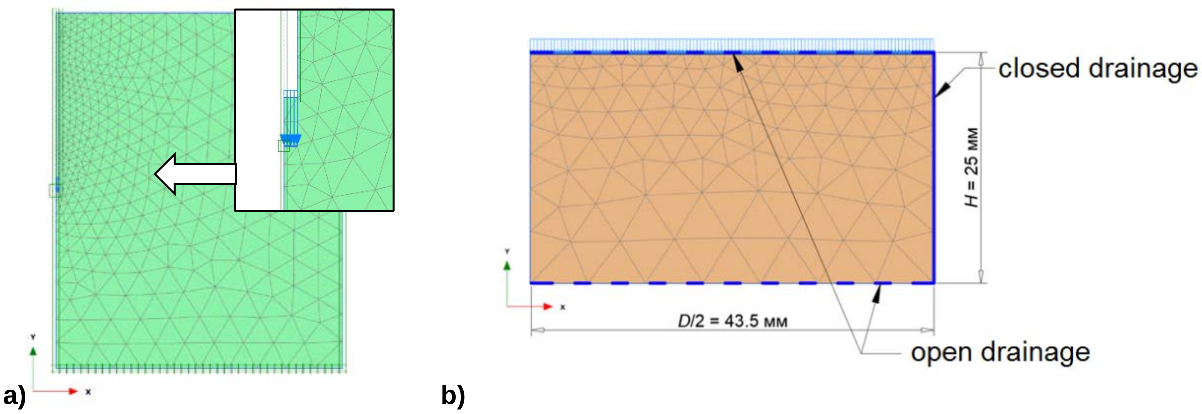

Figure 4. Calculation scheme to validation using back-analysis:
(a) – by plate load test; (b) – by consolidation tests.

3. Results and Discussion

3.1. Validation by triaxial test data

Fig. 5 shows the results of triaxial tests of sands at different confining pressure. It can be noted that the HS model implemented in the PLAXIS software describes the behavior of the soil under triaxial compression with high reliability. A similar character of loading curves and failure load was noted.

The results of the *validation by strength-type problem* were shown in Table 4. The estimate of the y_a parameter indicates that in the sands S(1)-S(3) the calculated $q_{\max}$ differs from the experimental ones by less than 5 %. The exception was the heterogeneous sand S(4), where the y_a deviation did not exceed 10 %, and the coefficient of variation did not exceed 20 %. This deviation is due to the influence of the silt particles content (see Fig. 3).

The MAE and $MAPE$ analyses give a similar picture. In homogeneous S(1)-S(3) sands, MAE = 10.0–52.6 kPa; in heterogeneous S(4), MAE = 42.0–254.3 kPa. Relative to the confining pressure, the values obtained were 5 to 15.5 % for S(1)-S(3) and 22 to 56 % for S(4), which are significant for strength-type problems. However, the MAE metric shows only the absolute error, with no reference to the absolute values of the system response. The more advanced $MAPE$ metric, normalized to observed values, does not exceed 5 % in S(1)-S(3) and lies between 7.4 % and 18.0 % in S(4). In this regard, the $MAPE$ metric is more illustrative. The MAE metric is presentable for analysis, but does not characterize the degree of influence of the error. MAE and $MAPE$ metrics always have positive characteristics and consider only the degree of deviation itself, without taking into account its nature (upward or downward).

The parameters y_a, ν and $MAPE$ are the most indicative for strength-type problem estimation. They show not only the nature of the deviation, but also its variability. The MAE itself can act only as an auxiliary characteristic and cannot be the main characteristic when performing validation.

It should be noted that the high values of the validation metrics obtained confirm the thesis about the necessity of determining the strength characteristics of the HS model on the basis of triaxial tests [28].

During the *validation by strain-type problem* based on visual assessment, it is obtained that the model describes most of the triaxial tests on the suitable level: the character and absolute values are similar. Differences are observed only in S(4), where the model curve describes observations "in the middle" (in the range ε_1 < 2–3 %), but visually very wide deviations from the experimental data associated with heterogeneity were noted.

Analysis using statistical metrics also indicates high reliability of the experimental data description. For homogeneous sands S(1)-S(3) R^2 = 0.813...0.987, η = 0.902...0.994; the lowest values were obtained for S(2) at σ_3 = 575 kPa, which was also noted visually – the model plot runs along the lower boundary of experimental diagrams. Nevertheless, the link between the calculated and observed values on the Cheddock scale is characterized as "very strong". For heterogeneous sand S(4) R^2 = 0.429...0.775 and η = 0.655...0.881, the relationship is characterized as "notable" and "strong", which is confirmed visually.

The ratio y_a for homogeneous and heterogeneous sands lies in the range of 0.904...1.090 and for most tests deviates by no more than 10 %. The largest deviations of the ratio are y_a = 0.904 for S(1) at σ_3 = 75 kPa, as confirmed by other metrics. The coefficient of variation ν for S(1)-S(3) sands lies in the range of 0.05...0.11 at $MAPE$ = 3.9–9.3 %, for heterogeneous sands it is shown in the range of 0.214...0.261 at $MAPE$ = 15.1–22.9 %. It is worth noting that the deviations obtained lie within the range of ≤ 0.30, which are considered permissible by GOST 20522-2012. This acceptable limit has been used in geotechnical engineering of the USSR and Russia for many years and its effectiveness was confirmed by many years of safe construction experience.

The parameter M^{SRQ} lies in the range of 0.01-0.06 for S(1)-S(3) and 0.05-0.15 for S(4). In S(1)-S(3) homogeneous sands, with minor deviations between calculated and experimental data ($MAPE$ < < 5–6 % and ν < 0.10), M^{SRQ} does not exceed the limits allowed in solid mechanics [19]. At the same time, for heterogeneous soils S(4) with moderate deviation y_a <10 % and values ν < 0.26, the parameter M^{SRQ} can lie both within the acceptable limits and exceed them. In this case the deviations y_a and ν can be considered acceptable still. In this regard, for soils, as materials with variability of mechanical properties (in comparison with other materials), the limiting values of M^{SRQ} from related disciplines are not suitable.

It is worth noting that, as in the case of the $MAPE$ metric, the parameter M^{SRQ} characterizes the absolute value of the deviation. However, the experimental deviations can be in different directions from the model, and the calculated curve can pass between the set of experimental curves and generally adequately describe the soil behavior. This is the advantage of the pair of parameters y_a and ν, which signal whether the model gives a safe or potentially dangerous result.

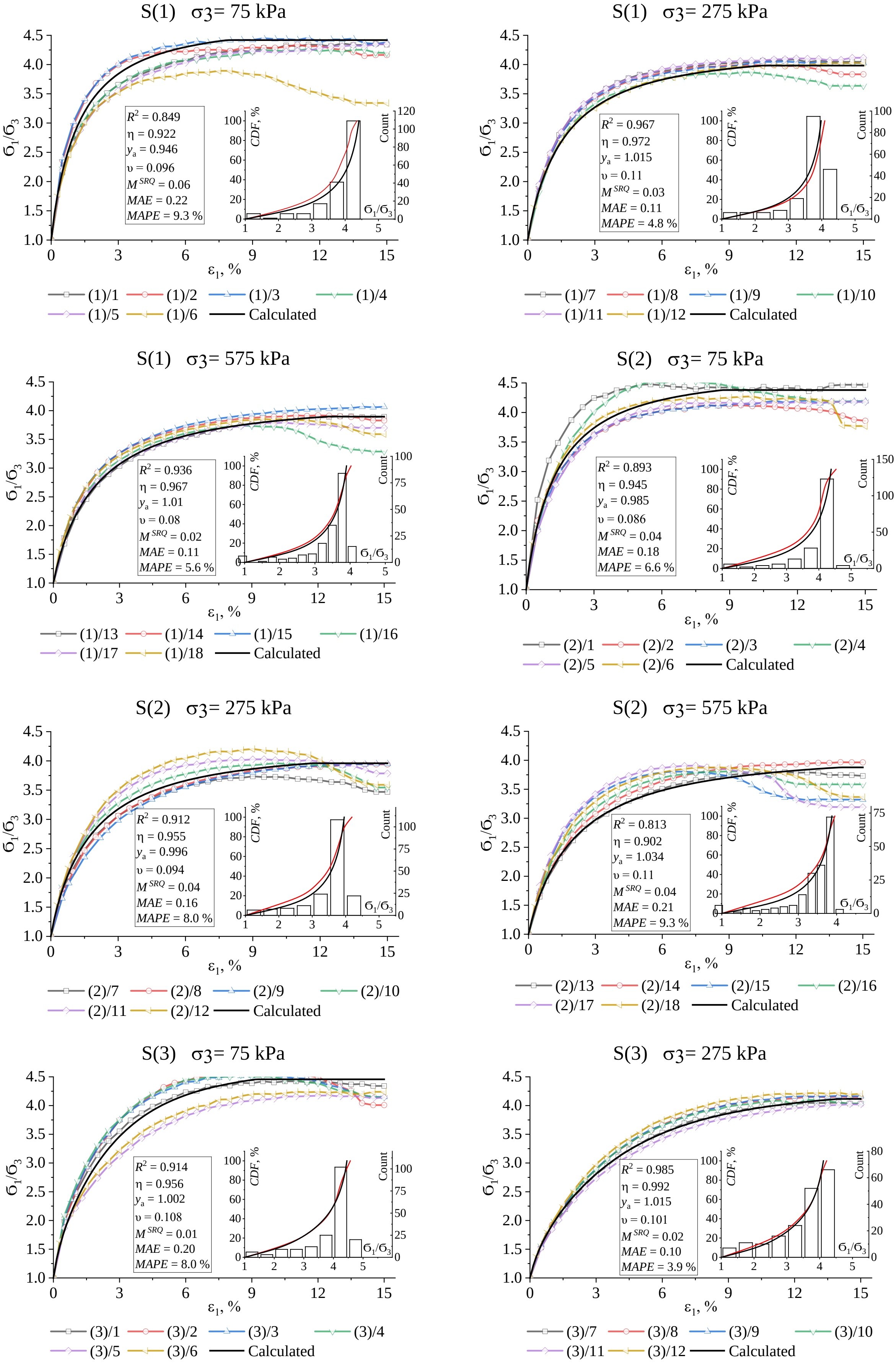

S(1) σ3= 75 kPa
R² = 0.849
η = 0.922
ya = 0.946
υ = 0.096
M SRQ = 0.06
MAE = 0.22
MAPE = 9.3 %
(1)/1 (1)/2 (1)/3 (1)/4
(1)/5 (1)/6 Calculated
S(1) σ3= 275 kPa
R² = 0.967
η = 0.972
ya = 1.015
υ = 0.11
M SRQ = 0.03
MAE = 0.11
MAPE = 4.8 %
(1)/7 (1)/8 (1)/9 (1)/10
(1)/11 (1)/12 Calculated
S(1) σ3= 575 kPa
R² = 0.936
η = 0.967
ya = 1.01
υ = 0.08
M SRQ = 0.02
MAE = 0.11
MAPE = 5.6 %
(1)/13 (1)/14 (1)/15 (1)/16
(1)/17 (1)/18 Calculated
S(2) σ3= 75 kPa
R² = 0.893
η = 0.945
ya = 0.985
υ = 0.086
M SRQ = 0.04
MAE = 0.18
MAPE = 6.6 %
(2)/1 (2)/2 (2)/3 (2)/4
(2)/5 (2)/6 Calculated
S(2) σ3= 275 kPa
R² = 0.912
η = 0.955
ya = 0.996
υ = 0.094
M SRQ = 0.04
MAE = 0.16
MAPE = 8.0 %
(2)/7 (2)/8 (2)/9 (2)/10
(2)/11 (2)/12 Calculated
S(2) σ3= 575 kPa
R² = 0.813
η = 0.902
ya = 1.034
υ = 0.11
M SRQ = 0.04
MAE = 0.21
MAPE = 9.3 %
(2)/13 (2)/14 (2)/15 (2)/16
(2)/17 (2)/18 Calculated
S(3) σ3= 75 kPa
R² = 0.914
η = 0.956
ya = 1.002
υ = 0.108
M SRQ = 0.01
MAE = 0.20
MAPE = 8.0 %
(3)/1 (3)/2 (3)/3 (3)/4
(3)/5 (3)/6 Calculated
S(3) σ3= 275 kPa
R² = 0.985
η = 0.992
ya = 1.015
υ = 0.101
M SRQ = 0.02
MAE = 0.10
MAPE = 3.9 %
(3)/7 (3)/8 (3)/9 (3)/10
(3)/11 (3)/12 Calculated
σ1/σ3
ε1, %
CDF, %
Count

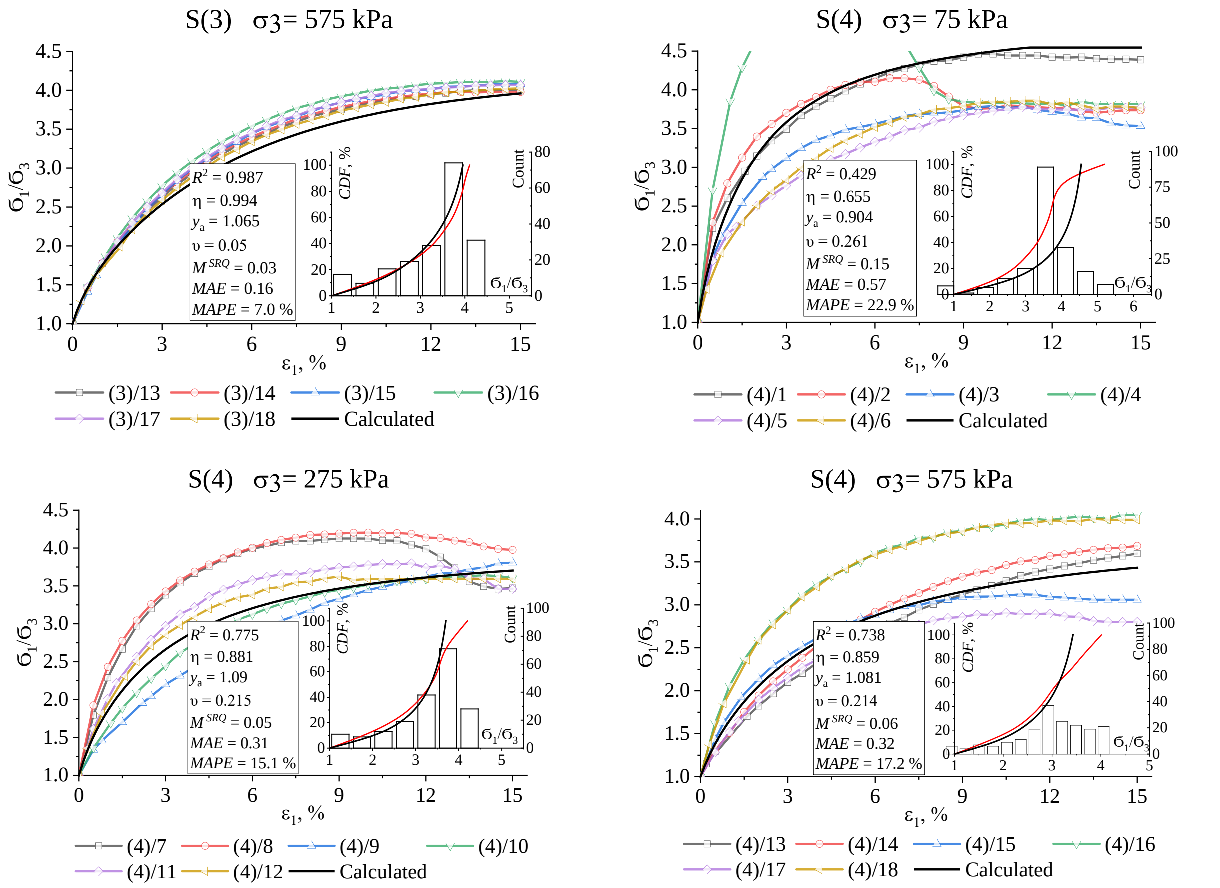

Figure 5. Results of validation by triaxial tests of sands S(1)-S(4) at different confining pressure.

Table 4. Results of calculation of the validation metrics for strength-type problem defined by triaxial tests.

Soil type	Confining pressure σ_3, kPa	$q_{\max} = (\sigma_1 - \sigma_3)_{\max}$			
		MAE, kPa	$MAPE$, %	y_a	ν
S(1) Medium sand	75	10.0	4.4	0.97	0.06
	275	23.6	2.8	1.02	0.03
	575	47.3	2.9	1.0	0.04
S(2) Medium sand	75	11.6	4.7	0.98	0.05
	275	25.4	3.1	1.01	0.05
	575	32.0	1.9	1.00	0.024
S(3) Fine sand	75	10.3	4.1	0.99	0.05
	275	16.2	1.9	1.00	0.023
	575	52.6	3	1.03	0.017
S(4) Fine sand	75	42.0	18.0	0.91	0.182
	275	62.0	7.4	1.07	0.085
	575	254.3	17.3	1.07	0.181

In general, the combination of all metrics allows one to perform a sufficiently complex analysis of the experimental data deviation from the calculated ones. It is reasonable to use the parameters y_a and ν as the main validation metrics according to the results of triaxial tests for strength-type problems and strain-type problems. R^2, η, $MAPE$ and M^{SRQ} parameters can also be used as additional parameters for strain-type problems validation. Using only the explanatory variables R^2 and η is insufficient, because although they can give low values in some cases, y_a can be close to 1 and ν can be within the acceptable limits.

3.2. Validation on oedometer test data

Oedometer tests are widely used to solve compression-type problems [29]. For the HS model, the m coefficient can be derived from triaxial m_s and oedometer m_{od} tests. Therefore, computational diagrams were constructed for both cases. Fig. 6 shows the experimental and calculated compression curves for soils S(1)...S(5).

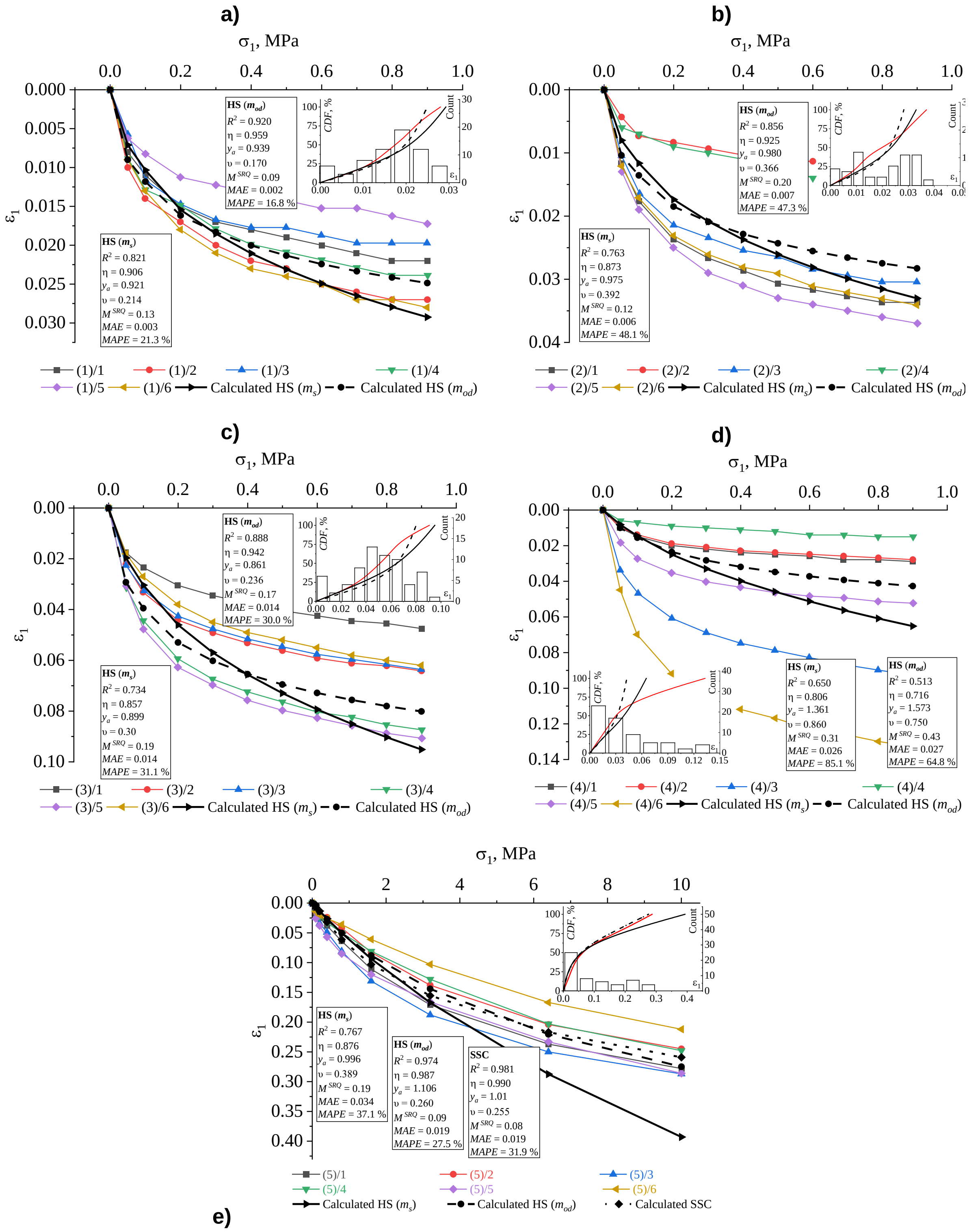

Figure 6. Results of validation by oedometer compression tests:
a – S(1); b – S(2); c – S(3); d – S(4); e – S(5).

A visual comparison of the curves indicates their similar nature. However, the test results can be divided into two groups.

The first group, which includes soils S(1), S(3) and S(5), is characterized by a "heap" arrangement of experimental curves. Here the metrics indicate a well-done description of the experiments by the model: R^2 = 0.734...0.981, η = 0.887...0.990 ("very strong" strength of relationship); y_a = 0.861...1.106, ν = 0.17...0.389, M^{SRQ} = 0.09-0.19. At the same time the parameter $MAPE$ = 21.3–37.1 % indicates a significant scatter.

The second group consists of soils S(2) and S(4), characterized by a wide scatter of experimental curves. Visual variation was confirmed by the values of the explanatory variables, which are 15–30 % lower than for the first group (R^2 = 0.513...0.856, η = 0.716...0.925). Although R^2 and η correspond to "strong" strength of relationship, other metrics suggest very significant deviations (y_a = 0.975...1.573, ν = 0.366...0.860, $MAPE$ = *47*.3–85.1 % and M^{SRQ} = 0.12–0.43). The deviations obtained for S(2) and S(4), as a rule, are confined to the first stage of loading application and at the subsequent stages the deformation practically does not differ from the calculated one (experimental and model curves are parallel). The indicated effect may be due to heterogeneity (in the case of S(4)), as well as to a loose fit of the oedometer stamps to the samples and does not characterize compressibility.

It can be seen that R^2 and η can indicate a high strength of relationship, while the model will deviate significantly from the experimental diagrams. As in the case of triaxial tests, the use of the R^2 and η metrics is not sufficient for a reliable statistical comparison and must be considered in correlation with y_a, ν and $MAPE$, M^{SRQ}.

It is worth noting that for the compression-type problem using the HS model, the calculations with m_{od} describe the tests better. The value of R^2 in the case of m_{od} is 10–30 % higher than in the case of m_s, with similar y_a. At the same time, the scatter of the data in the case of m_{od} is lower by 25–35 %. This confirms the thesis about the necessity of setting the parameter m depending on the problem to be solved. At the same time, for clayey soil S(5), the SSC model gives a more reliable description than HS.

3.3. Validation by consolidation test data

Fig. 7 shows the results of the consolidation tests of soils S(5), S(6) and S(7).

Based on the visual evaluation of the diagrams, it can be noted that the model curves satisfactorily describe the experimental data; significant differences were observed in the absolute deformations. The transition zones from primary consolidation to secondary consolidation (creep) in the model and experimental diagrams coincide; a similar slope of the curves in the creep stage was observed. The explanatory variables lie in the range: R^2 = 0.143...0.958 and η = 0.379...0.979 and indicate the strength of relationship from "moderate" to "very strong". At the same time, the deviation parameters lie in a satisfactory range: y_a = 0.815...1.390, ν = 0.02...0.327, M^{SRQ} = 0.04...0.28. Thus, as for other types of tests, the explanatory variables do not allow us to objectively characterize the model accuracy with the required reliability.

The values of the $MAPE$ parameter are close to the coefficient of variation. However, when comparing one experimental diagram with one model curve (e.g., Fig. 7b) $MAPE$ = 25.1 %, although the graphs run parallel (y_a = 0.815, ν = 0.02), i.e. no variability is observed. For consolidation tests, $MAPE$ does not show the objectivity of the estimate, because it characterizes the error in measured strains. On the contrary, the coefficient of variation does not take into account the mean relative values of the error, but considers their variability.

Wide scatter of strains of samples is caused by differences on conditionally instantaneous sections of compressibility at t < 1 min, which is characterized by closing of pore spaces with gas content. This is evidenced by the low values of the Skempton's coefficient B = 0.39–0.47, which should be taken into account when modeling performing [8]. Another reason for non-uniform precipitation is the uneven surface of the samples in contact with the plate load test (similar to the oedometer tests). Meschyan S.R. showed that such effects often occur in stiff clays, where it is difficult to ensure an absolutely smooth surface of the specimen contact with the stamps during specimen preparation [30].

The task of any consolidation analysis is to predict strains over time. Therefore, the absolute values of settlements in the validation should play a secondary role. For the tests in question, the comparison by t_{100} showed a satisfactory match: mean deviation $y_{a(t_{100})}$ = 0.82...1.352, $\nu_{(t_{100})}$ = 0.05...0.196, $MAPE_{(t_{100})}$ = 9.2...25.3 %.

In view of the above, validation based on consolidation test data should be performed on the basis of 100 % primary consolidation time as well as the slope of the consolidation curve during the creep stage. Comparison of calculated and experimental strain values at different points in time is an auxiliary element of validation.

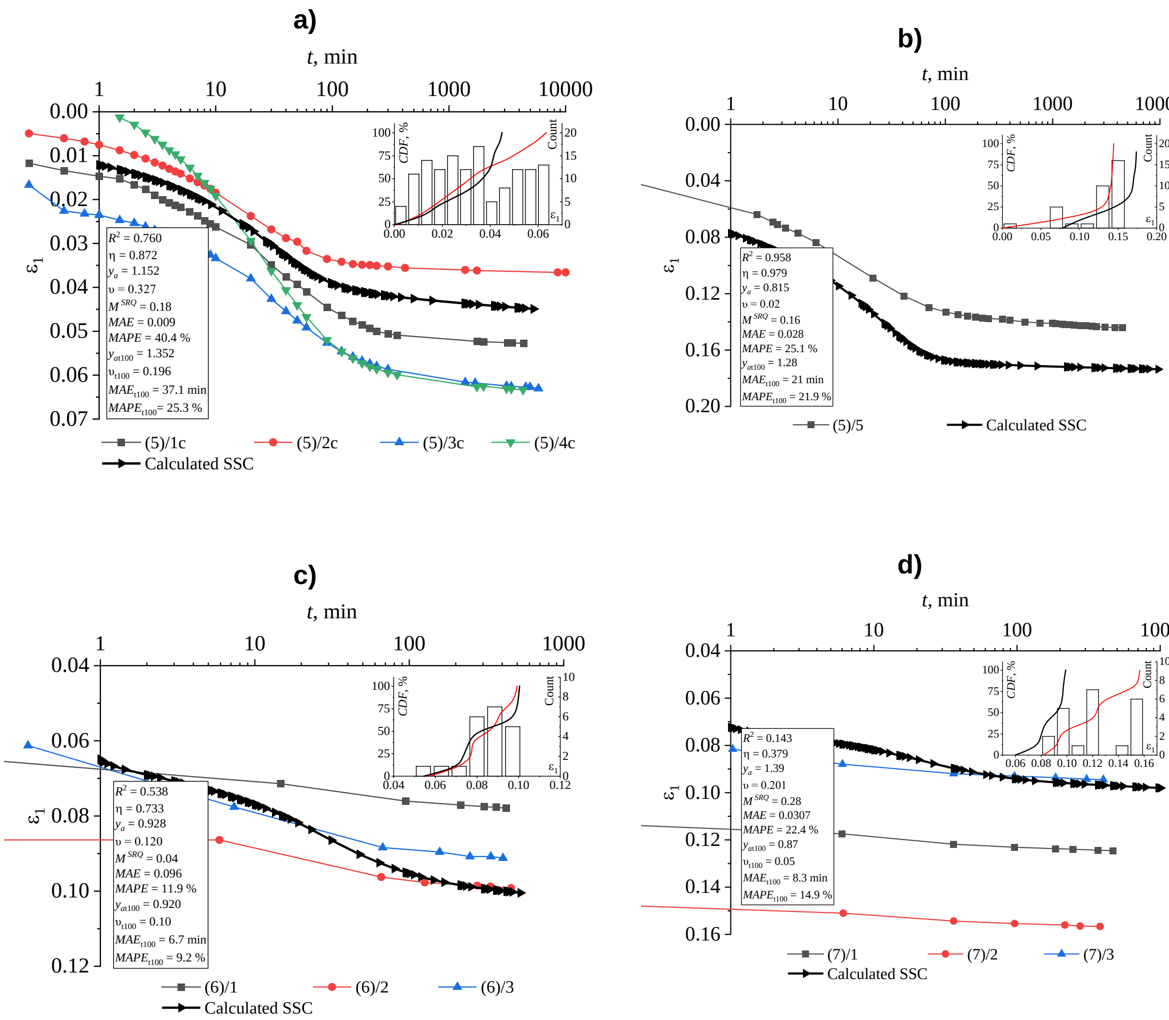

Figure 7. Results of validation by oedometer consolidation test: a – S(5), σ_1 = 0.55 MPa; b – S(5), σ_1 = 4 MPa; c – S(6), σ_1 =1.24 MPa; d - S(7), σ_1 =1.13 MPa.

3.4. Validation by plate load test data

Back analysis of the plate load test tests were performed for sands S(1), S(2), and S(4) (Fig. 8).

A visual comparison shows a good strain match on the primary loading up to 250 kPa. On the unloading path it can be seen that the stiffness E_{ur} is higher than that of the plate load tests. Coincidences on the unloading path are observed only for soil S(2) at a depth of 8.8–9.0 m. The simulated reloading path also differs from the experimental data.

In the analysis based on the validation metrics it can be noted that the differences between the model and calculated curves are insignificant: R^2 and η above 0.9, y_a = 0.923–1.20 at ν = 0.121...0.239, M^{SRQ} < 0.19. A separate deviation of variation coefficient ν = 0.39 is revealed for heterogeneous sand S(4) with "ideal" y_a = 1.017 and moderate $MAPE$ = 25 %.

When analyzing comprehensive stress paths (e.g., with unloading and reloading), the considered metrics do not always allow an objective evaluation of the analysis results. For simple oedometer and triaxial tests, the validation metrics characterized negligible deviations which were confirmed visually. For plate load tests with two stress paths, the metrics lie in satisfactory ranges, while a good visual match was observed in only 30 % of the curve sections.

Such significant discrepancies are explained by peculiarities of the HS model. First, the model parameters are determined on the basis of laboratory tests. Damage of samples during sampling, transportation and storage, lack of reliable data on density (in course of sand) and real stress state in the massif (for accurate laboratory tests) reduce the reliability of modeling. This causes the necessity to confirm the applied model parameters on the basis of plate load and pressuremeter tests. Secondly, the HS model takes into account isotropic hardening and the yield surface that can expand due to plastic straining but changes its position after the change of stress paths in principal stress space. In the process of unloading/reloading or non-linear stress paths, the position of yield surface changes, which affects the deformation behavior of soil. Therefore, for comprehensive stress paths, the model should be evaluated on the basis of visual assessment, and its permissibility should be evaluated by an analyst.

Considering the above features, the results of the back analysis can be called satisfactory. In the case of simple loading, validation approaches for plate load tests are similar, with triaxial and oedometer tests: first of all, they rely on a joint analysis together with y_a, ν, $MAPE$ and M^{SRQ}, and use the metrics R^2 and η as auxiliary. In case of a comprehensive loading trajectory, the analysis should be based on a visual evaluation and the metrics should have an auxiliary function.

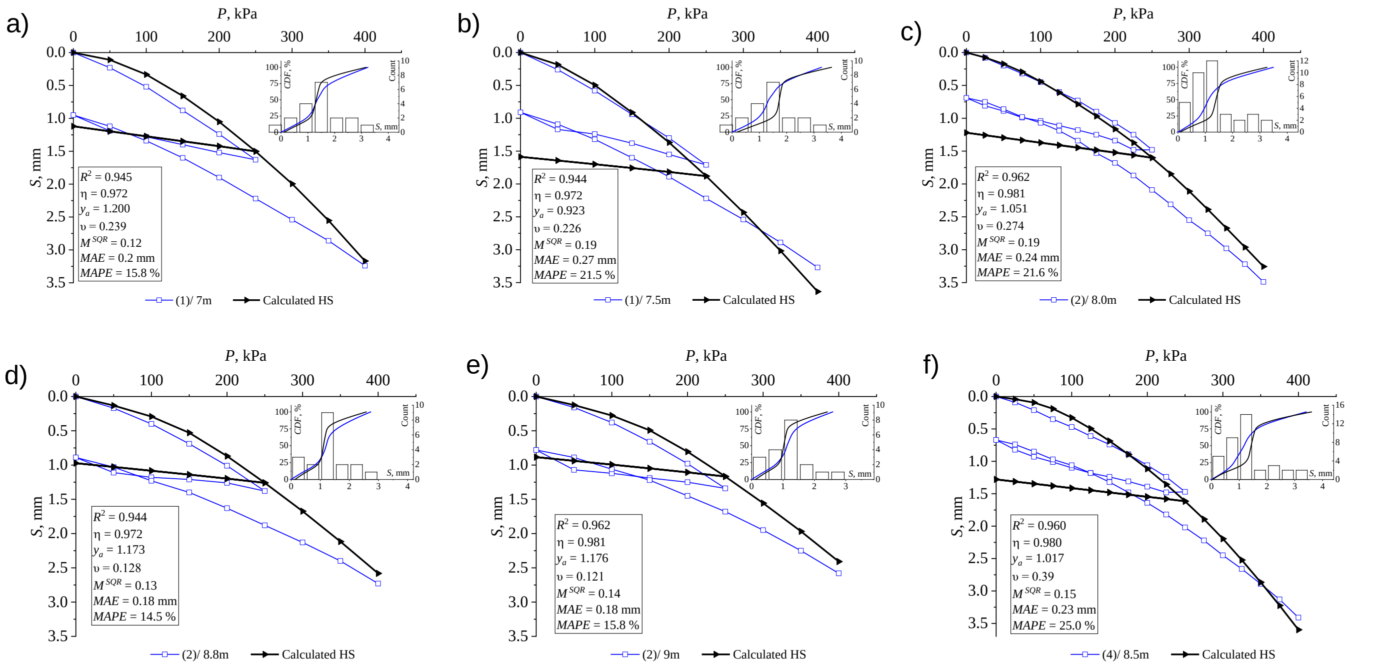

Figure 8. Results of validation by plate load tests for: a, b – S(1) at depths of 7.0 and 7.5 m; c, d, e – S(2) at depths of 8.0, 8.8 and 9.0 m; f – S(4) at depth of 8.8 m.

3.5. Acceptable values of validation metrics

In related disciplines, validation issues have advanced considerably over the past few years. In particular, there have been published works by Roache [31], Coleman and Steele [32], Oberkampf and Roy [33], Hazelrigg and Saari [34] which consider various aspects of validation. An important factor influencing the result of any validation is the experience and competence of the analyst performing the calculation and back analysis [34]. As a rule, the more experienced analyst performs validation for a particular task, the higher the probability of a successful result of verification. The biggest challenge is assessing the competence of the analyst. Validation issues in geotechnical engineering are complicated by the fact that geotechnical engineering is a branch of knowledge at the intersection of several specialties: civil engineer, engineer-geologist and mining engineer [35]. In order to obtain the required competence it is necessary to have at least 10–15 years of experience. In this regard, the issue of applying independent validation metrics and assigning their admissible limits in geotechnical engineering is quite acute.

In these conditions, visual and qualitative metrics used for geotechnical analysis, it is reasonable to supplement with independent metrics, which, for example, correspond to the provisions in other disciplines [17–19]. The analysis has shown that the validation metrics accepted in related disciplines are rather restricted and not suitable for geotechnical engineering. The influence of heterogeneity in the soil massif forces to use less stringent boundary metrics. However, to ensure high accuracy of predictions, it is necessary to provide a good description of the processes as a whole and to introduce restrictions on the scatter of data.

The analysis shows that the validation in geotechnical engineering can be conditionally divided depending on the problem to be solved: the strength-type or the strain-type analysis. The metrics used for estimation also depend on the problem to be solved (Table 5).

Table 5. Validation metrics depending on the test type and problem type to be solved.

Type of test	Validation metric	
	Main	Auxiliary
Triaxial tests - strength-type problem	y_a, ν and $MAPE$	MAE
- strain-type problem	Visual, y_a and ν	R^2, η, M^{SRQ} and $MAPE$
Oedometer tests	Visual, y_a and ν	R^2, η, M^{SRQ} and $MAPE$
Consolidation tests	Visual, $y_{a(t_{100})}$ and $\nu_{(t_{100})}$	y_a, ν, R^2, η, M^{SRQ} and $MAPE$
In-situ soil tests (plate load)	Visual, y_a and ν	R^2, η, M^{SRQ}, and $MAPE$
Stress path	Visual	y_a, ν, R^2, η, M^{SRQ} and $MAPE$

For the strength-type problem, the correctness of the model's description of soil failure is evaluated. To compare the experimental and simulated soil failure, the metrics y_a, ν and $MAPE$ proved to show better results. Considering that the strength-type problem determines the object safety, the peculiarities of the experimental data acquisition and models accuracy, the deviation value y_a, in the author's opinion, should not exceed 5–10 %.

The strain-type problem validation (triaxial, oedometer or plate load tests) assesses the correctness of the model's repeatability of soil deformation under load. Here it is reasonable to perform a visual assessment of stress-strain curves supported by the proposed metrics. As in the case of strength-type problem validation, the y_a and ν metrics showed the greatest efficiency. Metrics M^{SRQ}, $MAPE$, R^2 and η can be used as auxiliary. For the case of a comprehensive stress path (with unloading and reloading, along an atypical trajectory, etc.), visual assessment should be preferred. Model and experimental stress-strain curves in different load ranges may have different deviations (up or down). Because of this, it is more difficult to provide strict values of validation metrics. On the other hand, inaccuracies in the strain analysis affect the operation of the object (settlements, inclinations, crack opening, etc.) and do not affect safety. In view of the above, in the author's opinion, for the strain validation the deviation value y_a should not exceed 10–15 %, and M^{SRQ} should not exceed 0.3. For the explanatory variables R^2 and η were proposed to focus on the "very strong" and "strong" strength of relationship according to the Cheddock scale (Table 1). The use of a lower strength of relationship is inappropriate, as it indicates a bigger error value of the model. For comprehensive stress paths, the acceptability of the model should be evaluated by the analyst.

In case of the consolidation model validation, the advantage should be given to the behavior on a timeline. The estimation of absolute value strains should play a secondary role. Therefore, it will be correct to compare the time of the 100th primary consolidation t_{100} using the metrics $y_{a(t_{100})}$ and $\nu_{(t_{100})}$. Limit values of the validation metrics during consolidation are quite difficult to assign, since tests are usually performed under laboratory conditions on specimens sampled from the soil massif. Consolidation tests are the most sensitive to the quality of sampling, especially from large depths [36]. In this regard, the validation metrics should be assigned by the analyst, taking into account the statistical variability of specific experimental data.

For strength-type and strain-type problems the value of the variation coefficient ν must not exceed 0.3. The value of $\nu \leq 0.30$ is justified by many years of experience in the application of this limit in the USSR and Russia in the allocation of engineering-geological elements (Interstate Standard GOST 20522-2012). The use of a stricter coefficient of variation may be justified for materials with high reproducibility of properties (e.g., systematically erected embankments of homogeneous materials, concrete, metals, etc.). In the case of natural soils, this may lead to limitations on the use of non-linear models in heterogeneous soils. However, it may be justified in the case of high requirements for analysis accuracy.

The values of the $MAPE$ parameter when comparing a group of curves have close values to ν. When comparing with single experimental values, the analysis by MAE and $MAPE$ can give a more objective assessment. However, it is common in geotechnical engineering to consider statistical variability [37], in connection with which the analysis by ν is more preferable. Therefore, allowable values of MAE and $MAPE$ should be determined by the calculator for specific tasks.

For particularly critical objects (unique high-rise buildings, hydraulic structures, etc.) more stringent limits of validation metrics can be considered. Specific values of deviations should be determined by the analyst depending on the required accuracy of analysis, responsibility of the object and accident risk assessment. However, in the author's opinion, the application of more stringent metrics in soils, taking into account the above factors, is not justified.

If the model does not meet the specified validation metrics, additional correction factors can be introduced. As a first approximation, we can consider applying an additional correction factor equal to the value of the maximum deviation y_a.

Based on the estimates made for the proposed validation metrics for various tests, Table 6 was developed. The proposed metrics and their allowable values will make formalizing the performance of validation for geotechnical tasks possible.

Table 6. Acceptable values of validation metrics depending on analysis accuracy requirements and the problem type to be solved.

Requirements for analysis accuracy	Strain-type problem and consolidation					Strength-type problem	
	y_a	ν	M^{SRQ}	R^2	η	y_a	ν
Normal*	$0.85 \geq y_a \geq 1.15$	$\nu \leq 0.30$	$M^{SRQ} \leq 0.3$	$0.81 > R^2 \geq 0.49$	$0.90 > \eta \geq 0.70$	$0.90 \geq y_a \geq 1.10$	$\nu \leq 0.30$
High	$0.90 \geq y_a \geq 1.10$		$M^{SRQ} \leq 0.2$	$R^2 \geq 0.81$	$\eta \geq 0.90$	$0.95 \geq y_a \geq 1.05$	

Note: "*" is allowed for preliminary analysis with high requirements for analysis accuracy

Validation of non-linear models and their parameters using the specified acceptable values is of course a necessary but not sufficient metric for solving the problem of limiting equilibrium in the soil mass. Further, it is necessary to evaluate the influence of application of the validation metrics of Table 6. On the results of analysis of full FEM models using non-linear soil models for specific problems the deterministic [21–23] or stochastic (e.g., using the Monte Carlo method) [24, 25, 38] approaches can be used. It is also necessary to evaluate the applicability of validation metrics on more empirical data and monitoring results.

4. Conclusions

Geotechnical analyses are often performed using non-linear soil models. In order to obtain reliable results using non-linear models it is required to perform their validation. However, model validation in geotechnical engineering is performed expertly or visually, without applying special quantitative metrics. Model quantification requirements are widely used in related disciplines (hydro- and thermodynamics, solid mechanics). At the same time, permissible validation metrics accepted in related disciplines are rather restricted and are not applicable in geotechnical engineering, because soils, in comparison with other materials, have significant heterogeneity. Based on the analysis, the following conclusions were obtained.

- The following validation metrics can be used in geotechnical engineering: visual, the relative area between the calculated and model cumulative distribution function M^{SRQ}, mean average error MAE, mean absolute percentage error $MAPE$, coefficient of determination R^2, theoretical correlation ratio η, average ratio of experimental data to calculated y_a, coefficient of variation ν.

- Validation of the soil models can be divided depending on the problem to be solved: strength-type or strain-type problem. In the first case, the indicators at failure are compared (for example, for triaxial compression it is suggested to use the maximum deviator stress $q_{\max}$). In the second case, the stress-strain curves are compared.
- The metrics y_a and ν showed the greatest efficiency in the strength-type and strain-type problems. They take into account not only the nature of the deviation, but also its variability. Parameters M^{SRQ}, MAE and $MAPE$ take into account the absolute error, but ignore the direction of deviation. The deviations of the experimental data can be in different directions from the model, and yet, the model can adequately describe the behavior of the soil. The advantage of the pair of parameters y_a and ν is that they signal whether the model gives us a conservative or potentially dangerous result. The use of the R^2 and η metrics is not sufficient for reliable validation and should be considered together with y_a, ν, $MAPE$ and M^{SRQ}.
- Validation from oedometer consolidation test data should be based on an analysis of the 100 % primary consolidation time and the slope of the consolidation curve during the creep phase. Ancillary elements of validation should be presented as comparison of calculated and measured strain values at different points in time.
- When analyzing comprehensive stress paths (e.g., with unloading and reloading), the considered metrics do not always allow an objective assessment of the simulation results. Therefore, the advantage should be given to visual assessment.
- Acceptable values of validation metrics for geotechnical engineering are proposed (Table 6). The proposed metrics and their admissible values will allow formalizing the execution of validation for geotechnical tasks. At that, specific values of deviations should be determined by an analyst depending on the required accuracy of analysis, object responsibility and accident risk assessment. The application of the proposed metrics will allow systematization of the validations performed by different specialists and thereby increase the reliability of geotechnical analysis. In case the model does not fit into the required validation metrics, additional correction factors can be introduced.

In the future, it is advisable to: consider the applicability of these metrics to other soil test methods, evaluate the effect of metrics application on the results of full FEM models using non-linear soil models, and test the proposed validation metrics on a larger volume of data.

References

1. Duncan, J.M., Chang, C.-Y. Nonlinear Analysis of Stress and Strain in Soils. Journal of the Soil Mechanics and Foundations Division. 1970. Vol. 96 (5). Pp. 1629–1653. DOI: 10.1061/JSFEAQ.0001458
2. Schanz, T., Vermeer, P., Bonnier P. The hardening soil model: Formulation and verification. Proceedings of the Plaxis Symposium. Beyond 2000 in Computational Geotechnics. Rotterdam. Balkema, 1999. Pp. 281–290.
3. Roscoe, K.H., Burland, J.B. On the generalized stress-strain behaviour of wet clay. Papers of a Conference held in Cambridge. Engineering Plasticity. 1968. Pp. 535–609.
4. Muir Wood, D. Soil behaviour and critical state soil mechanics. UK. Cambridge University Press, 1991. 480 p. DOI: 10.1017/CBO9781139878272
5. Potts, D.M., Zdravkovic, L. Finite element analysis in geotechnical engineering: theory. London. Thomas Telford, 1999. 458 p.
6. Britto, A.M., Gunn, M.J. Critical state soil mechanics via finite elements. Chichester. Ellis Horwood Ltd., 1987. 488 p.
7. Ter-Martirosyan, A.Z., Sidorov, V.V., Ermoshina, L.Y. Opredelenie i verifikacziya parametrov modeli slabogo grunta v uchetom polzuchesti [Determination and verification of parameters of the soft soil with account for creep]. Vestnik MGSU. 2018. 6. Pp. 697–708. DOI: 10.22227/1997–0935.2018.6.697-708
8. Shulyatiev, O.A., Isaev, O.N., Nayatov, D.V., Sharafutdinov, R.F. Prognoz razvitiya deformaczij osnovaniya mnogofunkczional`nogo zhilogo kompleksa [Forecast of base strains development for a multifunctional residental complex]. Geotechnika. 2017. No. 2. Pp. 38–49.
9. Brinkgreve, R.B.J., Engin, E. Validation of geotechnical finite element analysis. Proceeding of the 18th International Conference on Soil Mechanics and Geotechnical Engineering. Paris, France. 2013. Pp. 677–682.
10. Szilvágyi, Z., Ray, R.P. Verification of the Ramberg-Osgood material model in midas GTS NX with the modeling of torsional simple shear tests. Periodica Polytechnica Civil Engineering. Budapest University of Technology and Economics, 2018. 62 (3). DOI: 10.3311/PPci.11191

11. Razvodovsky, D., Skorikov, A. Problemy` i vozmozhny`e puti razvitiya normativnoj literatury` v oblasti proektirovaniya svajny`kh fundamentov [Problems and possible ways of development of pile design building codes]. Bulletin of Science and Research Center "Stroitelstvo". 2020. 26 (3). Pp. 74–85.
12. Pruška, J. Comparison of geotechnic softwares – Geo FEM, Plaxis, Z-Soil. Proceeding of the XIII ECSMGE. Prague, Czech Republic. 2003. Pp. 819–824.
13. Anderson, K.H. et al. Suction anchors for deepwater applications. Frontiers in Offshore Geotechnics. Gourvenec & Cassidy. London, Taylor & Francis. 2005. Pp. 3–30. DOI: 10.1201/NOE0415390637.ch1
14. Jeffries, R.M. Interclay II project. A coordinated benchmark exercise on the rheology of clays. Final report. 1995. 362 p.
15. Schweiger, H.F. Results from numerical benchmark exercises in geotechnics. Proceeding of the 5th European Conf. Numerical Methods in Geotechnical Engineering. Paris. 2002. Pp. 305–314.
16. Shirokov, V.N., Golub, M.P. Shtampovy`e ispy`taniya kak komponent modelirovaniya v srede «PLAXIS» deformirovaniya svyazny`kh dispersny`kh gruntov v osnovanii sooruzhenij [Stamping tests as a component of modeling of cohesive disperse soils deformations in the structure bases using "PLAXIS" program]. Engineering survey. 2018. No. 12. Pp. 16–24. DOI: 10.25296/1997-8650-2017-12-16-24
17. ASME V&V 20-2009. Stanard for Verification and Validation in Computational Fluid Dynamics and Heat Transfer. The American Society of Mechanical Engineers.
18. ASME V&V 10-2006. Guide for Verification and Validation in Computational Solid Mechanics. The American Society of Mechanical Engineers.
19. ASME V&V 10.1-2012. An Illustration of the Concepts of Verification and Validation in Computational Solid Mechanics. The American Society of Mechanical Engineers.
20. Ferson, S., Oberkampf, W.L., Ginzburg, L. Model validation and predictive capability for the thermal challenge problem. Computer Methods Applied in Mechanics and Engineering. 2008. 197 (29-32). Pp. 2408–2430. DOI: 10.1016/j.cma.2007.07.030
21. Kolybin, I.V., Astryab, V.V. Determinirovanny`j podkhod k oczenke chuvstvitel`nosti MKE` modelej pri sovmestnom raschete sooruzheniya s osnovaniem [A deterministic approach to assessing the sensitivity of FEM models in the joint design calculation with the base]. Proceedings of the Gersevanov Research Institute of Bases and Underground Structures (NIIOSP). 2011. Pp. 156–169.
22. Barvashov, V.A., Boldyrev, G.G., Utkin, M.M. Raschet osadok i krenov sooruzhenij s uchetom neopredelennosti svojstv gruntovy`kh osnovanij [Calculation of settlements and tilts of engineering structures taking into account uncertainly of foundation soil properties]. Geotechnika. 2016. No. 1. Pp. 12–29.
23. Barvashov, V.A. Sensitivity of the "bed-structure" system. Soil Mechanics and Foundation Engineering. 2007. 44 (3). Pp. 87–93. DOI: 10.1007/s11204-007-0016-z
24. Sheinin, V.I., Lesovoi, Y.V., Mikheev, V.V., Popov N.B. An approach to reliability assessment in engineering calculations of foundation beds. Soil Mechanics and Foundation Engineering. 1990. 27 (1). Pp. 32–36. DOI: 10.1007/BF02306679
25. Skorikov, A., Pavlovskiy, N. Stokhasticheskij podkhod k oczenke nadezhnosti rezul`tatov rascheta osnovanij i fundamentov v zavisimosti ot chuvstvitel`nosti MKE`-modelej [Stochastic approach to assessing the reliability of the calculation results of bases and foundations depending on the sensitivity of the FEM models]. Bulletin of Science and Research Center "Stroitelstvo." 2021. 29 (2). Pp. 101–111. DOI: 10.37538/2224-9494-2021-2(29)-101-111
26. Vyalov, S.S. Rheological Fundamentals of Soil Mechanics. Elsevier, 1986. 564 p.
27. Chaddock, R.E. Principles and methods of statistics. Boston, Now-York, 1925. 471 p.
28. Sharafutdinov, R.F., Isaev, O.N., Morozov, V.S. Experimental Studies of Cohesionless Subsoil Dilatancy Under Conditions of Triaxial Compression. Soil Mechanics and Foundation Engineering. 2021. 57(6). Pp. 465–472. DOI: 10.1007/s11204-021-09694-3
29. Schanz, T., Vermeer, P.A. On the Stiffness of Sands. Pre-failure deformation behaviour of geomaterials In Jardine, R., Davies, M., Hight, D., Smith, A., Stallebras, S., editors. London. Telford, 1998. Pp. 383–387.
30. Meschyan, S.R. Experimental Rheology of Clayey Soils. Taylor & Francis, 1995. 460 p.
31. Roache, P.J. Fundamentals of Verification and Validation. Albuquerque, NM. Hermosa Publishers, 2009. 476 p.
32. Coleman, H.W., Steele, W.G. Experimentation, Validation, and Uncertainty Analysis for Engineers. 3rd ed. Hoboken, NK. John Wiley, 2009. 336 p.
33. Oberkampf, W.L., Roy, C.J. Verification and Validation in Scientific Computing. Cambridge University Press, 2010. 790 p.
34. Hazelrigg, G.A., Saari, D.G. Toward a Theory of Systems Engineering. Journal of Mechanical Design. 2022. 144 (1). 8 p. DOI: 10.1115/1.4051873
35. Lees, A.S. A competency based approach to managing skills in geotechnical numerical analysis. Proceeding of the XVI ECSMGE. 2015. Pp. 4283–4287.
36. Tanaka, H., Ritoh, F., Omuka,i N. Quality of samples retrieved from great depth and its influence on consolidation properties. Canadian Geotechnical Journal. 2002. 39 (6). Pp. 1288–1301. DOI: 10.1139/t02-064
37. Ermolaev, N.N., Mikheev, V.V. Nadezhnost` osnovanij i sooruzhenij [Reliability of the bases of structures]. Leningrad. Stroyizdat, 1976. 152 p.
38. Sheinin, V.I., Mikheev, V.V., Popov, N.B., Lesovoi Yu.V. Probabilistic calculation for the bed under an individual foundation in accordance with the second group of limiting states. Soil Mechanics and Foundation Engineering. 1991. 28 (2). Pp. 79–83. DOI: 10.1007/BF02316019

Information about authors:

Rafael Sharafutdinov, *PhD in Technical Sciences*
ORCID: https://orcid.org/0000-0002-5806-7190
E-mail: linegeo@mail.ru

Received 18.12.2022. Approved after reviewing 12.07.2023. Accepted 07.09.2023.

Magazine of Civil Engineering

ISSN 2712-8172

journal homepage: http://engstroy.spbstu.ru/

Research article

UDC 691.54

DOI: 10.34910/MCE.122.6

Alkali-activated bentonite clay-limestone cements

N.R. Rakhimova [1] ✉, ***V.P. Morozov*** [2], ***A.A. Eskin*** [2], ***B.M. Galiullin*** [2]

[1] *Kazan State University of Architecture and Engineering, Kazan, Russian Federation*

[2] *Kazan (Volga region) Federal University, Kazan, Russian Federation*

✉ *nailia683@gmail.com*

Keywords: geopolymers, mixtures, cementitious materials, compressive strength, microstructure

Abstract. The development of sustainable cements requires the expansion and optimization of the mineral resources base. In this study, the medium-grade bentonite clay and limestone as a promising, available, low carbon, and abundant starting materials, were investigated as binary precursors for eco-friendly non-clinker alkali-activated cements development. Properties of fresh and hardened pastes of blended alkali-activated cements were investigated by standard techniques depending on the mineralogical assemblage, fineness of precursors, formulation details. The reaction products and microstructures of alkali-activated calcined bentonite clay-limestone hardened pastes were analyzed using thermal, XRD, and SEM/EDS analyses. As a result, calcined bentonite clays at 39–47 % content of clay minerals were stated to be suitable as a primary precursor for alkali-activated cements incorporated with high loading of raw limestone. Optimum compositions consisted of 20–30 % calcined clay and 70–80 % limestone with compressive strength up to 34.2 MPa. In the designed cement calcined bentonite clay is the main reactive precursor that forms a mineral matrix sodium aluminosilicate hydrate gel N-A-S-H, whereas calcium carbonate is a much less reactive secondary precursor that participates in the formation of sodium (calcium) aluminosilicate hydrate gel N-(C)-A-S-H.

Citation: Rakhimova, N.R., Morozov, V.P., Eskin, A.A., Galiullin, B.M. Alkali-activated bentonite clay-limestone cements. Magazine of Civil Engineering. 2023. Article no. 12206. DOI: 10.34910/MCE.122.6

1. Introduction

Development of sustainable mineral binders that comply with increasing technical and ecological requirements and a general trend towards gradual decrease in their energy and resource intensities determines the expansion of the mineral resources range. The resource base of supplementary cementitious materials applied in increasing volumes for Portland clinker replacement in mixed cements has been reconsidered in recent decades to establish more available and wider range of mineral materials than traditional ones, such as blast furnace slag, fly ash, etc. As a result of ongoing studies conducted in this field, clays and calcium (magnesium) (C/M) carbonate rocks have been identified as the perspective sources for the production of low- [1–6] and non-clinker cements [7–13], including alkali-activated cements (AACs). The interest in these mineral sources is based not only on the large reserves and their ubiquitous availability, but also on their decreased global warming potential, lowered energy consumption, and multifunctional effect on the engineering performance of blended cements and concretes.

For a long time the limestone (LS) was assigned the sole role of an inactive filler for AACs. A great number of studies stated the beneficial effect of LS on the properties of fresh and hardened alkali-activated (AA) blast furnace slag, fly ash, calcined clays cements. The positive influence effect of C/M carbonates on the performance of AACs is based on the filler, nucleation, dilution, and chemical effects, which are conditioned by the chemical-mineralogical compositions of the primary precursors (Ca-free or Ca-rich), the nature and dosage of the alkaline component, and the content and fineness of LS or dolomite [14–21].

However, recent studies have stated that the chemical activity of LS in AA binder systems is underrated. Ortega-Zavala et al. [22], Aizat et al. [23], Yin et al. [24], Cousture et al. [25], and Lin et al. [26] reported that C/M carbonates can be used as primary precursors for AACs. However, LS and dolomite powders display noticeable reactivity only during long-term aging under a high alkaline dosage or pressure. Low chemical activity made it reasonable to use LS as a secondary precursor in AAC based on the low content of reactive calcined clays. Perez-Cortez et al. designed an AAC based on metakaolin (MK) and LS [10, 11]. The content of LS was as high as 80 % in optimal formulation, molar ratios of Na_2O/Al_2O_3 and SiO_2/Al_2O_3 were 0.94 and 3.54 (4.7 % Na_2O respective to mass of MK+LS). The compressive strength (CS) of the designed cement after 24 h of treatment at 60 °C was 51.9 ± 0.7 MPa. The microstructure of the hardened pastes was a dense matrix of reaction products with partly reacted LS particles, and the main reaction products were mixed (C,N)-A-S-H with N-A-S-H, C-A-S-H, and C-S-H. The introduction of LS to sodium silicate (SS)-activated MK decreased alkali component consumption, and changed the chemistry and assemblage of the reaction products. The main reaction products were the mixed gels of N-A-S-H and (N-(C)-A-S-H) with 3D network structures where Ca^{2+} replaced Na^{+} via an ion-exchange mechanism. Meanwhile, the properties of the proposed fresh and hardened AAC pastes were not comprehensively investigated, as the focus was on the CS of the hardened samples.

The high cost and scarcity of the high-grade MK clay deposits have intensified the worldwide research on evaluating the potential of relatively more abundant clay minerals – illite, montmorillonite etc. [27–30]. Bentonite clay, meanwhile, has not yet been explored in AAC with high content of LS.

Several studies have investigated the suitability of natural clay-C/M carbonate blends in the form of carbonate-containing clays with varying mineralogical composition for AACs production [31–38]. Both the content of clay and carbonate minerals and the calcination temperature are determining factors in the reactivity of multimineral carbonate-bearing clays because the decomposition temperatures of calcium carbonate and clay minerals are different. Thus, the normal temperature range providing the clay minerals dehydroxylation at 600–800 °C is insufficient for the complete decarbonization of C/M carbonates. However, calcium carbonate began to decompose at 750 °C [37], indicating that carbonate-containing clays after calcination at temperatures range of 750–800 °C are composed of not only reactive Si and Al but also certain amount of reactive Ca. Consequently, thermally treated carbonate-containing clays used as geopolymer precursors are referred to as Ca-aluminosilicates. D'Elia et al. [35] designed a geopolymer binder based on 6 M sodium hydroxide activated thermally treated carbonate-rich illite clay with a 34.2 % clay mineral and 31.2% calcite content, and the 2 d CS was as high as 20 MPa, whereas 28 d was > 30 MPa. The presence of reactive Ca in the calcined clay induced the co-precipitation of a mix of aluminium-enriched C-A-S-H and N-A-S-H gels, in which sodium was partially replaced by calcium (N,C)-A-S-H.

It should be noted, the literature lacks data on the feasibility of using bentonite clay-limestone co-calcination for the purpose of AAC production.

The object of this study is alkali-activated cement based on bentonite clay and limestone, the subject is the investigation of the properties of fresh and hardened pastes, reaction products assemblage, and microstructural characterization of this binder system.

The goal of this study is the development of alkali-activated cements based on bentonite clay and limestone for general construction purpose. In light of these previous research works, the objectives of the research are:

- feasibility investigation of AACs designs based partially or co-calcined bentonite clay and limestone;
- study on the effect of mineralogical assemblage, fineness of precursors, formulation details, curing conditions on engineering performance, reaction products, and microstructure of AACs based on bentonite clay-limestone mixture;
- study of the role of calcined bentonite clay and limestone in formation of reaction products of the AAC hardened pastes.

2. Materials and Methods

The bentonite clays and LS applied to prepare the AAC paste samples were obtained from the Russian Federation (Republic of Tatarstan) deposits. The mineralogical composition of the Clay 1 (Fig. 1): kaolinite-1A – 5.03 %, montmorillonite-15A – 29.96 %, montmorillonite-18A – 12.02 %, quartz – 25.58 %, muscovite-2M2 – 14.61 %, orthoclase – 7.05 %, clinochlore – 5.28 %, pyrite – 0.46 %; Clay 2 (Fig. 2): montmorillonite – 39 %, quartz – 15 %, albite – 12 %, mica – 11 %, clinochlore – 8 %, hornblende – 7 %, microcline – 6 %, calcite – 2 %.

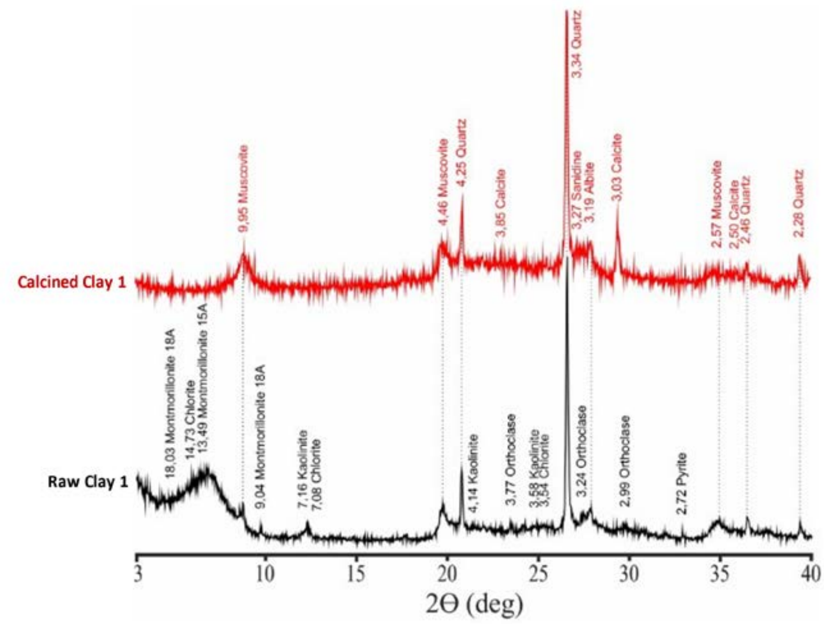

Figure 1. X-ray diffractograms of raw and calcined Clay 1.

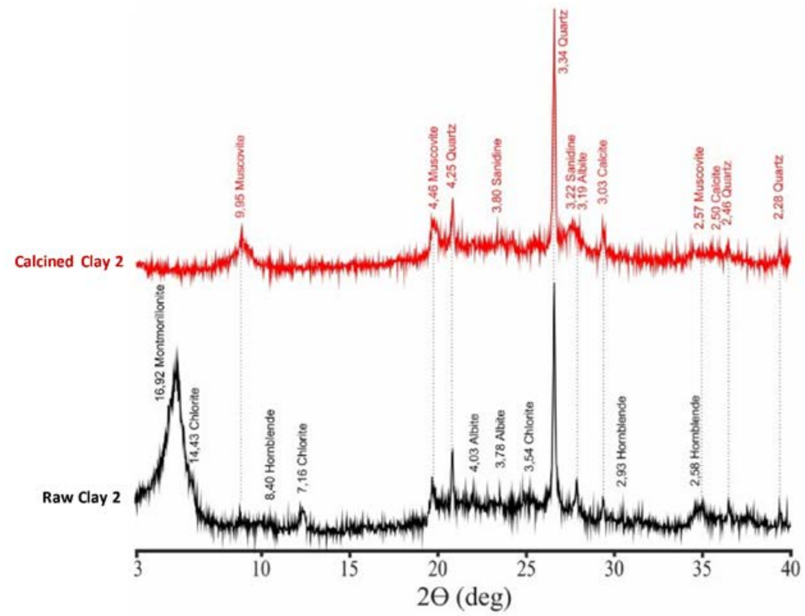

Figure 2. X-ray diffractograms of raw and calcined Clay 2.

Anhydrous solid sodium metasilicate (SSM) (Na_2SiO_3) provided by Meterra (RF) was used as the alkali reactant. An SS solution was prepared by dissolving SSM granules in deionized water and cooling it to room temperature for 24 h prior to use.

The bentonite clays or mixtures of bentonite clays and LS were calcined at 800 °C for 1 h. Calcined bentonite clay and LS were milled in a planetary mill MPL-1. The particle size distributions of the source materials were measured using a laser particle size analyzer (Horiba La-950V2). The materials were dispersed via ultrasound in ethanol as the dispersion medium. The particle size distributions of the starting materials are presented in Table 2 and Fig. 3.

Table 1. Particle size characteristics of the starting materials (μm).

Material	d10	d50	d90
Calcined Clay 1	7.7	24.1	116.2
Calcined Clay 2	9.8	20.9	88.6
Limestone	3.0	9.5	108.0

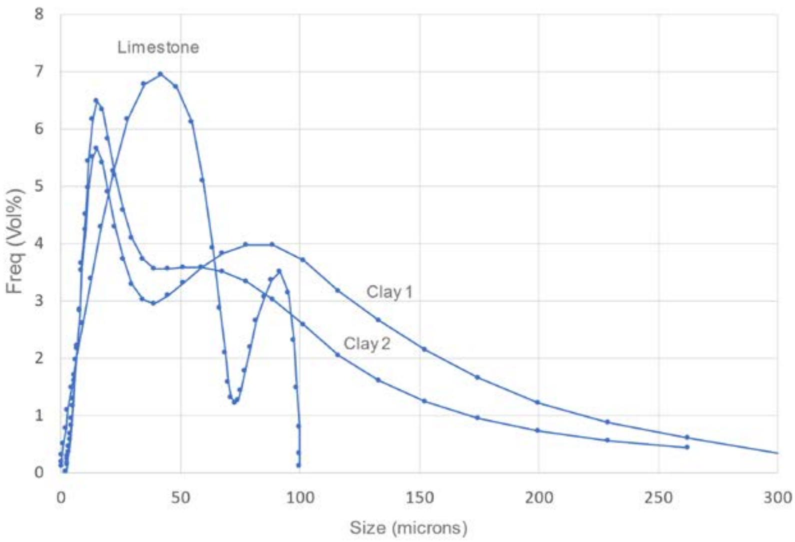

Figure 3. Particle size distribution of starting materials.

The dry mixes were kneaded for approximately 10 min with an alkali reactant solution (Fig. 4). The fresh pastes were manually cast into 25×25×25 mm cubic moulds and vibrated for 1 min to remove entrapped air. Two sets of samples were then prepared. CS of the hardened AAC pastes was tested after steam curing, following a thermal curing program of 24 h of presetting, 4 h to reach the desired temperature, 12 h of dwell time at 80 °C, and 3 h of cooling. Mechanical tests were conducted by applying a vertical load between the two parallel surfaces during casting. Each CS determination quoted was based on the average of six measurements from the same cast.

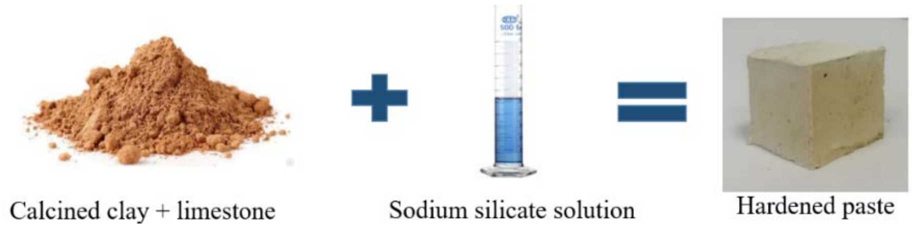

Figure 4. Preparation of AACs hardened pastes.

X-ray diffraction (XRD) and thermal analyses (TG/DSC) were conducted on ground clays and AAC hardened pastes. The XRD results were obtained using a D2 Phaser X-ray diffractometer in a Bragg-Brentano θ–2θ configuration with Cu Kα radiation operating at 40 kV and 30 mA. Data analysis was performed using the DIFFRAC plus Evaluation Package EVA Search/Match and PDF-2 ICDD database. The mineralogical composition of the clays was determined by analyzing the X-ray diffractograms of the software product Diffrac.eva V3.2. An STA 443 F3 Jupiter simultaneous thermal analysis apparatus was used for the TG/DSC. The clays and hardened AAC pastes were heated from 30 °C to 1000 °C at a heating rate of 10 °C/min. The data were analyzed using Netzsch Proteus Thermal Analysis software. Scanning electron microscopy (SEM; FEI XL-30ESEM) was performed at accelerating voltage of 20 keV.

The workability of the fresh pastes was evaluated using flow-table tests according to EN 1015-3. The water/binder ratio was regulated to maintain constant flowability ranging from 29.5 to 30.0 cm. The fresh pastes were placed into a standard conical ring, and free flow without jolting was allowed. Two perpendicular diameters were determined, and the mean value was recorded as the slump flow. The initial and final setting times were measured using the Vicat needle method according to EN 196-3. The determined values are the averages of three samples.

3. Results and Discussion

3.1. Development of AACs based on calcined bentonite clay and raw LS

3.1.1. Properties of fresh and hardened AAC pastes based on calcined bentonite clays and raw LS

The influence of the quantity of LS, calcined clay minerals, and SSM dosage on the CS of hardened AAC pastes is shown in Fig. 5. It can be observed from the presented data that the CS of the samples based on thermally treated Clay 1 is higher than those derived from Clay 2 due to greater amount of reactive phase provided by higher content of metamontmorillonite as well as presence of metakaolinite. Moreover, higher content of quartz in Clay 1 compared to Clay 2 can improve the CS by slowing down the crack growth in the AA cementitious materials [39]. As for the dosage of SSM, 5–10 % was optimal, and the use of a higher percentage of 15 % was not productive. An increase of the SSM percentage from 5 to 10 % logically positively affects the CS by ensuring higher completeness of the reaction process between the precursor and alkali component. The highest mechanical performance up to 34.2 MPa corresponded to a low content of calcined clays (20–30 %) and high content of LS (70–80 %), which agrees with the results of Perez-Cortez et al. [10, 11]. However, the CS values of MK-LS optimal formulations were lower than those obtained by Perez-Cortez et al. [10, 11]. This can be attributed to the differences in curing conditions and lower reactivity of 2:1 type clay mineral metamontmorillonite compared to metakaolin. The improvement in CS followed by an increase in LS replacement up to 80–90 % is probably attributed to several reasons. First, the filler effect of LS provides better packing density of precursor particles; secondly, an increase in the SSM/reactive phase ratio at higher LS dosages against the backdrop of LS poor chemical activity intensifies the formation of binder gel. The SSM/reactive phase ratio supposedly reaches optimal value for formation of continuous mineral matrix with CS and in a volume sufficient to solidify high content of LS when the dosage of calcined clay minerals is 9.4 % and 10.8 % in Clay 1 and Clay 2, respectively.

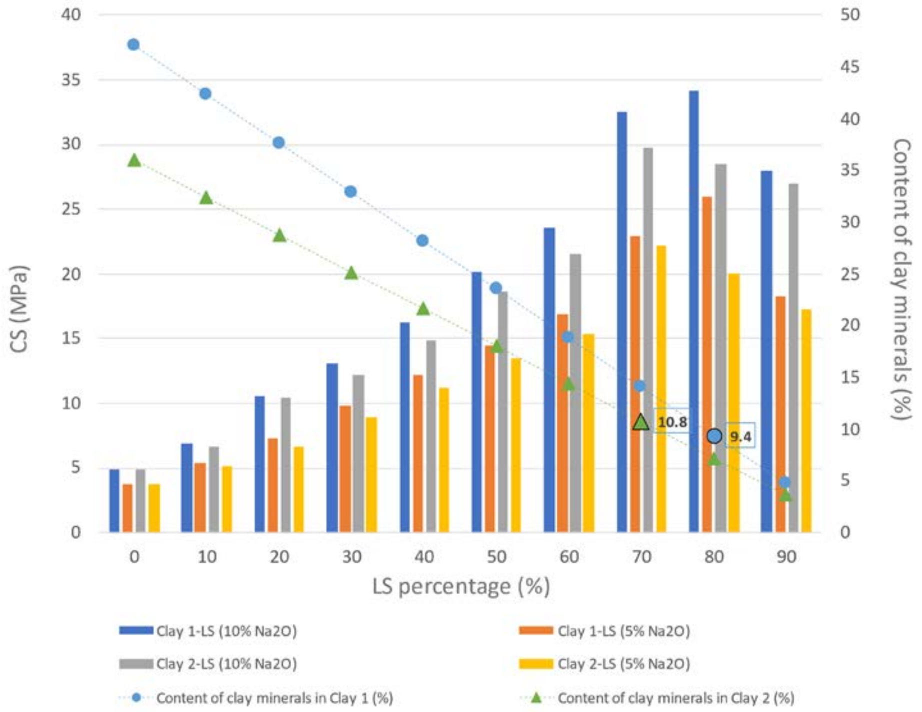

Figure 5. The influence of the quantity of clay minerals, LS, and SS dosage on the CS of the hardened AAC pastes.

The properties of the fresh AA calcined Clay 1-LS pastes are shown in Fig. 6. By increasing the amount of LS in the range of 0–90 %, a reduction can be observed in the water/binder ratio from 0.7 to 0.54, which agrees with numerous studies stating the dilution effect of LS [40–42]. Moreover, the setting times of the fresh pastes were shortened by an increase in LS loading. The reason of it is the lower amount of liquid phase at higher loadings of LS, greater ratio of SSM/reactive phase, and chemical reactions intensity between the alkali reactant and precursors blend.

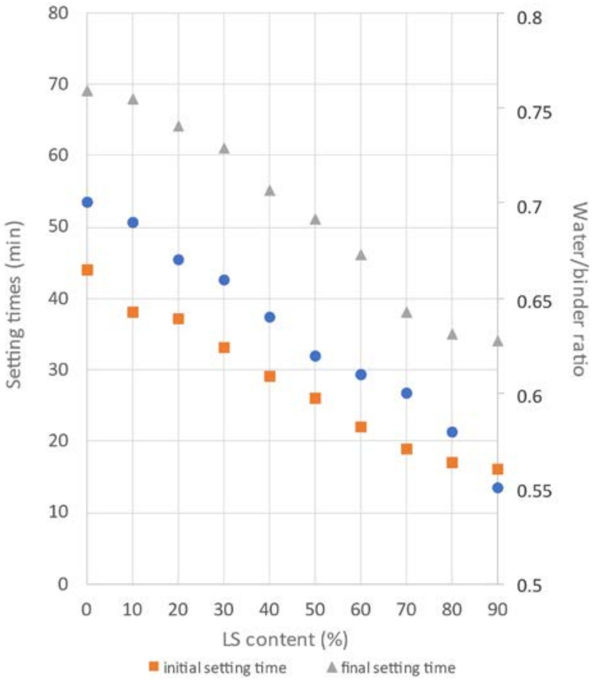

Figure 6. The properties of the fresh AAC pastes.

3.1.2. Reaction products and microstructure of hardened pastes based on calcined bentonite clays and raw LS

The results of the X-ray diffraction, thermal, and SEM/EDS analyses are shown in Figs. 7–9, performed for the optimal formulations of AAC hardened pastes based on calcined Clay 1 incorporated with 80 % of LS and activated by SSM solution (10 % by Na_2O). According to XRD, the main reaction product of hardened paste, based on the amorphous hump which is centralized between 26 and 29°2Ɵ, is a mixed N-A-S-H and N-(C)-A-S-H gel-like product [11], along with relic unreacted quartz, mica, and calcite. The binder hydrate gel is also supported by the results obtained through thermal and SEM/EDS analyses. The water loss of 4.52 % detected in the area of 50–175 °C reflects water evaporation and dehydration from the gel reaction product. However, the reactive phase composition in the studied cementitious system requires further more detailed investigation.

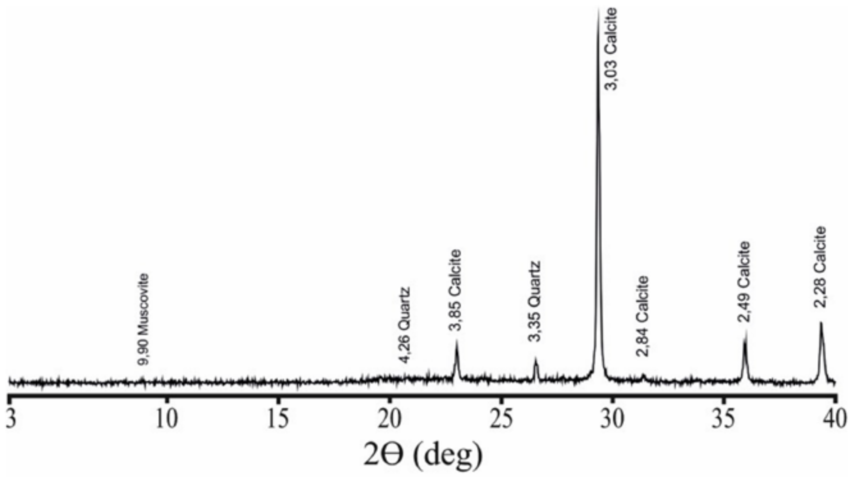

Figure 7. X-ray diffractogram of calcined Clay1(20)-LS(80)-based hardened paste.

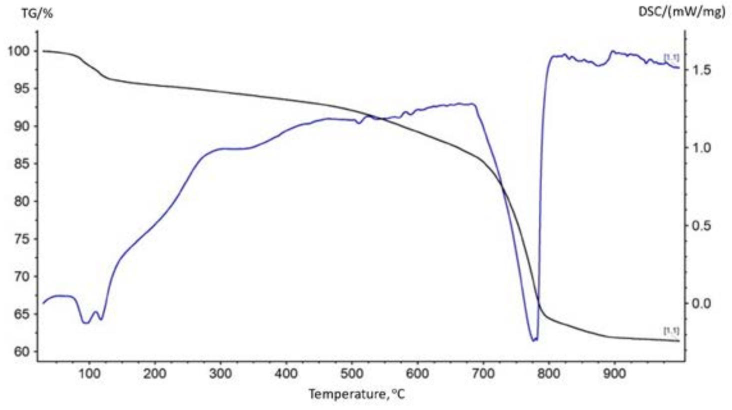

Figure 8. Thermal analyses (TG/DSC) of calcined Clay1(20)-LS(80)-based hardened paste.

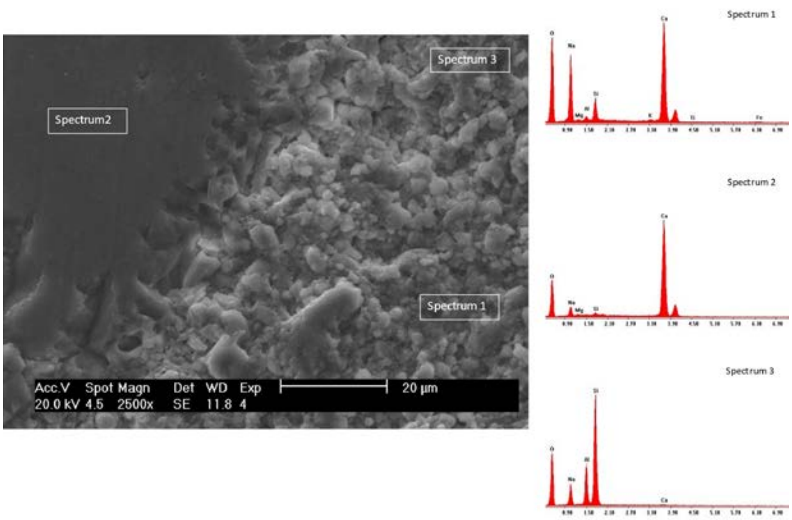

Figure 9. SEM/EDS of calcined Clay1(20)-LS(80)-based hardened paste.

3.2. Development of AACs based on calcined bentonite clay and raw LS

The mechanical properties of hardened pastes obtained by alkali activation of the calcined mixtures of bentonite clays and LS were not significantly different from those based on calcined clays and LS. Therefore, the joint thermal treatment of bentonite clay and LS did not result in formation of calcium silicates as it was stated for mixtures based on kaolin and limestone [38]. These hypotheses were confirmed by XRD and thermal analysis data presented in Figs. 10, 11. As can be seen from the presented data, the calcination of bentonite clay-LS mixtures leads only to dihydroxylation of clay minerals and decomposition of calcite.

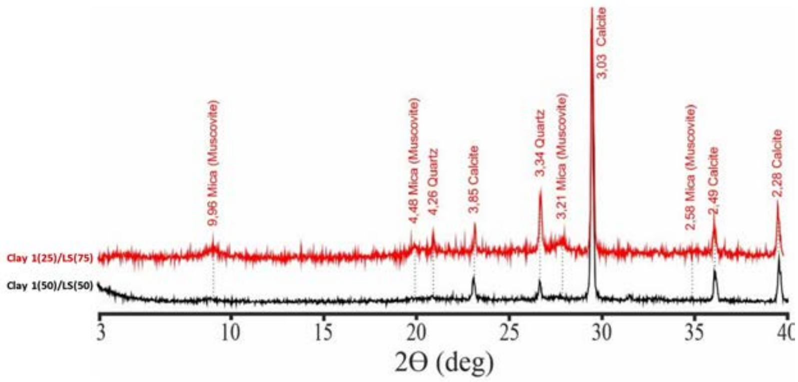

Figure 10. X-ray diffractogram of calcined mixtures Clay1(25)-LS(75) and Clay1(50)-LS(50).

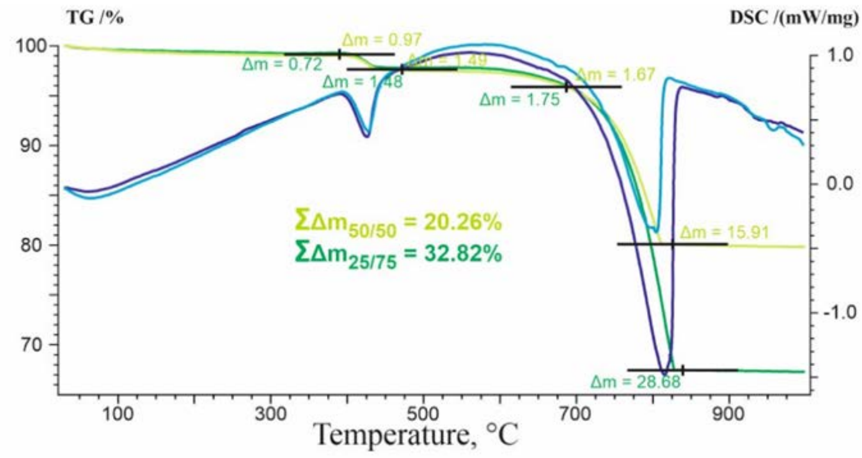

Figure 11. Thermal analyses (TG/DSC) of calcined mixtures Clay1(25)-LS(75) and Clay1(50)-LS(50).

4. Conclusion

The paper presented study results on the effects of formulation-processing factors (individual or complete thermal treatment of bentonite clay-LS, dosages of precursors and alkali reactant) on the properties of sodium-silicate activated fresh and hardened cement pastes, reaction products assemblage, and their microstructure. The following conclusions were drawn. Calcined bentonite clays at 39–47 % content of clay minerals were found to be suitable for AACs incorporated with high loading of raw LS. The thermal treatment of bentonite clay followed by mixing with raw LS was a more reasonable way to obtain mixed AAC compared to joint calcination of bentonite clay and LS. Optimum compositions consisting of 20–30 % calcined clay and 70–80 % LS had compressive strength up to 32 MPa. In the designed AAC based on the binary calcined clay-LS precursor, calcined clay is the main reactive precursor that forms a mineral matrix in the form of sodium aluminosilicate hydrate gel N-A-S-H, whereas calcium carbonate is a much less reactive secondary precursor that modifies the main binder gel by forming sodium (calcium) aluminosilicate hydrate gel N-(C)-A-S-H. An intermixed mineral matrix consisting of N-A-S-H and N–(C)-A-S-H gels binds the LS particles by forming a consolidated material. The effect of LS on the properties of fresh AAC pastes, which manifests in water demand and setting times reduction for blended fresh AAC paste, was based on the dilution effect. The strengthening effect of LS was based on filler, nucleation, and chemical effects.

Predominant content of raw LS contributes to low energy consumption of the proposed AACs. Presented outcomes contribute to the development of the raw materials base of sustainable cements.

References

1. Wang, D., Shi, C., Farzadnia, N., Shi, Z., Jia, H., Ou, Z. A review on use of limestone powder in cement-based materials: Mechanism, hydration and microstructures. Construction and Building Materials. 2018. 181. Pp. 659–672.
2. Wang, D., Shi, C., Farzadnia, N., Shi, Z., Jia, H. A review on effects of limestone powder on the properties of concrete. Construction and Building Materials. 2018. 192. Pp. 153–166.
3. Scrivener, K., Martirena, F., Bishnoi, S., Maity, S. Calcined clay limestone cements (LC3). Cement and Concrete Research. 2018. 114. Pp. 49–56.
4. Juenger, M.C.G., Snellings, R., Bernal, S.A. Supplementary cementitious materials: New sources, characterization, and performance insights. Cement and Concrete Research. 2019. 122. Pp. 257–273.
5. Sharma, M., Bishnoi, S., Martirena, F., Scrivener, K. Limestone calcined clay cement and concrete: a state-of-the-art review Cement and Concrete Research. 2021. 149. Pp. 106564.
6. Mukhametrakhimov, R.Kh., Lukmanova, L.V. Structure and properties of mortar printed on a 3D printer. Magazine of Civil Engineering. 2021. 102 (2). Pp. 10206.
7. Rakhimova, N.R. Calcium and/or magnesium carbonate and carbonate-bearing rocks in the development of alkali-activated cements – A review. Construction and Building Materials. 2022. 325. Pp. 126742.
8. Khalifa, A.Z., Cizer, ¨O., Pontikes, Y., Heath, A., Patureau, P., Bernal, S.A., Marsh, A.T.M. Advances in alkali-activation of clay minerals. Cement and Concrete Research. 2020. 132. Pp. 106050.
9. Cwirzen, A., Provis, J.L., Penttala, V., Habermehl-Cwirzen, K. The effect of limestone on sodium hydroxide-activated metakaolin-based geopolymers. Construction and Building Materials. 2014. 66. Pp. 53–62.
10. Perez-Cortes, P., Ivan Escalante-Garcia, J. Design and optimization of alkaline binders of limestone-metakaolin – A comparison of strength, microstructure and sustainability with portland cement and geopolymers. Journal of Cleaner Production. 2020. 273. Pp. 123118.
11. Perez-Cortes, P., Escalante-Garcia, J.I. Alkali activated metakaolin with high limestone contents – statistical modeling of strength and environmental and cost analyses. Cement and Concrete Composites. 2020. 106. Pp. 103450.
12. Yip, C.K., Provis, J.L., Lukey, G.C., van Deventer, J.S.J. Carbonate mineral addition to metakaolin-based geopolymers. Cement and Concrete Composites. 2008. 30 (10). Pp. 979–985.

13. Khaliullin, M., Gilmanshina, A. The effect of ground limestone on the properties of composite gypsum binder using thermally activated clay as a pozzolanic component. E3S Web of Conferences. 2021. 274. Pp. 04006.
14. Zhu, X., Kang, X., Deng, J., Yang, K., Jiang, S., Yang, C. Chemical and physical effects of high-volume limestone powder on sodium silicate-activated slag cement (AASC). Construction and Building Materials. 2021. 292. Pp. 123257.
15. Rakhimova, N.R., Rakhimov, R.Z., Naumkina, N.I., Khuzin, A.F., Osin, Y.N. Influence of limestone content, fineness, and composition on the properties and microstructure of alkali-activated slag cement Cement and Concrete Composites. 2016. 72. Pp. 268–274.
16. Cohen, E., Peled, A., Bar-Nes, G. Dolomite-based quarry-dust as a substitute for fly-ash geopolymers and cement pastes. Journal of Cleaner Production. 2019. 235. Pp. 910–919.
17. Kalinkin, A.M., Gurevich, B.I., Kalinkina, E.V., Chislov, M.V., Zvereva, I.A. Geopolymers based on mechanically activated fly ash blended with dolomite. Minerals. 2021. 11 (7). Pp. 700.
18. Alghamdi, H., Nair, S.A.O., Neithalath, N. Insights into material design, extrusion rheology, and properties of 3D-printable alkali-activated fly ash-based binders. Materials & Design. 2019. 167. Pp. 107634.
19. Yamb, E., Kaze, R.C., Nzengwa, R. Effect of limestone dosages on some properties of geopolymer from thermally activated halloysite. Construction and Building Materials. 2019. 217. Pp. 28–35.
20. Aboulayt, A., Riahi, M., Ouazzani Touhami, M., Hannache, H., Gomina, M., Moussa, R. Properties of metakaolin based geopolymer incorporating calcium carbonate. Advanced Powder Technology. 2017. 28 (9). Pp. 2393–2401.
21. Qian, J., Song, M. Study on influence of limestone powder on the fresh and hardened properties of early age metakaolin based geopolymer. Springer. Dordrecht. 2015.
22. Ortega-Zavala, D., Santana-Carrillo, J.L., Burciaga-Díaz, O., Escalante-García, J.I. An initial study on alkali activated limestone binders. Cement and Concrete Research. 2019. 120. Pp. 267–278.
23. Aizat, E.A., Al Bakri, A.M.M., Liew, Y.M., Heah, C.Y. Chemical composition and strength of dolomite geopolymer composites.: AIP Conference Proceedings 3rd Electronic and Green Materials International Conference, 020192-1–020192-4, 2017.
24. Yin, Q., Wen, Z.Y. Reaction between carbonaceous rocks and water glass. 12th International Congress on the Chemistry of Cement. Montreal Canada. 2007. p. 5.
25. Cousture, A., Gallias, J.-L. Study of a binder based on alkaline activated limestone. Construction and Building Materials. 2021. 311. Pp. 125323.
26. Lin, W., Zhou, F., Luo, W., You, L. Recycling the waste dolomite powder with excellent consolidation properties: Sample synthesis, mechanical evaluation, and consolidation mechanism analysis. Construction and Building Materials. 2021. 290. Pp. 123198.
27. Belviso, C., Cavalcante, F., Niceforo, G., Lettino, A. Sodalite, faujasite and A-type zeolite from 2:1 dioctahedral and 2:1:1 trioctahedral clay minerals. A singular review of synthesis methods through laboratory trials at a low incubation temperature. Powder Technology. 2017. 320. Pp. 483–497.
28. Garg, N., Skibsted, J. Dissolution kinetics of calcined kaolinite and montmorillonite in alkaline conditions: Evidence for reactive Al(V) sites. Journal of American Ceramic Society. 2019. 102 (12). 7720–7734.
29. Marsh, A., Heath, A., Patureau, P., Evernden, M., Walker P. Phase formation behaviour in alkali activation of clay mixtures. Applied Clay Science. 2019. 175. Pp. 10–21.
30. Garcia-Lodeiro, I., Cherfa, N., Zibouche, F., Fernandez-Jimenez, A., Palomo, A. The role of aluminium in alkali activated bentonites. Materials and Structures. 2014. 48. Pp. 585–597.
31. Dupuy, C., Gharzouni, A., Sobrados, I., Texier-Mandoki, N., Bourbon, X., Rossignol, S. Alkali-activated materials based on callovo-oxfordian argillite: formation, structure and mechanical properties. Journal of Ceramic Science Technology. 2018. 9 (2). Pp. 127–140.
32. Dupuy, C., Gharzouni, A., Texier-Mandoki, N., Bourbon, X., Rossignol, S. Thermal resistance of argillite-based alkali-activated materials. Part 1: effect of calcination processes and alkali cation. Materials Chemistry and Physics. 2018. 217. Pp. 323–333.
33. Gharzouni, A., Ouamara, L., Sobrados, I., Rossignol, S. Alkali-activated materials from different aluminosilicate sources: effect of aluminum and calcium availability. Journal of Non-Crystalline Solids. 2018. 484. Pp. 14–25.
34. D'Elia, A., Pinto, D., Eramo, G., Giannossa, L.C., Ventruti, G., Laviano, R. Effects of processing on the mineralogy and solubility of carbonate-rich clays for alkaline activation purpose: mechanical, thermal activation in red/ox atmosphere and their combination. Applied Clay Science. 2018. 152. Pp. 9–21.
35. D'Elia, A., Pinto, D., Eramo, G., Laviano, R., Palomo, A., Fernandez-Jimenez, A. Effect of Alkali Concentration on the activation of carbonate-high illite clay. Applied Clay Science. 2020. 10 (7). Pp. 2203.
36. Petlitckaia, S., Gharzouni, A., Hyvernaud, E., Texier-Mandoki, N., Bourbon, X., Rossignol, S. Influence of the nature and amount of carbonate additions on the thermal behaviour of geopolymers: a model for prediction of shrinkage. Construction and Building Materials. 2021. 296 (8). Pp. 123752.
37. Karunadasa, K.S.P., Manoratne, C.H., Pitawala, H.M.T.G.A., Rajapakse, R.M.G. Thermal decomposition of calcium carbonate (calcite polymorph) as examined by in-situ high-temperature X-ray powder diffraction. Journal of Physics and Chemistry Solids. 2019. 134. Pp. 21–28.
38. Rakhimova, N.R., Rakhimov, R.Z., Morozov, V.P., Gaifullin, A.R., Potapova, L.I., Gubaidullina, A.M., Osin, Y.N. Marl-based geopolymers incorporated with limestone: A feasibility study. Journal of Non-Crystalline Solids. 2018. 492. Pp. 1–10.
39. Mwiti, M.J., Karanja, T.J., Muthengia, W. J. Thermal resistivity of chemically activated calcined clays based cements. RILEM Bookseries. 2018. 16. Pp. 327–333.
40. Yamb, E., Kaze, R.C., Nzengwa, R. Effect of limestone dosages on some properties of geopolymer from thermally activated halloysite. Construction and Building Materials. 2019. 217. Pp. 28–35.
41. Aboulayt, A., Riahi, M., Ouazzani Touhami, M., Hannache, H., Gomina, M., Moussa, R. Properties of metakaolin based geopolymer incorporating calcium carbonate. Advanced Powder Technology. 2017. Pp. 28 (9).
42. Qian, J., Song, M. Study on influence of limestone powder on the fresh and hardened properties of early age metakaolin based geopolymer. Springer. Dordrecht. 2015.

Information about authors

Nailia Rakhimova, *Doctor of Technical Sciences*
ORCID: https://orcid.org/0000-0003-1735-1758
E-mail: nailia683@gmail.com

Vladimir Morozov, *Doctor of Geological and Mineralogical Sciences*
E-mail: Vladimir.Morozov@kpfu.ru

Alexey Eskin, *Doctor of Geological and Mineralogical Sciences*
E-mail: eskin.aleksey@gmail.com

Bulat Galiullin,
E-mail: taubulat@gmail.com

Received 09.02.2023. Approved after reviewing 12.07.2023. Accepted 12.07.2023.

Magazine of Civil Engineering

ISSN 2712-8172

journal homepage: http://engstroy.spbstu.ru/

Research article

UDC 624.1

DOI: 10.34910/MCE.122.7

Bearing capacity of frame-gantry pile foundations

T.V. Maltseva ✉, ***V.F. Bai, S.A. Erenchinov, A.V. Esipov, N.A. Chumanova***

Industrial University of Tyumen, Tyumen, Russian Federation

✉ *maltsevatv@tyuiu.ru*

Keywords: experimental flume, clay soil, of wedge-shaped piles, frame-gantry piles, the benchmarks using a special template, the deflectometers for measuring settlement, bases, foundations

Abstract. The object of the study is frame-gantry pile foundations embedded in the soil base. To improve the strength of weak soil base, various methods of reinforcement are used, including the foundation constructions in the form of wedge-shaped piles. The paper deals with laboratory studies of the soil base during the installation of small-scale wedge-shaped piles at different angle. The process of soil shearing under the influence of the loads is registered by deformation control benchmarks arranged in the form of a square grid. The interaction between the soil and the frame-gantry foundations appears in a change of the physical and mechanical characteristics in the near pile area. The tests revealed that when piles are installed at the angle of 30° the bearing capacity of the foundation increased. The average density in the fixed active zone of the soil area increased by 12 %, and the average porosity coefficient decreased by 20 %. The deformation modulus changed by 1.8–2.3 times. The angle of internal friction remained virtually unchanged.

Funding: The research was carried in the Soil Bases and Foundations laboratory of the Industrial University of Tyumen.

Citation: Maltseva, T.V., Bai, V.F., Erenchinov, S.A., Esipov, A.V., Chumanova, N.A. Bearing capacity of frame-gantry pile foundations. Magazine of Civil Engineering. 2023. Article no. 12207. DOI: 10.34910/MCE.122.7

1. Introduction

The need for infrastructure development due to population growth is forcing the society to build on the soils available in their locality. The main feature of the geological structure of the soil base of many regions of the world, in particular the Tyumen region, is its composition. The upper layers with a thickness of about 3 m are composed of soils with a deformation modulus of 9–20 MPa, and the underlying weak layers are formed by clayey soils of soft-plastic consistency. Weak soils (clay, loam, deformation modulus 2–7 MPa) have a thickness of 8 to 15 meters or more. At a depth of 13–15 m, there are strong underlying layers of soils. Increasing the bearing capacity of soil foundations and the development of effective solutions for the design and study of foundations on such soils becomes relevant. In most cases, weak water-saturated soils cannot be used as the foundation of buildings and structures without their reinforcement using, for example, pyramidal [1], gantry piles [2]. A lot of research is related to vertical wedge-shaped piles with various bulk materials. Such piles are considered in laboratory experiments [3], full-scale experiments [4], however, the authors do not take into account the effect of the pile inclination angle relative to the vertical on the bearing capacity of the soil foundation.

The paper [5] investigates experimentally and numerically the bearing capacity of steel wedge-shaped joints, and does not consider the bearing capacity of the soil foundation. The development of experimental methods for determining the bearing capacity of a piles is given in the works: composite helical micro piles [6], vertical fiberglass micro piles [7, 8], pyramidal-prismatic and prismatic piles for pressing [9].

Experiments with pyramidal-prismatic piles make it possible to reasonably assign length and dimensions cross section of their pyramidal segment.

The article [10] considers experimental studies carried out on conical piles based on the latest achievements. Experiments indicate the advantages of this type of piles compared to their cylindrical counterparts. Conical piles can be advantageous in terms of bearing capacity compared to cylindrical piles [11]. However, this study focuses on the behavior of conical piles buried in sandy soil.

The article [12] theoretically investigates the effect of vertical vibration on the compaction of soil reinforced with a conical pile during the laying process. It is shown that soil compaction has a significant impact on the soil base and the bearing capacity of the pile. It is also important to identify the mechanisms of the compaction effect of the "pile + soil" structure under static loading, but this fact is not considered by the authors of the article.

In the article [13] reviews the developments and applications of geosynthetics in soil stabilization and protection of coastal areas with emphasis on shoreline protection. Geosynthetic materials are widely used in the construction of sand piles reinforced along the contour [14–16] to increase the bearing capacity of the soil base. In [17], on the basis of the mechanical characteristics of a weak soil base reinforced with fiberglass, the mechanism of interaction between geosynthetics, piles and soil under the load from the embankment was analyzed.

All considered piles are vertical and the issue of changing the mechanical characteristics of the soil foundation reinforced with inclined piles remains unexplored.

In theoretical calculations of soil foundations, an increase in the forecast of the bearing capacity of the foundation occurs due to taking into account the plastic deformations of the soil [18], the viscoelastic properties of the soil [19, 20]. The paper [21] presents an experimental characterization of the crack pattern observed in compacted samples at optimum water content with and without fibers. Skirted foundations are popular due to relatively higher bearing capacity and greater stability compared to strip footing [22]. The works [23–25] present some methods for calculating soil bases reinforced in various ways.

In [26], the bearing capacity of a pyramidal pile was studied depending on its volume, length, soil conditions, and the angle (angle of 5–15°) of inclination of the pile faces, which is not enough to increase the bearing in low-rise construction. In designing, the calculated value of piles and foundations settlement does not take into account the nature of the interaction between the foundation and the soil base in the contact zone; the effect of compacted soil on the pile resistance during installation and during loading; uneven distribution of the contact pressure of the base on the pile surfaces.

Foundation structures (pyramidal, gantry piles) can cut through strong layers of soil and rest on a weak soil base, which significantly reduces the efficiency of using such foundations. In the publications reviewed above, there are no experimental studies related to the increase in the bearing capacity of the base by identifying the mechanism of interaction of inclined (at an angle of 30° to the vertical) conical piles with a base of weak soils such as clays and loams. The authors of the article tried to partially fill this scientific gap. A feature of this article, in contrast to the literature sources discussed above, is laboratory experiments with frame-gantry foundations made of wedge-shaped piles located at different angles to the vertical. The difference between the proposed design and the previously known portal foundations is that when the piles are tilted, an angle of 30° is the foundation support area. Due to the wedge shape of the piles, there is full contact of the lateral surface with the ground, compared to conventional prismatic piles. The experimental study aims to analyze the work of frame-gantry strip foundations on the action of vertical loads and their interaction with a weak soil base.

The **object** of the study is frame-gantry pile foundations embedded in the soil base.

The **subject** of the study is the bearing capacity of a weak clay base, together with the proposed foundation design and the assessment of the strength characteristics of the base. In the calculations, it is necessary to indicate the stiffness characteristics of the soil, taking into account the of frame-gantry piles (soil base and pile foundation), therefore, experimental studies aimed at determining the physical and mechanical characteristics in the interaction between soil and the pile foundation always remain an urgent task.

Thus, the interaction of the frame-gantry foundation and the soil foundation must be investigated experimentally for a complete analysis of the deformed state of the soil foundation. However, the control over the settlements of buildings, the determination of the stress-strain state in natural conditions is problematic due to the complexity of testing and measuring stresses and strains at individual points of the foundation. Therefore, the **purpose** of the presented article is to study the stress-strain state of the "soil + + foundation" system in laboratory conditions on small-scale models to identify the nature of the interaction between the soil foundation and the frame-gantry foundation model.

2. Methods

The authors carried out tests in the Soil Bases and Foundations laboratory of the Industrial University of Tyumen (city of Tyumen, Russian Federation). The purpose of the experiments was to determine the nature of soil compaction in the core when installing wedge-shaped piles at different angles, to determine the influence of various factors on the operation of the foundations under study and the behavior of the soil base near the pile array.

All experiments of frame-gantry foundations models were done in a specially created experimental setup made in the form of a metal tray with soil. The design of the experimental setup had been made in such a way that when testing model foundations, the conditions of a plane problem were simulated. The main feature of the experimental tray and the test scheme of the foundation model was the use of visual non-contact methods for studying the deformations of the soil mass in depth. The experimental setup was equipped with a large viewing window that allowed recording the main stages of the experiment. The experimental setup and the view of the foundation model are shown in Fig. 1.

The structural model of the frame-gantry foundation was adopted with a scale factor of 1:6. The parameters of geometric scaling were taken from the condition of reducing the influence of edge effects with the existing dimensions of the experimental tray. Models of wedge-shaped piles were made of dense Ash-type wood. The specific shape of the wedge piles was taken from the consideration of the optimal ratio of the pile length and the angle of the working faces convergence according to [27], and amounted to 3°. The structural rigidity of the grillage was provided by two metal studs with a diameter of 12 mm, placed in such a way as to perceive the moment arising from the rotation of the piles.

A clayey soil with a disturbed structure was used during the experiments. It was loam of soft plastic consistency, with a density ρ = 1.95-1.98 g / cm^3, humidity W = 25–27 %, porosity coefficient e = 0.7–0.74, angle of internal friction φ = 21.1–21.5^o, specific adhesion C = 23.5–25.5 kPa, Poisson's coefficient 0.35, die deformation modulus E = 14.5–16.5 MPa and modulus of elasticity E_u = 33–35 MPa. The physical and mechanical properties of the soils were determined immediately before the start of each experiment according to methods of field tests with piles (Russian State Standard GOST 5686-94 “Soils. Field test methods by piles”). The soil was placed in the tray by hand, in layers of 5–10 cm and compacted by manual tamping. Before laying the soil, all dense inclusions larger than 2 mm were removed. The arrangement of the deformation control benchmarks was done before laying the soil. First, a 2–3 cm soil layer was laid out on a wooden sheet moistened with water, then the contact surface was leveled with a wide spatula, then the benchmarks were set using a special template, as shown in Fig. 2, 3, on a square coordinate grid with dimensions of 0.02 × 0.02 m. Each benchmark was made in the form of a rigid cylindrical polymer tube with an outer diameter of 3.0 mm, an inner diameter of 1.0 mm and a length of 6 mm.

Figure 1. General view of the foundation.

The models were driven into the soil by percussion method with the help of a rubber construction hammer. Photos were taken through the viewing window every 10 strokes. The installation of piles was being performed until they reached the required level.

The general displacements of the gantry foundation model during settlement were measured by two deflectometers (deflectometer 6PAO, manufacturer – LLC "M-Service", Chelyabinsk city, Russian Federation). The deformation pattern of the model frames and soil was photographed during certain periods of their stepped loading. It is necessary to note that the deformations of the soil had conventionally stabilized by the time of shooting. As a criterion for the conditional stabilization of deformations, the upsetting rate, which is practically equal to zero, is taken.

During the experiments, a rigidly fixed digital camera recorded the current position of the deformation control benchmarks area. The obtained photographs and instrumental data before and after the deformation of the soil were combined. The movements of fixed marks (by distortion of squares) were measured. It was assumed that the deformation of the soil is uniform within any square; there are no relative movements of the marks and surrounding soil particles; friction of the soil against the transparent wall of the tray does not affect the movement of the marks (permissible when studying the qualitative pattern of deformations).

A modernized photogrammetry method was used in the experiment to observe the movements of controlled points along the depth in the cross section of the soil mass. The experiment was carried out in the plane of symmetry of the foundation models under study. The effectiveness of this method for the interaction between the foundation models and the soil base was shown in the works [28, 29].

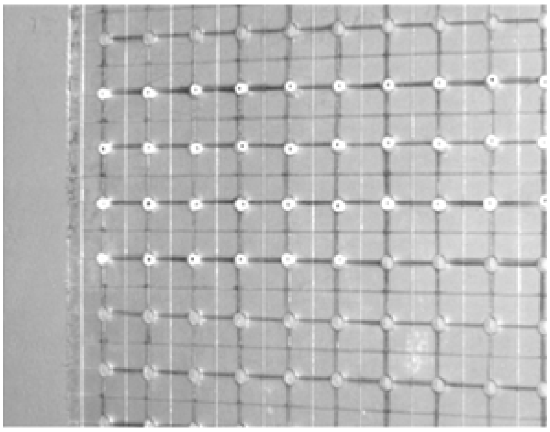

Figure 2. A template in the form of a square grid with side dimensions of 20×20 mm and holes for installing deformation benchmarks.

Figure 3. General view of the laboratory setup window with deformation benchmarks placed in the initial position.

To process the experimental data, dependences for specific adhesion and modulus of deformation were used from the tables of BCaR (Building Codes and Regulations) 2.02.01-83* (Foundations of buildings and structures):

$$C = 25e^2 - 84.4e + 72.3; \quad E = 57.1e^2 - 127.7e + 77.9,$$

where e is the porosity coefficient of the soil; C is the specific adhesion [kPa]; E is the modulus of deformation [MPa].

Since the process of piles installation will result in the soil deformation this fact will change the porosity coefficient therefore the main quantities become functions of deformation. In this regard, to calculate the settlement of frame-gantry foundations correctly and assess the soil strength under the piles, it is necessary to have data on changes in the specific gravity, deformation modulus, adhesion forces and the angle of internal friction of the soil in the process of driving wedge-shaped piles and static loading of frames.

For a complete analysis of soil deformation in the core under the same conditions, a series of comparative experiments was carried out to test three types of frame-gantry foundation models. The studied foundations consisted of two vertical piles, two piles inclined at an angle of 15° and two piles inclined at an angle of 30°, fixed by a rigid grillage.

In studies of soil deformation during pile driving, it was found that a compaction zone is formed around the driven pile because of soil movement in the space around the pile. During the movement of the pile, soil particles move under its lower end along a certain trajectory down and to the side, forming a compacted dumbbell-shaped zone along the side surface of the pile. In addition, it was determined in all three cases that part of the soil from the area close to the surface, and the soil from subsequent layers the pile had passed through were transferred along with it along the pile axis, i.e. soil compaction occurs in this zone.

It is believed that in the case of driving piles with a variable length section (pyramidal, conical, wedge-shaped, etc.) the soil compaction zone resembles an ellipsoid of rotation. The boundaries of the compacted soil are significantly more than 3 diameters away from the pile edge, and up to 50 % of the load is taken by the upper half of the pile. In all three cases, the well-known conclusion is confirmed that pile installation in the soil results in the improvement of physical and mechanical properties of the near-pile area of the soil base, although the nature of the compaction zone formation and its dimensions will differ slightly in each case.

3. Results and Discussion

Fig. 4–5 show the study results of the soil properties changes in compacted zones after the end of the single pile installation and the framed vertical piles installation. Studies have shown that when driving wedge-shaped piles in clayey soils of soft-plastic consistency, the compaction zones around one pile reach 4d – 4.5d in the horizontal direction (where d is the average cross-section diameter of the pile). In the plane of the tip, the compacted zones extend to a depth of 1.5d – 2.0d. The specific gravity of the soil varies on average from 19.5–19.8 kN/m^3 to 23.2–25.0 kN/m^3. Fig. 4-5 also show data on changes in the specific gravity of the soil at various distances from the axis and below the plane of the tip of vertical wedge-shaped piles. It can be seen from the given data, that the greatest compaction occurs in the plane of the pile tip and in the upper section, equal to 1/3-1/2 of the pile length.

From the given data it can be understood that the adhesion forces change on average from 0.024–0.025 MPa to 0.037–0.045 MPa, i.e. about 1.4–1.8 times.

Numerous checking of the experiment results has demonstrated that soil compaction in the near-pile area of conical piles does not affect the change of the internal friction angle. As a rule, this measurement is constant. The difference in measurement is only (3–5 %). Experiments have also established that there is a significant increase in the deformation modulus in the compacted zone (Fig. 4–5). As a result of pile driving, there was an increase in the modulus of deformation under the piles at a depth of 1.5d – 2.0d.

In the horizontal direction, the zone of change in the deformation modulus for single piles is 4d – 4.5d. The magnitude of the deformation modulus in the plane of the tip and in the upper section of the piles length (1/3–1/2 of the length) changed from 14.5–16.5 MPa to 29.7–39.1 MPa.

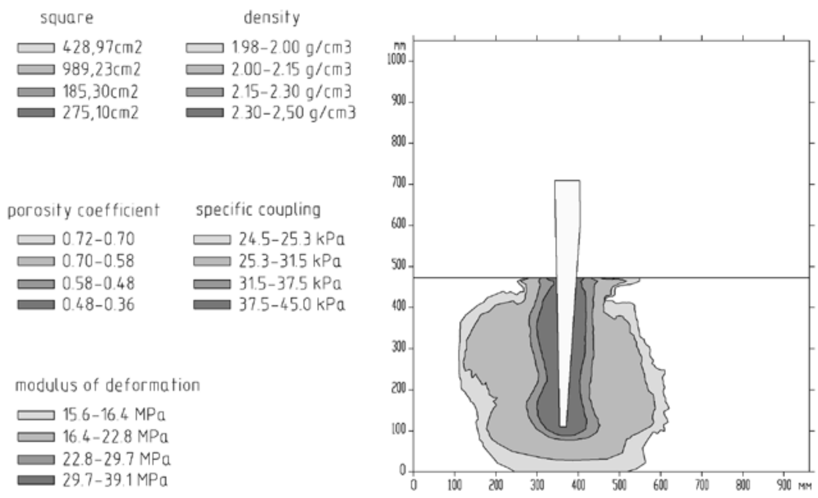

Figure 4. Contours of changes in the physical and mechanical properties of soils in the compacted zone during the installation of a single vertical pile.

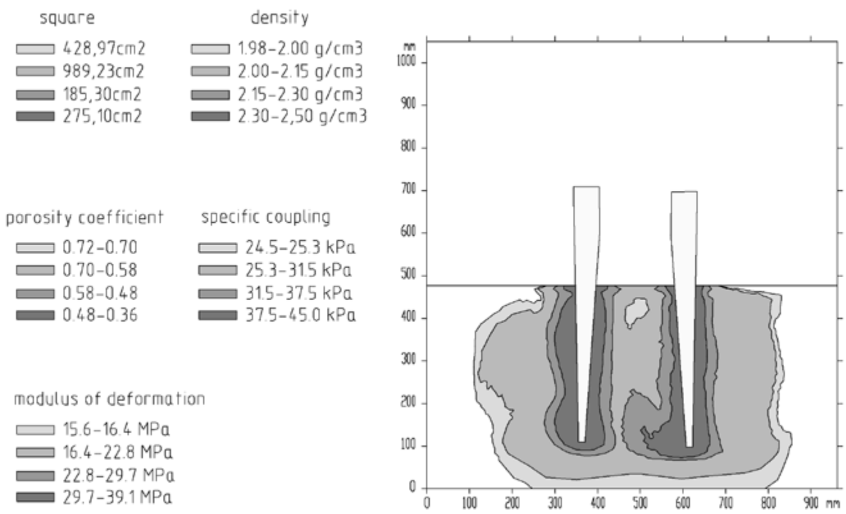

Figure 5. Contours of changes in the physical and mechanical properties of soils in the compacted zone during the installation of two vertical piles.

Figure 6-7 shows changes contours in soil properties in the compacted zones after the end of the single pile installation and the framed vertical piles installation inclined at an angle of 15°. Studies have shown that when driving wedge-shaped piles at an angle of 15° from the vertical, in clay soils of a soft-plastic consistency, the compaction zones from the inner face of one pile along the normal to its axis reach 4d – 5d (where d is the average cross-section diameter of the pile). In the plane of the tip, the compacted zones are distributed around the circumference and extend to a depth of up to 3d. The compaction of the soil is combined with the soil heaving on the outer face of the pile. It occurs as the reaction of the soil from the inner face of the pile, and the distribution of the compaction in this case has a different form. When the second inclined pile is installed, the compacted zones of the inner pile faces close together and form a compacted soil mass.The greatest compaction occurs in the area of the pile tips. An area of lower density is marked in the upper part of the piles; it is formed in the result of partial uplift of the soil in the upper part of the pile. The specific gravity of the soil varies on average from 19.7–19.8 kN/m^3 to 23.2–25.0 kN/m^3.

From the given data, it can be seen that the adhesion forces change on average from 0.023–0.024 MPa to 0.036–0.044 MPa, i.e. about 1.5–1.8 times. The modulus of deformation changes from 14.7–15.5 MPa to 28.5–37.8 MPa that is 1.9–2.4 times.

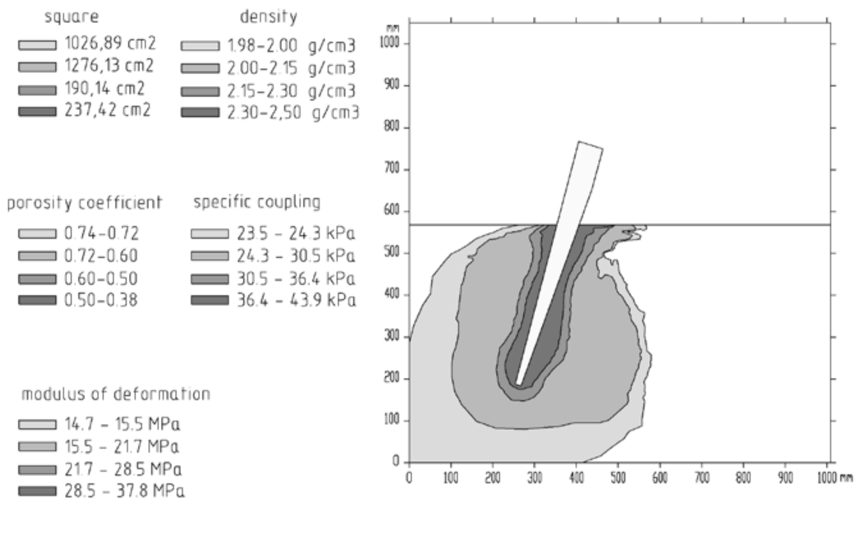

Figure 6. Contours of changes in the physical and mechanical properties of soils in the compacted zone during the installation of a single pile with a slope of 15°.

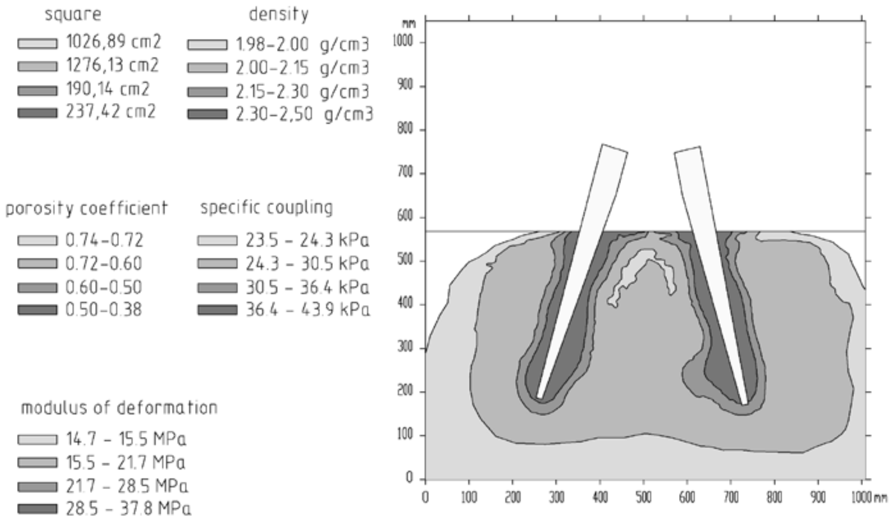

Figure 7. Contours of changes in the physical and mechanical properties of soils in the compacted zone during the installation of two piles with the slopes of 15°.

It should be noted that there is no mutual influence between the piles being installed at a distance of 4d. In this case, the change in soil properties in the active pile zones can be taken into account as for one pile.

Fig. 8–9 show contours of changes in soil properties in compacted areas after the installation of a single inclined pile and the framed inclined piles, the angle of piles inclination is 30° from the vertical.

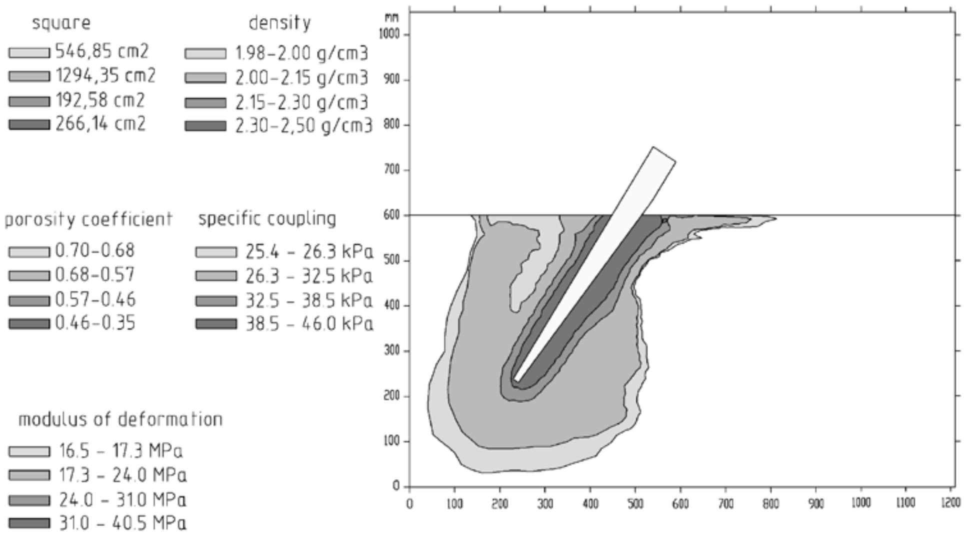

Figure 8. Contours of changes in the physical and mechanical properties of soils in the compacted zone during the installation of a single pile with a slope of 30°.

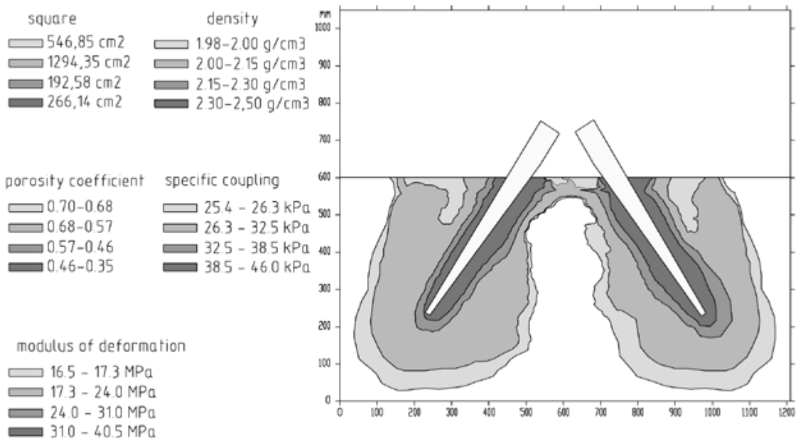

Figure 9. Contours of changes in the physical and mechanical properties of soils in the compacted zones during the installation of two piles with slopes of 30°.

Studies have shown that when wedge-shaped piles are driven at an angle of 30° from the vertical, as well as, when piles are driven at an angle of 15° the compaction zones have a nonhomogeneous distribution. From the inner face of one pile, along the normal to its axis, the compaction zones reach 3.5d – 4d (where d is the average cross-section diameter of the pile). In the plane of the tip, the compacted zones are distributed along the pile circumference and spread to a depth of up to 3 d. From the outer face of the pile, soil compaction occurs in the same way as in the case when the pile is driven at an angle of 15°.

The compaction is combined with a big heave, and the distribution of the compaction is nonhomogeneous. There is a zone of lower density in the upper part of the pile, which was not observed during the installation of a vertical pile and a pile with a slope of 15°. When the second inclined pile is being installed, the compacted zones of the inner face of the piles partially close in the upper part of the piles. Thus, when the piles are driven at an angle of 30°, the compacted zones in the near-pile area can be considered as with a single pile. The greatest compaction occurs in the area of the pile tips. An area of lower density is defined in the upper part of the piles. The specific gravity of the soil varies on average from 19.7–19.8 kN/m^3 to 23.2–25.0 kN/m^3.

From the given data, it can be seen that the adhesion forces change on average from 0.025–0.026 MPa to 0.038–0.046 MPa, i.e. about 1.5-1.7 times. The deformation modulus changed from 16.5–17.3 MPa to 31.0–40.5 MPa, i.e. 1.8–2.3 times.

The tests revealed that the density at the side face of the wedge-shaped pile support of the model changed from an average of 1.98 g/cm^3 to 2.5 g/cm^3, the porosity coefficient changed from 0.7 to 0.35. Concerning the initial measurements, the average density in the fixed active zone of the soil area increased by 12 %, and the average porosity coefficient decreased by 20 %. As the soil partially moved upwards during the pile installation, the soil from the outer face of the pile was subjected to less compaction. This situation is typical when piles are installed at the angle of 30°.

4. Conclusion

In laboratory conditions on small-scale models we studied the interaction of vertical frame-gantry strip foundations with different angles of inclination of wedge-shaped piles and a clayey base.The new design scheme of the frame-gantry strip foundation at an angle of 30° wedge-shaped piles with respect to the vertical allows the use of the upper layers of soil to distribute vertical static loads on the soil base of a larger area, in contrast to the existing frame-gantry piles. The settlement of the frame-gantry strip foundation, with the slope of the wedge-shaped piles at an angle of 30° relative to the vertical, is formed mainly due to the deformation of the uncompacted soil mass enclosed between the piles, which is 96 % of the entire settlement of the foundation. Experimental studies were carried out with the help of modern approved digital control and measuring systems, calibrated primary converters and calibrated instruments.

The test results also showed:

1. The outline of zones with altered soil characteristics depends on the angle of the piles inclination and the distance between them. The greatest bearing capacity has a foundation with a pile angle

of 30°. This shows that such a foundation design contributes to a better distribution of stresses in the soil mass. Considering the soil base of foundations with vertical and inclined piles at an angle of 15°, it can be noted that the soil shearing in the inter-pile space occurs largely together with piles.

This indicates that the settlement of the foundation takes place mainly due to the deformation of the underlying layer below the ends of the piles. It is noted that in the process of the soil base loading of a frame-gantry foundation with a pile inclination angle of 30°, an increase and closing of the compaction zones occur in the inter-pile space. A significant change in the density of the soil, by 30% from the initial one, occurs directly in the upper part between the piles of the frame during the foundation settlement. The foundation settlement takes place mainly due to the deformations of the non-compacted soil between the piles.

2. When wedge-shaped pile models are installed into loamy soil, the total deformation modulus $\left(E\right)$ and specific cohesion $\left(C\right)$ increase by 1.5–2.4 times, depending on the angle of installation. The angle of internal friction $\left(\varphi\right)$ practically does not change.
3. Bearing capacity at the same settlement of a frame-gantry foundation with wedge-shaped piles inclined to the vertical at an angle of 30°, compared to frame-gantry foundations with piles tilted to the vertical at an angle of 0° and 15°, was higher by 1.3 and 1.2 times, respectively , and when compared with conventional prismatic piles, the specific bearing capacity was 2.2 times higher.

References

1. Marchenko, V.S., Tugaenko, Yu.F. Polevye issledovaniya deformacii nesushchego grunta pod odinochnymi piramidal'nymi svayami i pod svajnymi fundamentami [Field studies of bearing ground deformation beneath single pyramidal piles and beneath pile foundations]. Osnovaniya i fundamenty. 1973. 6. Pp. 84–88. DOI: 10.1016/0148-9062(74)92131-7
2. Plahotnyj, G.N. Naturnye ispytaniya kozlovyh svaj, samoraskryvayushchihsya pri zabivke [Field tests of gantry piles, self-expanding when driving]. Godatnik na vysshiya inzhenerno-stroitelen institute. 1976. HKHVI t. sv. IV. Sofiya. 4. Pp. 41–50.
3. Liu, Y.-Y., Yeung, A.T., Zhang, D.-L., Li, Y. Experimental study on the effect of particle shape on stress dip in granular piles. Powder Technology. 2017. 319. Pp. 415–425. DOI: 10.1016/j.powtec.2017.07.021
4. Liu, Y.-Y., Zhang, D.-L., Dai, B.-B., Su, J., Li, Y., Yeung, A.T. Experimental study on vertical stress distribution underneath granular silos. Powder Technology. 2021. 381. DOI: 10.1016/j.powtec.2020.11.066
5. Mingju, Z., Zhitian, X., Pengfei, L. Bearing capacity and failure behavior of disconnectable coupling joint with double row wedges (DCJD) used in the prestressed internal bracing. Underground Space. 2021. 11. DOI: 10.1016/j.undsp.2021.11.003
6. Vatin, N., Ilizar, M., Nurmukhametov, R. Composite helical micro piles bearing capacity. IOP Conference Series: Materials Science and Engineering. 2020. 890(1). 012037. DOI: 10.1088/1757-899X/890/1/012037
7. Sabri, M.M.S., Vatin, N.I., Nurmukhametov, R.R., Ponomarev, A.B., Galushko, M.M. Vertical Fiberglass Micro piles as Soil-Reinforcing Elements. Materials. 2022. 15(7). 2592. DOI: 10.3390/ma15072592
8. Sabri, M.M.S., Vatin, N.I., Ponomarev, A.B., Nurmukhametov, R.R., Kostyukov, I.I. Settlement of Soil Reinforced with Vertical Fiberglass Micro-Piles. Materials. 2022. 15(14). 4744. DOI: 10.3390/ma15144744
9. Bekbasarov, I., Nikitenko, M., Shanshabayev, N., Atenov, Y., Moldamuratov, Z. TAPERED-PRISMATIC PILE: DRIVING ENERGY CONSUMPTION AND BEARING CAPACITY. News of the National Academy of Sciences of the Republic of Kazakhstan. Series of Geology and Technical Sciences. 2021. 6(450). Pp. 53–63. DOI: 10.32014/2021.2518-170X.119
10. Shafaghat, A., Khabbaz, H. Recent advances and past discoveries on tapered pile foundations: a review. Geomechanics and Geoengineering. 2022. 17(2). Pp. 455–484. DOI: 10.1080/17486025.2020.1794057
11. Lee, J., Paik, K., Kim, D., Hwang, S. Estimation of axial load capacity for bored tapered piles using CPT results in sand. Journal of Geotechnical and Geoenvironmental Engineering. 2009. 135(9). Pp. 1285–1294. DOI: 10.1061/(ASCE)GT.1943-5606.0000036
12. Wu, W., Jiang, G., Dou, B., Leo, C.J. Vertical Dynamic Impedance of Tapered Pile considering Compacting Effect. Mathematical Problems in Engineering. 2013. 304856. DOI:10.1155/2013/304856
13. Brian, O. Oyegbile, B., Oyegbile, A. Applications of geosynthetic membranes in soil stabilization and coastal defence structures. International Journal of Sustainable Built Environment. 2017. 6(2). Pp. 636–662. DOI: 10.1016/ j.ijsbe.2017.04.001
14. Usmanov, R., Mrdak, I., Vatin, N., Murgul, V. Reinforced soil beds on weak soils. Applied Mechanics and Materials. 2014. 633–634. Pp. 932–935. DOI: 10.4028/www.scientific.net/AMM.633-634.932
15. Moysya, A.A., Vatin, N.I. Thermally insulated shallow foundation on heaving soils. Civil Engineering Journal. 2009. 3(5). Pp. 7–10. DOI: 10.18720/MCE.5.1
16. Maltseva, T., Nabokov, A., Chernykh, A. Reinforced Sandy Piles for Low-Rise Buildings. Procedia Engineering. 2015. 117. DOI: 10.1016/j.proeng.2015.08.15
17. Sun, L., Zheng, J.J., Zhang, J., Ma, Q. Mechanical Performance of Geosynthetic-Reinforced Pile-Supported Embankments. Advanced Materials Research. 2010. 156–157. Pp. 1696–1701. DOI: 10.4028/www.scientific.net/amr.156-157.1696
18. Mirsaidov, M.M., Sultanov, T.Z. Assessment of stress-strain state of earth dams with allowance for non-linear strain of material and large strains. Magazine of Civil Engineering. 2014. 49(5). Pp. 73–82. DOI: 10.5862/MCE.49.8
19. Sultanov, T.Z., Khodzhaev, D.A., Mirsaidov, M.M. The assessment of dynamic behavior of heterogeneous systems taking into account non-linear viscoelastic properties of soil. Magazine of Civil Engineering. 2014. 45(1). Pp. 80–89. DOI: 10.5862/MCE.45.9
20. Khudayarov, B.A., Turaev, F.Z. Nonlinear vibrations of fluid transporting pipelines on a viscoelastic foundation. Magazine of Civil Engineering. 2019. 86(2). Pp. 30–45. DOI: 10.18720/MCE.86.4
21. Jamei, M., Alassaf, Y., Ahmed, A., Mabrouk, A. Fibers reinforcement of the fissured clayey soil by desiccation. Magazine of Civil Engineering. 2022. 109(1). 10914. DOI: 10.34910/MCE.109.14

22. Shukla, R.P. Bearing capacity of skirted footing subjected to inclined loading. Magazine of Civil Engineering. 2022. 110(2). 11012. DOI: 10.34910/MCE.110.12
23. Maltseva, T., Saltanova, T., Chernykh, A. Modelling a Reinforced Sandy Pile Rheology when Reacting with Water-saturated Ground. Procedia Engineering. 2016. 165. Pp. 839–844. DOI: 10.1016/j.proeng.2016.11.782
24. Maltseva, T.V., Trefilina, E.R., Saltanova, T.V. Deformed state of the bases buildings and structures from weak viscoelastic soils. Magazine of Civil Engineering. 2020. 95(3). Pp. 119–130. DOI: 10.18720/MSE.95.11
25. Korovkin, V., Kokoreva, K. Improving the Calculation of Urban Berthing Quays of Gantry Type in St. Petersburg. Procedia Engineering. 2015. 117. Pp. 197–205. DOI: 10.1016/j.proeng.2015.08.141
26. Khryanina, O.V., Bely, A.A. Factors affecting the bearing capacity of pyramidal piles. Modern scientific research and innovation. 2015. 4(1). URL: https://web.snauka.ru/issues/2015/04/51430
27. Fedorov, V.I. Sposob opredeleniya optimalnogo ugla sbega poverkhnosti stvolov piramidalnykh ili konicheskikh svay [Method for determining the optimal slope angle of the surface of the shafts of pyramidal or conical piles]. Patent for invention SU1740558A1
28. Stepanov, M., Melnikov, R., Zazulya, J., Ashihmin, O. Generation of stress-strain state in combined strip pile foundation beds through pressing of soil. MATEC Web of Conferences. 2017. 106. 02011. DOI: 10.1051/matecconf/20171060
29. Pronozin, Y.A., Stepanov, M.A., Rachkov, D.V., Davlatov, D.N., Chikishev, V.M. Laboratory investigation on interaction of the pile foundation strengthening system with the rebuilt solid pile-slab foundation. Civil Engineering Journal (Iran). 2020. 6(2). 263. DOI: 10.28991/cej-2020-03091468

Information about authors:

Tatyana Maltseva, *Doctor of Physical and Mathematical Sciences*
ORCID: https://orcid.org/0000-0002-0274-0673
E-mail: maltsevatv@tyuiu.ru

Vladimir Bai, *PhD in Technical Sciences*
E-mail: bajvf@tyuiu.ru

Sergey Erenchinov, *PhD in Technical Sciences*
E-mail: erenchinovsa@tyuiu.ru

Andrey Esipov, *PhD in Technical Sciences*
E-mail: esipovav@tyuiu.ru

Natalya Chumanova,
E-mail: chumanovana@tyuiu.ru

Received 11.10.2022. Approved after reviewing 07.08.2023. Accepted 13.09.2023.

Magazine of Civil Engineering

ISSN 2712-8172

journal homepage: http://engstroy.spbstu.ru/

Research article

UDC 624.012

DOI: 10.34910/MCE.122.8

Strengthening and restoration of damaged reinforced concrete structures with composite plastics

Zh.Sh. Mukhanbetzhanova

Kazakh National Technical University named after K.I. Satpayev, Almaty, Republic of Kazakhstan

sh.zhanna@bk.ru

Keywords: restoration of reinforced concrete structures, fiber-reinforced plastics, pre-stress, single-span reinforced concrete beam

Abstract. This paper considers directions to devise methods for restoring the operational suitability of reinforced concrete structures. Mistakes of designers and non-compliance with the concreting technology of monolithic reinforced concrete structures lead to the formation of cracks and deflections of unacceptable size in reinforced concrete beams and floor slabs, as well as to insufficient strength of the elements. Such structures require not only an increase in bearing capacity but also the restoration of the operational suitability of damaged structures. A technique for restoring the serviceability of bendable reinforced concrete structures with increased deflections and excessive crack opening is proposed. To restore bendable reinforced concrete structures, surface reinforcement with pre-stressed fiber-reinforced plastics is suggested, which is ensured by the creation of a building lift in the damaged elements. Unlike conventional reinforcement methods, surface reinforcement techniques are characterized by high gain efficiency, corrosion resistance, low labor intensity, and short terms of work; they ensure strength increase and provide for economic feasibility. This study's results established that the use of fiber-reinforced plastics not only increases the bearing capacity of reinforced concrete structures but also helps reduce the width of the cracks formed. Thus, it is possible to avoid an increase in the cross-section of structures and reduce the time of operations, which could lead to additional costs.

Acknowledgments: We express our sincere gratitude to the scientific supervisor, Head of the Laboratory of Reinforced Concrete Structures, KazNIISA, Professor A. Bespayev for support and training in the method for strengthening reinforced concrete structures.

Citation: Mukhanbetzhanova, Zh.Sh. Strengthening and restoration of damaged reinforced concrete structures with composite plastics. Magazine of Civil Engineering. 2023. Article no. 12208. DOI: 10.34910/MCE.122.8

1. Introduction

For more than 15 years, the use of fiber-reinforced tapes to strengthen reinforced concrete structures has been investigated worldwide but the relevance of studies is not lost since examining them requires a deeper understanding of the work of composite materials. Fiber-reinforced plastics are composite materials consisting of a plastic matrix and high-strength reinforcing fibers, supplied in the form of ribbons (lamellas), fabrics, or meshes [1–3]. Epoxy, phenolic, polyester, vinyl ester, or other organic resins are used as plastics. Reinforcing fibers are made, by using nanotechnology, from carbon, basalt, aramid, or glass [4–6]. The composite material is found in the form of reinforcing bars and tapes. During the entire time of studying the work of the material, researchers apply all types of composite materials to conduct tests. Some types may not be economically feasible [7–8]. To identify the reasons that lead to an increase in the cost of strengthening reinforced concrete structures, samples of reinforced concrete beams were examined. Many researchers study the reinforcement of structures rather than their restoration [9–10]. Therefore, studies on the restoration of reinforced concrete structures, and reducing the width of cracks formed as a result of overstressing them are relevant [11–13]. The process of surface strengthening of reinforced concrete structures takes several hours; the reinforced structure is able to perceive additional loads in 24 hours [14–15]. These reinforcement methods are widely used for longitudinal and transverse reinforcement of the stretched zone of reinforced concrete structures, as well as the construction of reinforcing clips in compressed elements.

To accomplish the aim, the following tasks have been set:

- to determine the dynamic and static strength based on the results of laboratory tests;
- to compare the estimated and experimental strains in the beams;
- to obtain the results of a practical assessment.

2. Methods

2.1. This study's object and methods

To assess the strength and deformation characteristics of concrete, concrete cubes with a face size of 150 mm and cylinders with a diameter of 150 mm and a height of 300 mm were tested. Concrete samples were tested under axial compression at the hydraulic press ALPHA 3-3000S (Germany, Form+Test) with a phased increase in the longitudinal compressive force at a speed of 0.3 MPa/s, up to the destruction of the sample. The value of the load increase step did not exceed 5÷8 % of the destructive load. In the process of static loading of the cylinders, longitudinal and transverse strains were measured using strain gauges with a base of 50 mm, glued to the side faces of the samples, as well as the automatic deformation meter AID-4M (Russia). Loading of experimental prisms was carried out along the physical axis of the samples in stages constituting 5–10 % of the destructive load.

The strength of concrete in the cubes was in the range of 27.9–32.7 MPa, with an average of 30.4 MPa (Fig. 1). The cylindrical strength of class B25 concrete is in the range of 19.9–21.5 MPa and averages 20.6 MPa (Fig. 2, a, b). Fig. 3 shows diagrams of the longitudinal and transverse strains of concrete obtained from cylinder tests, where each line is indicated by a separate color, indicating the number of cylinders tested. The marginal longitudinal strains of concrete at compression were in the range of – (23–25)·10–4 relative units, and the transverse strains of + (7–8)·10–4 relative units.

Figure 1. Testing a concrete cube at the hydraulic press ALPHA 3-3000S.

Figure 2. Concrete cylinder:
a – test at the hydraulic press ALPHA 3-3000S; b – devices to register strains.

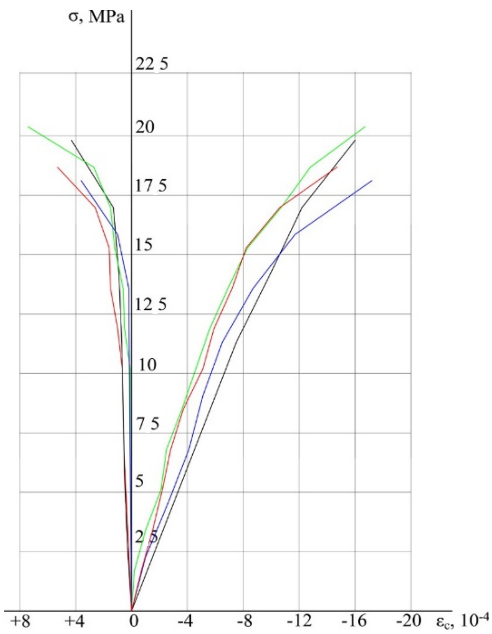

Figure 3. Diagram of longitudinal and transverse strains of concrete cylinders.

2.2. Methods of additional tests

To study the patterns of change in stiffness and crack resistance in the process of generating preliminary stress of fiber-reinforced plastics, additional tests were performed on three series of reinforced concrete beams with a cross-section of 120×200 mm and a length of 2200 mm. Experimental beams differed in the percentage of reinforcement of the stretched zone. Prototypes of the beams included three series of samples, differing in the percentage of longitudinal reinforcement. The beams from the first series had the least amount of stretched reinforcement (2 Ø 18 A500). We give the results of testing the beams from the first series. They were loaded with a hydraulic jack in stages accounting for 7–9 % of the destructive load. Comprehensive experimental studies of bendable and compressed elements reinforced with fiber-reinforced plastics included the study of the operation of normal and inclined cross-sections of bending structures [16]. The samples were subjected to surface reinforcement with carbon tapes glued to the compressed and stretched edge of the beams. The prototypes made from the B25 concrete class were tested according to the scheme of a single-span hinged beam loaded in a third of the span with equal concentrated forces. We studied the operation of normal cross-sections of bendable reinforced concrete structures on reinforced concrete beams tested according to the scheme of a single-span hinged-supported beam. The beams were loaded with two equal concentrated forces, which were generated by means of a load device for the bending bearing capacity of the beams. In the process of testing with the help of electric load cells with a base of 50 mm and the automatic deformation meter AID-4M with a division unit of 10–5 relative units, longitudinal strains of the beam were measured according to the height of the compressed concrete zone. With the help of load cells with a base of 20 mm, strains of stretched reinforcement were measured. Consequently, a pattern of the formations was recorded and the width of the crack opening was measured using a microscope with a division unit of 0.02 mm; the magnitude of the transverse load was recorded on the high-precision manometer of the hand pumping station (Fig. 4, 5). The load cells were connected to an automatic strain gauge. With their help, mechanical effects are converted into electrical signals and transmitted to the strain gauge bridge. Calibration of load cells was carried out using the readings of the strain gauge bridge and measuring the initial imbalance, as well as according to the data specified in the passport, which indicate the operating power transmission coefficient of the sensor.

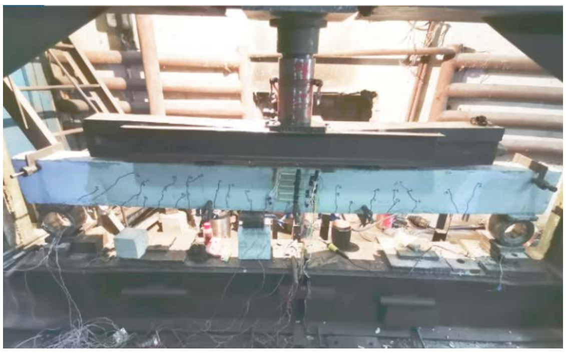

Figure 4. General view of reinforced concrete beam tests.

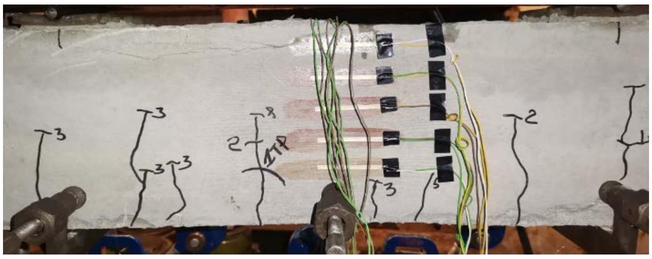

Figure 5. General view of load cells on concrete, normal cracks, and damage area of compressed concrete zone.

We loaded the samples with a transverse load in stages, constituting about 5–7 % of the destructive load, in several stages. At each stage, a load was generated that causes the predefined width of crack opening, then the load was removed and we loaded it in the next stage to a greater width of crack opening.

3. Results and Discussion

Most of the structures of civil, industrial, and bridge construction are built of reinforced concrete [17]. Given the huge investments in the construction sector, their deterioration is a serious issue for the countries that ensure their preservation [18]. Cracks that appear in reinforced concrete structures due to various factors are responsible for the integrity of a facility [19–22].

Fiber-reinforced composite materials (FRP) are increasingly being used as replacements for steel reinforcement in reinforced concrete structures. This is due to their excellent properties, such as low weight, resistance to the aggressive effects of acids, the ability to work at different temperatures, and mechanical strength [23–24]. Such advantages confirm the strength of FRP compared to alternative materials such as steel plates, and reinforcing bars [25]. FRPs, used in different forms, are effective in reinforcing damaged concrete structures [26]. Experimental studies [27] show that gluing FRPs and their full or U-shaped wrapping can significantly increase the bearing capacity of damaged reinforced concrete structures. Papers [25–26] considered options for replacing reinforcing bars with reinforcement made of composite material, which makes it impossible to restore structures in the process of its operation. The work of FRP on bending and sliding was also studied. These methods are used to provide peripheral and transverse limitations. This type of protection, in addition to strengthening the structure, can change the shape of the appearance of cracks and detachment from the concrete surface. For greater efficiency, FRP tapes are glued at a predefined angle. Study [28] shows that the use of inclined U-shaped laminates glued at the ends of the tested structures at an angle of 45° gives better results than similar gluing at a vertical angle. Gluing of external plates for structural restoration is currently studied as a method of increasing the shear strength and rigidity of reinforced concrete structures. The advantage of this method is the speed of operation, which is more economical compared to other reinforcement methods such as a concrete shell (jacket) or a complete replacement of the structure. More important is the fact that the method can be applied in the working condition of the structure [28]. The studies into the work of FRP with a reinforced concrete structure [27-29] determined at what angle of gluing a greater efficiency is achieved to strengthen the structure without restoration. Many studies have been conducted on the strength of damaged reinforced concrete structures [30] by making technological holes in a reinforced concrete structure, violating its integrity. Researchers report an experimental work [31] to increase the shear strength of reinforced concrete beams with a sprayed polymeric material reinforced with glass fiber. Methods to prevent exfoliation of composite tapes were investigated; the researchers used the anchoring method but disregarded methods of structural restoration.

The test procedure provides for the measurement of strains in the inclined and normal cross-sections under dynamic alternating loads that have not previously been examined by other authors, compared with static loads. The aim of this study is to determine the effectiveness of the use of FRP to strengthen damaged reinforced concrete structures and restore the cracks that have appeared as a result of static and dynamic loads. This will make it possible to restore the supporting structures without stopping their work without much labor and time costs.

3.1. Determining the dynamic and static strength of beams under laboratory conditions

With the magnitude of the bending moment in the beam B-18-1 equal to M = 4.42 kNm, a normal crack was formed in the zone of pure bending. Then, at the bending moment M = 13.24 kNm, the greatest width of the openings of normal cracks reached 0.13 mm, and the distance between normal cracks was in the range of 80–82 mm (Fig. 6).

Figure 6. General view of the beam B-18-1 after testing.

After generating a bending moment of M = 14.17 kNm, the vertical load was reset: that ended the first stage of our testing. Fig. 7 shows the plot of crack opening at all subsequent loading stages: each line indicates loading.

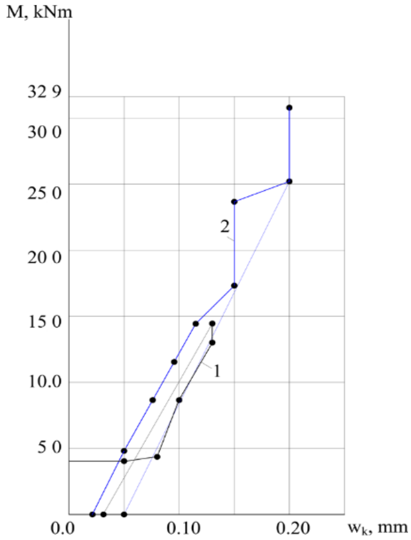

Figure 7. Evolution plot of normal cracks in the beam B-18-1.

In the second stage of the tests, the vertical load was increased to M = 19.12 kNm, and the opening width of normal cracks increased to 0.15 mm. In the next stages of loading, the load value was increased to M = 21.09 kNm, M = 25.51 kNm, and M = 26.0 kNm: no increase in the width of the normal crack opening was observed. Since the width of the crack opening has not increased, the pattern of the opening of normal cracks is given only for the first two stages of loading.

Along with the normal cracks in the zone of pure bending of the beam, there was an accelerated development of inclined cracks in the support zones. The first oblique crack was formed in the first stage of the test at a transverse force of V = 16.1 kN, and the opening width of the inclined cracks in the first stage of the tests at the transverse test V = 23.0 kN reached 0.30 mm. In the second stage of the tests at a transverse force of V = 23 kN, the opening width of the inclined cracks reached 0.40 mm, and with a transverse force of V = 30.1 kN, the opening width of inclined cracks reached 0.45 mm. In the third stage of tests at V = 33 kN, the opening width of inclined cracks reached 0.60 mm, and in the fourth stage of the test at V = 39.8 kN, the opening width of the inclined cracks reached 0.75 mm. In the fifth stage of the tests at V = 51.35 kN, the opening width of the inclined cracks reached 0.90 mm (Fig. 8). Loads are indicated under each line.

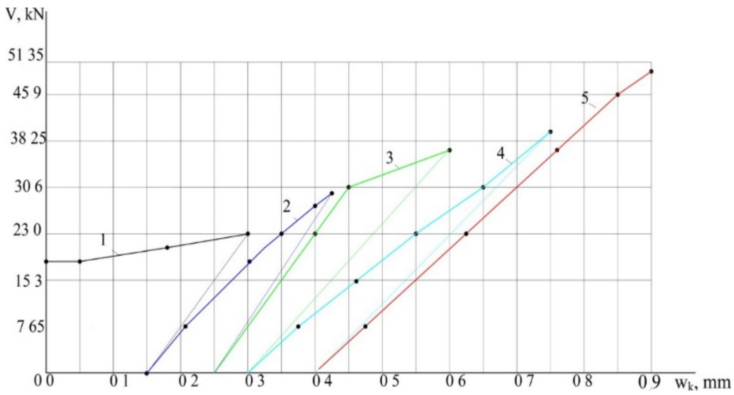

Figure 8. Evolution plot of inclined cracks un the beam B-18-1.

The beam collapsed in the zone of pure bending from the crushing of the compressed zone of concrete at a bending moment of M = 32.86 kNm (Fig. 9, a).

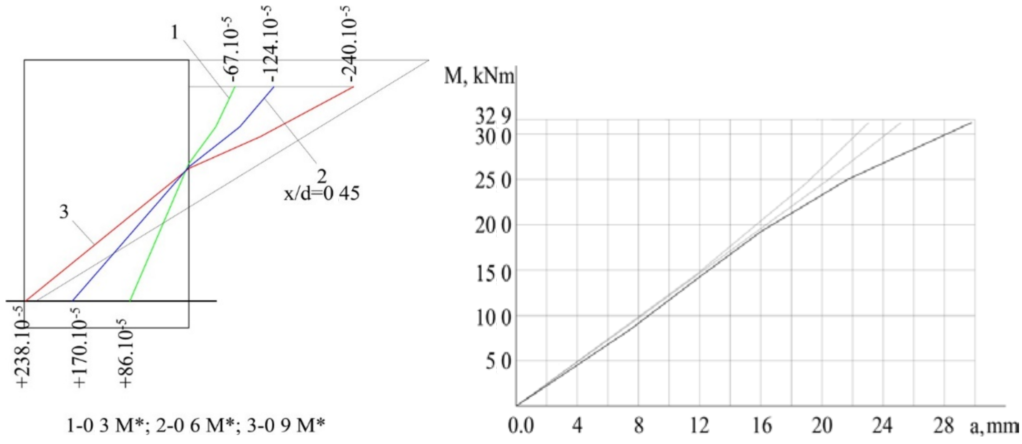

a ***b***

Figure 9. Diagram of beam destruction: *a* – distribution of strains across the cross-section height of the beam B-18-1; *b* – vertical deflections of the span of the beam B-18-1.

The relative value of the compressed concrete zone was ξ = d/h = 0.45 (Fig. 9, b), the magnitude of the vertical movements of the span part reached 28.6 mm, and the places of application of vertical forces were 22.8–25.1 mm, which were 1/70 and 1/63 of the span. Each line corresponds to the applied load.

3.2. Deformation calculation

The reinforcement of the beams in the stretched zone with two layers of laminate had little effect on the load of crack formation and the strength of normal cross-sections. However, the width of the crack opening was reduced by almost two times, the tensile strains in the laminate decreased by 65 %, and the vertical deflections decreased by 31 %.

Dynamic tests of the beams were carried out under cyclic alternating loading with the help of hydraulic jacks and a hydrodynamic installation with a frequency of about one hertz and an asymmetry coefficient of forces ρ = 0.1. The high amplitude of the greatest forces ensured the destruction of samples in 10÷300 cycles of loading. The empirical dependence of the destructive load (M_d) on the number of cyclic loads (n) is as follows:

$$\frac{M_d}{n} = 1.33 - 0.116 \lg n. \tag{1}$$

The estimated tensile resistance f_{vd} for FRP is determined from:

$$f_{yd} = \frac{f_{yk} * \gamma_{Ff}}{\gamma_f}. \tag{2}$$

The estimated tensile strains ε_f and the estimated value of the elastic modulus of deformation E_f for FRP are determined from the following formulas:

$$\varepsilon_f = \frac{\varepsilon_{uf} * \gamma_{Ff}}{\gamma_f}, \tag{3}$$

$$E_f = \frac{f_{yk}}{\varepsilon_{uf}}. \tag{4}$$

Exfoliation of the FRP can occur if the deformation in it cannot be perceived by the base.

The transverse strength of the oblique cross-section V_{cd} reinforced by FRP is defined as the sum of the cross-sectional strength without reinforcement and additional transverse force $V_{Rd,f}$, which is perceived by the FRP reinforcement:

$$V_{cd} = V_{Rd,c} + V_{Rd,xy} + V_{Rd,f}, \tag{5}$$

$$V_{Rd,f} = \frac{A_f \varepsilon_{fe} E_f \left(\sin(\alpha) + \cos(\alpha)\right)}{s_f}, \tag{6}$$

$$\varepsilon_{fe} = 0.004 \le 0.75\, \varepsilon_u, \tag{7}$$

where A_f, E_f, ε_{fe}, α, s_f are, respectively, the cross-sectional area and deformation of polymeric reinforcing meshes, their modulus of deformation, the angle of inclination, and the distance between the strips of reinforcing meshes, ε_u is the limit extensibility of polymeric reinforcing meshes.

Table 1 gives comparative indicators of the estimated and experimental strains across the height of the cross-section of the beams.

Table 1. Comparative data on estimated and experimental strains across the height of the cross-section of beams.

	The relative size of the compressed zone	ε_c, 10^{-5}	ε_s, 10^{-5}	The relative size of the compressed zone	**ε_s, 10^{-5}**
B-18-1	0.45	340	238	0.61	**223**
B-18-2	0.44	368	280	0.51	**326**

Data in Table 1 confirm the linear dependence of the relative height of the compressed zone of concrete on the percentage of longitudinal reinforcement of the stretched zone.

3.3. Results of the practical evaluation

We studied the strength of the inclined cross-sections of bendable elements reinforced with fiber-reinforced plastics during cyclic loading on similar reinforced concrete beams reinforced in the support zones with a surface sticker. The beams were tested according to the scheme of a single-span hinged supported beam loaded with two equal transverse forces separated from the supports at distances equal to l_{eq} = $1.75h$–$2.0h$. In the process of a phased increase in the vertical load after the formation of normal cracks in the zone of pure bending, the appearance of inclined cracks in the sup- port zone was observed. In the stage of accelerated opening of inclined cracks up to 3 mm, the destruction of the support zone occurred. After removing the reinforcement from the meshes, a crushing of the compressed concrete between the grids was detected. Strengthening of the support zone with vertical or inclined polymeric meshes led to a doubling of the strength of inclined cross-sections, and the strains of the fiber-reinforced meshes were 3–4 %. Along with the conventional scheme of the destruction of inclined cross-sections, an additional destruction scheme caused by the chipping of the protective layer of concrete under the strips of reinforcement nets was revealed. At the same time, the increase in strength did not exceed 50 %, and the largest strains of the meshes for the stage before the destruction were 1.8–2.5 %.

3.4. Discussion

Based on the results obtained from static tests (Fig. 9, *b*), it was determined that the strengthening of beams by gluing one layer of laminate on the stretched zone led to an increase in strength by 75 %. Strains of stretched steel reinforcement decreased by almost 10 %. This is due to an increase in the strength of the stretched reinforcement.

Our static tests were performed when the samples were loaded with a hydraulic jack (Fig. 4). The destruction of reinforced concrete beams without reinforcement was caused by the crushing of the compressed concrete zone in the zone of pure bending with the fluidity of the stretched steel reinforcement. When reinforcing the beams in the stretched zone with laminate tapes, along with the conventional scheme of the destruction of reinforced concrete structures, additional destruction schemes were revealed caused by the separation of the protective layer of concrete in the stretched zone or the separation of stretched laminate tapes from concrete. At the same time, an increase in the crack resistance and stiffness of normal sections was observed (Fig. 6). Taking into consideration the separation of the protective layer of concrete in the stretched zone, when calculating the required lifting of damaged reinforced concrete structures for their restoration, it is necessary to take the initial stiffness of the elements.

We identified options for the restoration of damaged reinforced concrete elements. Namely, the replacement of reinforcing rods [3], prone to corrosion, with rods made of composite material, strengthening reinforced concrete structures with composite plastics to increase their bearing capacity. Since materials have different bending moments, there was a separation of the protective layer of concrete from composite materials, which creates difficulties in studying and calculating.

In the future, other methods will be considered to advance the study into the work of FRP. Including the addition of fibers to the composition of concrete to increase their ability to bend in a stretched area.

4. Conclusion

1. The dynamic strength at cyclic loading of normal cross-sections of bendable elements strengthened in a stretched beam at a single load exceeded the static strength by 33 %. With an increase in the number of cyclic loads required for destruction from 2 to 280, the strains of the stretched laminate ranged from 1.88 ‰ to 2.05 ‰, and the vertical deflections increased by 26 %. Overall, the greatest strains of stretched laminate under dynamic loads were 45 % less than the strains of stretched laminate in static tests. The nature of the destruction of normal cross-sections of beams under dynamic loading differed little from the destruction of similar beams under static loading.

2. Prototypes were tested according to the scheme of a single-span hinged beam loaded in the span. Testing of the beams involved several stages of loading with unloading at different levels of force. Our results confirm the linear dependence of the relative height of the compressed concrete zone on the percentage of longitudinal reinforcement of the stretched zone.

3. When designing the restoration of normal cross-sections of damaged reinforced concrete structures with prestressed surface reinforcement with fiber-reinforced plastics, the following prerequisites should be met:

- when calculating the amount of required lifting of damaged reinforced concrete elements, take the initial stiffness of the intact element;
- the residual width of the opening of normal cracks when constructing an artificial construction lift, equivalent to the natural weight of the element being restored, should be taken to be equal to $a = 0.05–0.10$ mm;
- in most restored reinforced concrete structures, the residual opening width of normal cracks was about 50 % of the opening width of the existing cracks.

4. When designing the restoration of inclined sections of damaged reinforced concrete structures with prestressed surface reinforcement with fiber-reinforced plastics, the following prerequisites should be met:

- when calculating the amount of required lifting of damaged reinforced concrete elements, take the initial stiffness of the intact element;
- the estimated strength of the glued fiber-reinforced plastics must provide the strength of the inclined sections, exceeding the required strength of the inclined sections by 20 %;
- in most restored reinforced concrete structures, the residual opening width of the inclined cracks should not be less than $a = 0.20$ mm.

References

1. Krassowska, J., Piña, C. Flexural Capacity of Concrete Beams with Basalt Fiber-Reinforced Polymer Bars and Stirrups. Materials. 2022. 15 (22). 8270. DOI: 10.3390/ma15228270
2. Täljsten, B., Blanksvärd, T. Mineral-Based Bonding of Carbon FRP to Strengthen Concrete Structures. Journal of Composites for Construction. 2007. 11. Pp. 120–128. DOI: 10.1061/(ASCE)1090-0268(2007)11:2(120)
3. Chen, J., Teng, J. Anchorage strength models for FRP and steel plates bonded to concrete. Journal of Structural Engineering. 2001. 127. Pp. 784–791. DOI: 10.1061/(ASCE)0733-9445(2001)127:7(784)
4. Lu, X., Teng, J., Ye, L., Jiang, J. Bond–slip models for FRP sheets/plates bonded to concrete. Engineering Structures. 2005. 27. Pp. 920–937. DOI: 10.1016/j.engstruct.2005.01.014
5. Teng, J., Smith, S., Yao, J., Chen, J., Intermediate crack-induced debonding in RC beams and slabs. Construction and Building Materials. 2003. 17. Pp. 447–462. DOI: 10.1016/S0950-0618(03)00043-6
6. Dai, J., Ueda, T., Sato, Y. Development of the Nonlinear Bond Stress–Slip Model of Fiber Reinforced Plastics Sheet–Concrete Interfaces with a Simple Method. Journal of Composites for Construction. 2005. 9. Pp. 52–62. DOI: 10.1061/(ASCE)1090-0268(2005)9:1(52)
7. Sas, G., Täljsten, B., Barros, J., Lima, J., Carolin, A. Are Available Models Reliable for Predicting the FRP Contribution to the Shear Resistance of RC Beams? Journal of Composites for Construction. 2009. 13. Pp. 514–534. DOI: 10.1061/(ASCE)CC.1943-5614.0000045

8. Kotynia, R., Abdel Baky, H., Neale, K., Ebead, U. Flexural Strengthening of RC Beams with Externally Bonded CFRP Systems: Test Results and 3D Nonlinear FE Analysis. Journal of Composites for Construction. 2008. 12. Pp. 190–201. DOI: 10.1061/(ASCE)1090-0268(2008)12:2(190)
9. Triantafillou, T. Shear Strengthening of Reinforced Concrete Beams Using Epoxy Bonded FRP Composites. Structure Journal. 1998. 95. Pp. 107–115. DOI: 10.14359/531
10. Bespayev, A., Altigenov, U., Kuralov, U. Usileniye i vosstanovleniye izgibayemykh zhelezobetonnykh konstruktsiy predvaritelno napryazhennymi fibroarmirovannymi plastikami. Nauka i innovatsionnyye tekhnologii. 2018. 3 (8). Pp. 154–156.
11. El-Hacha, R., Wight, R., Green, M. Innovative System for Prestressing Fiber-Reinforced Polymer Sheets. Structure Journal. 2003. 100. Pp. 305–313.
12. Täljsten B. Defining anchor lengths of steel and CFRP plates bonded to concrete. International Journal of Adhesion and Adhesives. 1997. 17. Pp. 319–327. DOI: 10.1016/S0143-7496(97)00018-3
13. Banthia, N., Boyd, A. Sprayed fibre-reinforced polymers for repairs. Canadian Journal of Civil Engineering. 2000. 27. DOI: 10.1139/l00-027
14. Mukhanbetzhanova, Zh., Bespayev, A. Metod usileniya zhelezobetonnykh konstruktsiy, povrezhdennykh pri raznykh faktorakh. QazBSQA Khabarshysy. Құrylys konstruktsiyalary zhənе materialdary. 2022. 2 (84). Pp. 263–269. DOI: 10.51488/1680-080X/2022.2-19
15. Bespayev, A., Kuralov U., Altigenov U. Usileniye zhelezobetonnykh konstruktsiy polimernymi materialami. Vestnik Natsionalnoy inzhenernoy akademii RK. 2011. 2. Pp. 115–118.
16. Bespayev, A., Kuralov, U., Altigenov, U. The strengthening and renewing of damaged reinforced concrete structures by restressed fiber reinforced plastics. International scientific conference. Machines. Technologies. Materials. 2019. 3 (14).
17. Nawaz, W., Elchalakani, M., Yehia, Sh., Pham Th. The effect of CFRP strip stirrups on the shear strength of SCC high strength lightweight concrete beams. Structures. 2022. 47 (1). Pp. 709–724. DOI: 10.1016/j.istruc.2022.11.026
18. Aydın, E., Boru E., Aydın, F. Effects of FRP bar type and fiber reinforced concrete in the flexural behavior of hybrid beams. Construction and Building Materials. 2021. 279. 122407. DOI: 10.1016/j.conbuildmat.2021.122407
19. Tang, Y., Jiang, T., Wan, W. Structural monitoring method for RC column with distributed self-sensing BFRP bars. Case Studies in Construction Materials. 2022. 17. E01616. DOI: 10.1016/j.cscm.2022.e01616
20. Bakis, C., Bank, L., Brown, V., Cosenza, E., Davalos, J., Lesko, J. Fiber-Reinforced Polymer Composites for Construction. Journal of Composite Construction. 2002. 6. Pp. 73–87. DOI: 10.1061/(ASCE)1090-0268(2002)6:2(73)
21. Elchalakani, M., Yang, B., Mao, K., Pham, Th. Mechanical properties of fiber reinforced polymer (FRP) and steel bars. Geopolymer Concrete Structures with Steel and FRP Reinforcements. 2022. Pp. 75–135. DOI: 10.1016/B978-0-443-18876-3.00002-5
22. Hollaway, L. A review of the present and future utilization of FRP composites in the civil infrastructure with reference to their important in-service properties. Construction and Building Materials. 2010. 24. Pp. 2419–45. DOI: 10.1016/j.conbuildmat.2010.04.062
23. Yang, J., Haghani, R., Blanksvärd, T., Lundgren, K. Experimental study of FRP-strengthened concrete beams with corroded reinforcement. Construction and Building Materials. 2021. 301. 124076. DOI: 10.1016/j.conbuildmat.2021.124076
24. Zhou, J., Li, Ch., Yoo, D., He J., Feng, Zh. Modified softened membrane model for ultra-hogh-performance fiber-reinforced concrete solid and hollow beams under pure torsion. Engineering Structures. 2022. 270. 114865. DOI: 10.1016/j.engstruct.2022.114865
25. Lin, X., Zhang, Y. Bond–slip behaviour of FRP-reinforced concrete beams. Construction and Building Materials. 2013. 44. Pp. 110–117. DOI: 10.1016/j.conbuildmat.2013.03.023
26. Triantafyllou, G., Rousakis, T., Karabinis, A. Effect of patch repair and strengthening with EBR and NSM CFRP laminates for RC beams with low, medium and heavy corrosion. Composites Part B Engineering. 2018. 133. DOI: 10.1016/j.compositesb.2017.09.029
27. Singh, S. Shear response and design of RC beams strengthened using CFRP laminates. International Journal of Advanced Structural Engineering. 2013. 5 (1). DOI: 10.1186/2008-6695-5-16
28. Fu, B., Tang, X., Li, L., Liu, F., Lin, G. Inclined FRP U-jackets for enhancing structural performance of FRP-plated RC beams suffering from IC debonding. Composite Structures. 2018. 200. Pp. 36–46. DOI: 10.1016/j.compstruct.2018.05.074
29. Hussein, M., Afefy, H., Khalil, A-H. Innovative repair technique for RC beams predamaged in shear. Journal of composites for construction. 2013. 17. DOI: 10.1061/%28ASCE%29CC.1943-5614.0000404
30. Campione, G., Minafò, G. Behaviour of concrete deep beams with openings and low shear span-to-depth ratio. Engineering Structures. 2012. 41. Pp. 294–306. DOI: 10.1016/j.engstruct.2012.03.055
31. Hussain, Q., Pimanmas, A. Shear strengthening of RC deep beams with openings using sprayed glass fiber reinforced polymer composites (SGFRP): Part 1, Experimental study. KSCE Journal of Civil engineering. 2015. 19. Pp. 2121–2133. DOI: 10.1007/s12205-015-0243-1

Contact:

Zhanna Mukhanbetzhanova, *PhD*
ORCID: https://orcid.org/0000-0002-9672-4374
E-mail: sh.zhanna@bk.ru

Received 17.01.2023. Approved after reviewing 07.08.2023. Accepted 15.09.2023.

Magazine of Civil Engineering

ISSN 2712-8172

journal homepage: http://engstroy.spbstu.ru/

Research article

UDC 691.5

DOI: 10.34910/MCE.122.9

Performance of aluminium shaving waste and silica fume blended mortar

M.O. Yusuf

Department of Civil Engineering, College of Engineering, University of Hafr Al Batin, Hafr Albatin, Saudi Arabia

moruf@uhb.edu.sa, *moruff@gmail.com*

Keywords: compressive strength, hydration, thermal conductivity, supplementary cementitious materials, silica fume, microstructure

Abstract. This study investigates the impact of aluminium shaving waste (ASW or A_x: 0.0, 1.0, 1.5, 2 wt%) on the silica fume (SF or S_y: 0-10 %) blended ordinary Portland cement (OPC or $C_{88\text{-}100\%}$) mortar. The sample was designated as $C_{100-x-y}S_yA_x$ and the evaluations were done through their performances in terms of workability, compressive strength, thermal residual strength and microstructural characteristics in comparison with the OPC only mortar ($C_{100}S_0A_0$). The increase in ASW/SF ratio enhanced the workability of SF blended ($C_{90-x}S_{10}A_x$). The unit weight of mortar reduced with increase in ASW/SF ratio so that 19.7 % was lost with the incorporation of 2 % of ASW. ASW induced effervescence of hydrogen gas in the fresh sample thereby leading to unit-weight reduction. The inclusion of 1 % ASW in ternary blending gave the optimum performances of 28-day strength (53.8 MPa) and residual thermal (300 °C, 1 h) strength of 56 MPa that had a comparable value to OPC mortar (55 MPa) unexposed to the thermal treatment. ASW also caused thermal stability in SF-ASW blended mortar as addition of 0.5, 1.5 and 2 % ASW caused 33.8, 15.6 and 33.4 % loss in 28-day strengths, respectively, while the least was observed in 1 % ASW sample with the loss of 8.8 %. Finally, ASW enhanced weight reduction (at 300 °C for 1 h) as the unit weight reduced by 1.75, 4.89, 3.30 and 1.86 % in $C_{89.5}S_{10}A_{0.5}$, $C_{89}S_{10}A_1$, $C_{88.5}S_{10}A_{1.5}$ and $C_{88}S_{10}A_2$, respectively, in comparison with $C_{100}S_0A_0$. Mayenite and muscovite could be formed as products when ASW is used as supplementary materials in silica fume blended mortar production.

Acknowledgements: The authors would like to appreciate the remarks of the anonymous reviewer who has greatly improved the manuscript. The continuous support of University of Hafr Al Batin is appreciated.

Citation: Yusuf, M.O. Performance of aluminium shaving waste and silica fume blended mortar. Magazine of Civil Engineering. 2023. Article no. 12209. DOI: 10.34910/MCE.122.9

1. *Introduction*

Production of ordinary Portland cement that is used as a binder in mortar and concrete involves breaking down limestone with high amount of energy; this leads to proliferation of carbon dioxide, which causes global warming by damaging the ozone layer. The use of supplementary cementitious (SCMs) materials such as pozzolanic (fly ash, palm oil fuel ash, metakaolin and silica fume) and and other hydraulic materials such as ground granulated blast furnace slag (GGBFS) have been adopted by several researchers towards achieving cost efficiency and sustainable environment. Utilization of solid wastes has significantly reduced the volume of landfills in our environment. This solid waste could emanate from agricultural and industrial wastes. The industrial wastes such as iron-filling, cement kiln dust, and glass wastes have been recently reported to have contributed significantly to both fresh and hard properties of pastes, mortars, and concrete [1].

One of these industrial wastes is aluminium shaving waste (ASW), which is obtained through aluminium frames reshaping process by using lathe or turret mills. Aluminum (Al) is a non-ferrous metal reported to be light, conductive, and corrosion resistant. It can attract oxygen, and has viable potential for engineering applications since the end of the 19th century [2]. International Aluminium Institute (IAI) reported 5,273 thousand metric tons of aluminium production as of February 2023, while the main aluminium scraps came from construction and automobile industries [3]. The carbon dioxide equivalent (CO_2e) owing to recycling of aluminium waste amounted to 22 million metric tons with substantial part obtained from the thermal energy source. It becomes imperative for civil engineers to develop a technique towards ensuring some aluminium wastes are safely used in concrete and mortar production.

In this regard, Ofuyatan et al. [4] used varied aluminium shaving waste (ASW) in volume of 1–2 % and studied its contribution to the bond strength of laterized concrete beams with a view to minimize industrial waste. They reported that ASW decreased compressive strength but increased bond strength of reinforcement with concrete. Lower diameter bar of 16 mm performed better than a 20 mm diameter bar. Gulmez [5] also used 1-4 wt% of ASW as fine aggregate with a noticeable decrease in bulk density while flexural strength and transport characteristics increased due to more porosity of the matrix. Tang Van et al. [6] also used the combination of 30 % fly ash (FA) and ASW to achieve production of aerated concrete with lower density and modulus of elasticity, but higher porosity. The 28-day compressive strength of 52.7 MPa was achieved due to silica and alumina interaction [7]. Shabbar et al. [8] also reported inclusion of 0.5 to 1 wt% of aluminium (Al) powder decreased the elastic modulus and density of concrete. Moghaddam et al. [9] also asserted that Al nanoparticles can react with portlandite to produce aluminosilicate-hydrate gel while its synergy with glass waste could reduce the absorption of the samples.

Furthermore, Kuziak et al. [10] investigated alumina powder in two different types of cement (CEM 1 and III) and discovered that the rate of hydrogen gas effervescence in Al-blended binder depends on the amount of portlandite that accompanied hydration process as this could have a negative effect on strength [11]. Moreover, incorporation of 1 wt% alumina into slag blended cement (CEM III) could cause cracks due to the interconnected pore formations. In addition, an introduction of alumina into a lime-dominated binder could also have a negative impact on strength and density of the binder, especially in an aerated concrete. Similarly, Ramamurthy et al. [12–13] indicated that lime/cement ratio plays a significant role for strength and density. Autoclave curing of aerated mortar with high aluminium content (0.6–0.8 %) could lead to coalescence of discreet pores thereby causing minimization of pore total surface areas, which in turn may result in a decrease in the strength of the products [14].

Narayanan et al. [15] asserted that curing methods for aerated concrete play a significant role in the microstructural properties, chemical compositions, and density of aerated concrete with the incorporated aluminium powder. Sabapathy et al. [3] incorporated 0.5–2 vol% aluminium fiber in concrete samples with a view to enhance the compressive and split tensile strengths at a water/binder ratio of 0.6 (M20), 0.45 (M30) and 0.4 (M40). The optimum fiber content for compressive strength and split tensile strength were 0.5 % and 2 %, respectively. Elinwa and Mbadike [16] also asserted that large aluminium waste (AW) content within 5–40 % in concrete can be used as a retarder with 10 % being the optimum for compressive and flexural strengths.

Moreover, Azarhomayun et al. [17] used Al powder to reduce free shrinkage and crack width in concrete but also increase the restrained drying shrinkage by 18 %. The presence of excessive AW embedded in concrete could cause cracks due to pressure exerted by Al corrosion products rather than effervescence of hydrogen [18]. Faez et. al. [19] found that alumina nanoparticles (2.5 %) blended with silica fume (10 % SF) enhanced 90-day compressive and split tensile strengths by 86 % and 47 %, respectively. Besides, adding aluminium nanoparticles with SF could reduce water absorption of concrete samples.

Despite the plethora of the studies on the incorporation of aluminium waste in aerated an lightweight concrete, little is known of the impact of the synergy between Al shaving waste (ASW) and SF in terms of strength, nature of the product, microstructure, and thermal performance of their combination in ternary blended mortar that comprises SF, ASW and OPC. It is expected that utilization of these solid wastes will reduce the amount of solid waste in landfill on one hand while it will also have a significant impact on the mechanical and microstructural properties of the final product.

This study is aimed at providing necessary information with a view to bridging the gap needed for the deeper understanding of the synergy of ASW and SF in mortar production. It also makes alternative materials available for repair and rehabilitation of concrete structure while ensuring a safe environment by limiting ASW in dumpsites or landfills.

2. Methods and Materials

2.1. Materials

2.1.1 Aluminium shaving waste

Aluminium shaving waste (ASW) as shown in Fig. 1 is a by-product from an aluminium frame processing factory obtained through grinding and cutting by lathe machine (Fig. 1). The oxide composition mainly comprises alumina with traces of Fe_2O_3, CaO, MgO, SrO and TiO_2 as shown in Table 1. Fig. 2 shows the X-ray diffractogram of the ASW.

Figure 1. Aluminium shaving.

Table 1. Oxides composition of the raw materials.

Oxides	Silica fume	Cement	Aluminium shaving waste
SiO_2	95.85	20.17	-
Al_2O_3	0.26	5.58	99.10
Fe_2O_3	0.05	2.86	0.16
CaO	0.21	63.51	0.09
MgO	0.45	3.15	0.58
Na_2O	0.40	0.12	-
K_2O	1.22	0.57	-
SO_3	1.00	2.56	-
SrO	-	-	0.01
TiO_2	-	-	0.04
$SiO_2+Al_2O_3+Fe_2O_3$	96.16	28.61	99.26
Specific gravity (water)	2.25	3.15	1.18
LOI (%)	2.48	2.80	20.0

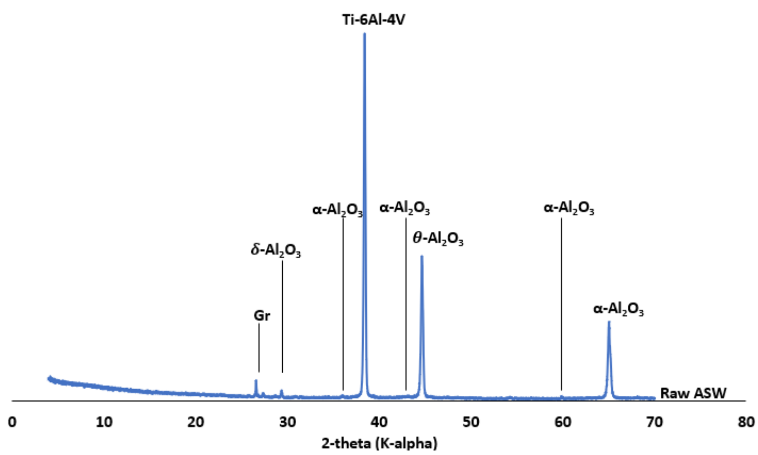

Figure 2. X-ray diffraction of aluminium shaving waste powder.

2.1.2 Cement

Type 1 ordinary Portland cement (OPC) was prepared in accordance with ASTM C 150 [20] with specific gravity (by water) of 3.15 and its oxides composition as shown in Table 1. The surface area and loss on ignition (LOI) are 329.5 m^2/kg and 2.8 %, respectively, while SiO_2, Al_2O_3, and Fe_2O_3 were summed up to 28.61 %. Fig. 3 shows the chemical compounds present in OPC as used in the study.

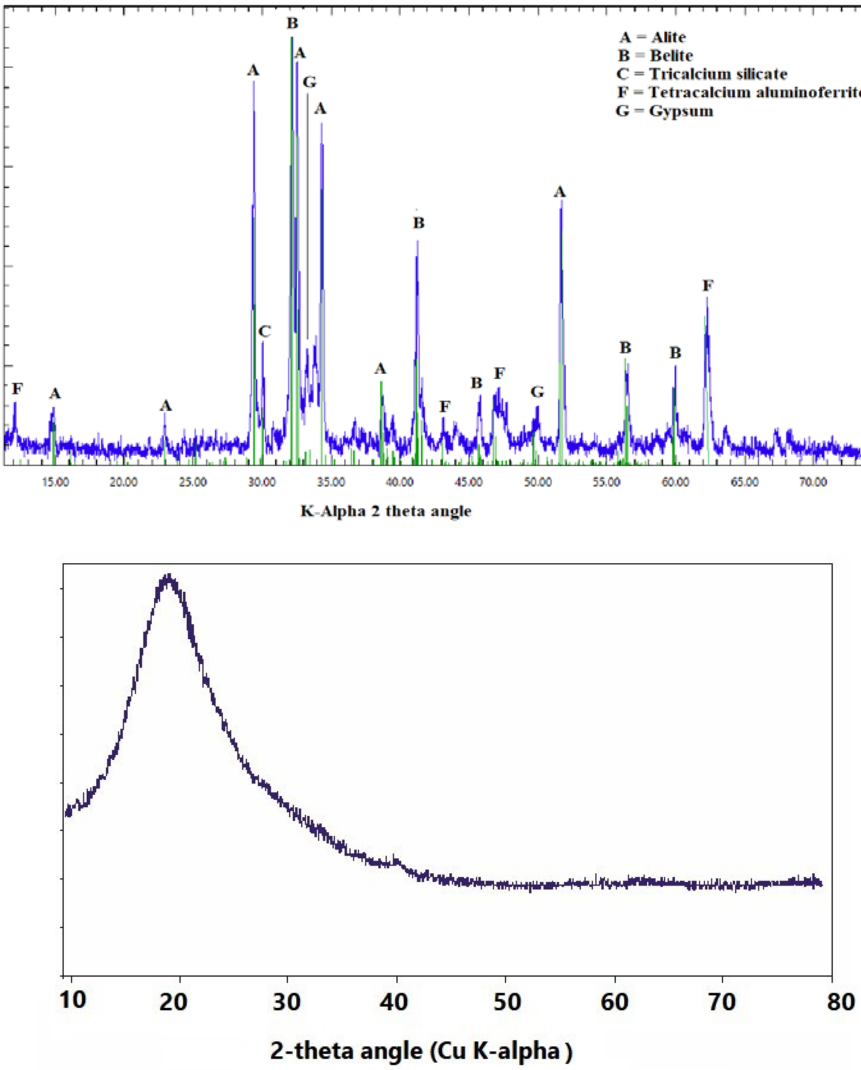

Figure 3. XRD diffractogram of ordinary Portland cement (topmost) and the silica fume (bottom).

2.1.3 Silica fume

Silica fume (SF) is commercially obtained with a relative density, LOI and surface area of 2.25, 2.48 %, and 22,800 m^2/kg, respectively with the sum of SiO_2, Al_2O_3, and Fe_2O_3 being 96.2 % as shown in Table 1, while Fig. 3 (bottom) shows its XRD diffractogram.

2.1.4. Fine aggregates

Natural sand in saturated surface dry (SSD) conditions whose moisture content and absorption were 3.43 and 6.14 %, respectively. The fine aggregate passes through a 2.36 mm sieve (No. 8) in accordance with ASTM C 157/C 157M – 08 [21]. The fineness modulus and relative density (water) were 2.8 and 2.71, respectively.

2.1.5 Superplasticizer

The superplasticizer (Glenium 51®) was used to enhance the consistency of the mixture. It is polycarboxylic ether and the proportion used was 1 % of the total binder (OPC, SF, and ASW).

2.2. Experimental tests

2.2.1 Workability

The consistency of the mortar sample was tested by using flow table in accordance with ASTM C 1437-20 [22].

2.2.2. Compressive strength

The compressive strength was determined by using 50 mm cubic samples, room-cured and subsequently exposed to thermal (300 °C for 1 h) treatment, in accordance with ASTM C 109 [23]. The testing was done by a universal testing machine at the ages 7, 14, and 28 days with the loading rate of 0.9 kN/s. The compressive strength was taken as the average of the three samples.

2.2.3 Unit weight of samples

The unit weight (KN/m^3) of samples was determined by measuring the mass (kg) of the samples at specific days, multiplying it by the acceleration due to gravity (10 m/s^2) and dividing it by the volume of the sample (125×10^{-6} m^3).

2.3 Characterization and morphology of the samples

XRD Bruker apparatus model d2-Phaser with CuKa radiation (40 kV, 40 mA) was used to determine the compound present in the product of ASW-SF blended mortar with a scan speed of 2.5°/min and continuous scanning with 2-theta angle range of 10–80°. The raw and post thermally treated ASW powder were tested to understand its phase transformation. Fourier transform infrared (FTIR) spectroscopy measurements of ASW-SF paste were conducted by using Perkin Elmer 880 spectrometer. The scanning electron microscopy and energy dispersive spectroscopy (SEM+EDS) instrument model 5800 LV manufactured by JEOL was used at an accelerating voltage of 20 kV for the microstructural characterizations and elemental compositions of the paste samples.

2.3. Sample preparation

2.4.1 Sample designation

The samples were composed of OPC (88-100%), ASW (0, 0.5, 1, 2 %) and 10% SF. The sample was designated as $C_{OPC\%}S_{SF\%}A_{Al\%}$, and thus a sample that contained 88 % OPC, 10 % SF and 2 % ASW, was designated as $C_{88}S_{10}A_2$, while the control was taken as the sample that contained OPC only, labelled as $C_{100}S_0A_0$.

2.4.2 Mix design

Mix design of the sample is given in Table 2 with the total binder of 350 kg/m^3 such that the water/binder ratio is 0.4. The binder/sand ratio was maintained at 2.5 while ASW/binder ratio varied from 0 to 2 % at the interval of 0.5.

2.4.3 Mixing procedure

Mixing was done in the following way. OPC, SF, and ASW were mixed dry for 3 mins. Half of the needed water together with the superplasticizer was poured into the mixer and then mixed for 3 mins to form a grout. Fine aggregates were then added and mixed for additional 2 mins before adding the other half of the water mixed with superplasticizer for 3 mins to achieve a homogenous mixture. Steel moulds with the dimensions of 50×50×50 mm were then oiled for easy demoulding, and to receive the fresh mortar. The cast specimens were left in the moulds for 24 h before being demoulded and then placed in the curing tank for a specified number of days (7, 14, 21 and 28 days) before being tested for compressive strength at a loading rate of 0.9 kN/s.

Table 2. Mixture proportion of aluminium shaving waste blended mortar.

Designation	Cement kg/m^3	Silica fume kg/m^3	Aluminium shaving waste kg/m^3	Sand kg/m^3	water kg/m^3	SP kg/m^3
$C_{100}S_0A_0$	350.00	0	0.00	875	140	3.5
$C_{90}S_{10}A_0$	315.00	35	0.00	875	140	3.5
$C_{89.5}S_{10}A_{0.5}$	313.25	35	1.75	875	140	3.5
$C_{89}S_{10}A_1$	311.50	35	3.50	875	140	3.5
$C_{88.5}S_{10}A_{1.5}$	309.75	35	5.25	875	140	3.5
$C_{88}S_{10}A_2$	308.00	35	7.00	875	140	3.5

3. Results and Discussions

3.1. Oxide compositions and compound in aluminium shaving waste

Table 1 shows the oxide composition of aluminium shaving waste, and it is mainly composed of 99 % alumina with traces of calcium, magnesium, iron, titanium, and strontium oxides. The ASW is very stable at thermal exposure to the tune of 1000 °C; the loss on ignition (LOI) was 20 % while the specific gravity (water) is 1.18. The presence of graphite in the X-ray diffraction (XRD) diffractogram as shown in Fig. 2 increased the value of LOI recorded while the observable main crystalline phases in ASW are graphite (COD#1200018), calcite (COD#1010962), titanium (COD# 9011600), and α-alumina (α-Al_2O_3) (COD#1533936).

The crystalline phases include graphite and Ti-6Al-4V (TC4) at the 2-theta angle of 27 °C and 39 °C, respectively. Upon subjecting it to 1000 °C as shown in Fig. 4, graphite and T4 phase disappeared thereby leading to the formation of more crystalline phases of κ-Al_2O_3 and α-Al_2O_3 and spinel (COD#9001364). This resulted in lowering of the amorphous content of ASW [24]. It has been reported that δ- and γ-alumina could transform into more crystalline phases of α- and θ-alumina with low surface area [24]. Comparing Figs. 2-4 makes it apparent that subjecting ASW to elevated temperatures transforms it into more crystalline phase.

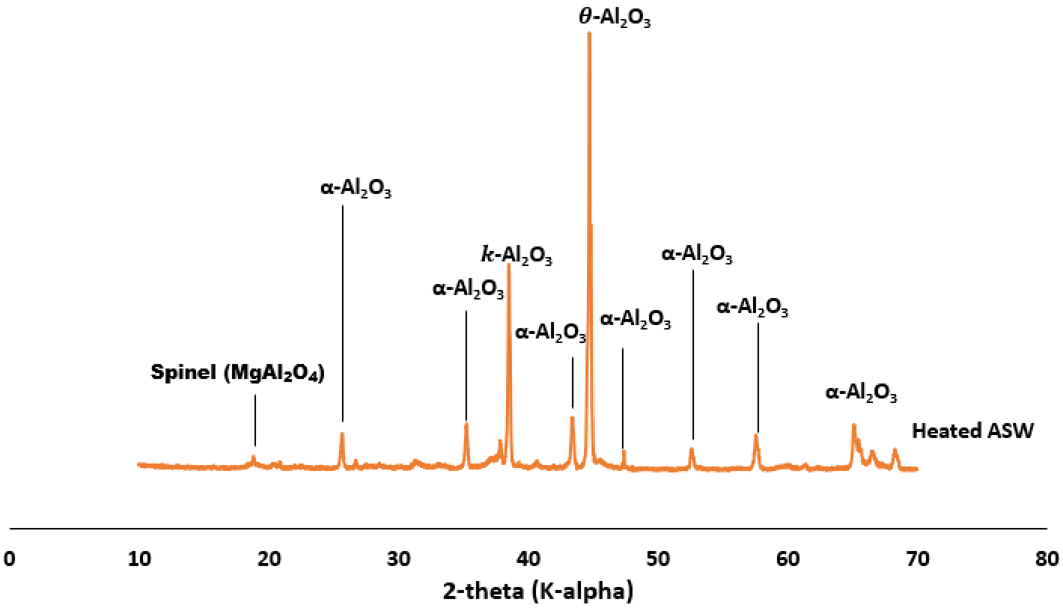

Figure 4. Phases of compounds formed upon subjecting ASW to 1000 °C.

3.2. Workability of the mortar

From Fig. 5, OPC mortar ($C_{100}S_0A_0$) had a flow diameter of 225 mm, which decreased by 20 % upon adding SF. The incorporation of 0.5 % ASW to OPC mortar ($C_{99.5}S_0A_{0.5}$) increased the consistency by 11.11 % whereas that of 10 % SF-ASW blended mortar reduced it by 6, 4.8 and 2.0 %, upon adding 0.5, 1, and 1.5 % ASW, respectively. As ASW became 2 %, no change was observed in the consistency of the mortar. Therefore, flowability of ASW-SF blended mortar was increasing with ASW/SF ratio. With reference to $C_{100}S_0A_0$, the consistency of 10 % SF–ASW blended mortar increased by 4.4 %, 5.8 %, 8.9 %, and 11.11 % as ASW was 0.5, 1, 1.5 and 2 %, respectively.

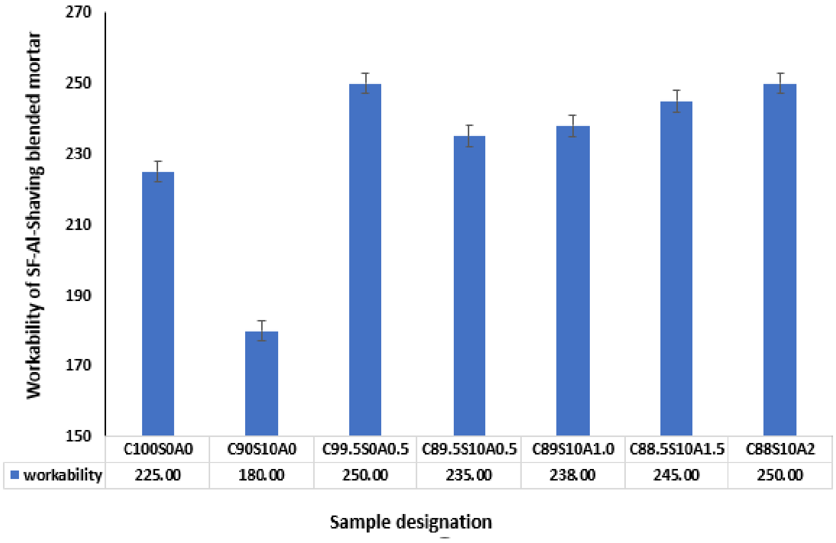

Figure 5. Consistency of SF-ASW blended mortar.

Furthermore, by comparing 10%SF–x%ASW blended mortar with SF-OPC mortar (no ASW), the workability increased by to 30.56, 32.22, 36.11 and 38.89 % with ASW content (x) of 0.5, 1, 1.5 and 2 %, respectively. This suggests that incorporation of ASW enhanced the flowability of SF-OPC mortar as shown in Fig. 5. The increase in the consistency of the mortar could be due to the reaction of portlandite with Al [25, 26] as shown in Eq. (1) thereby leading to the formation of entrapped hydrogen gas (Fig. 6) that formed a spherical ball within the matrix.

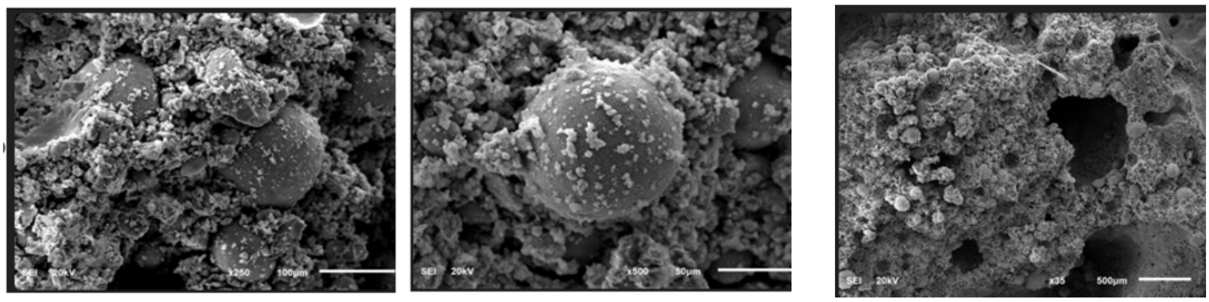

Figure 6. Formation of spherical bubble due to formation of hydrogen gas.

The presence of Al also enhances the formation of ettringite $Ca_6Al_2(SO_4)_3(OH)_{12}\cdot 26H_2O$ due to its interaction with portlandite and water to form calcium aluminate hydroxide and liberation of hydrogen gas as shown in Eq. (1):

$$2\mathrm{Al}+3\mathrm{Ca}\left(\mathrm{OH}\right)_2+6\mathrm{H_2O}\rightarrow 3\mathrm{CaO.Al_2O_3.6H_2O}+3\mathrm{H_2}. \tag{1}$$

The formation of hydrogen gas led to internal bubble formation that later caused pore formation due to the effervescence of the gas as shown in Fig. 6. This reaction becomes spontaneous due to formation and oxidation of $Al(OH)_3$ that accompanies dissolution of OPC that leads to the formation of hydroxyl ions.

The presence of hydroxyl ion oxidizes $Al(OH)_3$ to become $Al(OH)_4$ ion thereby making ASW undergo continuous corrosion as shown in Eq. (2) [27]. The corrosion of ASW and effervescence of hydrogen gas led to loss of fluidity of the mortar. This phenomenon depends on the concentration and quantity of ASW present in the mixture.

$$\mathrm{OH^-}+\mathrm{Al(OH)_3}\rightleftharpoons \mathrm{Al(OH)_4^-}. \tag{2}$$

At lower ASW incorporation of 0.5 % without the presence of SF, the workability increases due to attachment of Al to OH ions thereby causing disintegration of hydrogen bonding within the ettringite formation. The presence of ASW led to formation of Al-OH thereby decreasing OH^-/Al ratio, which induces ionic repulsion within ettringite. This explains why $C_{100}S_{10}A_{0.5}$ has better consistency (250 mm) compared to $C_{100}S_0A_0$ (225 mm) as shown in Fig. 5. Upon introducing SF into the mixture, silicic acid ($Si(OH)_4$) would be formed thereby reducing the pH of the mixture. The presence of SF-ASW reduces the viscosity of the mixture. This is further enhanced by the fineness of SF.

3.3. Unit weight of samples

Inclusion of the ASW and SF decreased the unit weight of the blended and OPC mortar due the specific gravity and escape of hydrogen from the pores within the matrix. With reference to $C_{100}S_0A_0$ (Fig. 7), the unit weight of OPC mortar increased from by 1.65 % within the 1 to 7 days, while it was 2.1 % in 10%SF-OPC mortar. The addition of 0.5, 1, and 1.5 % ASW made the increment to be 0.68 %, 3.93 %, and 4.33 %, respectively in 10%SF+ASW blended mortar. Upon increasing the ASW to 2 %, there was a decrease in unit weight by 5.42 %. Within the interval of 7-14 days, the increment became 0.24 % in $C_{100}S_{10}A_0$ but increased to 0.68 % in $C_{90}S_{10}A_0$. Inclusion of 0.5 % ASW led to an increase in the unit weight by 0.68 %, but reduced by 2.7 %, 2.8 %, and 5.9 %, upon adding 1, 1.5, and 2 % ASW, respectively. Within the interval of 14 to 28 days, the unit weight of OPC mortar and SF-blended mortar increased by 0.89 % and 0.34 %, respectively. The unit weight in 10%SF+ASW reduced by 0.08, 0.35, 1.06 and 0.64 % in $C_{89.5}S_{10}A_{0.5}$, $C_{89}S_{10}A_1$, $C_{88.5}S_{10}A_{1.5}$ and $C_{88}S_{10}A_2$, respectively.

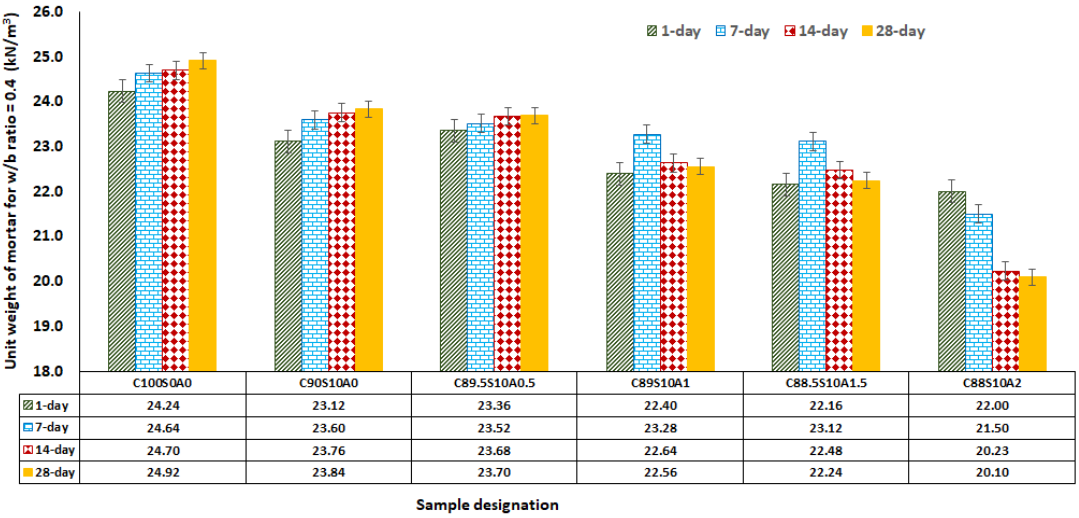

Figure 7. Change in unit weight of SF-ASW blended mortar with age.

Fig. 8 shows the OPC samples exposed to thermal (300 °C) treatment lost 13.0 % of unit weight, and upon incorporating 10%SF and ASW, the loss in unit weight reduced to 12.0 %, 4.2 %, 4.3 % in $C_{89.5}S_{10}A_{0.5}$, $C_{89}S_{10}A_1$, and $C_{88.5}S_{10}A_{1.5}$, respectively, while a 4.4 % increment in unit weight was recorded in $C_{88}S_{10}A_2$. The loss in unit weight was due to removal of water from the capillary of the matrix and the disappearance of the embedded hydrogen gas. By comparing the unit weight of OPC sample ($C_{100}S_0A_0$) subjected to 300 °C, inclusion of ASW in SF blended mortar increased post-thermal unit weight by 1.75, 4.89, 3.30 and 1.86 % in $C_{89.5}S_{10}A_{0.5}$, $C_{89}S_{10}A_1$, $C_{88.5}S_{10}A_{1.5}$ and $C_{88}S_{10}A_2$, respectively.

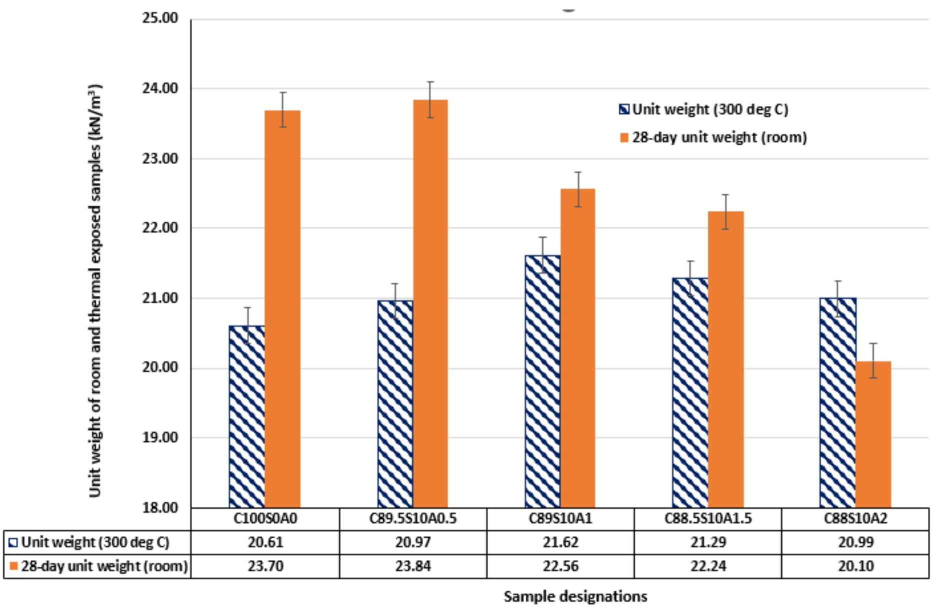

Figure 8. Unit weight of samples due to room curing and thermal treatment.

3.4. Compressive strength of ASW-SF blended mortar

As seen in Fig. 9, the presence of ASW without SF ($C_{99.5}S_0A_{0.5}$) reduced the 7, 14 and 28-day strengths by 23.3, 8.7 and 16.7 %, respectively, in comparison with OPC mortar ($C_{100}S_0A_0$). Upon adding only SF into OPC mortar ($C_{90}S_{10}A_0$), the 7 and 14-day strengths reduced by 14.2 and 14.6 %, respectively, while its 28-day strength increased by 7.1 % due to secondary hydration process of pozzolanic material in the matrix.

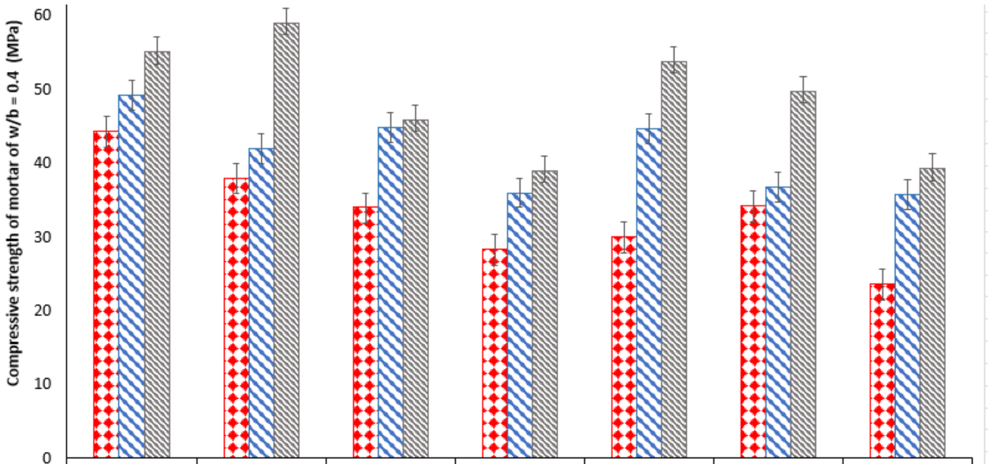

	C100S0A0	C90S10A0	C99.5S0A0.5	C89.5S10A0.5	C89S10A1.0	C88.5S10A1.5	C88S10A2.0
7-day	44.30	38	34.00	28.30	30.00	34.20	23.63
14-day	49.20	42	44.90	36.00	44.70	36.80	35.70
28-day	55.10	59	45.90	39.03	53.82	49.80	39.27

Sample designations

Figure 9. Compressive strength of ASW-SF blended mortar.

However, blending 0.5 % ASW with SF ($C_{89.5}S_{10}A_{0.5}$) further reduced the 7, 14 and 28-day strengths in comparison with $C_{100}S_0A_0$ by 36.1, 26.8 and 29.2%, respectively. In $C_{89}S_{10}A_1$, the reductions in strengths compared to $C_{100}S_0A_0$ were 32.3, 9.1 and 2.3 %, respectively. Increasing the ASW to 1.5 % and 2 % caused further reduction of 7, 14 and 28-day strengths to 22.8, 25.2 and 9.6% ($C_{88.5}S_{10}A_{1.5}$), and 46.7, 27.4 and 28.7 %, respectively ($C_{88}S_{10}A_2$) compared to $C_{100}S_0A_0$. Besides, the rate of strength gain in $C_{100}S_0A_0$ increased from 7 to 14 days and from 14 to 28 days by 11.1 and 12 %, respectively. For SF+OPC mortar, the rate from 7 to 14 days reduced by 4.8 % and 31.3 % in $C_{90}S_{10}A_0$ and $C_{88.5}S_{10}A_{1.5}$, respectively while the strength increased by 189.8, 146, 343 and 361.8% in $C_{99.5}S_0A_{0.5}$, $C_{89.5}S_{10}A_{0.5}$, $C_{88}S_{10}A_1$, and $C_{88}S_{10}A_2$, respectively. The rate of strength gain from 14 to 28 days increased by 237.53, 70.14, and 194.6 % in $C_{90}S_{10}A_0$, $C_{89}S_{10}A_1$ and $C_{88.5}S_{10}A_{1.5}$, and decreased by 81.43, 29.81 and 16.61 % in $C_{99.5}S_0A_{0.5}$, $C_{89.5}S_{10}A_{0.5}$ and $C_{88}S_{10}A_2$, respectively, in comparison with $C_{100}S_0A_0$.

This implies that ASW contributes to the strength development through their attachment with free silica to form aluminosilicate products. This aluminosilicate network contributes to the skeletal framework to induce strength gain as indicated in Fig. 9. Moreover, the portlandite that ought to react with SF to produce additional CSH was consumed by ASW (Eqs. (1), (3)) thereby leading to the evolution of hydrogen that caused the reduction in the unit weight of the samples as shown in Fig. 7.

$$CS + H \rightarrow CSH + CH. \tag{3}$$

The ASW-SF blended OPC mortar ($C_{89}S_{10}A_1$) performs better than SF blended mortar ($C_{90}S_{10}A_0$). The optimum quantity to foster performance in ASW-SF blended mortar is 1%, since the Sulphate/Al ratio plays a key role in the formation of aluminoferrite mono-sulphate (Afm), unlike low density Aft with pore filling characteristics, which can improve the compressive strength [28]. Afm has greater density due to increase in Sulfate/ASW ratio at lower substitution up to 0.5 %, that can cause weak microstructure. Lower sulfate/ASW ratio could also lead to lower compressive strength due to more porosity that accompanies the evolution of hydrogen gas within the matrix. This explains the reason why $C_{88.50}S_{10}A_{1.5}$ and $C_{88.50}S_{10}A_2$ have lower strengths in comparison with $C_{89}S_{10}A_1$. The presence of ASW reduces the dilution effect of SF during pozzolanic reaction in mortar production.

XRD in Fig. 10 shows the possible formation of mayenite ($Ca_{12}Al_{14}O_{33}$), ettringite and muscovite ($K_2(Al_2O_3)_3(SiO_2)_6H_2O$), which further justify the possibility of Eq. 1. The dual presence of ettringite and mayenite due to reaction of ASW with gypsum and other cement compounds could be responsible for the decrease in the compressive strength in comparison with $C_{100}S_0A_0$ and $C_{89}S_{10}A_0$. It also shows that the presence of ASW does not prevent the formation of calcium silicate hydrate (CSH) and portlandite ($Ca(OH)_2$) as clearly shown in Fig. 10, while the presence of C_4AF, alite (C_3S) and belite (C_2S) could be due to the presence of unreacted cement within the matrix. The removal of hydrogen gas led to more microstructural voids that induced carbonation thereby leading to the formation of calcium carbonate or calcite ($CaCO_3$).

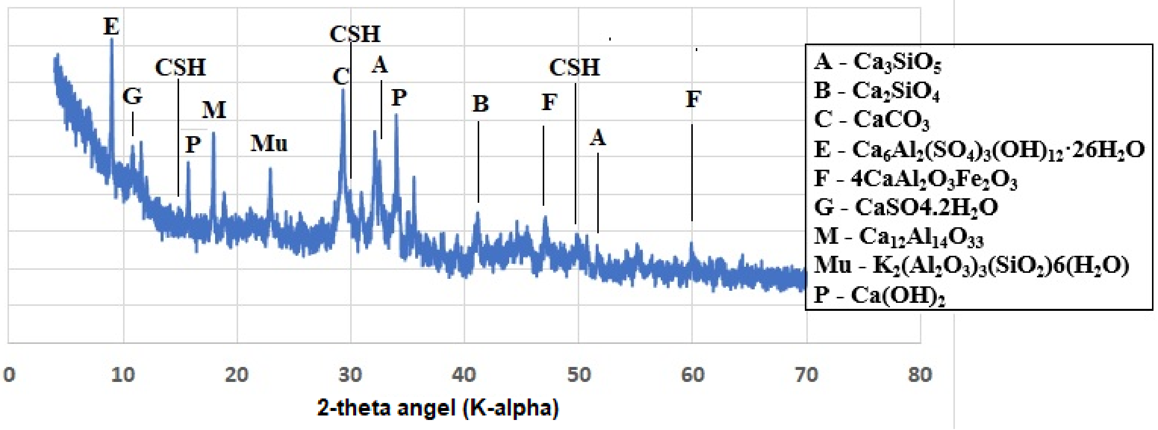

Figure 10. X-ray diffractogram of the SF-ASW ternary blended paste.

Fig. 11 shows the Fourier transform infrared (FTIR) spectroscopy and indicates asymmetric stretching of Al-O bond and Al_2O_3 vibration at 1119 cm^{-1} and 997 cm^{-1}, respectively, while wavenumber 874 cm^{-1} indicates C-O vibration from the carbonate source. Besides, C-O vibration due to carbonation (region B) is indicated in the wavenumber 2336 cm^{-1} [18, 29]. Similarly, region A and C point to OH and HOH vibration were due to the presence of portlandite. The presence of ASW does not appear to affect the C-O band at 1420 cm^{-1}, but in contrast, it has significant impact on Si-OH and HOH bending mode vibration in water at 1638 cm^{-1} due to interaction with tricalcium aluminate (C_3A) to form aluminosilicate bonds [30]. The calcium aluminate phase has been assigned by Tarte [26] to the wavenumber with 700–900 cm^{-1} for condensed aluminate $CaO.Al_2O_3$, $12CaO.7Al_2O_3$ and theta-Al_2O_3, which was further supported by Yusuf [29], and Fernendez-Carrasco et al. [25, 29].

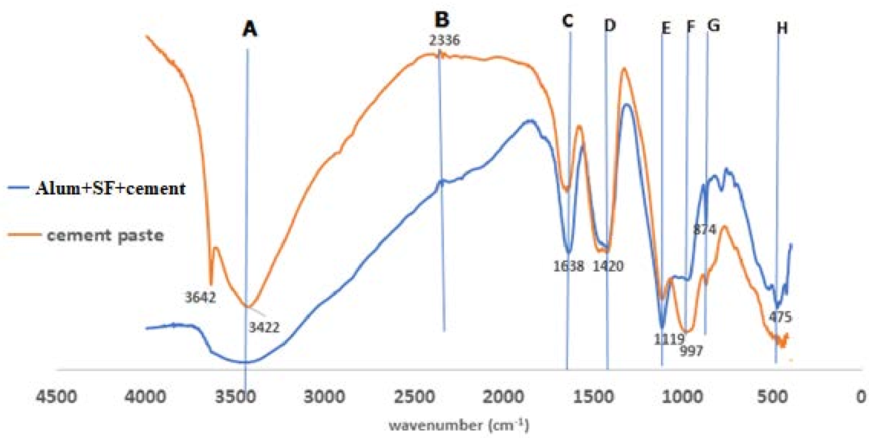

Figure 11. FTIR of ASW blended paste in comparison with OPC cement paste.

The isolated and condensed octahedral AlO_4 were identified at wavenumber 650–800 and 530–400 cm^{-1}, respectively [26]. Therefore, the peak at point G in Fig. 11 can be said to be due to the presence of calcium aluminate hydroxide (CAH). Besides, the OH/HOH vibration was noted at 3422 cm^{-1} while the absence of ASW in the control sample (hydrated cement) led to the presence of OH peaks at 3642 cm^{-1}, which was absent in ASW blended mortar.

3.5. Thermal residual strength of ASW-SF blended mortar

By comparing 28-day strength, addition of ASW into OPC mortar caused reduction in compressive strength at room temperature (Fig. 12). There is a decrease in the residual thermal strength in OPC due to microstructural disintegration as the thermal residual 28-day strength was 37 % less than that at room temperature. However, under thermal treatment (300 °C for 1 h), addition of 0.5, 1, 1.5 and 2 % ASW caused increase in strength by 18.5, 29.2, 2.4, 11 and 26.2 % in comparison with $C_{100}S_0A_0$ as noted in $C_{99.5}S_0A_{0.5}$, $C_{89.5}S_{10}A_{0.5}$, $C_{89}S_{10}A_1$, $C_{88.5}S_{10}A_{1.5}$, and $C_{88}S_{10}A_2$, respectively. Both SF and ASW have positive impacts on thermal treatment by incorporating 0.5, 1, 1.5 and 2 % ASW, through the achievement of positive strength gains of 39.8, 43.5, 61, 50.4 and 29.7 %, respectively.

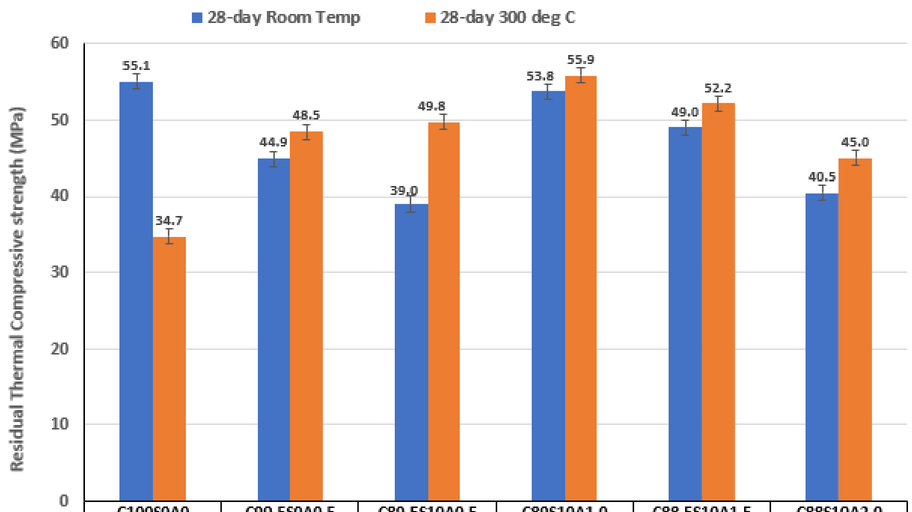

	C100S0A0	C99.5S0A0.5	C89.5S10A0.5	C89S10A1.0	C88.5S10A1.5	C88S10A2.0
28-day Room Temp	55.1	44.9	39.03	53.8	49.03	40.50
28-day 300 deg C	34.70	48.5	49.80	55.85	52.20	45.00

Figure 12. Compressive strength of alumina blended mortar.

Inclusion of ASW contributed significantly to the thermal residual strength as compressive strength by 8, 27.6, 3.8, 3.5 and 11.1 % in $C_{99.5}S_0A_{0.5}$, $C_{89.5}S_{10}A_{0.5}$, $C_{89}S_{10}A_1$, $C_{88.5}S_{10}A_{1.5}$, and $C_{88}S_{10}A_2$, respectively. There is no observable physical deterioration in any of the samples. Therefore, the optimum thermal performance was observed when the ASW inclusion is 0.5 % in the presence of SF ($C_{89.5}S_{10}A_{0.5}$) even though the maximum thermal strength was obtained with 1 % ASW. This indicates that the presence of ASW+SF improves thermal performance due to attachment of Si to Al in tetrahedral coordination to induce the formation of zeolite-like product (CASH) as observable in geopolymer synthesis [31–33].

3.6. Microstructure and elemental ratio of ASW-SF blended paste

Fig. 13 shows the contribution of ASW to the microstructural morphology and the elemental compositions of the product formed. The region 1 and 3 indicate that the general spectrum of ASW-Si blended paste was such that Ca/Si ratio was 1.83 and 2.9, respectively, while the region 4 at which Aft or ettringite was formed had the Ca/Si ratio of 3.34. At the region 2 where the bubbles formed, the Ca/Si ratio decreases to 0.76. The low Ca/Si ratio in this region causes a decrease in the compressive strength recorded when compared to SF-ASW based samples. Calcium to carbon (Ca/C) ratios are 1.25 and 1.68 at regions 1 and 3 while the region 4 (where Aft formed) had 1.40. The presence of graphite in ASW as noticed in the XRD in Fig. 2 was supported by the presence of carbon in the energy dispersion spectroscopy (EDS) (Fig.13). The presence of a bubble could make the matrix susceptible to carbonation thereby causing Ca/C to be 0.76 (region 2). The presence of Fe in region 1 pointed to the possibility of unreacted cement powder that contained tetracalcium aluminoferrite (F-C_4AF) as shown in the XRD in OPC raw powder (Fig. 2).

4. Conclusions

This paper investigates the impact of the synergy of silica fume (SF) and aluminium shaving waste (ASW) on the strength and thermal performance of ternary blended mortar comprising ordinary Portland cement, aluminium shaving waste powder and silica fume (OPC+ASW+SF). The following conclusions can be drawn:

1. Silica fume reduced the workability of mortar and concrete whereas the use of ASW enhanced the consistency of the binder by up to 32 % at the level of 0.5–2 % without compromising the strength significantly.

2. ASW enhanced the formation of calcium aluminate hydrate (CAH) together with calcium silicate hydrate (CSH). This is established by the presence of mayenite and muscovite among the peaks identified by X-ray diffractogram.

3. Thermal exposure of ASW-SF sample to 300 °C for 1 hr significantly reduced the unit weight of the samples by 12.03, 4.16 and 4.27 % for 0.5, 1 and 1.5 %, respectively while 2 % ASW led to an increase

in the unit weight of the sample by 4.4 %. It implies that 0.5 % ASW had the most significant effect on the density of the sample.

4. The strength gain in 10%SF-0.5%ASW and 0%SF-0.5%ASW blended mortar exposed to 300 °C for 1 hr were 8 % and 26 % when compared to those produced at room temperature. Exposing ordinary Portland cement (OPC) to similar condition led to 37 % decrease in strength compared to those prepared at room temperature.

5. The optimal 28-day strength performance of the mortar of 53.8 MPa was obtained in the sample produced with 10%SF, 1 % ASW and 89 % OPC. There was 3.9 % gain in strength when the samples were exposed to 300 °C for 1 hr.

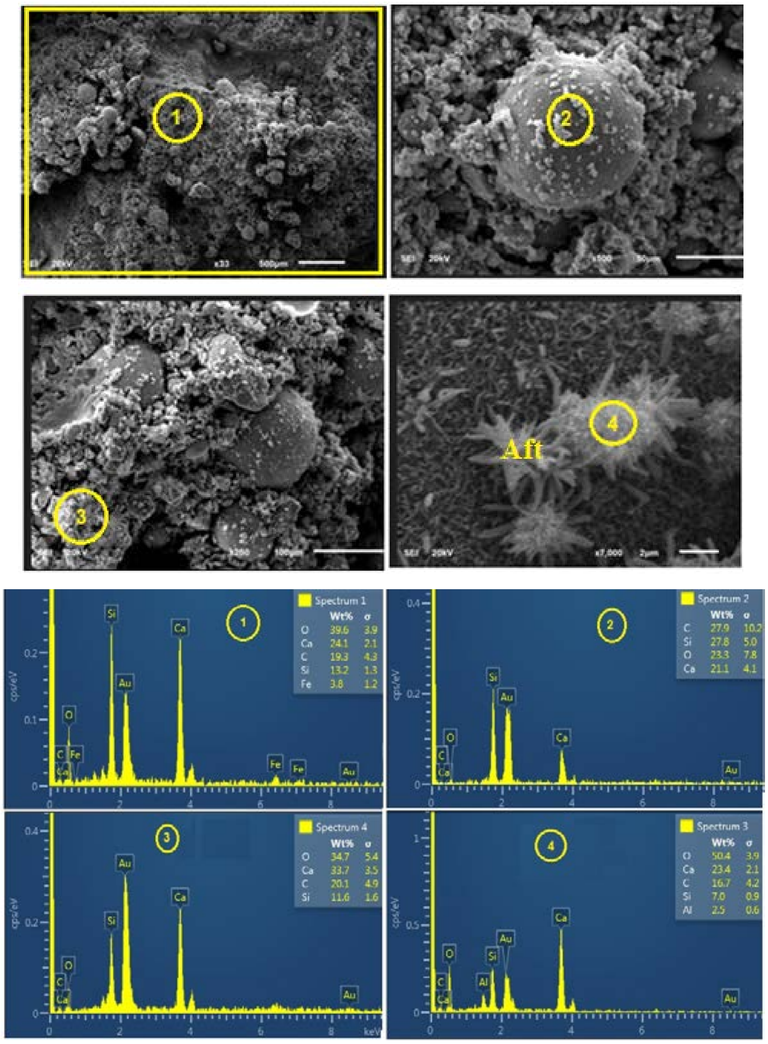

Figure 13. Morphology of SF-ASW blended mortar.

References

1. Gerbelova, H., Spek, M.V., Schakel, W. Feasibility assessment of CO_2 capture retrofitted to an existing cement plant: post-combustion vs. Oxy-fuel combustion technology. Energy Procedia. 2017. 114. Pp. 6141–6149. DOI: 10.1016/j.egypro.2017.03.1751
2. Ungureanu, C.A., Das, S.K., Jawahir, I.S. Life-cycle cost analysis: aluminum versus steel in passenger cars. Aluminum Alloys for Transportation, Packaging, Aerospace, and Other Applications. 2007. Pp. 11–24.
3. Sabapathy, Y.K., Sabarish, S., Nithish, C.N.A, Ramasamy, M., Krishna, G. Experimental study on strength properties of aluminium fibre reinforced concrete. Journal of King Saud University – Engineering Sciences. 2021. 33(1). Pp. 23–29. DOI: 10.1016/j.jksues.2019.12.004
4. Ofuyatan, O. et al., Effect of waste aluminium shavings on the bond characteristics of laterized concrete. Advances in Materials Research. 2019. 8(1). Pp. 25–36. DOI: 10.12989/amr.2019.8.1.025
5. Gulmez, N. Reuse of industrial metal wastes as partial replacement of aggregates in mortar production, DÜMF Mühendislik Dergisi. 2021. Pp. 875–880. DOI: 10.24012/dumf.1051502
6. Tang, V.L., Vu, K.D., Ngo, X.H., Vu, D.T., Bulgakov, B., Bazhenova, S. Effect of Aluminium Powder on Light-weight Aerated Concrete Properties. E3S Web of Conferences. 2019. 97. DOI: 10.1051/e3sconf/20199702005

7. Kinoshita, H. et al. Corrosion of aluminium metal in OPC- and CAC-based cement matrices. Cement and Concrete Research. 2013. 50. Pp. 11–18. DOI: 10.1016/j.cemconres.2013.03.016
8. Shabbar, R., Nedwell, P., Wu, Z. Mechanical properties of lightweight aerated concrete with different aluminium powder content, in MATEC Web of Conferences. 2017. 120. DOI: 10.1051/matecconf/201712002010
9. Moghaddam, H.H., Lotfollahi-Yaghin, M.A., Maleki, A. Durability and mechanical properties of self-compacting concretes with combined use of aluminium oxide nanoparticles and glass fiber, International Journal of Engineering, Transactions A: Basics. 2021. 34(1). Pp. 26–38. DOI: 10.5829/IJE.2021.34.01A.04
10. Kuziak, J., Zalegowski, K. Jackiewicz-Rek, W., Stanisławek, E. Influence of the type of cement on the action of the admixture containing aluminum powder. Materials. 2021. 14(11). DOI: 10.3390/ma14112927
11. Shabbar, R., Nedwell, P., Al-Taee, M., Wu, Z. Effect of Different Aluminium Powder Content on the Behaviour of Aerated Concrete: Experimental and Finite Element Validation, International Journal of Materials, Mechanics and Manufacturing. 2018. 6(2). Pp. 155–158. DOI: 10.18178/ijmmm.2018.6.2.367
12. Ramamurthy, K., Narayanan, K. Factors influencing the density and compressive strength of aerated concrete. Magazine of Concrete Research. 2000. 52(3). Pp. 163–168. DOI: 10.1680/macr.2000.52.3.163
13. Muthu Kumar, E., Ramamurthy, K. Effect of fineness and dosage of aluminium powder on the properties of moist-cured aerated concrete. Constr Build Mater. 2015. 95. Pp. 486–496. DOI: 10.1016/j.conbuildmat.2015.07.122
14. Guglielmi, P.O., Silva, W.R.L., Repette, W.L., Hotza, D. Porosity and mechanical strength of an autoclaved clayey cellular concrete. Advances in Civil Engineering. 2010. 7. DOI: 10.1155/2010/194102
15. Narayanan, N., Ramamurthy, K. Structure and properties of aerated concrete: A review. Cement and Concrete Composites. 2000. 22(5). Pp. 321–329. DOI: 10.1016/S0958-9465(00)00016-0
16. Elinwa, A.U., Mbadike, E. The use of Aluminum waste for concrete production. Journal of Asian Architecture and Building Engineering. 2011. 10(1). Pp. 217–220. DOI: 10.3130/jaabe.10.217
17. Azarhomayun, F., Haji, M., Kioumarsi, M., Shekarchi, M. Effect of calcium stearate and aluminum powder on free and restrained drying shrinkage, crack characteristic and mechanical properties of concrete. Cement and Concrete Composites. 2022. 125. 104276. DOI: 10.1016/j.cemconcomp.2021.104276
18. Herting, G., Odnevall, I. Corrosion of Aluminium and Zinc in Concrete at Simulated Conditions of the Repository of Low Active Waste in Sweden. Corrosion and Materials Degradation. 2021. 2(2). Pp. 150–163. DOI: 10.3390/cmd2020009
19. Faez, A., Sayari, A., Manie, S. Mechanical and Rheological Properties of Self-Compacting Concrete Containing Al_2O_3 Nanoparticles and Silica Fume, Iranian Journal of Science and Technology - Transactions of Civil Engineering. 2015. 44. Pp. 217–227. DOI: 10.1007/s40996-019-00339-y
20. ASTM C150-07, Standard Specification for Portland Cement. ASTM International, 2007.
21. ASTM C157, Standard Test Method for Length Change of Hardened Hydraulic-Cement Mortar and Concrete, 2008.
22. ASTM C1437-20, Standard Test Method for Flow of Hydraulic Cement Mortar. ASTM International, 2020.
23. ASTM C109/C109M-20, Standard Test Method for Compressive Strength of Hydraulic Cement Mortars (Using 2-in. or [50-mm] Cube Specimens). ASTM International, 2020.
24. Morterra, C., Magnacca, G. A case study: surface chemistry and surface structure of catalytic aluminas, as studied by vibrational spectroscopy of adsorbed species. Catal Today. 1996. 27(3–4). Pp. 497–532. DOI: 10.1016/0920-5861(95)00163-8
25. Fernández-Carrasco, L. Torrens-Martín, D. Morales, L.M, Martínez-Ramírez, S. Infrared Spectroscopy in the Analysis of Building and Construction Materials. Infrared Spectroscopy – Materials Science, Engineering and Technology. Prof. Theophanides Theophile, Ed. 5100 Rijeka Croatia: Tech, 2012. Pp. 369–381. DOI: 10.5772/36186
26. Tarte, P. Infra-red spectra of inorganic aluminates and characteristic vibrational frequencies of AlO_4 tetrahedra and AlO_6 octahedra. Spectrochim Acta A. 1967. 23(7). Pp. 2127–2143. DOI: 10.1016/0584-8539(67)80100-4
27. Studart, A.R., Innocentini, M.D.M., Oliveira, I.R., Pandolfelli, V.C. Reaction of aluminum powder with water in cement-containing refractory castables. Journal of the European Ceramic Society. 2005. 25(13). Pp. 3135–3143. DOI: 10.1016/j.jeurceramsoc.2004.07.004.
28. Hartman, M.R., Berliner, R. Investigation of the structure of ettringite by time-of-flight neutron powder diffraction techniques. Cement and Concrete Research. 2006. 36(2). Pp. 364–370. DOI: 10.1016/j.cemconres.2005.08.004
29. Yusuf, M.O. Bond Characterization in Cementitious Material Binders Using Fourier-Transform Infrared Spectroscopy. Applied Sciences. 2023. 13(5). Pp. 3353. DOI: 10.3390/app13053353
30. Gatta, G.D., Hålenius, U., Bosi, F., Cañadillas-Delgado, L., Fernandez-Diaz, M.T. Minerals in cement chemistry: A single-crystal neutron diffraction study of ettringite, $Ca_6Al_2(SO_4)_3(OH)_{12}{\cdot}27H_2O$. American Mineralogist. 2019. 104(1). Pp. 73–78. DOI: 10.2138/am-2019-6783
31. Yusuf, M.O., Megat Johari, M.A., Ahmad, Z.A., Maslehuddin, M. Effects of addition of $Al(OH)_3$ on the strength of alkaline activated ground blast furnace slag-ultrafine palm oil fuel ash (AAGU) based binder. Construction and Building Materials. 2014. 50. Pp. 361–367. DOI: 10.1016/j.conbuildmat.2013.09.054
32. Fernández-Jiménez A and Palomo, A. Composition and microstructure of alkali activated fly ash binder: Effect of the activator. Cement and Concrete Research. 2005. 35(10). Pp. 1984–1992. DOI: 10.1016/j.cemconres.2005.03.003
33. Alonso, S., Palomo, A. Alkaline activation of metakaolin and calcium hydroxide mixtures: influence of temperature, activator concentration and solids ratio. Materials Letters. 2001. 47(1-2). Pp. 55–62. DOI: 10.1016/S0167-577X(00)00212-3

Information about authors:

***Moruf O. Yusuf,** PhD*
ORCID: https://orcid.org/0000-0002-8134-5435
E-mail: moruf@uhb.edu.sa
E-mail: moruff@gmail.com

Received 03.05.2023. Approved after reviewing 08.08.2023. Accepted .14.08.2023

Magazine of Civil Engineering. 2023. 122(6). Article No. 12210

Magazine of Civil Engineering

ISSN 2712-8172

journal homepage: http://engstroy.spbstu.ru/

Research article

UDC 624.94.014.2:624.044.3

DOI: 10.34910/MCE.122.10

Accounting of plastic deformations in the calculation of frames using the displacement method

A.N. Potapov [1] ✉, ***S.V. Shturmin*** [2]

[1] *South-Ural State University, Chelyabinsk, Russian Federation*

[2] *Daegu University, Gyeongsan, Republic of Korea*

✉ *potapov.alni@gmail.com*

Keywords: stiffness, deformation, elastoplasticity, nonlinear analysis, plastic zone, limiting load

Abstract. Method for calculating statically indeterminate frames taking into account plastic deformations, which is based on the use of a schematized diagram of material with hardening is proposed. Two types of standard beams with supports are used during the implementation of the displacement method (DM) like the elastic solution of the problem: “fixed” - “pinned” and “fixed” – “fixed”, but unlike the elastic solution, standard beams contain special zones that besides elastic part include elasto-plastic zone (EPZ), plastic zone (PZ) and reinforcement zone (RZ). Therefore, as the stresses in these zones did not exceed the yield stress in the nonlinear frame calculation, we took measures to transform the PZs into equal strength plastic zones (ESPZ). The calculations were made for both types of beams for all unit and load impacts. The frame calculation consists of three stages (elastic, elasto-plastic and plastic). At the elastic and elasto-plastic stages, yield moment and plastic moment diagrams and the corresponding loads are determined. For a practical use of the DM in a nonlinear frame calculation, two simplifying prerequisites are introduced, with the help of which a stress-strain state is modeled in two zones: EPZ and PZ. According to the prerequisites, deformation of fibers occurs without hardening in EPZ and with hardening in PZ. The plastic stage of the calculation is performed at a given length of the PZ using the method of sequential loadings. At each iteration with small loading steps, incremental equations for DM are written, which establish relations between incremental moments and the incremental load, which allows us to build a resulting moment diagram. This diagram represents a sum of the moment diagram obtained at the elastic and elasto-plastic stages and the diagrams of incremental moments at all previous loading steps of plastic stage. According to the resulting diagram, the length of the PZ can be calculated, together with the limiting load. The calculation is considered complete if the length of the PZ does not exceed the specified value within the margin of error. Proposed algorithm is illustrated with an example of static calculation of 2-storey steel frame which perceives horizontal load actions that model a seismic impact.

Citation: Potapov, A.N., Shturmin, S.V. Accounting of plastic deformations in the calculation of frames using the displacement method. Magazine of Civil Engineering. 2023. Article no. 12210. DOI: 10.34910/MCE.122.10

1. Introduction

Elastic-plastic deformations are generally accounted within the framework of the limiting equilibrium theory, which is based on the representation of an ideal elastic-plastic behavior of the material. The theory was developed by Soviet scientist A.A. Gvozdev, who in 1938 formulated three basic limiting equilibrium theorems (static, kinematic and duality theorems) [1]. The creation of this theory allowed to developed effective methods for calculating and designing many structures, especially reinforced concrete structures.

According to Prandtl diagram, the stresses of the construction material in the most loaded element cannot exceed the limit of yielding, and if the load is increased, the internal forces will be redistributed from more loaded elements to less loaded ones where the plastic state has not been reached yet. It is assumed that in a bended element that has reached the limiting equilibrium, the cross section is completely in the plastic state (a plastic hinge occurs), and the adjacent sections are in the elastic-plastic state, where the elastic core is retained.

In scientific literature, the concept of PZs is used mainly in seismic construction. For the first time, this concept was introduced by T. Paulay and I.N. Bull [2] in the calculation of reinforced concrete earthquake-resistant frames. Experts are long familiar with the fact that plastic deformations have the ability to absorb seismic energy, transforming it into thermal energy and then dissipating it into the environment. The article [3] proposes a method for evaluating the plastic design characteristics of beams and connections which may affect a seismic response of frame structures. The ability of loaded structural elements to absorb and dissipate energy generally ensures a decrease in the seismic impact on the frame. Thus, the structure, apart from its main designation, also works as an energy absorber. However, the operation of the structure beyond the limit of elasticity often leads to material degradation and destruction in these zones [4]. To overcome such weaknesses of concrete buildings as brittle fracture and lack of plasticity of the material, developments are underway to create new materials. In [5], the use of the reinforced fiber cement composite “HPFRCC” with increased of material ductility and high ability to absorb energy was shown. Experimental results showed that the use of HPFRCC layers in reinforced concrete beams allows to increase the ultimate load, the characteristics of the plastic hinge and the ability to redistribute the moment of these beams compared to the reference beam.

Developments related to the use of PZs aroused considerable interest among experts; they were consolidated in regulatory documents (codes) of the United States and other countries [6–8]. There appeared many papers covering a wide range of issues related to PZ parameters, such as the length of a zone, its location in the structure, the number of PZs, etc. Most of these studies deal with design features of PZs in reinforced concrete (RC) [9–17] and metal [18–22] structures. The problem of accounting for PZs is basically studied as applied to cyclic loadings of structures associated with seismic effects [9–11], [15–17], [19–22].

The articles [9–17] deal with the design features of PZs in reinforced concrete (RC) structures. In [9], a numerical analysis of the behavior of plastic hinges was carried out for bending structural elements, using the DIANA computational software. With the calibrated FEM model, the extent of the rebar yielding zone, concrete crush zone, curvature localization zone and the real plastic hinge length are studied.

In publications [10–15] discuss issues of studying the plastic hinge length of reinforced concrete columns. In [10], studies were carried out in the nonlinear version of the SAP2000 8 program for 4- and 7-story flat reinforced concrete (RC) frames, where the properties of plastic hinges are set by default according to ATC-40 [6]. PZs were determined at both ends of the beams and columns. It was shown by the example of a numerical experiment that the length of the PZ considerably influences relative horizontal displacements of the frame top. It was noted that this value differed by 30% when the plastic hinge length was modeled by different formulas: for the length $l_p = 0.5h$, where h is the height of the cross section of the element set by default [6], and for lengths l_p recommended in the works of R. Park, T. Paulay, M.J.N. Priestley et al. In [11] the plastic hinge behavior was studied for cyclic and monotonic loading using 3D FEM. Lengths of the plastic hinge zones include reinforcement yielding zone, curvature localization zone, concrete crushing zone and equivalent plastic hinge of RC column. It has been shown that for cyclically loaded columns this length is larger than that of monotonically loaded ones. Influence of the various parameters on this length was studied. It was noted that parameters such as the aspect ratio of the column and the hardening modulus of reinforcement loading and loading scheme defined by the number of cycles have a significant impact on it. Based on the numerical results under cyclic and monotonic loadings, a simple empirical model for the equivalent length of PZ under cyclic loading is proposed. This model takes into account the change in the length of PZ as far as the number of load cycles changes. However, dependence between the PZ length and the amplitude of the cyclic load has not been investigated. In study [12] considers similar problems as in [11], but taking into account the use of fiber reinforced polymer (FRP). Parametric studies of the plastic hinge length were first carried out for the calibrated FEM model, and then an improved model for FRP in RC columns was proposed. In [13] discusses the problem of assigning the PZ length in a RC column under the cyclic action of a lateral force and axial load. Behavior of plastic hinge under lateral and axial loading was studied. The influence of column size, physical and mechanical properties of reinforcement and concrete, the number of longitudinal bars, its diameters and other parameters on the length of PZ were taken into account. It notes the role of the principal reinforcement in a deformed member with particular emphasis on the part of the reinforcement that is strained beyond the yield stress in the hardening field. The article [14] proposes an expressions which allow to predict the equivalent plastic hinge length according to physical properties of HPFRCC material. On the basis of the probabilistic approach, [15] proposes a method for determining the length of the PZ in a RC column. A plastic hinge mechanism was constructed, in which a probabilistic model of the plastic zone length takes into account unknown parameters of the model using experimental data.

The article [16] studies the elastic-plastic response of the cylindrical composite sandwich panel under the action of lateral pulse pressure loading. Nonlinear differential equations of motion are solved benefiting from DQ–Newmark numerical method. It studies the development of elastic-plastic deformations in the facesheets of the core layers of the sandwich panel with different exposure modes. In particular, it is shown that plastic zones are first formed along the sides of the sandwich panel, and with the passage of time these zones progress towards the center of the panel.

The article [17] discusses a method for calculating reinforcement in earthquake-resistant RC buildings and structures which is based on theoretical basis of concept of nonlinear static analysis. The need for a justification of consistency of hinge zones design characteristics and its design parameters adopted at a conceptual design stage is explained. It is explained that length of an RC member end intended for arranging strengthened web reinforcement and a plasticity length of hinge zone may in fact have different values for the same element.

The articles [18–22] deal with the features of designing PZs in metal structures. In [18] developed a two-node super-element with generalized elasto-plastic hinges for static and cyclic analysis of frame structures. As opposed to the distributed plasticity analysis, the super-element uses a model with two generalized (concentrated) plastic hinges located at the ends of the elastic beam element. These hinges are modeled by a set of axial and rotational elastic-plastic springs and are used to reproduce plastic properties in the axial and angular direction of the element. This ensures elongation or shortening of the plastic hinge along the axial rod axis, as well as changes in the element rotation angle. Thus, the conditions for the interaction between the axial forces and bending moments in the plastic hinge zone are created. In the nonlinear calculation of beams and frames the dependence “force-displacement” was studied. The bearing load is estimated using plasticity models witch are related to the concept of a generalized plastic hinge. The same ideas were used in [19] only in the analysis of impact loadings. A model for nonlinear dynamic analysis of steel frame structures subjected to impact is presented. The generalized plasto-elastic hinges at the both ends of the rigid element, behavior of which is managed by the yield surfaces of super-elliptic shape was developed. An examples of impact calculation of the frames was considered. The graphs of cross-section displacement was shown. Articles [16, 17] does not include an analysis of relations between the amplitude values of loading and the length of PZ.

To analyze frame tubular structures, a number of plastic mechanisms have been developed that allow us to use of the same generic cyclic plasticity format [20]. In accordance with this format, each plastic mechanism is determined by an energy function, a yield surface, and a plastic flow potential. This allows us to create a set of functions regulating the elastic and plastic characteristics of the plastic mechanism’s cyclic model.

When analyzing steel frames fabricated according to the “strong columns - weak beams” design concept, after an earthquake, as noted in [21], major yielding zones and, as a result, fractures in the steel beam end are observed. In this regard, the authors of this article proposed a composite beam-to-column connection, including a friction damper. The composite beam consists of a steel base and an ultrahigh-performance concrete (UHPC) layer located in the upper part of the ultrahigh-strength concrete (UHPC). The designated plastic hinge length is limited by the level regulated by design features of the connection (l_p = 120, 240 mm). The force producing the yielding in UHPC layer was define in five experimental models at the moment of friction damper slip. Authors of [22] continued experimental and analytical studies of the seismic characteristics of the proposed device, in particular, they noted that the device was resistant to damage when the plastic zone length at the beam ends was l_p = 120 mm. For the noted length of PZ recommended thickness is 100 mm for UHPC layer and 20 mm for the steel layer.

It should be noted that the concept of PZ is considered as a zone of equal resistance or a zone of equal bearing capacity, since its construction is based on the limiting equilibrium theory. Therefore, the stresses inside these zones should not exceed the yield stress σ_y.

This article proposes a new approach to the calculation of statically indeterminate frames using the displacement method, based on a physically nonlinear material deformation according to a hardening diagram (Fig. 1). It is worth acknowledging that an initial attempt of this approach was undertaken in [23]. However, the method employed a less precise mathematical model. Consequently, an accurate evaluation of its performance is necessary once all the assumptions applied to the current model are implemented. According to the bilinear diagram with hardening, when a limiting state appears in any section of the structure, a further load increase will lead to an increase in internal forces and stresses exceeding the yield stress σ_y. As a result, a plastic zone (PZ) of some length l_p will appear. A fragment of an earthquake-resistant frame which includes PZ in edges of crossbar with length $2l$ is shown on Fig. 2. Red dotted line corresponds the level of stress σ_y and plastic moment $M_0 = W_0\sigma_y$, where W_0 is plastic section modulus. Since building codes do not allow the presence of plastic deformation in the joints of structures, PZ is designed at a distance ul from the column in the reinforcement zone (RZ), where load-bearing capacity of crossbar is provided on account of its increased stiffness. It should be noted that this is not the only way to relocate the plastic zone out of joints [24]. An elasto-plastic zone (EPZ) with length *d* and elastic moment $M_e = W_x\sigma_y$ (W_x is elastic section modulus) is located between PZ and elastic zone.

Since the stresses within the length l_p must not exceed the yield stress and correspond to the equal strength zone, measures should be taken to increase the element stiffness in the section with the stresses $\sigma_{max} > \sigma_y$. To this end, the element stiffness should vary according to the variable law and be consistent with the nature of the bending moment.

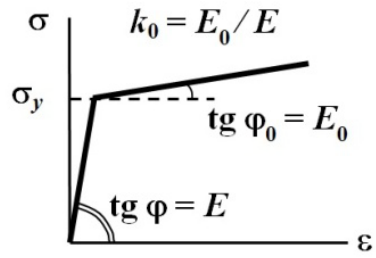

Figure 1. Diagram of the linearly hardening material deformation.

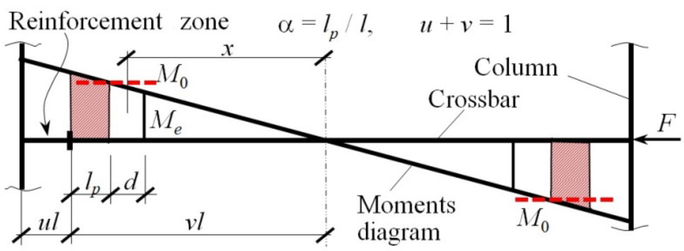

Figure 2. PZ with length l_p in a crossbar of a seismic-resistant frame.

2. Methods

To account for PZs in a statically indeterminate frame based on a bi-diagonal diagram, the displacement method (DM) is used as a calculation algorithm. The solution of the problem of transforming the area with nonlinear deformations into an equal strength plastic zone (ESPZ) should be integrated into the calculation algorithm of the method and performed in parallel with the nonlinear process of determining the limiting load F_0 for a given length of the PZ.

In case of a nonlinear calculation of frames by the DM, as well as in the classical version of this method, standard elements are used - beams with two types of supports: “fixed” - “pinned” and “fixed” – “fixed”, which should be designed for different types of unit and load impacts. However, unlike the classical version, the calculations of both types of beams should be performed taking into account the presence of ESPZs. These zones should contain the parameters determining their relative length $\alpha = l_p/l$, (l is beam length), location in the beam span, the law of variation of the area moment of inertia of the section within the length of the PZ and the physical and mechanical properties of the material. As a result, the calculated characteristics of standard beams will have the same coefficients as in the classical approach, but unlike them, they will contain additional dimensionless functions $f_j(\alpha)$, characterizing the nonlinear operation of the standard element.

In order to make non-linear calculation more accessible for the design engineer, two new premises are introduced that complement the well-known hypotheses of DM related to sequence of evolution of stress-strain state in EPZ and PZ.

First prerequisite: the deformation of the fibers of EPZ occurs by theory of idealized elasto-plastic operation of material (i.e. without hardening) with a variable modulus of elasticity which complying with the quadratic law.

Second prerequisite: the deformation of the fibers of PZ with length l_p occurs by bilinear diagram with constant hardening modulus E_0.

According to theory of idealized elasto-plastic body, a changing of size of elastic layer within EPZ length d complying with the quadratic law [25] $y = f(x_1) = \frac{h}{2}\sqrt{\frac{x_1}{d}}$ (Fig. 3). This allows assuming that the value of elasticity modulus in EPZ is proportional to the ratio of height of the elastic core to cross-sectional height.

$$E_x = E\sqrt{\frac{x_1}{d}}(x_1 \in [0; d]). \tag{1}$$

Stress in PZ: $\sigma \geq \sigma_y$, therefore all fibers deformed with constant hardening modulus E_0.

In the study [23], the segment addressing the non-linear deformation of the beam is also divided into two distinct sections. Moreover, there are no difference for the PZ segment compared to the current methodology. However, concerning the EPZ (referred to as the intermediate section in [23]), the elastic modulus is established using a constant value denoted as kE, which depends on the stiffness coefficient k. The coefficient k assumes values within the range $k \in [1, k_0]$. Since the coefficient k is unknown, estimating the stress-strain state within the EPZ becomes challenging. Additionally, determining the critical loads corresponding to the PZ since it is required to build a series of curves for different values of k. The uncertainty associated with the k coefficient serves as motivation for revising this mathematical model. In this article, this significant drawback of the previous model is overcome by introducing a quadratic dependence (1) for the quantity E.

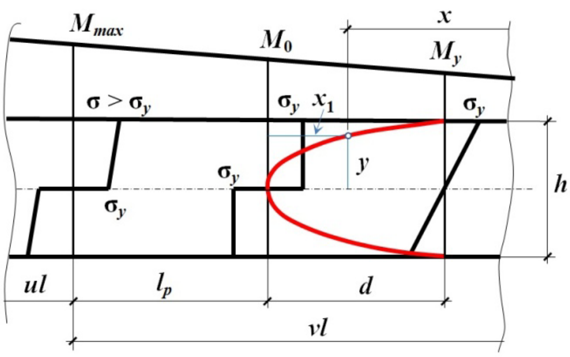

Figure 3. Plastic and elasto-plastic zones.

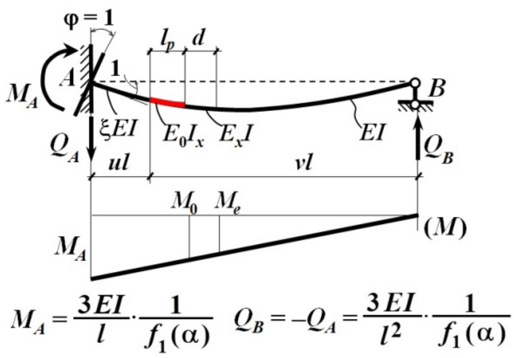

Figure 4. Design scheme of beam with ESPZ (“fixed” – “pinned”) at a unit turn of fixed support.

Equal strength plastic zones. As it follows from the review, when the deformation of the frame caused by the seismic action, PZs can occur in the end parts of both horizontal frame elements — crossbars, and vertical elements — columns. The procedure of design an ESPZ for horizontal frame elements is shown below (Fig. 2).

In case of the linear law of the moment diagram, it is also convenient to take a linear dependence of the expression of the area moment of inertia for the creation of an ESPZ $\left(x \in \left[lv - l_{pi}, lv\right]\right)$:

$$I_x = I\frac{x}{l(v - \alpha)} \tag{2}$$

For standard beam supported according to the "fixed – pinned" concept, the rated forces for the rotating the fixed support by an angle $\varphi=1$ (Fig. 4) are shown. The correction nonlinear function $f_1(\alpha)$ has the form:

$$f_1(\alpha)=\left(1-v^3\right)/\xi+3\alpha\beta(v-\alpha/2)/k_0+m\beta^3(6-4m+\frac{6}{5}m^2)+\beta^3(1-m)^3, \quad (3)$$

where

$$\beta=(v-\alpha), m=\left(1-\frac{M_e}{M_0}\right). \quad (4)$$

$\alpha=l_p/l$, $k_0=E_0/E$, ξ is the stiffness coefficient of the support zone.

In the absence of PZ $(l_p=\alpha=0)$ nonlinear function (3) takes more simple form:

$$f_1(0)=(1-v^3)/\xi+v^3(1+3m-m^2+\frac{1}{5}m^3). \quad (5)$$

The dimensionless function (3) contains four terms, each of which takes into account the contribution made to the overall ductility δ_{11} by the corresponding bar section, including the reinforcement zone (1st term), the plastic zone (2nd term), and the elasto-plastic zone (3rd term), elastic part (4rd term).

The 2nd term in (3) was obtained for a section of the length l_{pi} taking into account the variable stiffness (2):

$$\delta_{11}^{(PZ)}=\int_{vl-l_p}^{vl}\frac{x^2dx}{E_0I_x}=\int_{vl-l_p}^{vl}\frac{xl(v-\alpha)dx}{E_0I}=\frac{l^3}{3EI}\cdot 3\alpha(v-\alpha)(v-\alpha/2)/k_0.$$

Third term for the part with length $d=m\beta l$ was obtained with the variable stiffness E_xJ taking into account (1):

$$\delta_{11}^{(EPZ)}=\int_{vl-l_p-d}^{vl-d}\frac{x^2dx}{E_xI}=\frac{\sqrt{d}}{EI}\int_{vl-l_p-d}^{vl-d}\frac{x^2dx}{\sqrt{vl-l_p-x}}=\frac{l^3}{3EI}\cdot m(v-\alpha)^3(6-4m+\frac{6}{5}m^2).$$

During nonlinear calculation of the frame taking into account PZ the correction function such as (3) and (5) are used for the various standard beams that form a basic structure of DM. Nonlinear calculation is aimed at determining the limiting values of bending moments (M_p diagram) and limiting load F_p for the certain length of PZ l_p.

Three stages of frame calculation (elastic, elasto-plastic and plastic).

Elastic stage. A definition of the yield moments (M_{el} diagram) and the yield load F_e occurs at this stage:

- plotting the bending moment M diagram arising under the action of given load F;
- determination the ratio $k_e=M_e/M_j$ for the critical cross-section *j* with the moment M_j;
- with the help of coefficient k_e the M diagram and the load F getting closer to the yield level:

$$M_{el}=k_eM,\ F_e=k_eF. \quad (6)$$

Elasto-plastic stage. According to 1st prerequisite a definition of the plastic moment M_{p0} diagram and the plastic load F_{p0} for the length of PZ l_p = 0:

- calculation of non-dimensional functions $f_j(0)$ such as (5);
- determination of the stiffness matrix based on function $f_j(0)$ in DM basic structure;

– solving the system of canonical equations of DM from unit load and plotting the diagram of bending moment $\bar{M}$;
– determination of the incremental load dF according to equality of incremental moment $dM_k = \bar{M}_k \cdot dF$ and ordinate $(M_0 - M_e)$ in cross-section k on the line between RZ and EPZ:

$$dF = \frac{M_e}{\bar{M}_k} \cdot \frac{m}{1-m}, \tag{7}$$

– determination of the limiting load F_{p0} and the moment diagram M_{p0} (for l_p = 0):

$$F_{p0} = F_e + dF, M_{p0} = M_{el} + \bar{M} dF. \tag{8}$$

The plastic stage of the calculation is performed at a given PZ length l_p using the method of sequential loadings [26]. For each loading stage dF, we use incremental ratios connecting the diagrams of incremental moments and incremental loads.

Incremental system of resolving equations of DM has the form:

$$K(\alpha_{i-1}) dZ_i + R_{dF,i-1} = 0, \tag{9}$$

$$dZ_i = -\left[K(\alpha_{i-1})\right]^{-1} \cdot R_{dF,i-1}, \tag{10}$$

$$dM_{pi} = \bar{M}(\alpha_{i-1}) \cdot dZ_i + dM_{F,i-1}, \tag{11}$$

where $K(\alpha_{i-1})$ is the stiffness matrix of the frame including PZ at the 1st step of loading;

$R_{dF,i-1}$ is the response vector in DM basic structure caused by incremental load dF;

dZ_i is the incremental displacement vector;

$\bar{M}(\alpha_{i-1}), dM_{F,i-1}$ are the moment matrix caused by a unit loads and the incremental moment vector caused by incremental loads obtained in DM basic structure.

For the first loading stage, the initial PZ length l_{p1} can be taken based on the linear nature of the distribution of forces, for example, for the diagram M_{p0} multiplied by the coefficient $n = 1 + dF / F_e$. Based on the calculated correction (nonlinear) functions $f_j(\alpha_1)$, where $\alpha_1 = l_{p1}/l$, we form the coefficients (reactive forces) of the system of canonical equations (10) and the right sides of the equations from incremental loads dF. During the action of a horizontal seismic load the vector $dM_F^{(i-1)}$ in (12), is usually equals zero. After solving the system (11) and obtaining the diagram of incremental moments dM_{p1}, we build a resulting diagram: $M_{p1} = M_{p0} + dM_{p1}$, from which we calculate the PZ length l_{p2} for the next iteration step by the maximum value of the moment ($> M_0$). We simultaneously determine the current limiting load: $F_{p1} = F_{p0} + dF$. The obtained length is used to determine nonlinear functions $f_j(\alpha_2)$ for the second loading stage. In each i-iteration, we built: the incremental moment diagram dM_{pi}, the resulting diagram M_{pi}, the limiting load F_{pi}:

$$M_{pi} = M_{p,i-1} + dM_{pi}, F_{pi} = F_{p,i-1} + dF, \tag{12}$$

correction functions $f_j(\alpha_i)$ and the PZ length l_{pi}. The loading process continues until the obtained value does not reach the specified length l_p according to the inequality:

$$(l_p - l_{pi}) \le eps. \tag{13}$$

The proposed approach is illustrated by an example of a static calculation of a two-story frame on the action of horizontal forces simulating the seismic impact.

3. Results and Discussion

The design scheme of a two-story steel frame is shown in Fig. 5a (F = 40 kN, F_1 = –0.3F, $F_2 = F$, l = 300 cm, h_1 = 1.9l, h_2 = 1.6l). The crossbar of the lower story is made of a wended I-beam No. 26 (shelf - sheet 0.6×12.0 cm; wall - sheet 0.5×24.8 cm: I_x = 2958.5 cm^4; W_x = 227.58 cm^3); the crossbar of the top floor and the vertical elements are made of twin channels No. 20.

The strength and deformability characteristics are yield stress and ultimate strength, respectively: σ_y = 345 MPa, σ_u = 490 MPa, set after break ε_u = 0.21. The modulus of elasticity is E = 2.1·10^5 MPa, the modulus of hardening is $E_0 = (\sigma_u - \sigma_y)/(\varepsilon_u - \sigma_u / E) =$ 647.33 MPa. The elastic moment and the plastic moment are, respectively: $M_e - W_x\sigma_y =$ 78.51 kN·m, $M_0 = W_0\sigma_y =$ 91.08 kN·m, where W_0 = 1.16W_x; flexural stiffness of the bars – EI = 6212.85 kN·m^2, $E_0 I$ = 20.59 kN·m^2; the coefficient k_0 = 0.0033.

The preliminary calculation shows that the maximum bending moments occur in the end parts of the crossbar of the 1st floor. The PZ is designed at u = 0.05 and ξ = 1.5 (Fig. 5a).

The example aims to show the method of nonlinear calculation of frame using DM with determination of limit loads F_p for the given ESPZ length l_p. The lengths of PZ from 2 cm to 14 cm, multiple of 2 cm, are considered.

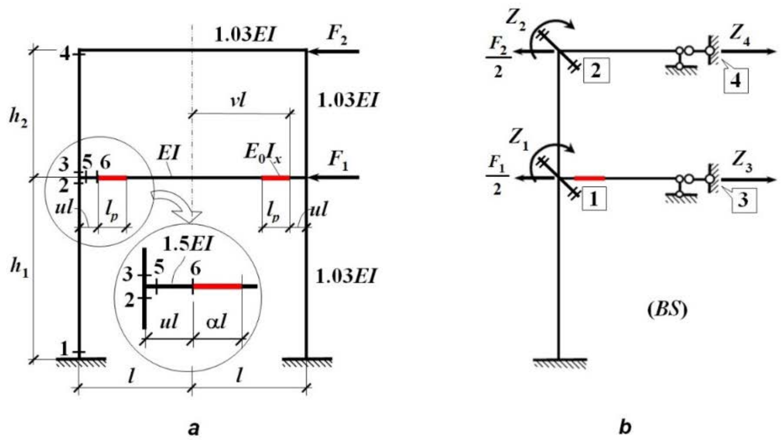

Figure 5. Design scheme of a two-story frame with plasticity zones in the crossbar of the 1st floor (a); b – basic structure of the DM taking into account the frame symmetry.

Due to the frame symmetry, the basic structure of the MD has four unknowns – two angular and two linear displacements Z_k (Fig. 5b). The numbering of additional bonds is shown by the numbers in small squares. For the plotting the diagram of unit moment M_1 we use the solution obtained for standard beam on Fig. 4 for the rotating the fixed support by an angle φ = 1 taking into account (5) within the length of PZ. The relative length α_i of the ESPZ is formed in a nonlinear process at each i-th loading stage.

The pattern of solving is shown below. From the preliminary frame calculation (at F = 40 kN), we obtain the highest stresses in section 6 (Fig. 5a). According to (6) (at k_e = 1.15), we will obtain a moment diagram M_{el} and the yield load F_e = 46.08 kN. As a result of elasto-plastic calculation (7), (8) we will obtain a values of limiting load F_{p0} = 54.1 kN and a moment diagram M_{p0} (at l_p = 0). The diagram M_{p0} is shown at right half of the frame (Fig. 6, blue, the values are given in brackets).

Coeffisients of the system of canonical equations of DM (9) at i th step of loading are:

– the elements of stiffness matrix $K(\alpha_i)$:

$$r_{11} = \left(4.732 + 3\frac{1}{f_1(\alpha_i)}\right)\frac{EI}{l}, r_{12} = 1.284\frac{EI}{l}, r_{13} = 0.701\frac{EI}{l^2}, r_{14} = -2.408\frac{EI}{l^2}, r_{22} = 5.652\frac{EI}{l},$$

$$r_{23} = -r_{14}, r_{24} = r_{14}, r_{33} = 4.808\frac{EI}{l^2}, r_{34} = -3.01\frac{EI}{l^3}, r_{44} = -r_{34};$$

– the elements of the vector R_{dFi} from incremental loading dF:

$$R_{1dF} = R_{2dF} = 0, R_{3dF} = -0.15dF, R_{4dF} = 0.5dF.$$

During the iterations when finding the limiting load for a given length l_p, we adjust the parameter α_i and the function (3) $f_1(\alpha_i)$.

A diagram of incremental bending moments for the 1st loading stage dF = 0.087 kN is shown on the left half of the frame (Fig. 6). At the initial stage, when we set the PZ length on the assumption of a linear nature of the distribution of moments: $l_{p0} = vl(1 - M_0/M_6)$ = 0.142 cm, where $M_6 = 1.0005M_0$, we form the correction function (3) f_1 = 1.614. After solving the system of the canonical equations of the DM and building the diagram of incremental moments dM_{p1} (shown on the left half of the frame, Fig. 6), we obtain the resulting diagram $M_{p1} = M_{p0} + dM_{p1}$ (the diagram M_{p1} is on the right half of the frame, Fig. 6). According to the results of the 1st iteration, the ESPZ length was l_{p2} = 0.392 cm, the load was $F_{p1} = F_{p0}+dF$ =54.2 kN. At the next loading steps for a given length l_p = 2 cm, the following results were obtained: l_{pi} = 2.001 cm, F_{pi} = 54.77 kN. The final nonlinear moment diagram M_p is shown on the left half of the frame (Fig. 7). The bending moment at the left end of the ESPZ (section 6) was M_6 = 91.72 kNm > M_0 = 91.08 kNm. The stresses in the supporting part of the frame were: σ_1 = –238 MPa, in the upper node σ_4 = 236.2 MPa; the stresses in the node of the 1st floor σ_5 = 282.8 MPa < σ_y = 345 MPa; $\sigma_6 = \sigma_7 = \sigma_y$.

The moment diagram M_p for the length l_p = 14 cm obtained at the limiting load F_p = 59.8 (65.18) kN is shown on the right half of the frame (Fig. 7). Stresses in support zone of frame: σ_1 = 344.6 MPa, in upper joint σ_4 = 341.6 MPa, in 5th joint σ_5 = 295.4 MPa, stresses $\sigma_6 = \sigma_7 = \sigma_y$.

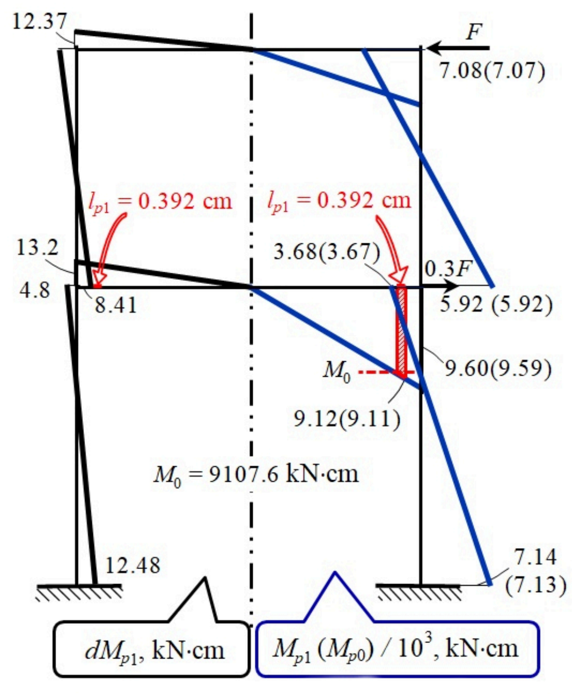

Figure 6. Bending moment diagrams at the first loading step at l_{p1} = 0.392 cm: to the left – incremental dM_{p1}.

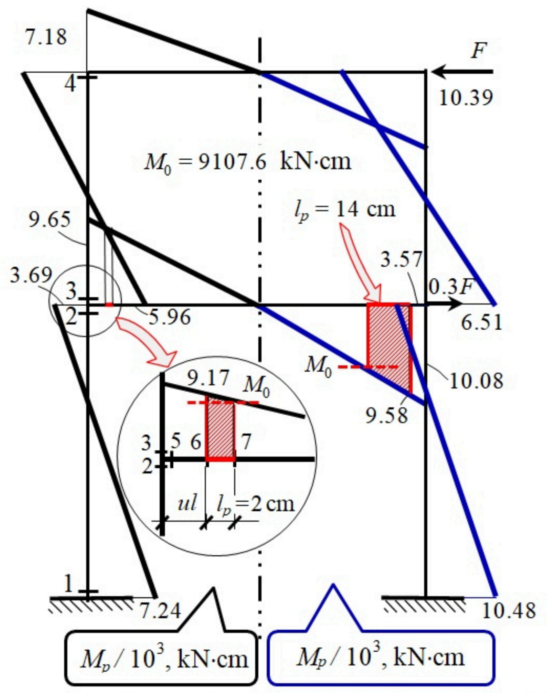

Figure 7. Bending moment M_p at the ESPZ length: l_p = 2 cm (to the left); l_p = 14 cm (to the right).

The nature of the change of bending moments depending on external load is shown at Fig. 8. Beginning with yield level when F_e = 46.075 kN the moments for each cross-section (shown in numbers) show weak nonlinearity at first (before PZ appears with F_{p0} = 54.11 KN). Then it begin to deviate significantly from the linear characteristics of the moments (dotted lines on the graph). Horizontal dashdotted lines show the level of load bearing capacity of the frame elements. For RZ (section 5) it is equals 1.34M_0.

Fig. 9 shows more common picture of the change of limiting loads depend on ESPZ length. Graphs show two limiting load curved lines for corresponding lengths l_p obtained when the plastic deformations in EPZ was taken into account (red line) and when it was not (blue line). The differences of values do not exceed 1%. Collapse load P_0 = 77.18 kN is calculated by limiting equilibrium method and shown by the black horizontal line.

For comparison consider the analysis of the steel frame performed in articles [19], [20]. One of the models of the frame (S3 model) considered by the authors of [19], [20] has a number of similar features with the model given in current study:

the lengths of plastic zones: the lengths l_p from 0 cm to 14 cm in steps of 2 cm were considered in current study; the length l_p = 12 cm was considered in S3 model;

the location of PZ is nodal zone of the I-beam and besides the beam in the S3 model is composite;

presence of RZ with the length of 15 cm in current study (Fig. 5) and 29 cm in S3 model;

construction material in the current study and in S3 model have the same mechanical characteristics;

the plastic zone is presented as ESPZ;

However, there are significant differences between these two schemes associated with the formulation of the research problem and the design features of PZ. The main difference of S3 model is that this zone includes a composite rectangular layer with the size of 120×300 mm (20 mm steel plate and 100 mm UHPC layer) and friction damper instead of I-beam. The length of PZ is constant (l_p = 12 cm). The yielding of fibers in the layer of this zone causes by a cyclic load acting the crossbar in the vertical direction. The amplitude of cyclic load is 13.5 kN. It is transmitted to the PZ as a longitudinal force N which creates tension-compression deformations. The longitudinal force cannot exceed the value of 100 kN because the friction damper will slip otherwise.

It should be noted that the limiting load for PZ with the length of l_p = 12 cm is 66.42 kN (Fig. 9). From the above it follows that these differences do not allow us to compare the limiting loads of both cases.

Thus, a method is proposed to the nonlinear calculation of statically indeterminate frames based on the DM which can be used in the design of structural systems in regions of an increased seismic activity in addition to the limiting equilibrium method.

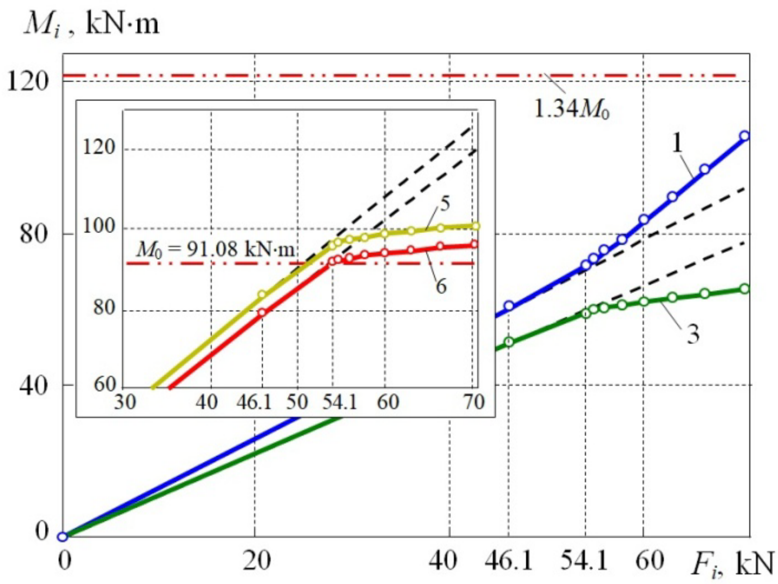

Figure 8. Bending moments in the frame cross-sections (numbers on graphs) depending on the load (dotted line is elastic response).

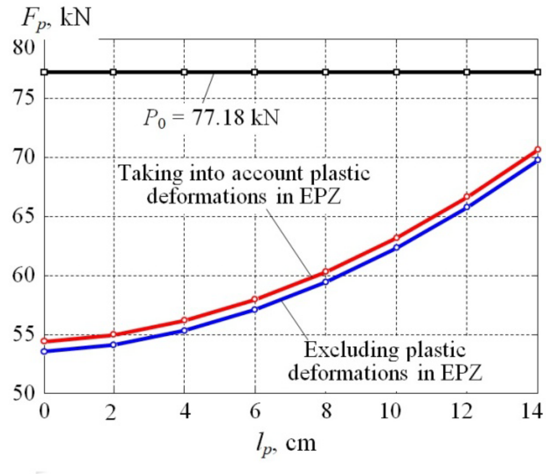

Figure 9. Limiting loads for the corresponding ESPZ.

Recommendations for future research. Further research is necessary to enhance the mathematical models of elastic-plastic calculation. Some important questions that need to be addressed are:

- simulation of the stress-strain state of the rod in the zone of non-linear deformations incorporating linear hardening of the material;
- one of the key areas of research is the development of a set of standard elements, such as statically indeterminate beams, in which calculations for single actions take into account the plastic zone. Specifically, it is important to address the issues related to calculating a rigidly fixed beam with two plastic zones located at its end parts;
- development and construction of a complete system of correction (nonlinear) functions, taking into account corrections to the linear calculation of the frame.

In addition, an important element of the study is the development of a methodology that provides the procedure for embedding the proposed scheme for the nonlinear calculation of frames into the algorithm of mathematical models for the calculation of seismic-resistant frames with PE.

4. Conclusions

This article proposes a new approach for conducting static analysis of bar frames, which incorporates plastic zones using the displacement method in conjunction with the sequential loading method. To implement this approach, two important theoretical problems had to be solved. The first involved developing a stress-strain model for a rod within the zone of elastic-plastic deformations using the linear theory of material hardening. The second involved calculating standard elements (statically indeterminate beams) for single actions, while taking into account special zones, such as plastic, elastoplastic, and reinforcement zones. Based on the research, the following conclusions were drawn:

1. To divide the zone of physically non-linear deformations of the beam into two areas (EPZ and PZ), two simplifying prerequisites were introduced. The simulation of stress-strain state of the rod in each of these areas was carried out. In EPZ, fibers' deformation occurs according to the theory of an ideal elastic-plastic body, without hardening and with a variable modulus of elasticity. In PZ, the deformation of all fibers occurs beyond the elastic limit, with a constant hardening modulus E_0.

2. In the EPZ section, the height of the elastic layer changes according to a quadratic law, therefore, for the variable modulus of elasticity, a quadratic dependence is also adopted, according to which the value of E_x is proportional to the ratio of the elastic core of the section $2y$ to the height of the section h.

3. In the plastic deformation zone, in order to ensure that the normal stresses do not exceed the yield strength and correspond to the zone of equal capacity, a linear dependence is adopted for the moment of inertia of the section, which is consistent with the linear character of the moment diagram.

4. The introduced dependences of the modulus of elasticity in the EPZ and the moment of inertia in the PZ are represented by convenient analytical functions. This allows to perform calculations of standard elements for single actions and construct correction (nonlinear) functions that take into account corrections to a linear calculation.

5. A computational scheme for a nonlinear analysis of statically indeterminate frames by the displacement method was created based on the calculation of standard elements and constructed correction functions. This was achieved using a step-by-step procedure of the method of successive

loadings with small steps. In this case, a complex nonlinear problem is divided into a sequence of linear problems, which are solved at each stage as elastic problems. The system of canonical equations of the displacement method is written in increments for fixed values of the correction functions $f_j(\alpha_i)$. During the transition from one loading stage to another, the length of the PZ l_{pi} increases, with subsequent adjustment of the correction functions.

6. An example of a nonlinear calculation of a 2-story steel frame for the action of horizontal forces was used to demonstrate the reliable operation of the nonlinear analysis algorithm. This included determining the limiting values of the load and internal forces (bending moment diagrams) for a given length of the PZ. All the main stages of the analysis were presented, including the limiting elastic, limiting plastic, intermediate, and final states of the structure model. The analysis showed that, in practical calculations of seismic-resistant frames, plastic deformations in the EPZ can be neglected.

References

1. Rzhanitsyn, A.R. Predel'noye ravnovesiye plastinok i obolochek [Limit equilibrium of plates and shells]. Moscow: Nauka, 1983. 288 p. (rus)
2. Paulay, T., Bull, I.N. Shear effect on plastic hinges of earthquake resisting reinforced concrete frames. Comite Euro-International du beton. Bulletin d' Information. Paris, 1979. 132. Pp. 165–172.
3. Gusella, F., Orlando, M., Peterman, K.D. On the required ductility in beams and connections to allow a redistribution of moments in steel frame structures. Engineering Structures. 2019. 179. Pp. 595–610. DOI: 10.1016/j.engstruct.2018.11.009
4. Travush, V.I., Krylov, S.B., Konin, D.V., Krylov, A.S. Ultimate state of the support zone of reinforced con-crete beams. Magazine of Civil Engineering. 2018. 83(7). Pp. 165–174. DOI: 10.18720/MCE.83.15
5. Ehsani, R.E., Sharbatdar, M.K.Sh., Kheyroddin, A.Kh. Ductility and moment redistribution capacity of two-span RC beams. Magazine of Civil Engineering. 2019. 90(6). Pp. 104–118. DOI: 10.18720/MCE.90.10
6. ATC-40 Seismic Evaluation and retrofit of concrete buildings. California. USA, 1996. 334 p.
7. NZS 3101. Part 2. 2. 2006. Code of design practice for the design of concrete structures. New Zealand Standrds Association. Wellington, 17 p.
8. Eurocode 8 (EUR 25204 EN – 2012): Seismic design of buildings. Worked examples. 522 p.
9. Zhao, X., Wu, Y.-F., Leung, A.Yt., Lam, H.F. Plastic length in reinforced concrete flexural members. Procedia Engineering. 2011. 14. Pp. 1266–1274. DOI: 10.1016/j.proeng.2011.07.159
10. Inel, M., Ozmen H.B. Effects of plastic hinge properties in nonlinear analysis reinforced concrete buildings. Engineering Structures. 2006. 28. Pp. 1494–1502. DOI: 10.1016/j.engstruct.2006.01.017
11. Yuan, F., Wu, Y.-F. Effect of load cycling on plastic hinge length in RC columns. Engineering Structures. 2017. 147. Pp. 90–102. DOI: 10.1016/j.engstruct.2017.05.046
12. Yuan, F., Wu, Y.-F., Li, C.-Q. Modelling plastic hinge of FRP-confined RC columns. Engineering Structures. 2017. 131. Pp. 651–668. doi: 10.1016/j.engstruct.2016.10.018
13. Megalooikonomou, K.G., Tastani, S.P., Pantazopoulou, S.J. Effect of yield penetration on column plastic hinge length. Engineering Structures. 2018. 156. Pp. 161–174. DOI: 10.1016 /j.engstruct.2017.11.003
14. Pokhrel, M., Bandelt, M.J. Plastic hinge behavior and rotation capacity in reinforced ductile concrete flexual members. Engineering Structures. 2019. 200. 109699. DOI: 10.1016/j.engstruct.2019.109699
15. Ning, C.L., Li, B. Probabilistic approach for estimating plastic hinge length of reinforced concrete columns. ASCE Journal of structural engineering. 2016. 142(3). 04015164(15). DOI: 10.1061 /(ASCE)ST.1943-541X.0001436
16. Ahmadi, S.A., Pashaei, M.H., Jafari-Talookolaei, R.A. Three-dimensional elastic-plastic pulse response and absorption of curved composite sandwich panel using DQ – Newmark method. Engineering Structures. 2019. 189. Pp. 111–128. DOI: 10.1016/j.engstruct.2019.03.041
17. Sosnin, A.V. Two-step-state reinforcement estimation technique of the elements of rc frame buildlngs and structures under seismic loads using pushover analysis concept. Part 1: research objective, technique framework, research information base and strategy of determining of hinge zone features. Bulletin of the South Ural State University. Ser. Construction Engineering and Architecture. 2018. 18(1). Pp. 5–31. (rus.). DOI: 10.14529/build180101
18. Alhasawi, A., Heng, P., Hjiaj, M., Guezouli, S., Battini, J.-M. Co-rotational planar beam element with generalized elasto-plastic hinges. Engineering Structures. 2017. 151. Pp.188–205. DOI: 10.1016/j.engstruct.2017.07.085
19. Heng, P., Alhasawi, A., Battini, J.-M., Hjiaj, M. Co-rotating rigid beam with generalized plastic hinges for the nonlinear dynamic analysis of planar framed structures subjected to impact loading. Finite elements in analysis and design. 2019. 157. Pp. 38–49. DOI: 10.1016/j.finel.2018.11.003
20. Tidemann, L., Krenk, S. A robust frame element with cyclic plasticity and local joint effects. Engineering Structures. 2018. Vol. 168. Pp. 191–204. DOI: 10.1016/j.engstruct.2018.04.041
21. Deng, K., Wang, T., Kurata, M., Zhao, C., Wang, K. Numerical study on a fully-prefabricated damage-tolerant beam to column connection for an earthquake-resilient frame. Engineering Structures. 2018. 159. Pp. 320–331. DOI: 10.1016/j.engstruct.2018.01.011
22. Deng, K., Zheng, D., Yang, C., Xu, T. Experimental and analytical study of fully prefabricated damage-tolerant beam to column connection for earthquake-resilient frame. ASCE Journal of structural engineering. 2019. 145(3). 04018264(10). DOI: 10.1061/(ASCE)ST.1943-541X.0002270
23. Potapov, A.N. The elastoplastic calculation of frames using the displacement method. International Journal for Computational Civil and Structural Engineering. 2019. 15(3). Pp. 120–130.
24. Eom, T., Park, H., Hwang, H., Kang, S. Plastic hinge relocation methods for emulative PC beam-column connections. ASCE Journal of structural engineering. 2016. 142 (2). DOI: 10.1061/(ASCE)ST.1943-541X.0001378
25. Sokolovsky, V.V. Teoriya plastichnosti [Theory of the plasticity]. Moscow: High School, 1969. 608 p. (rus)

26. Petrov, V.V. Nelineynaya inkremental'naya stroitel'naya mekhanika [Nonlinear incremental structural me-chanics]. Moscow: Infra-Inzheneriya, 2014. 480 p. (rus)

Information about authors:

Alexandr Potapov, *Doctor of Technical Sciences*

ORCID: https://orcid.org/0000-0002-9079-2667

E-mail: potapov.alni@gmail.com

Sergei Shturmin*,*

ORCID: https://orcid.org/0000-0002-7911-2691

E-mail: sturmakmlp@gmail.com

Received 24.08.2020. Approved after reviewing 10.03.2023. Accepted 11.03.2023.